Miriam Zarza Moreno

Licenciada em Física

Monte Carlo simulations for dosimetric verification in photon and electron beam radiotherapy

Dissertação para obtenção do Grau de Doutor em
Engenharia Biomédica

Orientador: Doutora Grisel Mora Paula, CFNUL/FC
Co-orientador: Professora Doutora Adelaide de Jesus, FCT/UNL
Professor Doutor Nuno Teixeira , FCM/UNL

Júri:

Presidente: Doutor Fernando José Pires Santana
Arguente(s): Doutor José Pedro Miragaia Trancoso Vaz
Doutor Carlos Manuel Azevedo Sousa Oliveira

Vogais: Doutor Francisco José Cerqueira Alves
Doutor Nuno José Coelho Gomes Teixeira
Doutora Maria Adelaide de Almeida Pedro de Jesus
Doutora Grisel Margarita Mora Paula

FACULDADE DE CIÊNCIAS E TECNOLOGIA
UNIVERSIDADE NOVA DE LISBOA

To all of them who believe in the possibility of making real their ”always” *dream...*

Forte não é aquele que nunca cai mas sim aquele que sempre se levanta

Acknowledgments

..... October 2005, the beginning of a new adventure .....

Back stay the cold Germany, the country where I began my interest in the physics research. New year, new life and why not Lisbon? All the stars were showing me the way to Portugal; an unknown country for me at that time, but nowadays my home country.

I arrived in Lisbon with an adventure in mind: to do my Ph.D. work, an ”always” dream. I knew that it would not be an easy task, but I was sure that it would be an excellent opportunity for my professional and personal life. Now, after 6 years of changes and efforts, I finish this adventure; an adventure which would have been not possible without the support, help and love of a long list of people:

First of all, I would like to express my gratitude to my supervisor Doctor Grisel Mora for the inestimable support in pedagogical aspects and also in theoretical and practical supports that she has always manifested along this work. A special thanks for supplying the necessary criticism to evaluate the papers and this thesis.

Professor Dr. Adelaide Pedro de Jesus for having orientated this work and, particularly, for believing in me from the first time I met her at Bochum (Germany) in 2004 until today. She gave me the opportunity to join the Lisboa group in 2005, introducing me to the exciting field of nuclear astrophysics in Portugal for one year. I want also to thank her for allowing me to reach a dream in the medical physics area, the present Ph.D. work. Her constant support and advices during all the phases of my work is gratefully acknowledged.

I would like to thank Professor Dr. Nuno Teixeira for having oriented the experimental part of this thesis and for opening the door of the radiotherapy departments where this research has been developed.

I would like to express a very special thanks to all the physicist colleagues working at the different

radiotherapy departments where this work has been developed: Centro Oncologico Dra. Natalia Chaves, SAMS of Lisbon and Hospital de Santa Maria. A special thanks to Enga. Iola Cardoso, Engo. Luis Madureira, Enga. Ana Catarina Souto and Enga. Dalila Mateus for their great patience in listening the mountains of doubts that I had during this work. Thanks for the fruitful discussions we had.

To Fundação para a Ciências e Tecnologia for its financial support through the grant.

To Centro de Física Nuclear da Universidade de Lisboa for its financial and technological supports to do my Ph.D.

To my recent colleagues of the ENAPG group, a great thanks for their support in the last phase of the work. A special thanks to Enga. Ana Henriques, Engo. Jorge Machado and Dr. Pamela Teubig for believing in me during the last and difficult phase of the work. I'll never forget our coffee breaks.

To my "scientific father" and friend, Daniel Galaviz Redondo, for introducing me in the world of physics research in 2003 at Darmstadt (Germany). "Dani, aquí la tienes. Gracias por haberme dado a conocer el mundo de la investigación en física y especialmente por haber estado cerca en los momentos más difíciles del camino".

To my best portuguese friends Micaela Fonseca and Cecilia Borges for all the positive energy and strength that they always transmitted me along this work.

To D. Luisa, Sr. Vitor, Vitor Luis, Susie and my lovely Leonardo and Miriam, for the special moments I spent with all of them during this time. They are a wonderful family and I'll always take them in my heart. "Obrigado pela amizade e o carinho que me ofereceram durante estes anos".

To you, Valter, for being always close even a thousand miles of distance away. We can shine! "Obrigada por teres acreditado sempre no meu valor e me teres feito perceber que posso brilhar".

And, finally, I cannot finish my acknowledgments without thanking to my family who constantly supported me with their love and allowed me to complete this work. This thesis is dedicated to them.

"A mi familia por la fuerza y el cariño que me regalaron durante esta fase de mi vida. Papá, mamá, Carlos y abuelos, siempre estuvisteis presentes en mi mente y en mi corazón a pesar de la distancia. Luchasteis por hacer realidad mis sueños y nunca tendré amor suficiente para compensar todo aquello que hicisteis por mí. Esta tesis es vuestra."

..... Adventure finished! Being eager for the new one .....

Abstract

One of the primary requirements for successful radiotherapy treatments is the accurate calculation of dose distributions in the treatment planning process. Monte Carlo (MC) dose calculation algorithms are currently recognized as the most accurate method to meet this requirement and to increase even further dose accuracy.

The improvements in computer processor technology and the development of variance reduction techniques for calculations have led to the recent implementation and use of MC algorithms for radiotherapy treatment planning at many clinical departments.

The work conducting to the present thesis consists of several dosimetric studies which demonstrate the potential use of MC dose calculations as a robust tool of dose verification in two different fields of external radiotherapy: electron and photon beam radiotherapy.

The first purpose of these studies is to evaluate dose distributions in challenging situations where conventional dose calculation algorithms have shown some limitations and it is very difficult to measure using typical clinical dosimetric procedures, namely in regions containing tissue inhomogeneities, such as air cavities and bones, and in superficial regions.

A second goal of the present work is to use MC simulations to provide a detailed characterization of photon beams collimated by a multileaf collimator (MLC) in order to assess the dosimetric influences of these devices for the MC modeling of Intensity Modulated Radiotherapy (IMRT) plans. Detailed MC model of a Varian 2100 C/D linear accelerator and the Millenium MLC incorporated in the treatment head is accurately verified against measurements performed with ionization chambers and radiographic films.

Finally, it is also an aim of this thesis to make a contribution for solving one of the current problems associated with the implementation and use of the MC method for radiotherapy treatment planning, namely the clinical impact of converting dose-to-medium to dose-to-water in treatment planning and dosimetric evaluation. For this purpose, prostate IMRT plans previously generated by a conventional dose algorithm are validated with the MC method using an alternative method, which involves the use of non-standard CT conversion ramps to create CT-based simulation phantoms.

Keywords: Monte Carlo algorithms, Radiation Dosimetry, Air Inhomogeneity, Multileaf Collimator, Superficial Dose, Intensity Modulated Radiotherapy.

Contents

THESIS AIM AND OUTLINE **xix**

I INTRODUCTION

1 Introduction to external beam radiation therapy **3**

1.1 Brief introduction 3

1.2 Techniques in external radiotherapy 5

1.3 The importance of accuracy in radiation delivery 8

2 Fundamentals of radiotherapy physics and dosimetry **11**

2.1 Interaction of ionizing radiation with matter 11

2.1.1 Photon interactions in matter 12

2.1.1.1 Types of interaction mechanisms 12

2.1.1.2 Attenuation coefficients 18

2.1.1.3 Relative predominance of individual effects 20

2.1.2 Electron and positron interactions in matter 21

2.1.2.1 Types of interaction mechanisms 21

2.1.2.2 Stopping power and range 23

2.1.2.3 Restricted stopping power 26

2.2 General concepts of clinical radiation dosimetry 27

2.2.1 Basic dosimetric quantities 27

2.2.2 Basic theorems and principles 31

2.2.2.1 Inverse-square law 31

2.2.2.2 Charged particle equilibrium 32

2.2.2.3 Cavity theory 34

2.2.3 General considerations of basic dosimetry 36

II MATERIALS AND METHODS

3 Radiation treatment and dosimetry equipment 41

3.1 Medical linear accelerator 41

3.1.1 General description of an electron linear accelerator 42

3.1.2 Treatment head components 43

3.2 Radiation dosimetry equipment 47

3.2.1 Ionization chamber dosimetry 48

3.2.2 Film dosimetry 53

3.2.2.1 Radiographic film 54

3.2.2.2 Radiochromic film 57

4 Monte Carlo simulation techniques in radiation therapy 61

4.1 General fundamentals of the Monte Carlo method 61

4.2 Why use Monte Carlo in radiotherapy? 63

4.3 Simulation of Photon and Electron Transport 65

4.4 The EGSnrc Code System 73

4.4.1 General Description 73

4.4.2 BEAMnrc: A linac modeling tool 77

4.4.3 DOSXYZnrc: Phantom dose calculation tool 78

4.4.4 Variance Reduction Techniques and Efficiency Improvements 81

III ELECTRON BEAM RADIOTHERAPY APPLICATION

5 Dosimetric effect of shallow air cavities in high energy electron beams 87

5.1 Motivation 87

5.2 Material and Methods 89

5.2.1 Air cavity phantom 89

5.2.2 Monte Carlo simulations 90

5.2.2.1 Benchmark of linear accelerator model 94

5.2.2.2 Electron Beam Characterization 96
5.2.3 Measurements 100
5.2.3.1 Home-built PMMA phantom 100
5.2.3.2 Radiochromic film dosimetry 101
5.3 Results 104
5.3.1 Air cavity effect for standard 10 x 10 cm^2 field 104
5.3.1.1 Central-axis PDD variation due to the presence of air cavity 104
5.3.1.2 Off-axis dose variation due to the presence of the air cavity 108
5.3.1.3 Influence of air cavity on spectral distributions 110
5.3.2 Air cavity effect for fields shaped by Cerrobend blocks 115
5.4 Conclusions 117

IV PHOTON BEAM RADIOTHERAPY APPLICATION

6 Monte Carlo modeling of a 6 MV Varian 2100C/D medical accelerator 123
6.1 Linear accelerator model 123
6.2 Determination of primary electron beam parameters 131
6.3 Beam spectral characterization at phantom surface 143
6.4 Conclusions 152

7 Varian Millennium 120-leaf MLC in Monte Carlo simulations 153
7.1 Monte Carlo MLC model description 153
7.2 Experimental commissioning of MLC model 157
7.2.1 Monte Carlo simulations 157
7.2.2 Experimental measurements 160
7.2.3 Benchmark tests and results 161
7.3 Conclusions 173

8 Assessing Multileaf Collimator effect on the build-up region for 6 MV photon beams 175
8.1 Motivation 175
8.2 Monte Carlo evaluation of the MLC effect 178
8.2.1 Monte Carlo calculation techniques 178

8.2.2 Dose contribution from the total- and MLC-scattered particles: dependence on field size . . . 181
8.2.3 MLC effect on spectra at the phantom surface . . . 184
8.3 Experimental evaluation of the MLC effect . . . 188
8.3.1 Ionization chamber measurements . . . 188
8.3.2 MLC effect on depth ionization curves: dependence on field size . . . 189
8.4 Experimental validation of MC calculated dose in the build-up region . . . 191
8.5 Conclusions . . . 194

9 The use of non-standard CT conversion ramps for Monte Carlo verification of 6 MV prostate IMRT plans 197
9.1 Motivation . . . 197
9.2 Material and methods . . . 200
9.2.1 Treatment planning . . . 200
9.2.2 Monte Carlo calculations . . . 202
9.2.3 CT conversion ramps . . . 205
9.2.4 Dose to medium to dose to water conversion . . . 207
9.3 Results and discussion . . . 208
9.3.1 Material composition and density effect on MC dose distributions . . . 208
9.3.2 Eclipse TPS and MC dose comparison . . . 214
9.4 Conclusions . . . 217

V CONCLUSIONS

10 Conclusions 221

List of Figures

1.1 Schematic illustration of three different radiotherapy modalities 6
1.2 Dose dependence of tumor control probability (TCP) and the probability of normal tissue complication (NTCP) 9

2.1 Schematic diagrams of the main interaction processes of the photons with matter . . 13
2.2 Mass attenuation coefficient for water 19
2.3 Relative importance of the three major types of photon interactions 20
2.4 Parameters in an electron collision with atom 22
2.5 Stopping power for electrons in tissue and bone compact (ICRU): Collision and radiative components 25
2.6 Relationship between absorbed dose and collision kerma for a megavoltage photon beam as function of depth in a medium 33
2.7 Diagram illustrating the definition of the percentage depth dose and transversal dose profiles in a rectangular phantom 37

3.1 Schematic drawing of the main components incorporating a medical linear accelerator and the collimator systems 42
3.2 Diagram showing the components of a typical medical linear accelerator head working in both photon and electron mode 44
3.3 Scheme of an ionization chamber emerged in water 48
3.4 Pictures of the PTW Semiflex of 125 cm^3 volume and PTW PinPoint chambers . . . 50
3.5 Pictures of the parallel-plate PTW Roos and Adv. Markus chambers 51
3.6 Typical response curve, i.e. net optical density versus dose curves of radiographic films for direct x-ray exposure 57
3.7 Composition of a Gafchromic EBT film 58

4.1 Schematic representation of the MC simulation of an electron by successive steps of *condensed history* . . . 68
4.2 Representation of the methodologies (class I and class II) adopted by MC algorithms of an electron discrete event . . . 70
4.3 Electron pathlength correction in a MC simulation . . . 71
4.4 Schematic drawing of the boundary problem in the condensed-history method for the simulation of the electron transport . . . 72
4.5 The structure of the EGSnrc code system . . . 76
4.6 DOSXYZnrc default ramp for converting CT-number to material density . . . 80

5.1 Recycling effect on DOSXYZnrc dose calculations . . . 92
5.2 Isodose distribution for a 12 MeV electron beam shaped by a cerrobend block . . . 93
5.3 Comparison of the water-air stopping power ratio given in the IAEA protocol (TRS-398) and those calculated for realistic Siemens Primus electron beams of 12 and 18 MeV using the SPRRZnrc code . . . 95
5.4 On-axis depth dose in a water phantom relative to the dose maximum and lateral profiles at depths below the water surface for the 12 and 18 MeV beams from Siemens Primus with 10 x 10 cm^2 field (100 cm SSD) . . . 96
5.5 Energy distributions and mean energy profiles of electrons and photons present in 12 and 18 MeV beams from Siemens Primus with 10 x 10 cm^2 field (100 cm SSD) . . . 98
5.6 Fluence profiles and angular distributions of electrons and photons present in the 12 and 18 MeV beams from Siemens Primus with 10 x 10 cm^2 field (100 cm SSD) . . . 99
5.7 Scheme of sagittal and transverse views of the home-built PMMA phantom including an air cavity with area S and thickness L used for measurements and modeled for MC dose calculations . . . 100
5.8 EBT film samples exposed by the 18 MeV electron beam in a heterogeneous phantom containing the cavity of 1 x 1 x 2.8 cm^3 . . . 102
5.9 Energy dependence of the calibration curve for Gafchromic EBT film . . . 104
5.10 On-axis PDD curves measured and MC calculated in heterogeneous phantom including an air cavity of varied area and thickness for an electron beam of 12 MeV . . . 105
5.11 On-axis PDD curves measured and MC calculated in heterogeneous phantom including an air cavity of varied area and thickness for an electron beam of 18 MeV . . . 107

5.12 MC calculated and measured X dose profiles (X axis) at 3.3 cm and 4.2 cm depth in an heterogeneous phantom for a 12 MeV electron beam 109
5.13 MC calculated and measured X dose profiles at 3.3 cm depth in an heterogeneous phantom for a 18 MeV electron beam 110
5.14 Electron energy spectra calculated at a depth of 3.3 cm in a PMMA phantom with and without an air cavity of varying dimensions, area S or thickness L, irradiated by a 12 MeV electron beam 112
5.15 Angular spectra of electrons calculated at a depth of 3.3 cm in PMMA homogeneous and heterogeneous phantoms with an air cavity of varying dimensions, area S or thickness L, irradiated by a 12 MeV and 18 MeV electron beams 114
5.16 MC calculated PDD curves in heterogeneous phantoms irradiated with an 12 MeV electron beam collimated using a cerrobend cutout 115
5.17 Calculated lateral profiles (3.3 cm) in heterogeneous phantoms irradiated with an 12 MeV electron beam collimated using a cerrobend cutout 116

6.1 Schematic drawing of Varian 2100C/D linac components modeled in Monte Carlo simulations 126
6.2 Schematic draw of (a) the bremsstrahlung target of W/Cu and (b) flattening filter geometry for 6 MV photon beam 128
6.3 Bremsstrahlung spectra generated by a 6.0 MeV electron beam with 1.0 mm radius . 129
6.4 Flowchart of the procedure to find the accurate description of the incident electron beam at the target, namely electron energy E_i and radius R_i. 133
6.5 Influence of the energy of incident electron beam on PDD curves for a 30 x 30 cm^2 field138
6.6 Influence of the energy of incident electron beam on lateral profiles for a 30 x 30 cm^2 field 140
6.7 Influence of electron beam radius on Y dose profile for a 30 x 30 cm^2 field 141
6.8 Lateral dose profile for 4 x 4 cm^2 and 10 x 10 cm^2 at several depths for the final benchmarked 6 MV photon beam 143
6.9 Planar fluence *vs* off-axis distance calculated with contributions from photons and electrons reaching a plane at 100 cm across 10 x 10 cm^2 field for a 6 MV photon beam144
6.10 ZLAST distributions of photons for the 10 x 10 cm^2 field for a 6 MV photon beam . . 147

6.11 On-axis energy spectra of photons and electrons reaching a plane at 100 cm and scored inside the 10 x 10 cm^2 field for a 6 MV photon beam 148
6.12 Comparison of photon energy spectra (on-axis) for 3 different field sizes at 100 cm SSD and 6 MV photon beam 149
6.13 Mean energies of the photons and electrons as function of the distance to the central beam axis for a 6 MV photon beam and a 10 x 10 cm^2 field at SSD of 100 cm 150
6.14 Angular distribution of photons and electrons at SSD = 100 cm inside a 10 x 10 cm^2 field for a 6 MV photon beam 151

7.1 Varian Millennium 120-leaf MLC geometry 154
7.2 Geometry of DYNVMLC CM modeling the Millennium MLC. 155
7.3 The effects of the interleaf air gap on the leakage profiles for a 6 MV photon beam . . 163
7.4 The effects of leaf density on the leakage profiles for a 6 MV photon beam 165
7.5 Film measured and MC calculated leakage transmission dose profile through opposing leaves completely closed at the central axis of a 10 x 10 cm^2 field defined by jaws for a 6 MV beam 167
7.6 Depth-dose and off-axis profiles (X and Y axis) measured with the PinPoint ion chamber and calculated with MC in water for MLC defined static fields 169
7.7 Film measured and MC calculated profile in water irradiated for a ”alternate even and odd” leaf shape with a 6 MV photon beam 170
7.8 Measured and calculated dose profiles for a pyramid intensity pattern delivered using a dynamic mode for a 6 MV photon beam 172

8.1 Schematic representation of the simulated geometry of the Varian 2100C/D linac head and water phantom, showing also the location of the two phase space scoring planes considered for the simulations. 178
8.2 Simulated water phantom geometry for surface and build-up dose calculations 180
8.3 MC calculated depth dose curves in the build up region for the MLC defined field size of 10 x 10 cm^2, 4 x 4 cm^2, 2 x 2 cm^2 in comparison to the MLC open field ones . . . 182
8.4 MC calculated depth dose curves in the build up region for the MLC defined field size of 3 x 7 cm^2 in comparison to the MLC open field respective one 183

8.5 Relative planar fluence of total particles and electrons as a function of the distance to the beam axis for different MLC defined field sizes 185
8.6 Contribution of particles and electrons scattered from jaws and MLC to relative planar fluence profile (X axis) for 10 x 10 and 2 x 2 cm^2 MLC defined fields 186
8.7 On-axis energy spectra of electrons reaching the scoring plane for 2 x 2 cm^2 and 10 x 10 cm^2 MLC defined fields and the respective MLC open fields 187
8.8 Comparison of measured PDIs in the dose build-up region of a water phantom for different MLC defined field and the respective MLC open field 190
8.9 Measured PDIs compared to MC calculated PDDs in the dose build-up region in water with a cylindrical and a Roos parallel-plate chambers for different MLC defined fields 191
8.10 Water to air stopping power ratios against depth calculated for different MLC defined fields and 6 MV photon beam 194

9.1 Transversal CT slices for patient 3 illustrating the delineations of the PTV volumes for each treatment phase, the femoral heads and the bladder) 201
9.2 Schematic diagram of set-up for the MC simulation of IMRT treatment plans performed using BEAMnrc code 203
9.3 The CT ramp for the conversion of CT values to material type and densities according to the conventional CTCREATE ramp 206
9.4 Comparison of dose profiles calculated along the X axis for MC phantoms (y = -16.13 cm) 209
9.5 Comparison of dose profiles calculated along the X axis for MC phantoms (y = -20 cm)210
9.6 Comparison of dose profiles calculated along the Y axis for MC phantoms (x= -6.03 cm and x= -0.78 cm) 211
9.7 DVHs of the PTV, rectum and left femoral head calculated by MC in patient phantoms built using different CT conversion ramps 213
9.8 Comparison of isodose distribution for the Phase I of the IMRT treatment in patient 1 calculated by Eclipse TPS and by Monte Carlo 215
9.9 Comparison of DVH curves calculated by Eclipse TPS and by Monte Carlo for the PTV, rectum and the left femoral head 216

List of Tables

1.1 Estimates of uncertainty in absolute dose for a complete radiotherapy procedure . . 10

4.1 CT numbers and density range for the four materials used in the ramp for converting CT numbers to material parameters 80

5.1 Variations of the thickness L and square area S of the air cavities considered in the study 89

6.1 Energy and radius combinations of incident electron beam impinging on target 133

6.2 Summary of the number of particles scored in the phase space file and the CPU time used for the BEAMnrc simulations for various field sizes using an electron beam of 6.2 MeV and 1.5 mm radius impinging on the bremsstrahlung target 134

6.3 Transport parameters and variance reduction techniques selected in the commission process of 6 MV photon beam 136

6.4 Photon fluence along the X-axis of photons and electrons contributions in a plane at 100 cm (SSD) for a 10 x 10 cm^2 field for a 6 MV photon beam 146

6.5 Photon fluence along the X-axis of photons and electrons contributions in a plane at 100 cm (SSD) for a 4 x 4 cm^2 field for a 6 MV photon beam 146

6.6 Photon fluence along the X-axis of photons and electrons contributions in a plane at 100 cm (SSD) for a 30 x 30 cm^2 field for a 6 MV photon beam 147

7.1 Film measured and MC calculated MLC transmission with different MLC leaf densities for a 6 MV photon beam 164

7.2 MLC transmission through the closed leaves measured and MC calculated with different sizes of MLC abutting leaf air gap for a 6 MV photon beam 166

8.1 Surface dose calculated in the voxel from 0 to 0.025 cm depth for different MLC defined field sizes 184
8.2 Geometric characteristics of the ionization chambers used for the surface and build-up dose measurements 189
8.3 MC calculated and measured doses at depths of 0.25 and 0.52 cm in a water phantom for a 6 MV beam and three different MLC defined fields 192

9.1 Typical number of beams, beam angles and jaws openings of IMRT treatment plans . 202
9.2 CT conversion ramps used to build Monte Carlo phantoms from the CT data set of patients 207

List of Abbreviations, Acronyms and Symbols

A	Mass number
AE	Electron Threshold Energy for Explicit Electron Interaction Modeling
AP	Photon Threshold Energy for Explicit Electron Interaction Modeling
CAX	Central Axis
CM	Component Module
CPE	Charged Particle Equilibrium
$CSDA$	Continuous Slowing Down Approximation
CT	Computed Tomography
d_{eff}	Shift of effective point of measurement
$DICOM$	Digital Imaging and Communications in Medicine
D_{max}	Maxima Absorbed Dose
d_{max}	Depth of Maximum Dose
D_{med}	Absorbed dose in a medium
DVH	Dose Volume Histogram
$ECUT$	Electron Cutoff Energy
EGS	Electron Gamma Shower
Gy	Gray
I	Intensity of radiation
$ICRP$	International Commission on Radiological Protection
$ICRU$	International Commission on Radiation Units and Measurements

$IMRT$	Intensity Modulated Radiation Therapy
$(\overline{L}/\rho)_{air}^{med}$	Restricted mass collision stopping power ratio of the medium-to-air
m	Mass
MeV	Mega electron-volt
MC	Monte Carlo
$MERT$	Modulated Electron Radiation Therapy
MLC	Multileaf Collimator
MU	Monitor Units
MV	Megavoltage
PBC	Pencil Beam Convolution
$PCUT$	Photon Cutoff Energy
PDD	Percentage depth dose
$PMMA$	Polymethyl methracrylate, ”Lucite”
$PRESTA$	Parameter reduced electron-step transport algorithm
PTV	Planning Target Volume
S_T	Total unrestricted stopping power in medium
S_c	Collision unrestricted stopping power
S_r	Radioactive unrestricted stopping power
$(S/\rho)_{air}^{med}$	Mass stopping power ratio of the medium-to-air
SAD	Source-Axis Distance
SSD	Source-Surface Distance
TPS	Treatment Planning System
Z	Atomic number
μ	Energy absorption coefficient in medium
ρ	Density

Thesis aim and outline

Motivation

External radiotherapy is currently the most common technique used for the treatment of many types of cancer. The main objective of radiotherapy lies in the delivering of a very accurate dose to a well-defined target volume with minimal absorbed dose to the surrounding normal tissue, especially highly radiosensitive organs. In order to achieve this goal, one of the primary requirements is to ensure that the treatments are delivered in accordance with the dosimetric intentions. It has been clearly demonstrated that, an overdosage of radiation can lead to severe side effects, while an underdosage can reduce significatively the probability for a patient cure.

The calculation of radiation dose distributions plays an important role in the treatment of patients requiring external radiotherapy. The accuracy of dose calculations is crucial to the quality of treatment planning and consequently to the effectiveness of the radiotherapy treatment.

Most of the conventional dose calculation algorithms implemented in the majority of the treatment planning systems at radiotherapy departments are known to be inaccurate when radiation disequilibrium conditions exist, such as near tissue inhomogeneities, for small radiation fields or for dose gradient regions (e.g. superficial regions). Examples of these algorithms are pencil-beam and superposition-convolution algorithms.

The validation of these dose calculation algorithms is commonly performed by comparisons with measured data. The reliability of measured data sets is however very dependent on several aspects, such as the stability of the accelerator (e.g., energy, output, flatness, and symmetry) or on the choice of detector and experimental set-up. These limitations may thereby restrict the number of comparison points and introduce dosimetric problems to the verification.

All above-mentioned limitations of conventional algorithms and measurements have become

even more significant since the implementation of new advanced radiotherapy techniques, such as 3D - conformal and Intensity Modulated Radiotherapy (IMRT) techniques. These techniques involve higher complexity in the planning and validation of the treatments due to the use of high-dose gradients regions, small fields and the incorporation of new dynamic collimation devices such as multileaf collimator (MLC), which can introduce important effects on the final dose output. Under these circumstances, the requirements of high accuracy for the dose calculations plays a more important role.

For the last years, dose calculation algorithms based on the Monte Carlo (MC) method have been shown to be a powerful tool to overcome the existing limitations, not only of conventional algorithms, but also of experimental procedures. These algorithms are currently recognized as the most accurate method to calculate dose, since particle histories are simulated explicitly based on physical interaction probabilities inside an arbitrary media for a wide range of complex radiation treatment conditions.

Due to the ability of the MC method to accurately compute dose for complex delivery scenarios along with the improvements in computer technology, this method has now the potential to replace conventional dose calculation algorithms in radiotherapy treatment planning systems and also to be used as alternative method to measurements for quality assurance of treatments, specially for those treatments delivered with advanced techniques. Currently, MC treatment planning systems are quickly becoming a real possibility in clinical settings.

The present thesis uses the MC method for the verification of calculated dose in two challenging situations: tissue inhomogeneity and surface regions. It aims, on one side, to circumvent problems associated with conventional procedures of dosimetric verification of radiotherapy treatments and, on the other side, enables the study of dosimetric and physical characteristics which are difficult or impossible to assess from measured data or conventional dose calculation algorithms.

In the context of the thesis, a detailed characterization of electron and photon beams of different energies and field configurations has also been performed using Monte Carlo simulations. The adequate beam characterization represents an essential component of the accuracy of dose calculation and it has become even more important with the implementation of more conformal and advanced radiotherapy techniques, such as Intensity of Modulated Radiotherapy (IMRT). The introduction of the dynamic conformation devices, such as multileaf collimators, in the accelerator heads to provide more conformed and modulated dose distributions can introduce changes in the characteristics of

the incident beams, demanding thus a better knowledge of the beam characteristics. The present work aims also to introduce a detailed assessment of the characteristics of the Varian Millenium 120-leaf MLC used for the MC modeling of IMRT plans.

It is also an objective of this thesis to contribute to the implementation of Monte Carlo based planning systems, participating thus to the widespread effort performed by the international radiotherapy community to overcome long-standing problems found in the implementation of this algorithms at clinic settings.

Thesis Outline

This dissertation is organized in five parts. The first part provides a general introduction to radiotherapy with emphasis in external beam therapy (**Chapter 1**) and, on the other hand, to the physics of the radiation transport, including the basic particle interaction processes in matter and the definition of basic quantities describing the effects of these interactions (**Chapter 2**).

In the second part of this dissertation, the materials and methods used for the present investigation are introduced. First, it is given a brief overview of the production of electron and x-ray beams by a medical linear accelerator (linac) for use in external beam radiotherapy (**Chapter 3**). Second, the basic concepts of ionometric and film dosimetry are described. This second part concludes with a general description of Monte Carlo simulation of radiation transport, in particular the EGSnrc Monte Carlo code, which is the code used for the dose calculations in this work (**Chapter 4**). A discussion of variance reduction techniques and efficiency enhancing methods integral to MC calculations is also given.

The third and the fourth parts contain the main body of the dissertation, that is, the description of the dosimetric studies developed during the course of this research.

The third part is dedicated to electron radiotherapy and it presents a systematic study assessing air cavities perturbation on electron dose distributions by using both Monte Carlo simulations and experimental measurements (**Chapter 5**).

The fourth part is focused on photon radiotherapy. **Chapter 6** presents the MC modeling of the Varian 2100C/D linear accelerator as well as the experimental validation of this model through comparison against experimental measurements. A detailed description of the Monte Carlo model used for the multileaf collimator (MLC) embedded in the previous accelerator is discussed in **chapter 7**. This chapter includes also the dosimetric verification of the MLC model using ionization chamber and

film measurements. The influence of the MLC on superficial dose for photon beams was evaluated in chapter 8 using MC simulations and measurements carried out with several types of ionization chambers. Finally, **chapter 9** presents a clinical study assessing the dosimetric differences between dose-to-medium and dose-to water for prostate IMRT plans calculated by Monte Carlo methods.

The fifth and last part of the dissertation summarizes the main conclusions arisen from the investigations performed in this thesis and highlight topics for future work (**Chapter 10**).

Part I

INTRODUCTION

Chapter 1

Introduction to external beam radiation therapy

1.1 Brief introduction

The discovery of x-rays by Wihelm Röntgen in 1895 marked the beginning of a new physics branch: medical physics, which is concerned with the application of physics to medicine. This field covers a broad range of technologies and applications, ranging from diagnostic methods (x-ray imaging, x-ray computed tomography, nuclear medicine, ultrasound imaging, etc.) over techniques for the treatment of human disease (radiation therapy, image guided therapy, laser treatment techniques) to supportive fields like medical image processing, quality assurance and radiation dosimetry. From all these areas of speciality, the field of interest of this thesis is radiotherapy, although radiation dosimetry will also be briefly referred along the course of the investigations here presented.

Radiotherapy (RT) is an important form of cancer treatment used for more than 100 years. The goal of radiotherapy is the eradication of tumor cells with the use of ionizing radiation, while minimizing the damage to the surrounding healthy tissue. In fact, the ionizing radiation deposits energy in the tumor cells as result of the ionization caused by the radiation interaction with the medium. This deposited energy damages the genetic material (DNA) or other important biological molecules, leading to the destruction of these cells or inhibiting further cell division.

The origin of radiotherapy is assigned to the discovery of the x-rays, but it starts only to prospers

in the early 1900s mainly due to the important contribution of the Nobel Prize winner scientist Marie Curie, who discovered the radioactive elements, polonium and radium. This discovery marked the beginning of a new era. The radium started to be used in various forms to treat cancer disease until the mid 1900s, when cobalt and cesium units were introduced as the new landmarks for cancer research and treatment. Since then, many alternative medical procedures were developed, namely medical linear accelerators (linacs) which are currently the most frequently devices used for radiotherapy.

With the discovery of the computed tomography (CT) in the 1970s [Houn79], the delivery of three-dimensional (3D) radiotherapy became a possibility and, at the same time, CT improved the ability of physicians to directly define the dose delivered to a treatment volume previously defined on the patients anatomy.

During the last two decades, most of the developments in radiation medicine were related to the integration of computers in imaging, the development of digital diagnostic imaging techniques and the incorporation of computers into therapeutic dose delivery with high-energy linear accelerators, among others. The recent improvements of imaging technologies along with the development of new radiation delivery equipments has resulted in the emergence of more advanced techniques. These advanced techniques represent an important change in radiotherapy, since they allow the design and implementation of relatively complex radiotherapy treatments where the delivery of radiation to the tumor volume can be achieved with high levels of dose and a high degree of accuracy without affecting surrounding tissues.

Generally, radiotherapy can be delivered through three different forms depending on the location of the radiation source: externally (teletherapy or external radiotherapy), internally by a radioactive source inside the body (brachytherapy) or by administration of radiopharmaceuticals (metabolic radiotherapy). The subject of this thesis is related to external beam radiotherapy and further discussion will be restricted to this method.

External radiotherapy is the most commonly used form of radiotherapy, where the radiation directed to the tumor comes from outside the body. Electrons and photons (x- and γ-rays) are the two type of ionizing radiation widely used in external radiotherapy in the present days. The photons are usually provided by a radioactive source as cobalt-60 emitting two gamma rays of 1.17 and 1.33 MeV or from a linear accelerator producing x-rays up to 25 MV [1]. Electron beams with energies in

the range 4 - 25 MeV are also generated from linacs.

More recently, heavy charged particles (hadron radiotherapy) as protons and carbon ions are being used to treat cancer patients at some radiotherapy departments [Wil46, Jak03]. Although hadron therapy has shown many advantages over electron and photon beams (e.g. more precision of dose location and high effectiveness of treatment), its use is still limited at few radiotherapy departments due to the complexity and the high cost of the devices required for the beam production. Nevertheless, the effort of the research community to investigate the viability of these type of particles for external radiotherapy has increased noticeably in the last years.

1.2 Techniques in external radiotherapy

Different techniques have been developed for the delivery of external radiotherapy treatments using electron and x-ray beams produced by linear accelerator machines. This section gives a brief overview of the development of these techniques, with a special attention on IMRT for photon beams which is the technique used in the context of this thesis.

2D conventional radiotherapy

In the early days of radiotherapy, conventional radiotherapy consisted of 2D planning methods that involved a radiographic film or a image localization procedure. Rectangular fields with shielding and beam-modifying devices (blocks and wedges) were used to obtain conformity and minimize the dose in the normal tissue (figure 1.1A). The treatment plans using this technique mainly consists of a single beam with an uniform intensity delivered from several directions to the treatment volume (target volume). This technique was well established at most radiotherapy centers, because it is generally quick and reliable. However, its use has shown to be limited to the cases where the tumor is symmetrically shaped and centrally located in the body with minimal number of surrounding critical organs. Since normally tumors have no rectangular shape, this technique was not very satisfying because, depending on the actual shape of the tumor, a lot of healthy tissue could be irradiated, leading to a high radiation toxicity of healthy tissues close to the target volume.

[1] Therapeutic and diagnostic γ- and x- rays are conventionally expressed in kilovolts or megavolts (kV or MV). This voltage indicates the maximum electric potential used by the linac to produce the photon beam. The beam is so made up of a spectrum of energies, where the maximum energy corresponds approximately to the electrical potential times the electron charge.

Three-dimensional (3D) conformal radiotherapy

By the mid-1990s, the advances in technology and software allowing the calculation and delivery of non-uniform fluence maps on three-dimensional (3D) patient volumes enabled the clinical implementation of new delivery techniques, 3D-conformal radiotherapy. This implementation was also motivated by the development achieved in medical imaging with the emergence of the computed tomography.

The goal of this technique is to conform the profile of each radiation beam to the shape of the target volume by using a variable number of static beams. In this case, the radiation beams normally have a uniform intensity across the field and they are shaped with irregular geometries using the projection of the target volume (figure 1.1B). The final contribution of all beams lead to a high conformity of dose to the the target volume. In order to shape the beam, different types of device can be used as MLC for photon beams or Cerrobend blocks inserted in the applicator for electron beams, among others. The great advantage of 3D - conformal radiotherapy in relation to conventional radiotherapy is the reduction of the relative toxicity of radiation to the surrounding normal tissues due to the improvement of dose conformity to the target volume. As consequence, higher doses of radiation can be used to treat the tumor and thereby to increase the effectiveness of the treatment.

Figure 1.1: Schematic illustration of three different modalities of radiotherapy: A. 2D- conventional, B. 3D-conformal and C. Intensity Modulated Radiotherapy (IMRT) [www.precisionradiotherapy/PE-IntroRad.htm]

Intensity Modulated Radiotherapy (IMRT)

IMRT is a more advanced development of 3D conformal radiotherapy where, in addition to the shape of the radiation beam, the intensity of the beam can be also modulated [Webb03], as it can be schematically seen in figure 1.1C. Unlike 3-D conformal radiation therapy that is delivered using a single radiation beam, IMRT is delivered as a sequence of many small beams that enter the body from many angles. These multiple thin beams allow that the intensity of radiation within each field can be modulated to achieve a better conformity to the tumor. This leads again to higher doses in the tumor and lower doses to the surrounding sensitive structures and organs at risk.

The technique of IMRT was initially developed using photon beams; however, recent research has also investigated the plausibility of this techniques for electron radiation therapy, known as Modulated Electron Radiotherapy or MERT [Ma00a].

Of the various alternatives proposed for the delivery of IMRT, the most frequently used is that modality based on the use of multileaf collimators (MLC). This type of collimator is made up of individual leaves of a high atomic number material, usually tungsten, that can move in and out of the field to produce a sequence of complex field shapes or beam apertures.

3D conformal radiation therapy also uses a multileaf collimator to customize the shape of the beam. However, the leaves of the collimator are not allowed to move in and out within that particular field, therefore, the shape of the beam for each field stays the same during the treatment.

Two types of MLC-based IMRT delivery modes are clinically used, namely "*step-and-shoot or static (SMLC)*" and "*sliding window or dynamic (DMLC)*". The differences between both basically relates to the different ways used to deliver the radiation, segmented and dynamic, respectively.

In the step-and-shoot mode, the intensity of the modulated fields are delivered with a sequence of small segments or subfields, each one with an uniform intensity. The multiple segment fields are set up at selected orientations of the gantry and the beam is only turned on when the leaves of the MLC are stationary in each of the specific segment positions, i.e. the MLC does not move while the beam is on.

In the dynamic mode, the fields are delivered in a dynamic way with the leaves of the MLC moving during the irradiation of the patient. For a fixed gantry position, the position of the MLC leaves is swept across the target volume with the beam turned on to produce the desired fluence map.

In contrast with the previous techniques, for the dosimetric planning of IMRT a method called

inverse treatment planning is used to find the optimal position and movement for the leaves of the MLC during irradiation. In inverse treatment planning a certain target volume must be defined in the treatment planning system and a desired dose for this target must be prescribed. The treatment planning system will then try to optimize the positions and movements of the MLC leaves so that the prescribed dose is homogeneously distributed across the target volume only. Usually not only the target volume but also the organs at risk are defined and dose volume constraints are given by the planner in order to further enhance the result of the dose optimization algorithm.

New different approaches to deliver IMRT have been developed during the last years: Intensity Modulated Arc Therapy (IMAT), volumetric arc therapy (VMAT), Cyberknife, Image-guided radiation therapy (IGRT), among others. IMAT is a rotational approach in which both the gantry and the leaves of the MLC move during arc beam delivery. More recently introduced, the Cyberknife integrates a compact photon beam linear accelerator mounted on a robotic arm with advanced image guidance technology to deliver concentrated beams of radiation from multiple positions and angles.

1.3 The importance of accuracy in radiation delivery

It has previously been mentioned that the main goal of the radiotherapy is focused on the destruction of tumor cells with ionizing radiation while limiting the damage to the surrounding healthy tissue. The destruction of tumor cells occurs through the ionization of the medium by the radiation, which leads to the deposition of energy. The extent of the damage caused by the radiation is therefore a direct result of the amount of energy deposited per unit mass, i.e. the absorbed dose. Hence, a central point for the success of any radiotherapy treatment stays on the exact knowledge of the radiation dose delivered to the patient.

The importance of accuracy in radiation delivery is most apparent by observing biological effects. In particular, the dose dependence of two biological parameters are usually evaluated for this purpose, namely the local tumor control probability (TCP) and the normal tissue complication probability (NTCP) as a function of the absorbed radiation dose in tissue. The irradiated volume in a patient contains usually both targeted and normal tissues; thereby the optimal radiotherapy plan will maximize TCP while minimizing NTCP. Figure 1.2 illustrates the sigmoidal dependence of both TCP and NTCP values on the radiation dose.

From the figure, it is seen how the TCP rises sharply starting from a particular absorbed dose,

while the NTCP rises sharply at a slightly higher absorbed dose. Thus, any uncertainty on delivered dose may either result in an underdosage of the tumor or a complication for normal tissue. In fact, as stated in the AAPM Report No 85 [AAPM85], a dose error of 5 % may lead to a change in TCP of 10 or 20 % and to an even larger change of 20 to 30 % in NTCP. The need of accurate dose calculation is thus imperative.

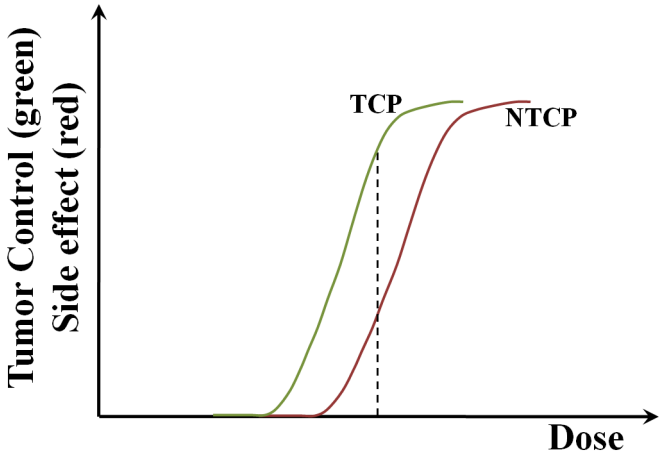

Figure 1.2: Dose dependence of tumor control probability (TCP) and the probability of normal tissue complication (NTCP). The vertical line indicates a certain dose in the steep part of both curves. Uncertainties in delivered dose might worsen the clinical outcome due to either reduction of TCP or increase of NTCP.

In a radiotherapy treatment, a large number of steps are involved between the dose prescription and the final delivery of the dose, e.g. machine calibration, dose calculation, acquisition of patient-specific tumor information, patient positioning, patient motion, etc. During each of this steps, small uncertainties are involved, accumulating to a large overall uncertainty for the full process of dose delivery. These uncertainties may be categorized as random and non random (systematic) uncertainties and they are combined in quadrature to obtain the overall uncertainty of the complete radiotherapy process. The uncertainties that occur during the treatment planning will impact on the entire treatment and are therefore systematic. On the other hand, those uncertainties that occur during the treatment delivery will be however random errors as they will affect the treatment by different amounts at each fraction of the treatment delivery. Their estimates are summarized in table 1.1.

In 1976, the ICRU Report 24 [ICRU24] concluded that an uncertainty less than 5 % at the 2σ level is required for dose delivery to the planning target volume. To satisfy this recommendation,

each step involved in the radiotherapy treatment must be performed with an accuracy much better than 5 %.

Table 1.1: Estimates of uncertainty (in terms of one standard deviation) in absolute dose in the patient for the complete treatment procedure using megavoltage photons [AAPM85].

Source of Uncertainties	**Uncertainty** (%)
Dose at the calibrated point in water	2.5
Additional uncertainty for other points	0.6
Beam Monitor stability	1.0
Beam flatness	1.5
Patient data	1.5
Patient setup and organ motion	2.5
Overall (excluding dose calculation)	4.3
Dose calculation algorithm	1.0/**2.0**/**3.0**/5.0
TOTAL	4.4/**4.7**/**5.2**/6.6

After evaluating the contribution of each step, it was observed that the use of an extremely accurate dose calculation algorithm will not automatically lead to very low uncertainties in clinical dose delivery, since several other factors contribute significantly to the overall uncertainty. However, it was claimed that the dose calculation step should be accurate to within 2-3 % to achieve the 5 % requirement of the overall uncertainty. The accuracy of the dose calculation algorithm plays therefore an important role in a radiotherapy treatment.

More details about the accuracy of the existing algorithms used for the dose calculation will be briefly referred in the chapter 4, where it is also stressed the Monte Carlo method as the most accurate solution to meet the above-mentioned requirement of 3 % uncertainty in the dose.

Chapter 2

Fundamentals of radiotherapy physics and dosimetry

This chapter provides a brief introduction to the basic physics of the radiation interaction with matter and introduces several basic quantities used in characterizing radiation.

2.1 Interaction of ionizing radiation with matter

Ionizing radiation is characterized by the ability to ionize matter through electromagnetic interactions[Att86]. Typically, ionizing radiation can be classified into two main categories depending on the mode of ionization:

- *directly ionizing radiation*: Charged particles (electrons/positrons, alpha particles, etc.) which deposit energy in the medium through direct one-step processes involving inelastic Coulomb-interactions with orbital electrons and other charged particles present in the medium.
- *indirectly ionizing radiation*: Neutral particles (photons and neutrons) which interact with the medium following a process of two steps: 1) energy transfer to charged particles in medium and 2) energy deposition in medium by released charged particles.

Both directly and indirectly ionizing radiations are actually used in the diagnosis (medical imaging) and the treatment of cancer (radiotherapy, radiation oncology, etc.). Particularly, in radiotherapy,

which is the topic of the present thesis, photons and electrons are considered the main choice for the treatment of disease with radiation and they are used in more than 90 % of radiotherapy treatments.

Next sections introduce briefly the different mechanisms of interaction of photons and electrons with matter and discuss the quantitative probabilities of each of these mechanisms occurring in different regions of energy. This is helpful, not only to understand better how the radiation interacts with the living tissue, but also for later discussion of the results.

2.1.1 Photon interactions in matter

2.1.1.1 Types of interaction mechanisms

As previously referred, photons ionize matter indirectly, i.e. the photon interactions in a medium release charged particles (electrons or positrons), which in turn deposit energy through direct Coulomb interactions with the orbital electrons of the atoms.

The five major interaction processes which the photons can undergo when interacting with matter are:

- Photoelectric absorption effect
- Incoherent (Compton) scattering
- Pair production
- Coherent (Rayleigh) scattering
- Photonuclear reactions

In general, the probability of occurrence of the above interactions depends both on photon energy and atomic number of the medium. For the energy range applied in radiotherapy, the four first interactions show the highest probability to occur. However, only the first three interactions lead to energy deposition, as they result in the transfer of energy to electrons which will then be imparted to matter in small Coulumb-force interactions along their tracks. The Rayleigh scattering, which is sometimes referred to as coherent scattering, is an elastic interaction where the photon looses almost no energy and only the direction of the incident photons changes. Therefore, this process can

not contribute to the transfer of energy to the medium. Figure 2.1 illustrates a scheme of these four first processes.

The photonuclear reactions are commonly ignored in dosimetry considerations, since this kind of process occurs with a very low probability and is just dominant for higher energies above 10 MeV.

A review of each of the above processes is presented next, with a special attention to the three first interactions since they play the major roles at the energies commonly used in the radiotherapy. In addition, it is briefly discussed the relative dependence of each process on energy and material as well as the respective contribution to the total probability.

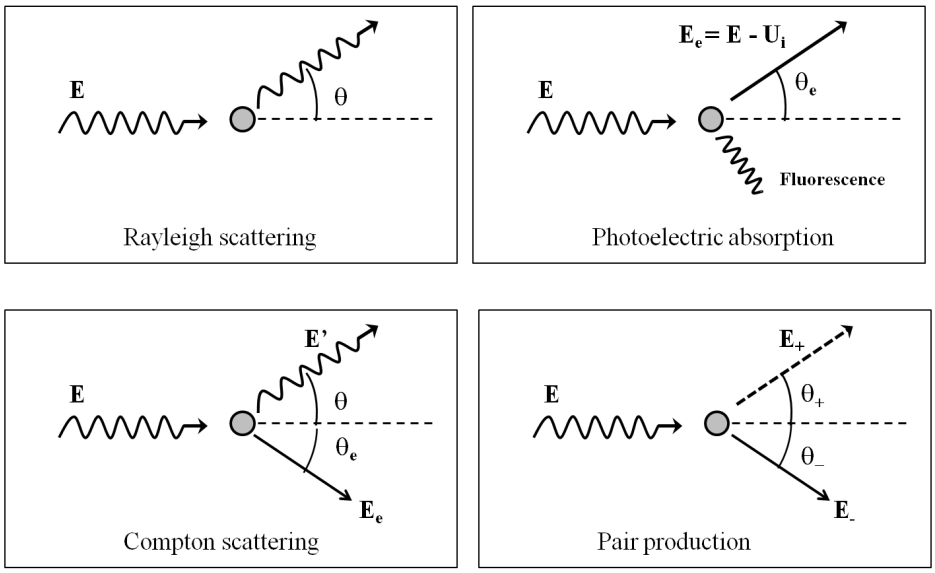

Figure 2.1: Schematic diagrams of the main interaction processes of the photons with matter: Rayleigh scattering, Photoelectric effect, Compton scattering and Pair production.

Photoelectric effect

The photoelectric effect is the predominant mode of interaction for photons of low energy, in the energy range of several eV to around 0.1 MeV. In this process, the incident photon interacts with a tightly bound electron (inner shells as K, L, M or N) and it is completely absorbed in the interaction and the electron (named *photoelectron*) is ejected from the atom (see figure 2.1).

In order for the photoelectric effect to occur, the incident photon energy has to be higher than the binding energy of the electron. Thus, part of the photon energy is used to overcome the binding energy and free the electron from the atom and the residual energy is transferred to the kinetic energy of the escaping electron. The photoelectron appears thus with an kinetic energy given by:

$$E_e = E - U_i \tag{2.1}$$

where E is the energy of the incoming photon and U_i is the binding energy of the electrons in the atomic shell.

As result of the emission of the electron, the atom is left in an excited state with a vacancy in the ionized shell. This vacancy can be quickly filled through the capture of an outer orbital electron and, therefore, one or more characteristic x-ray photons (fluorescent photons) may also be generated. In some fraction of the cases, the emission of Auger electrons may substitute for the characteristic X-ray in carrying away the atomic excitation energy.

The probability of occurrence of the photoelectric effect varies roughly whit the energy of the incident photon and the atomic number Z of the medium, as follows:

$$\tau \propto \frac{Z^n}{(h\nu)^3} \tag{2.2}$$

where the exponent n varies between 3 and 4 over the photon energy region of interest. The units of the cross section τ are cm^{-2}.

According to this equation (2.2), it can be observed how the photoelectric effect will be enhanced for photons of relatively low energy and for materials of high atomic number Z.

The angular distribution of the emitted electrons depends on the energy of the incident photon. For low photon energy, the electrons are predominantly ejected at 90° relative to the photon direction. With increasing the photon energy, the electrons are emitted in more forward directions [Att86].

Compton effect

The Compton effect is the dominant mode of interaction in the energy range from several hundred keV to several MeV and therefore it represents the major mechanims of interaction for most photon energies used in radiotherapy.

When the Compton scattering occurs, the incident photon transfers part of its energy to an

electron and it is deflected through an angle θ with respect to its original direction (see figure 2.1). In contrast to the photoelectric effect, the electron struck by the incoming photon is a lightly bound electron, i.e. an outer shell electron, and it is thus assumed that it is initially free and at rest.

In the collision, the photon transfers a portion of its energy to the electron, which will departs at angle θ_e with a kinetic energy given by:

$$E_e = E - E' \tag{2.3}$$

where $E = h\nu$ and $E' = h\nu$ are the energy of the incident and scattered photons, respectively.

Simple energy and momentum conservation constraints can be used to derived the relation between the energy of incident and scattered photons, given by the next equation:

$$E' = \frac{E}{1 + (\frac{E}{m_o c^2})(1 - cos\theta)} \tag{2.4}$$

in which the m_o is the electron's rest mass and c is the speed of light in vacuum.

This relation shows that the energy of the scattered photon depends not only on the energy of incident photon but also on its scattering angle θ. From equation 2.4, it is clear observed that as the energy of the scattered photon increases, the photon is deflected to more and more forward directions. For a given incident photon energy, there exits a minimum energy for the scattered photons (corresponding to a maximum energy for the scattered electron), corresponding to the backward direction at $\theta = 180^\circ$

$$E'_{min} = \frac{m_o c^2/2}{1 + m_o c^2/2E} \tag{2.5}$$

Finally, the angle θ of the emitted electron is related to the energy and angle of incident photon through the next equation:

$$cot\theta_e = \left(1 + \frac{E}{m_o c^2}\right) tan\left(\frac{\theta}{2}\right) \tag{2.6}$$

From equation 2.6, it is interesting to notice that the electron angle is thus always confined to the forward direction ($0 \leq \theta_e \leq 90^\circ$), whereas the photon can be scattered to any direction. On the other side, it is also observed that, as the energy of the incident photon increases, the electrons tend to be scattered to more forward directions and the transfer of the energy to the electrons also increases.

Compton scattering is the only type of interaction that is not highly dependent on the Z of the medium, but it depends on the incident energy and the density of the material. In particular, the probability of occurrence of this effect decreases with increasing photon energy and it shows to be proportional to the material density. The total cross-section is derived according to the *Klein - Nishina* formalism [Eva55], assuming for that unpolarized and unbound electrons, as follows:

$$\sigma \propto Z\sigma_e \propto \frac{Z}{E} \tag{2.7}$$

where σ_e is the the total Klein - Nishina cross section per electron [Att86]. The units of the cross section σ are cm^{-2}.

Pair production process

Pair production refers to the creation of an electron and a positron pair from a photon in the field of an atomic nucleus (see figure 2.1). In order to this interaction to occur, the photon energy should be greater than the rest energy of the electron-positron pair, that is, $E \geq 2mc^2 = 1.022$ MeV.

When this process takes place, the massive nucleus recoils whit negligible energy and, therefore, the photon energy is converted into mass rest energy ($2mc^2$) plus kinetic energy of the electron (E_-) and positron (E_+):

$$E = 2mc^2 + E_- + E_+ \tag{2.8}$$

The kinetic energy received by the electron and positron is not necessarily equal, but it can be estimated an average kinetic energy ($\overline{T}$) of:

$$\overline{T} = \frac{E - 1.022MeV}{2} \tag{2.9}$$

For photon energies close to the threshold energy $2mc^2$, the created electron and positron travel almost in opposite directions to each other. For energy above this threshold, the pair can travel in a more forward direction. In this last case, the average angle of the particle emission relative to the original photon direction is roughly:

$$\overline{\theta} \cong \frac{mc^2}{\overline{T}} \tag{2.10}$$

The probability of occurrence of the pair production process is governed by the theory of *Bethe and Heitler*. According to this formalism, the probability increases rapidly as the photon energy increases and it is also strongly dependent on the atomic number as Z^2:

$$\kappa \propto Z^2 logE \tag{2.11}$$

The units of the cross section κ are cm^{-2}.

Pair production can also occur in the field of an atomic electron, but the probability is considerably smaller and the energy of the photon has to be higher than $4mc^2$. This process is usually know as *triplet production*, since three particles are resulting from the interaction: electron/positron plus the orbital electron.

Rayleigh scattering

It has been previously mentioned that the Rayleigh scattering is a elastic scattering where the photon loose none of its energy and it is just redirected through a small angle θ (see figure 2.1). The probability of occurrence of this process decreases with the incident photon energy, but it increases with the atomic number of the medium as follows:

$$\sigma_R \propto \frac{Z^2}{(h\nu)^2} \tag{2.12}$$

The units of the cross section σ_R are cm^{-2}.

The relative importance of the Rayleigh scattering is in the low energy regime, but it contributes only a few percent or less to the total attenuation cross section. On the other side, it is important to point out that this mechanism of photon interaction does not contribute to the kerma or dose, since no energy is transferred during this interaction. Based on that, this kind of process is more important in imaging applications than in radiotherapy.

Photonuclear reactions

At energies above 10 MeV photonuclear reactions can occur, in which the high-energy photon is absorbed by the atomic nucleus and a nucleon is then emitted. The most likely result of this interaction is the emission of a single neutron through a (γ,n) reaction, even though the emissions of charged particles such as protons or alpha particles or even more than one neutron (γ,2n) reactions can also

occur with less probability. Generally, the contribution to the total attenuation cross-section of the photonuclear reactions is very small (about 5 %) and therefore they do not play a role in general photon attenuation studies. On contrary, they are of considerable importance for shielding calculations as consequence of the neutron emission. In this particular work, this process does not play an important role since the maximum energy of photons used for the investigation is around 6 MeV.

2.1.1.2 Attenuation coefficients

When the photons travels thought the matter, they can undergo one or a combination of the above processes depending on their energy and also they can be transmitted out of the medium without undergoing any interaction.

This transport through matter is ruled statistically by the probability per unit distance traveled by the photon, called *linear attenuation* coefficient and denoted by μ. This coefficient is frequently known as macroscopic cross section (cm^{-1}) and it can be expressed as the product of the atomic density N = $\rho N_A/A$ and the total cross section σ_{total} (cm^{-2}) as:

$$\mu = N\sigma_{total} \Leftrightarrow \mu = \frac{\rho N_A}{A}\sigma_{total} \tag{2.13}$$

Based on this coefficient, the number of photons passing a certain thickness x of a medium decreases following an exponential function as:

$$N = N_o e^{-\mu x} \tag{2.14}$$

with N_o being the incident number of photons.

In general, the total linear attenuation coefficient is represented as the sum of attenuation coefficients for all individual interactions that a photon of given energy may have with atoms of a specific material. As discussed above, the interactions of interest in the therapeutic energy range are basically three: the photoelectric effect, the Compton scattering and the pair production; thereby the linear attenuation coefficient relative to these three process will compose the total linear attenuation:

$$\mu = \mu_{ph} + \mu_{comp} + \mu_{pair} = \frac{\rho N_A}{A}\Big(\tau + \sigma + \kappa\Big) \tag{2.15}$$

where μ_{ph}, μ_{comp}, and μ_{pair} denote the linear attenuation coefficient for the photoelectric, Comp-

ton and pair production, respectively. The corresponding cross section for theses interactions are denoted by τ, σ and κ, as previously discussed.

Figure 2.2 shows the total mass attenuation coefficient for water plotted against photon energy. In addition to the total coefficient, the coefficients for the individual components (photoelectric effect, Compton scattering, pair production and Rayleigh scattering) are also shown.

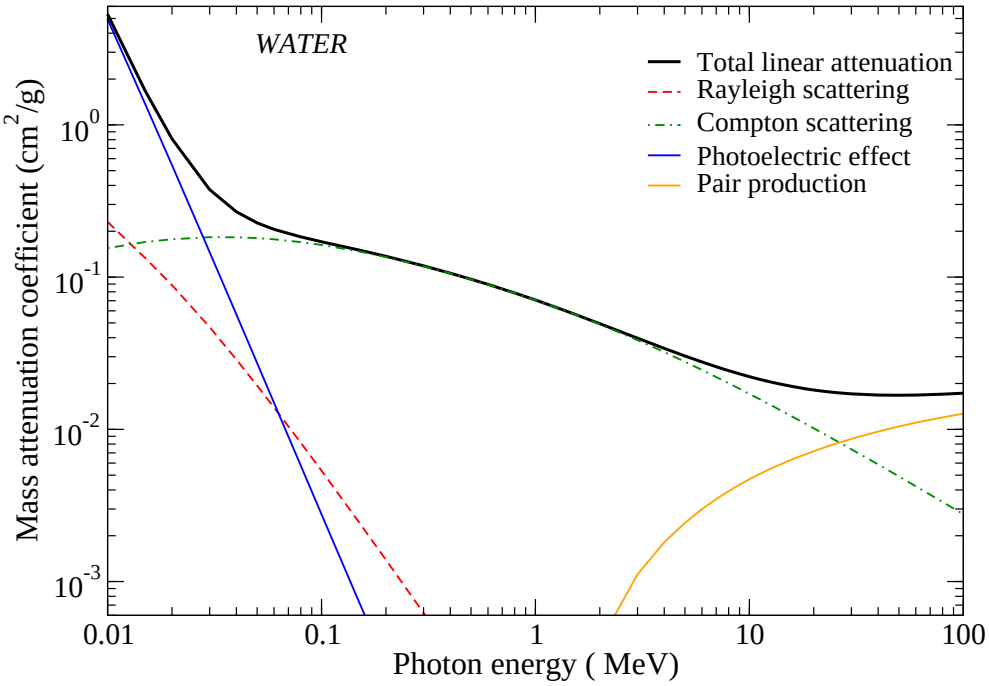

Figure 2.2: Linear attenuation coefficient of photons of different energies in water (equivalent to body tissue). The relative contribution of photoelectric, Compton scattering and pair production processes are illustrated. The data were extracted from the NIST/XCOM: Photon Cross Sections Database (www.nist.gov/pml/data/xcom/index.cfm).

As seen from equation 2.13, the linear attenuation coefficient of a given material is directly proportional to the density of the material. In order to eliminate the density dependence, the *mass attenuation coefficient*, μ/ρ (where the ρ is the mass density of the medium), is used instead.

The mass attenuation coefficient can be divided into two parts, namely the energy transfer coefficient (μ_{tr}/ρ) related to the transfer of energy to charged particles and the energy scatter coefficient (μ_s/ρ) which applies to the energy converted into scattered photons. It can also happen that a part of the energy transfer to the electrons is not deposited locally within the medium along the electron track, being lost by emission of bremsstrahlung photons. This fact is described by the mass energy absorption coefficient (μ_{en}/ρ) which is given by:

$$\frac{\mu_{en}}{\rho} = (1-g)\frac{\mu_{tr}}{\rho} \tag{2.16}$$

where g refers to the fractional energy of the electrons that is lost as bremsstrahlung. This fraction g is negligible for photons of low energy, but it becomes significant at high energies and in materials of high atomic number Z.

2.1.1.3 Relative predominance of individual effects

The linear attenuation coefficient is characteristic of both the medium and the photon energy. Figure 2.3 shows an overall picture of the dependence of the relative magnitude of the different interaction processes on energy E and atomic number Z. Curves of Z vs E corresponding to equal probabilities of the photoelectric and the Compton processes (left) and of the Compton and the pair production processes (right) are also presented.

As shown, the photoelectric effect is dominant at low energy range. As the energy increases, the Compton effect becomes the most important process and, at higher energies ($>$ 5 MeV), the pair production is the interaction more likely to occur. Additionally, it can also be seen in this figure, that the middle interval, with the Compton scattering predominance, is broader for media with low atomic number.

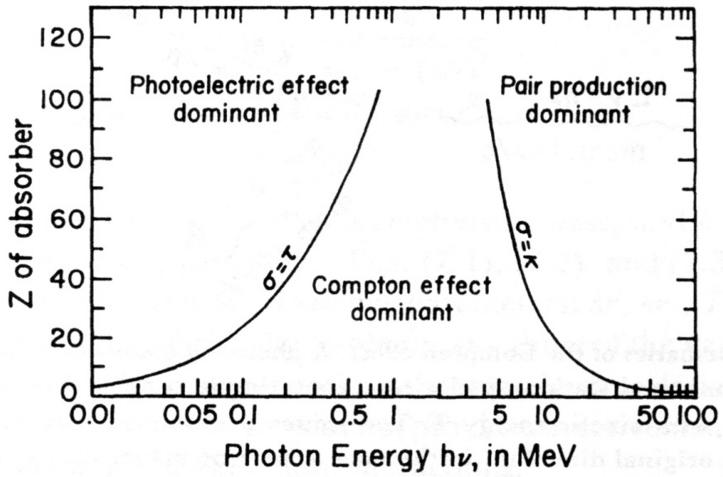

Figure 2.3: Relative importance of the three major types of photon interactions. The curves show the values of Z and E for which the two types of effects are equal [Att86].

In particular, for water and tissue with an effective atomic number $Z_{effective} \approx 7.0$, this region ranges from $\sim$ 20 KeV up to $\sim$ 20 MeV, indicating thus that for most of radiotherapy studies and treatments, the most important interaction of photons with tissues is the Compton scattering. On the other hand, the interval of influence of the photoelectric effect and the pair production is increased for high-Z materials.

2.1.2 Electron and positron interactions in matter

Electrons play an important role in medical physics. They are used directly as beams for cancer therapy, but also they are responsible for the energy deposition in matter by photon beams. Therefore, these charged particles govern the experimental and theoretical aspects of radiation dosimetry.

Contrary to photons which can pass through the matter with no interactions at all, charged particles[2] cross the medium loosing almost continuously their energy through ionization and excitation of atoms and through Coulomb interactions with the external nuclear field until they come to rest.

Additionally, it is important to point out that, compared to heavy charged particles, electrons and positrons have a different behavior when passing through matter, although they undergo the same kind of interactions. Because of their small mass, electrons (and positrons) can loose a large fraction of their energy in a single collision with an atomic electron (which have equal mass as the incident electron) and, they can also be scattered into relatively large angles. Furthermore, in contrast to heavy charged particles, the electrons have a high probability of being sharply deflected and accelerated by the nuclei resulting in the emission of bremsstrahlung photons. Next paragraphs are focused on the interaction of electrons and positrons in matter and further details about this subject are presented.

2.1.2.1 Types of interaction mechanisms

In general, when electrons pass through a medium they interact through Coulomb forces with nuclei and orbital electrons. The collisions they can undergo may be elastic, when only a change of direction occurs, or inelastic when energy is also transferred. The type of interaction will depend on the energy of the incident electron and the distance of approach of the electron to the atom, that is, the *impact parameter b vs.* the atomic radius *a* (figure 2.4).

[2] In the context of the present work, charged particles are considered to be electrons or positrons. Within the following no distinction between electrons and positrons is drawn, i.e. electrons are used as a synonym for both.

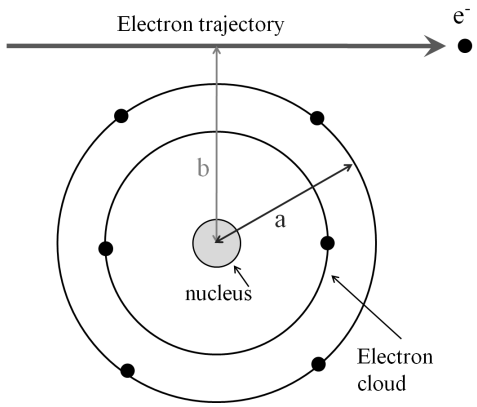

Figure 2.4: Parameters in an electron collision with atom: *a* is the classical atomic radius and *b* is the impact parameter.

The inelastic interactions can be categorized into three main groups[Att86]:

- **Soft collisions** (b >> a): The electron is affected by the Coulomb force field of the atom as a whole. The atom is thereby distorted, excited it to a higher energy level or ionized with ejection of an orbital electron. The net effect of this collision is the transfer of a very small amount of energy to an atom of the medium. The excited or ionized atom will return to its ground state with the emission of characteristic x-rays or Auger-electrons. This process is clearly the most probable and it represents roughly half of the energy transferred by an electron to the medium.

- **Hard collisions** (b $\sim$ a): The interaction of the electron with a single orbital electron of the atom becomes more likely. As a result, the orbital electron is ejected with energy enough for traveling a certain distance away from the point of interaction. This high-energetic electrons are called δ- or knock-on electrons. They are characterized for being energetic enough to undergo similar interactions to those experienced by the primary electrons, producing thus their own ionizations and excitations. Similarly to the soft collisions, characteristic x-ray and/or Auger electrons can be emitted due to the excitation of the atom. Although hard collisions occurs with a lower probability compared to soft collisions, the energy lost by incident electrons by both collision processes is generally comparable.

- **Radiative interactions** (b << a): Under this conditions, the electrons will interact mainly with the nucleus. The electrons are deflected and accelerated rapidly by the electric field of

the atomic nucleus, leading to the emission of bremsstrahlung photons. The probability of occurrence of this interaction varies with nearly Z^2 and increases with the energy and the inverse square of the mass of the particle. This last fact explains why the radiative process is much more important for electrons than for heavy charged particles. The bremsstrahlung radiation is characterized by a continuous energy spectrum where the maximum energy that a bremsstrahlung photon can reach corresponds to the energy of the electron producing the radiation. Around 2-3 % of the electrons traveling near to the nucleus will undergo this radiative process.

In addition to the radiative process, the interaction of the electron with the nucleus can result in an *elastic* scattering where the electron is just deflected from its original direction without transferring any energy to the medium. This process is the most important for electrons since it occurs in about 98 % of the cases in which the electron passes near the nucleus and it is the main reason of why the electrons follows so tortuous paths along their path [Att86]. This elastic scattering is especially significant for materials with high atomic number Z, as the cross section per atom is proportional to Z^2.

2.1.2.2 Stopping power and range

Due to the Coulomb force, electrons are strongly influenced by the surrounding environment and, as it has been above referred, they interact and loose energy continuously as they pass through a medium and come to rest. In this case, the stopping power, $S = dE/dx$, which gives the amount of energy transferred to the medium per unit thickness of travel (with units of MeV/cm), is used to characterize this process. Due to the dependence of the stopping power on the density of the material, a more fundamental and more commonly used way of describing the rate of energy loss is to specify the rate in terms of the density thickness, rather than the geometrical length of the path. This quantity is called mass stopping power S/ρ and it is given as:

$$\frac{S}{\rho} = \frac{1}{\rho}\frac{dE}{dx} \tag{2.17}$$

The units of this quantity is MeV cm^2/g.

The total mass stopping power $(S/\rho)_{total}$ consists of the sum of two components, the losses by ionization due to the collisions (soft and hard) S_{coll} and the losses by radiative interactions S_{rad}:

$$S_{total} = S_{coll} + S_{rad} \tag{2.18}$$

This distinction between losses is important since the absorbed dose in the medium will be different: the energy may be deposited along the volume surrounding the ionization track of the electron due to inelastic collisions with the atomic electrons, but also it can be carried away from the point of interaction by bremsstrahlung or δ - rays, without contributing locally to the dose (see section 2.1.2.3).

The mass stopping power of electrons due to the collisions is given by a modified version of the *Bethe-Bloch* formula [Bet53], as follows:

$$\left(\frac{S}{\rho}\right)_{coll} = \frac{2\pi r_e^2 m_0 c^2}{\beta^2}\left(\frac{N_A Z}{A}\right)\left[ln\frac{\tau^2(\tau+2)}{2(I/m_0c^2)} + F^{\pm}(\tau) - \delta - 2\frac{C}{Z}\right] \tag{2.19}$$

with

$$F^{\pm}(\tau) = 1 - \beta^2 + \left[\frac{\tau^2}{8} - (2\tau+1)ln2\right]/(\tau+1)^2 \tag{2.20}$$

where r_e is the classical electron radius, m_0 is the mass of the electron, $\beta = v/c$ is the ratio of the electron velocity v to the velocity of light c, $\tau = T_0/(m_0c^2)$ is the ratio of kinetic energy of the electron to its rest mass energy, N_AZ/A the number of electrons per gram of medium and I the mean excitation energy of the atoms. The formula was also corrected for two factors that become significant at very high and moderately low energies. One is the shielding of distant electrons because of the polarization of orbital electrons by the electric field of the moving electron; this is called *density effect* and is denoted by the term δ in Eq. 2.19. The second correction term applies at lower energies and depends on the orbital velocities of the electrons. This term is usually named as *shell correction* and it is represented by the term C/Z in Eq. 2.19.

The stopping power varies slowly with particle energy and is proportional to the atomic number Z of the material. Also, it can be seen that the collision stopping power varies as $(1/v^2)$, i.e. inversely with the energy of the electron.

On the other hand, the radiative stopping power is approximately given by *Heitler* [Eva55] for electron energies up to 100 MeV. This can be given by:

$$S_{rad} = \left(\frac{dE}{dx}\right)_{rad} \propto \rho \cdot \left(\frac{e}{m_e}\right)^2 \cdot Z^2 \cdot E_{tot} \tag{2.21}$$

which shows that the radiative term of the stopping power depends on the total energy of the electron E_{total}, the type of particular nucleus, i.e. the density ρ and the atomic number Z. More detailed discussion about this topic can be found in [Att86].

In figure 2.5, the total, collision and radiative stopping powers of tissue and compact bone (ICRU) are plotted. As shown, the collision stopping power for tissue have the highest influence on the low-energy range (up to 70 MeV), whereas the lost due to the radiative interactions become more significant from 70 MeV, increasing as the energy of the electron increases. Additionally, it can be also observed that the radiative stopping power for compact bone is larger than for water due to the (Z^2) dependency of this effect. The collision stopping power for bone is however reduced compared to the one for tissue. Note that the stopping power for tissue can be considered equal to the one for water since the difference between both media is just within 1%.

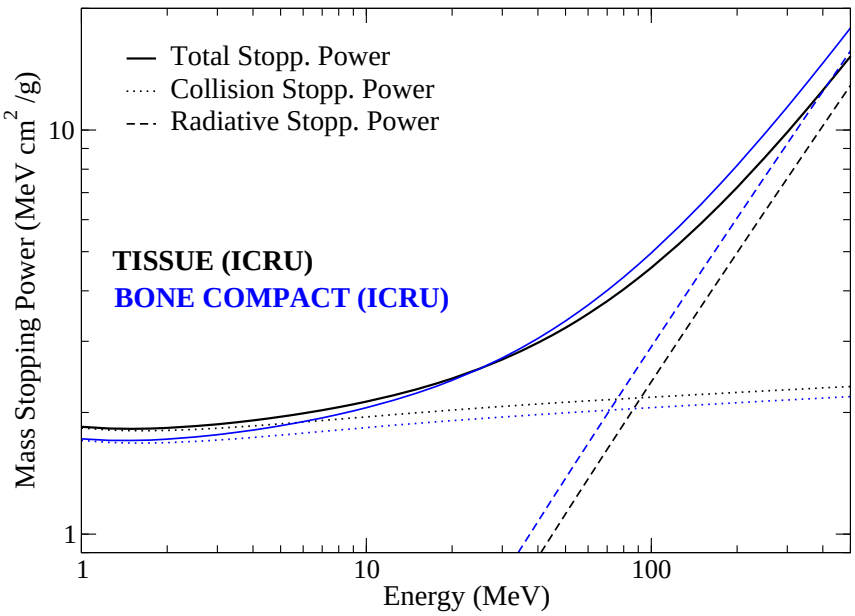

Figure 2.5: Mass stopping power for electrons in tissue (or water, the difference between the two is within 1%) and compact bone (ICRU). The collision and radiative components of the stopping power are also illustrated. The data was extracted from the NIST/ESTAR database (http://physics.nist.gov/PhysRefData/Star/Text/ESTAR.html).

As previously mentioned, most of the collision and radiative interactions transfer individually only a small fraction of the incident energy and it is convenient to assume that the electron is moving through the medium loosing its kinetic energy gradually and continuously. This approach is often referred to as the *continuous slowing down approximation* (CSDA). However, it is known that the collisions which occur along the path of an electron are governed by probability theories and there

are statistical fluctuations in the number of collisions and in the amount of energy lost in each collision. So, a number of identical particles traveling under identical conditions do not loose the same energy as they pass a given region or interval. This phenomenon is called *energy straggling*. Similarly, it is also defined the *range straggling* which reflects the existence of different pathlengths for particles of identical energies, as consequence of the statistical variations in the rates of energy loss.

Because of the large number of interactions undergone by an electron (or positron) as traveling through a medium, it is possible to define the mean distance traveled by the electron before coming to rest. This is the *range* and has an uncertainty equal to the range straggling. Based on the CSDA approximation, one analytical concept for range estimation can be defined for an electron of initial energy E_0 by integrating the reciprocal total stopping power ratio as:

$$R_{CSDA} = \int_0^{E_0} \left(\frac{S_{total}}{\rho} \right)^{-1} dE \tag{2.22}$$

In general, the CSDA range can be considered as a good estimation of the range of electrons; however it is just an approximation of the real value and also it should not be mistaken with the *depth of penetration* in a given direction. On one side, the actual range is usually somewhat smaller, since, as previously discussed, the discrete creation of secondary particles with certain energy may occur. On the other side, the depth of penetration is further decreased due to the curved trajectories of an electron scattered in the medium.

2.1.2.3 Restricted stopping power

In many applications of radiation dosimetry, it is interesting to determine the energy transferred to a localized region of interest. The use of the above mass stopping power (Eq. 2.17) incorporating the collision stopping power caused by both hard and soft collisions may overestimate the absorbed energy in that specific and localized region. As previously mentioned, the δ- rays resulting from hard collisions may be energetic enough to carry their energy to a significant distance from the path of the primary electron, escaping thus from the region of interest.

It is for this purpose that it has been introduced the concept of restricted collision stopping power, denoted as L_Δ. This quantity is defined as the linear rate of energy loss due only to collisions in which the energy transfer does not exceed a specified threshold value Δ:

$$L_\Delta = \left(\frac{dE}{dx}\right)_\Delta \tag{2.23}$$

This parameter has dimensions of stopping power and it is usually expressed in units of keV/μm.

The application of the restricted stopping power is of particular importance for ionometric dosimetry where the main idea is to measure the energy absorbed locally within the volume of the chamber air cavity (see below the section concerning the Cavity Theory). Another concept of this quantity is related to the Monte Carlo simulations, where the absorbed dose is calculated in some specific and usually small regions and hence, the use of the restricted stopping power becomes primordial.

2.2 General concepts of clinical radiation dosimetry

As seen above, the result of the interaction of the radiation with matter is the transfer of a certain amount of energy to the matter through the processes of ionization and excitation. Based on this consideration, there are many different quantities and units commonly used to describe and quantify this energy transfer. An important basis for these concepts was provided in the 60's and 70's by the International Commission on Radiological Units and Measurements (ICRU). The ICRU has developed and recommended a set of fundamental quantities and units in dosimetry which has been in wide use for decades and has been vital to the successful exchange of information, and comparison of results.

In the following some of these basic principles and quantities in the context of ionizing radiation are discussed. This is not intended to be a complete review, it rather serves as a brief introduction covering the topics needed in later chapters.

2.2.1 Basic dosimetric quantities

Generally, radiation fields are specified with two classes of radiometric quantities referring either to the number of particles or to the energy transported by these particles. These are widely used in practical applications of ionizing radiation as they provide a complete description of the field. In the context of the present work, the characterization of electron and photon beams which are presented in the following chapters are based on some of the radiometric quantities described below.

Fluence

The particle *fluence* ϕ gives the number of particles dN that cross a sphere of unit cross-sectional dA:

$$\phi = \frac{dN}{dA} \tag{2.24}$$

which is usually expressed in units of cm^{-2}.

An additional definition of fluence, simplifying the description of the radiation field, was introduced by Roesch and Attix [Att86] and it is called *planar fluence*. The planar fluence is defined as the number of particles crossing a giving plane per unit area and, contrarily to the fluence, this quantity depends on the angle of incidence of the particle beam.

Energy fluence

The *energy fluence* ψ, which is a measure of the total amount of energy entering or leaving a small volume, is defined as

$$\psi = \frac{dR}{dA} \tag{2.25}$$

where dR denotes the radiant energy incident on a spherical volume of cross-sectional area dA. The unit for energy fluence is J m^{-2}. By radiant energy R it means the energy (excluding rest energy) of the particles emitted, transferred or received by all the particles striking the spherical volume.

For the special case where only a single energy E of particles is presented, the energy fluence can be determined as the product of the particle fluence ϕ and the particle energy E, as follows:

$$\psi = \frac{dN}{dA}E = \phi E \tag{2.26}$$

For polyenergetic beams where the beam consists of particles with a specific energy spectra, it is necessary to weight each energy component by the number of particles at each energy. In this case, the concept of energy fluence spectrum $\psi_E(E)$ is thus required:

$$\psi_E(E) = \frac{d\psi}{dE}(E) \tag{2.27}$$

Kerma

As previously mentioned, indirectly ionizing radiation transfer energy to secondary charged particles, which subsequently release their energy to the medium with a specific mass. This is the case of photons, which will impart their energy to electrons of the medium and these electrons will then deposit their energy through ionizations and excitations.

Regarding this subject, a conceptional description of the first step of energy transfer from photons to electrons is given by the quantity *kerma*, *'Kinetic Energy Released per unit Mass'*. This quantity relates to the kinetic energy of all the charged particles liberated by uncharged particles and it is defined as:

$$K = \frac{dE_{tr}}{dm} \tag{2.28}$$

in which dE_{tr} is the expectation value of the energy transferred to the charged particles in a finite volume V at a point P and dm is the mass of the volume V where the energy was transferred. The unit for kerma is the same as for dose, that is, the Gray (Gy) with 1 Gy = 1 J/kg.

As stated above in section 2.1.2, electrons traveling through a medium can loose their energy in two major ways: collisions (soft and hard) and radiative interactions. As defined, the kerma takes into account the kinetic energy received by the charged particles. This energy will be therefore lost by the electrons in both above referred processes. It is thus possible to separate the kerma into two different components:

$$K = K_c + K_r \tag{2.29}$$

where K_c and K_r refer to 'collision' and 'radiative' interactions, respectively.

Absorbed dose

The absorbed dose D is probably the key quantity in respect to the clinical effects of the radiation interaction with matter. This concept is relevant to all types of ionizing radiation fields, either directly ionizing, such as electrons, either indirectly ionizing, such as photons. According the ICRU Report (1980), absorbed dose is defined as the mean energy imparted $d\epsilon$ by the ionizing radiation to the absorbing material of mass dm:

$$D = \frac{d\epsilon}{dm} \tag{2.30}$$

The unit for dose is the Gray (Gy).

It is important to point out that the energy included in the definition of the absorbed dose is the energy actually transferred from the radiation, independently of the type of radiation. Thus, whereas the concept of kerma deals only with primary interactions in matter, absorbed dose deals with all the interactions taking place in the medium.

Closely related to the absorbed dose is the kerma, in particular the collision part of the kerma (K_c). It is known that the absorption of energy does not take place at the same location as the transfer of energy described by the kerma. However, both quantities are related to each other when conditions of charged particle equilibrium (CPE) exist at the point of dose calculation, that is, if each charged particle of given energy leaving the volume is replaced by an identical particle entering the volume. Further details about the CPE conditions are given in section 2.2.2.2. Under this conditions, the following relation can be found:

$$D \overset{CPE}{=} K_c \tag{2.31}$$

Exposure

Exposure, X, is defined by the ICRU as the quotient of dQ by dm where dQ is the absolute value of the total charge of the ions of one sign produced in air, being dm the mass of air where all the electrons produced by photons are completely stopped, that is,

$$X = \frac{dQ}{dm} \tag{2.32}$$

The SI unit for exposure is Ckg^{-1}.

This quantity presents some limitations in its definition. The first one is that exposure must occur in air and it is not possible to speak of exposure inside other material. On the other hand, the concept of exposure is only defined for photons (x- and γ -rays) and for energies greater than 3 MeV due to the need of charged particle equilibrium.

For photons, exposure can be also expressed in terms of the collision kerma K_c in air as follows:

$$X = (K_c)_{air}\left(\frac{e}{W}\right)_{air} \tag{2.33}$$

where e/W is the inverse of the mean energy required in air to create an ion pair. For dry air, the value of $(W/e)_{air}$ is found to be a constant of 33.97 J/C.

Under conditions of charged particle equilibrium, it can be also written the following relationship between dose in air and exposure:

$$D_{air} = (K_c)_{air} = X\left(\frac{W}{e}\right)_{air} \tag{2.34}$$

2.2.2 Basic theorems and principles

2.2.2.1 Inverse-square law

In external photon beam radiotherapy, as it will later described in section 3.1.2, the primary photon source is located at the target of a high atomic number, where electrons incident, resulting in the emission of bremsstrahlung photons. This source is often assumed to be a point source, irradiating to all directions downwards from the target, but with a forward-directed directional distribution. The collimating system incorporated in the treatment head then shapes the radiation into a diverging beam with a well-defined, but possibly irregular, cross-sectional shape. A cross-section with area A at distance f_a from the point source is geometrically related to an area B at distance f_b as:

$$\frac{A}{B} = \frac{{f_b}^2}{{f_a}^2} \tag{2.35}$$

The number of photons emitted by the photon source that cross the area A, i.e. the photon fluence, is denoted by ϕ_A. If no interactions occur in the air between the planes located at f_a and f_b, the same number of photons cross both areas. Hence, the following equality holds:

$$\phi_A A = \phi_B B \Leftrightarrow \frac{\phi_A}{\phi_B} = \frac{B}{A} = \frac{{f_a}^2}{{f_b}^2} \tag{2.36}$$

Equation 2.36 implies that in absence of attenuation, the photon fluence is inversely proportional to the square of the distance from the source. The same relationship applies also for the energy fluence ψ. This inverse-square law is extensively utilized in dose calculations, when the distance of the calculation point from the source is changed.

2.2.2.2 Charged particle equilibrium

Charged particle equilibrium (CPE) is an important concept in external dosimetry, especially for photon radiation, since it allows establishing the relations between certain basic quantities.

The basis of the CPE is the existence of an energy balance in a 3D space. Generally, CPE exits for a volume V, if each charged particle of a given type, energy and direction leaving V is replaced by an identical particle of the same type and energy entering the volume V.

One important consequence of the CPE conditions is the equivalence of the absorbed dose and the kerma. In general, the transfer of energy (kerma) from a photon beam to charged particles at a particular location does not lead to the absorption of energy by the medium (absorbed dose) at the same location, basically due to the finite range of the secondary electrons released by photon interactions. However, it is possible to establish a relation between both quantities when it exists electronic equilibrium at the point of calculation. In fact, since photons (from Compton scattering or from pair annihilation) mostly escape from the volume of interest, it is possible to relate absorbed dose usually to collisional kerma K_c by Eq. 2.31.

Generally, in more realistic situations CPE is not usually achieved. There are two clear instances where CPE is not expected to be achieved: (1) in the build-up region of a beam where the dose increases before decreasing exponentially; (2) near the edges of a finite beam at distances between the beam edge and the point under consideration larger than the maximum secondary electron range (penumbra region).

Figure 2.6 shows the relation between absorbed dose D and collision kerma K_c for a megavoltage photon beam as function of depth in a phantom of a given medium. As shown in the panel (a) of the figure, at or near the entrance surface of the medium the absorbed energy (absorbed dose) is smaller than the transferred energy (kerma). Initially, the kerma is maximal at the surface of the irradiated material because the particle fluence is greatest at this point. As the photon beam penetrates the medium, the charged particle fluence and, consequently, the absorbed dose increases as a function of depth until the depth of maximum dose (z_{max}) is attained.

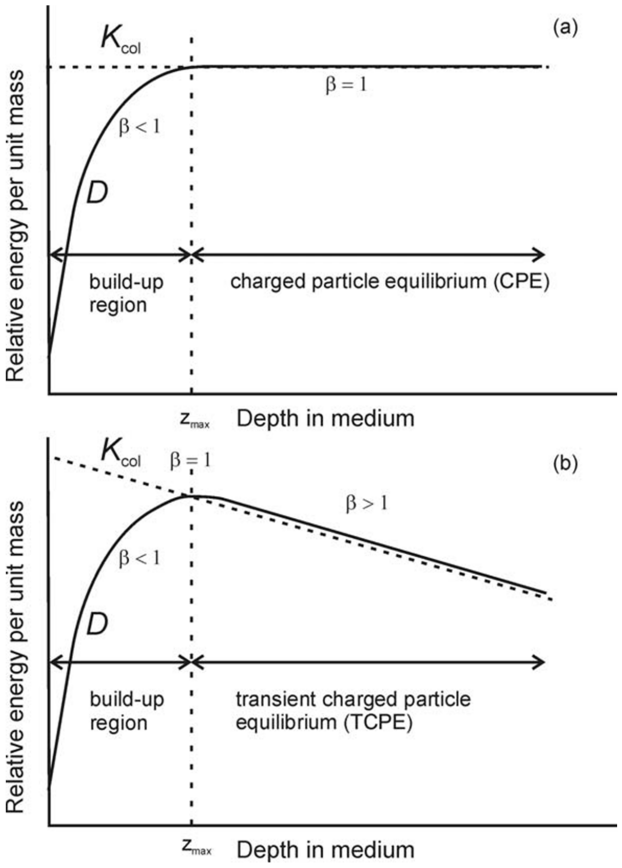

Figure 2.6: Relationship between absorbed dose and collision kerma for a megavoltage photon beam as function of depth in a medium. The factor β is defined as $\beta = D/K_{col}$. (figure by [Pod05])

Beyond z_{max}, if there are no attenuation of the photon beam, the electronic equilibrium (CPE) is achieved and both magnitudes become equal. In a more realistic situation, however, to satisfy the condition of uniform charged particle fluence along the depth is strictly impossible due to photon divergence and attenuation. In this case, the equality between K_c and D fails after z_{max}, but there is a constant relation between both quantities (figures 2.6b). In fact, the attenuation of the beam reduces thereby its intensity and, as a result, absorbed energy (absorbed dose) becomes greater than energy transfer (kerma).

2.2.2.3 Cavity theory

In dosimetry, in order to measure the absorbed dose at a point in a medium, a dosimeter is usually placed at that point of measurement. In general, the medium in the sensitive volume of dosimeters, which may be considered as a cavity, differs from the medium where it is placed in. In the following, it is assumed that the dosimeter is an ionization chamber and therefore its sensitive volume consists of air. This is the most common dosimeter used currently for dosimetry at radiotherapy departments.

If the material of the dosimeter is the same or equivalent to the medium of interest then the dose to the medium (D_{med}) is directly equivalent to the measured dose (D_{det}). However, this situation is generally unrealistic and most of the dosimeters do not measure the dose in water or biological tissue. In this case, in order to determine the absorbed dose in the medium (D_{med}), it is necessary to apply some conversion factors f to the dose obtained from these measurements. This leads thus to the relation,

$$D_{med} = f D_{det} \tag{2.37}$$

where the correction factor f can be usually derived and evaluated from a cavity theory.

Bragg - Gray cavity theory

The first theory developed to give a relationship between the absorbed dose in a dosimeter and the dose in the medium containing the detector is the *Bragg - Gray* theory. Two conditions must be met for the Bragg-Gray theory to be applicable. Firstly, the idealized concept of this theory requires the cavity to be small enough not to perturb the fluence of electrons crossing it, requiring small dimensions compared to the range of electrons. Secondly, only charged particles entering the idealized cavity contribute to the dose absorbed in it (referred to as D_{air}) and, thus, no photon interactions may occur within the cavity, being therefore ignored.

Using Eq. 2.37 and considering a constant fluence ϕ of electrons in the medium containing the dosimeter and also in the medium of the dosimeter (air), the ratio of the absorbed doses between both media is simply given by

$$\frac{D_w}{D_{air}} = \frac{\phi \cdot \left(\frac{\overline{S}}{\rho}\right)_w}{\phi \cdot \left(\frac{\overline{S}}{\rho}\right)_{air}} = \frac{\left(\frac{\overline{S}}{\rho}\right)_w}{\left(\frac{\overline{S}}{\rho}\right)_{air}} \tag{2.38}$$

with the unrestricted mass collision stopping powers averaged over the whole spectrum. The Bragg - Gray conditions demand an equilibrium of all electrons including δ-electrons created by hard collisions, which implies no creation or absorption of these electrons inside the cavity.

The absorbed dose in an air cavity D_{air} can be determined by measuring the charge Q produced in the gas using Eq. 2.34, that is:

$$D_{air} = (K_c)_{air} = X\left(\frac{W}{e}\right)_{air} \Longleftrightarrow D_{air} = \frac{Q}{m_{air}}\overline{W}_{air} \tag{2.39}$$

using the definition of exposure or equivalently, being m_{air} the mass of air in the cavity in which the charge Q is produced. Using now the Bragg - Gray cavity theory, the dose in a medium (D_m) is thus given by:

$$D_m = \frac{Q}{m_{air}}\overline{W}_{air}\left(\frac{\overline{S}}{\rho}\right)^m_{air} \tag{2.40}$$

where $\left(\frac{\overline{S}}{\rho}\right)^m_{air}$ is the medium-to-air stopping power ratio.

Spencer - Attix cavity theory

An extension of the Bragg - Gray theory was proposed by Spencer and Attix. The *Spencer - Attix* cavity theory is a more general formulation that takes into account that δ - electrons can have sufficient energy to move away from the site and produce further ionization. Some of these energetic electrons released in the air cavity would reduce the energy absorbed within the cavity, requiring thus a modification of the stopping power ratios. For the stopping powers calculation, this theory divides the electrons into two groups discriminated by a cut-off energy Δ:

- fast electrons with kinetic energies E larger than or equal to Δ traversing the cavity and depositing energy in collisions limited to Δ. These electrons are considered part of the spectrum, which has consequently a low energy threshold of Δ and a high energy threshold of E_{max}, where E_{max} represents the initial electron kinetic energy.

- slow electrons with kinetic energies E less than Δ that are unable to cross the cavity and thus depositing energy on the spot.

According to this classification, the ratio of doses in the cavity (D_a) and the surrounding medium (D_w) following the Spencer - Attix theory is given by the expression:

$$\frac{D_w}{D_{air}} = s^{\Delta}_{w,air} = \frac{\int_{\Delta}^{E_{max}} \phi_{E,w} \left(\frac{L}{\rho}\right)_{\Delta,w} dE + \left(\phi_E(\Delta)\right)_w \cdot \left(\frac{S(\Delta)}{\rho}\right)_w \cdot \Delta}{\int_{\Delta}^{E_{max}} \phi_{E,w} \left(\frac{L}{\rho}\right)_{\Delta,air} dE + \left(\phi_E(\Delta)\right)_w \cdot \left(\frac{S(\Delta)}{\rho}\right)_{air} \cdot \Delta} \tag{2.41}$$

where $\left(\frac{L}{\rho}\right)_{\Delta,w}$ is the restricted stopping power evaluated at energy Δ, $\phi_{E,w}$ is the electron fluence in the medium differential in energy including the δ-rays. The second terms of the numerator and denominator of Eq. 2.41 accounts for energy deposition by those electrons falling below Δ in energy while passing the cavity and are the so-called track-ends terms approximated by Nahum (1978). The choice of Δ is more or less arbitrary. It must ensure that the exit of electrons with energies below Δ is compensated by electrons with energy larger than Δ, but stopping inside the cavity, i.e. creating the δ-electron equilibrium. Usually Δ is set to 10 keV, the average energy needed by an electron to just cross a cavity of a typical ionization chamber. More precisely, Δ depends on the exact shape and dimension of the cavity.

It is important to point out here the fact that the Spencer - Attix theory assumes also an idealized cavity within a surrounding medium. Nevertheless, in reality, a perturbation of the dose measured by the dosimeter always occurs, caused by the finite size of the detector volume and the construction with materials differing from water (atomic composition and density). As it will further be discussed in section 3.2, the dose measured in a dosimeter needs to be corrected by several factors p_i to account for the perturbations of the electron fluence:

$$D_w = D_{air} \cdot s^{\Delta}_{w,air} \cdot \prod p_i \tag{2.42}$$

2.2.3 General considerations of basic dosimetry

Generally, radiation dosimetry can be divided into two different procedures, namely *absolute* and *relative dosimetry*. Whereas the absolute dosimetry is based on the dose measured at a given point, in the relative dosimetry the dose measured at a given point of interest under certain irradiation

conditions is compared to the measured dose value obtained at a reference point under specific reference conditions.

All the information provided either ionization chamber or other dosimeter may allow the performance of a 3D-characterization of the dose distribution for each type of radiation, material and setup. Clinically, the characterization is usually performed through *percentage depth* dose and *transversal dose profiles* (figure 2.7). The first type of profiles are defined as the quotient, expressed as percentage, of the absorbed dose at any depth d to the absorbed dose at a fixed reference depth d_0, along the axis of the beam (usually, Z axis). For photon beams, the typical reference depth is taken at the position of the maximum dose, denoted as d_{max}.

$$PDD(z) = \frac{D(z)}{D(d_{max})} \times 100\% \tag{2.43}$$

For radiotherapy beams, percentage depth doses (PDD) are usually calculated or measured for a given field size and at a predetermined distance SSD (source-to-surface distance)[3]. Typically, tables of percentage depth dose data for clinical use are usually provided for a variety of field sizes (from 2 x 2 up to 30 x 30 cm^2) at a standard SSD of 100 cm.

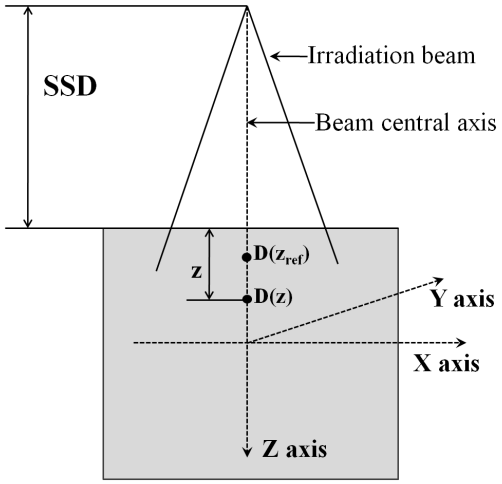

Figure 2.7: Diagram illustrating the definition of the percentage depth dose and transversal dose profiles in a rectangular phantom.

Transversal dose profiles are determined across the given field (usually, X or Y axis) at a spec-

[3]Source-to-Surface Distance (SSD) corresponds to the distance between the radiation beam source and the surface patient or the surface of the water phantom

ified depth. This type of profiles are important to determine the appropriate field size of a radiation beam and to ensure thus an adequate dosimetric coverage of the tumor.

In addition to these profiles, it is also usual to obtain a 2D distribution of the dose at a given depth or location. This 2D diagrams are usually known as isodose lines maps, which gives a scheme of the points or zones in a medium that receive equal doses of radiation.

In the present thesis, dose distributions in terms of percentage depth dose, dose profiles and isodose line distributions are calculated and measured in several phantoms (water, acrylic, CT-based phantoms) for different field configurations and type of beams (electron and photon beams).

Part II

MATERIALS AND METHODS

Chapter 3

Radiation treatment and dosimetry equipment

3.1 Medical linear accelerator

Since the inception of radiotherapy, several types of machines and units have been used for medical purposes. Originally X-ray tubes were used to treat superficial malignancies due to a limited penetration depth. Most deep target treatments used initially radioactive isotopes as radiation source (e.g. cobalt-60 therapy unit), until the medical linear accelerator (linac) was invented in the 1960s.

The most common type of accelerator in use today is the electron linear accelerator. These medical linear accelerators can be used in two distinct operation modes: electron mode and photon mode. In electron mode primary electrons are used for treatment, in photon mode photons are produced for treatment.

In the context of this thesis, two different electron linear accelerators, a Siemens PRIMUS and a Varian 2100C/D, were used to develop the presented studies. In particular, the Siemens PRIMUS was used in electron mode, while the Varian 2100C/D linac was considered for the studies using photon beams.

3.1.1 General description of an electron linear accelerator

For the production of therapeutical radiation, the following basic elements of the accelerator are needed: the high frequency source, usually a magnetron or a klystron, the electron source and acceleration unit, the bending magnet, which is inside the treatment head and the treatment head which includes several systems for the collimation and modulation of the beam. Figure 3.1 shows a schematic overview of the main components incorporated into a medical linear accelerator.

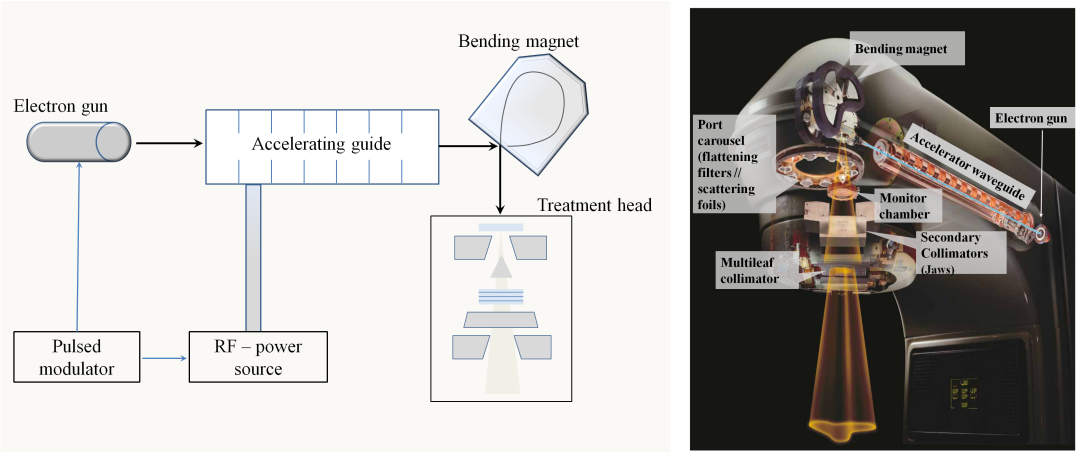

Figure 3.1: Left figure shows a schematic drawing of the main components incorporating a medical linear accelerator. Right figure is a zoom of the collimator systems. Note that the figure illustrates components incorporated in both electron and photon modes of a linear accelerator. [Varian Medical Systems, Palo Alto, CA].

This type of accelerator accelerates electrons using high frequency electromagnetic waves through a linear tube.

Initially, electrons are generated by an **electron gun**. In this structure, a heated cathode in the form of spiral tungsten filaments liberates electrons thermally. These electrons are then focused into a pencil beam by a curved focusing electrode and accelerated to a typical energy of 20 keV toward the perforated anode through which they are finally injected into the horizontal **accelerating waveguide**.

The acceleration of electrons in the accelerating waveguide is achieved through the application of electromagnetic waves of frequency in the microwave region ($\sim$ 3000 MHz) that have been confined and structured by the use of a cavity waveguide. The microwave radiation, used in the accelerating waveguide, is produced by the radiofrequency (RF) power generation system, which consists of two major components: a RF power source and a pulsed modulator. The RF power source is either a

magnetron or a klystron. Both are devices using electron acceleration and deceleration in vacuum for production of high power RF fields. The pulsed modulator produces the high voltage (100 kV), high current (100 A), short duration (1 s) pulses required by the RF power source and the electron gun.

The simplest kind of an accelerating waveguide is obtained from a cylindrical uniform waveguide by adding a series of disks with circular holes at the center, placed at equal distances along the tube. These disks divide the waveguide into a series of cylindrical cavities that form the basic structure of the accelerating waveguide in a linac. The cavities have two purposes: on one hand, to couple and distribute microwave power between adjacent cavities and, on the other hand, to provide a suitable electric field pattern for acceleration of electrons.

After the accelerator unit, the horizontal beam of electrons needs to be redirected in vertical direction towards the treatment head. Commonly, a 270° **bending magnet** is used for this purpose. The magnet has also two other functions. It produces inhomogeneous magnetic fields that focus the electrons and an energy filter or a slit is fitted in the magnet design to remove electrons that are not within 3 % of the nominal peak of selected electron energy. By changing the bending magnets current, the energy of the electron beam can be selected from an energy spectrum of accelerated electrons.

Finally, the electron beam deflected by the magnet is directed into to **treatment head**. The treatment head contains a series of components, which influence the production, shaping and monitoring of the clinical photon and electron beams used for the radiotherapy treatments. The mechanical support by which the accelerator and the treatment head are held in position, which can be turned, is usually called the ”*gantry*”. Next sections summarize the components incorporated into a treatment head working in both electron and photon modes.

3.1.2 Treatment head components

The components incorporated in the treatment head of a linac and placed in the path of the electron beam exiting the bending magnet are different as the accelerator works in electron or photon mode. Figure 3.2 shows schematic drawings of the different components used by a treatment head as it is used in photon and electron modes.

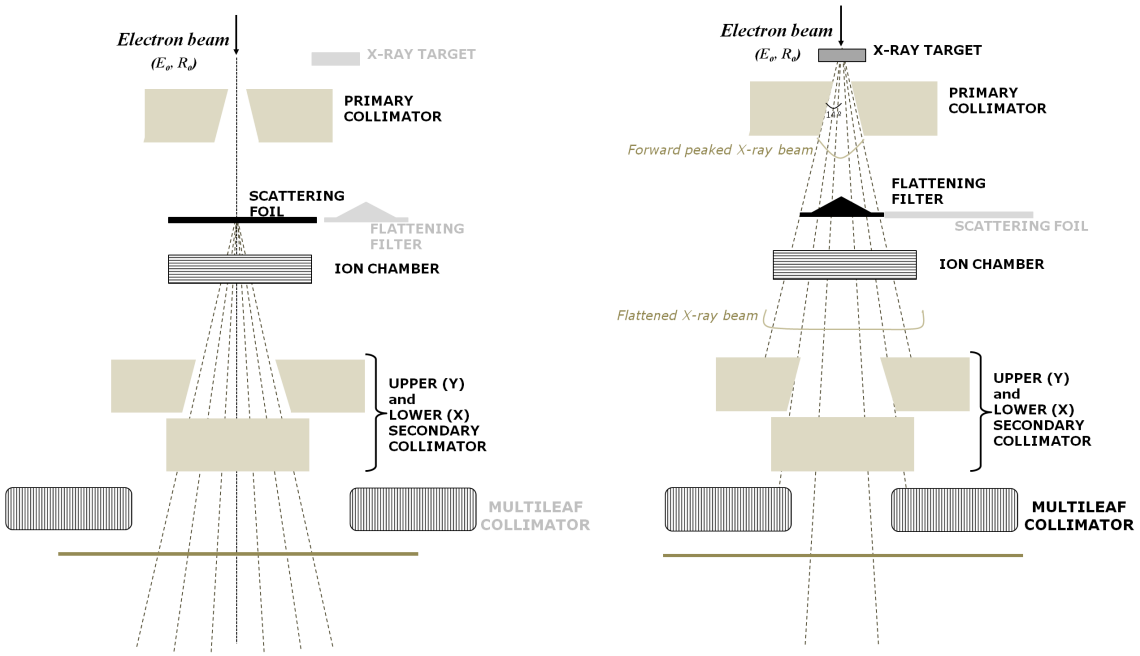

Figure 3.2: Diagram showing the components of a typical medical linear accelerator head working in (a) electron mode and (b) photon mode. The important components used in each delivery mode are indicated in black, while the unnecessary components for the respective delivery mode are indicated in gray.

Photon mode

Photon beams (x-rays) are produced by the electron beam exiting the bending magnet predominantly through the bremsstrahlung process within a *target* of high atomic number (high-Z) placed in the electron beam path. Tungsten (W) is normally used for this component due to both its high-Z and high resistance to heat deformation. The ability to resist heat deformation is important since in a typical W target only $\sim$ 1% of the incident electron energy emerges as bremsstrahlung photons. The remaining energy is lost to heat in the target. This heat is dissipated by the accelerator's cooling system. A copper foil recovers the downstream face of the tungsten slab and is in thermal contact with the accelerator's cooling system to dissipate heat and reduce secondary electron production.

At high electron energies, the average *radian* angle of the emitted bremsstrahlung photons is given approximately by $m_o c^2/E_0$ where $m_o c^2$ is the electron's rest energy and E_o its total energy. The produced photon beam is highly forward peaked and shows the characteristic spectra of bremsstrahlung photons, i.e. a continuous energy distribution with a maximum energy corresponding to the kinetic energy of the electron producing the bremsstrahlung spectra.

A primary collimation of the photons emerging from the bremsstrahlung target is performed using a tungsten collimator with a conical opening defining an angle of 14° from the target surface. The conical beam exiting the *primary collimator* is cylindrically symmetric about the beam's central axis. This collimator is fixed immediately after the target and removes photons traveling outside a defined divergence from the central beam axis. The conical opening of the primary collimator defines the maximum size of the radiation field which can be defined, e.g. a conical opening of 14° represents a maximum field size of 50 x 50 cm^2 at a distance from the source (SSD) of 100 cm. This maximum field size is later truncated subsequently with adjustable rectangular collimator or jaws.

Bremsstrahlung photons emerging from the electron target and primary collimator are highly forward peaked, that is, the beam contains a significantly higher intensity of high energy photons directed along the beam's central axis (a product of the angular bremsstrahlung cross-section). A conical beam-*flattening filter* is used for photon beams in order to make uniform the forward-biased photon intensity. Such a filter attenuates the photon beam more strongly in the central parts and mainly removes low energy photons without changing the spectral shape of the higher energies. In addition to the flatten function of the filter, it has shown to have a high influence on the photon field. On one hand, it scatters photons, it reduces the mean photon energy by pair production and Compton scattering and it absorbs low energy photons, leading to a hardening of the beam. On the other hand, the filter reduces the overall intensity of the photon beam and contaminate the photon field with charged (electrons) and uncharged (neutrons) secondary particles. The exact alignment of the filter with respect to the beam is of course critical.

It is important to point out that the combination of target thickness/composition with flattening filter shape/composition gives rise to the spectral and penetration properties of the beam. In fact, different (in dimension and material) targets and filters are used for different energies.

The delivery of radiation by a medical accelerator is monitored by a special *ionization chamber* system placed after the flattening filter. The monitoring system consists of several ion chambers or a single chamber with multiple plates. Ion chambers are used to measure beam uniformity and intensity, and provide a relative measure of radiation output. This monitor chamber is calibrated in terms of monitor units (MU), where 100 MU define 1 Gy under reference conditions (i.e. maximum dose depth, d_{max}, in a water phantom irradiated with a 10 x 10 cm^2 photon field at SSD of 100 cm). Since the chambers are in a high intensity radiation field and the beam is pulsed, it is important to make sure that the ion collection efficiency of the chambers remains unchanged with changes in

the dose rate. Contrary to the beam calibration chambers, the monitor chambers in the treatment head are usually sealed, so that their response is not influences by temperature and pressure of the outside air.

After passing through the monitor chamber, the photon beam is further collimated into a specific field size by two pairs of tungsten blocks moving in orthogonal directions (X and Y directions), called *secondary collimator* or jaws. For most linacs, each block (or jaws) can be moved independently with respect to the central beam axis to create a rectangular field with sizes ranging up to 40 x 40 cm^2 at the isoplane, which is usually placed at 100 cm. The two pairs of jaws are referred to as X and Y, with the position of each jaw (X1, X2, Y1, Y2) denoting the field edge at the isoplane.

Under the secondary collimator is the *multileaf collimator* (MLC). This device consists of a set of movable leaves of tungsten which allow to create irregular field shapes. Specifically, this type of collimators are widely used in radiotherapy techniques such as 3D - conformal and IMRT. MLCs are currently available from several manufacturers. In general, the MLC designs from the various manufactures differ in the way they are coupled to the secondary collimators and also in their physical and dosimetric characteristics.

Electron mode

When a linac is working in electron mode, the bremsstrahlung target is rotated out of position and the flattening filter is replaced by an electron *scattering foil* system. This system is composed of two scattering foils. The first foil is typically constructed from a thin sheet of high-Z material and is designed to spread the electron beam. The second foil, located downstream of the first foil, is used to flat the electron beam and may be constructed from a thicker low-Z foil with a higher Z region fused to the foil in the region of the beam central axis.

For electron mode, additionally to the primary and secondary collimators, electron beams also rely on electron beam *applicators* (cones) for beam collimation. The applicators are attached to the treatment head, just below the exit window. The main feature of the applicators is to improve the collimation of the beam close to the patient surface. As it is well known, the electrons contrary to photons, have a high scattering probability as they travel in a medium. In the treatment head after passing through the scattering foil, the electrons are scattered by the other components of the accelerator head as well as by the air column between the exit window and the patient and, thereby, they need to be more conformed.

In conjunction with the electron applicators, conformed field shaping of electron beams is usually achieved using *shielding blocks* or *special cutouts*. Typically, a lead or metal alloy (e.g. cerrobend) cutout may be constructed and placed on the applicator as close to the patient as possible. Currently, there are standard cutout shapes which have been preconstructed and are ready for use at the treatment time, but there are also custom cutout shapes designed for a specific patient treatment.

In addition to the cutouts for the conformation of electron beams, several studies have been recently published assessing the possibility of collimating and modulating electron beams with photon-based MLCs. The use of MLCs should be a more rapid and accurate solution to deliver highly conformed dose distributions [Salg10].

Linacs in the present thesis

In this thesis, all the dosimetric studies performed using photon beams have been developed in the *Varian 2100C/D* linear accelerator installed at the *Centro Oncológico Dra. Natália Chaves (Carnaxide)*. This accelerator was equipped with a Millenium MLC of 120 tungsten leaves (80 inner leaves of 0.5 cm width and 40 outer leaves of 1.0 cm width projected to isocenter). A beam energy of 6 MV has been used for all works.

The dosimetric studies performed using electron beams have been developed in the *Siemens Primus* and *Siemens Oncor* linear accelerators installed at the *Virgen Macarena Hospital in Seville* and *Santa Maria Hospital in Lisbon*, respectively. Both Siemens accelerators have the same head geometry, with the exception of the multileaf collimator (MLC), which is only incorporated in the Siemens Oncor accelerator. In the context of present thesis, the MLC collimator has been not employed in the investigations using electron beams, therefore, both Siemens accelerators may be considered geometrically equivalents. The collimation of the electron beams has been only performed using secondary collimators, electron applicators and cerrobend cutout. Beam energies of 12 and 18 MeV have been used for the work.

3.2 Radiation dosimetry equipment

In the context of present thesis, it has been necessary to perform some experimental validations of dose distributions previously calculated using Monte Carlo methods. Measurements of absorbed dose have been performed using dosimeters. These are devices in which the absorbed dose de-

posited in its sensitive volume by ionizing radiation produces some measurable change in its properties, as for example, a change in the measured charge (ionization chambers), measured light output (TLD) or a visible chemical reaction (photographic film), among others.

Two different types of dosimeters have been used to carry out the measurements in the present studies, namely ionization chambers and photographic films (radiographic and radiochromic films). The features and use of these dosimeters are briefly outlined next.

3.2.1 Ionization chamber dosimetry

Ionization chambers have become the standard dosimeter for clinical dosimetry because of their long-term stability, high precision, direct readout and relative ease of use. Typically, an ionization chamber used for clinical radiation dosimetry consists of a thin wall of material such as graphite surrounding a small but well-known volume of air (figure 3.3).

The passage of radiation through the air causes ionization, resulting in ion pairs, typically positive ions and free electrons. A high voltage is applied across the chambers, between the wall and the electrode, to divide and collect the ion pairs produced by ionizing radiation. The resulting current is then measured by an electrometer and can be converted to absorbed dose after the application of several correction factors. The applied voltage is high enough to collect the surrounding charge but not so high as to induce secondary electrons from the initially accelerated electrons.

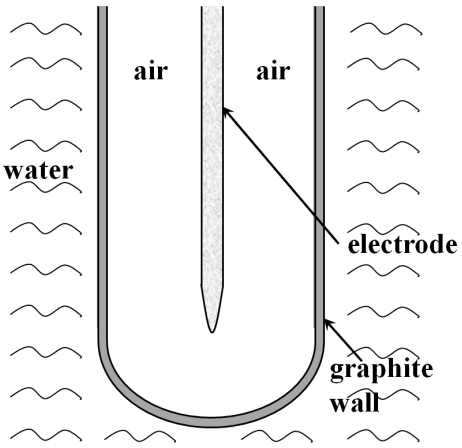

Figure 3.3: Scheme of an ionization chamber emerged in water, which illustrates the situation in a dose measurement with an ionization chamber.

One of the major limitations of the ionization chambers is that they do not have sufficient spatial resolution due to their size. Additionally, ionization chambers just allow to measure dose around a point or in 1-D. However, 2-D or 3-D measurements of static radiation fields are also possible by either translating the ionization chamber using motorized water phantoms or using an array of ionization chambers.

Ionization chambers are commercially available in a variety of designs and sizes, corresponding to the desired sensitivity. Typically, the two different designs more used in clinical dosimetry are the *parallel* and *cylindrical* geometric. A plane parallel chamber consists of two separated electrodes parallel to each other and perpendicular to the primary beam direction, leaving an air-filled gap in between, which serves as the sensitive volume. This type of chamber is usually recommended for high energy electron dosimetry. In contrast, cylindrically shaped ionization chambers (also known as thimble or compact chambers) are the most commonly used for photon dosimetry. This type of chamber consists of a cylindrical air volume with a central electrode inside and a surrounding cylindrical wall perpendicular to the primary beam direction. This is the case illustrated in figure 3.3.

In the context of the present thesis, the following cylindrical ionization chambers were used for the dosimetric measurements:

- **Semiflex chamber (model PTW 31002)**: With a sensitive volume of 0.125 cm^3, the semiflex chambers are thimble chambers designed for therapy dosimetry, mainly for dose distribution measurements in motorized water phantoms. This chamber is the ideal compromise between small size for reasonable spatial resolution and large sensitive volume for precise dose measurements. Moreover, this chamber provides enough signal to be used for high precision absolute dose measurements. This type of chamber exhibits no significant dose rate or energy dependence (high energy photon beams ^{60}Co- 25 MV quality photon beams). Due to its dimensions, the field size is restricted to fields larger than 3 x 3 cm^2 (right picture of figure 3.4).

- **PinPoint chamber (model PTW 31006)**: The PinPoint chamber consists of a 2 mm diameter and 5 mm long cylindrical air chamber with a central steel electrode with a PMMA (covered with graphite) wall and a sensitive volume of 0.015 cm^3. The PinPoint chambers have been specially designed for relative beam profile measurements as well as for the characterization of radiation fields where a superior spatial resolution is desired, such as in the build-up regions.

Furthermore, this chamber is an optimal detector for measuring output factors [1]and fields in the range between 2 x 2 cm^2 and 10 x 10 cm^2. The PinPoint chamber can be positioned in 2 directions for optimal spatial resolution, but the preferable direction is perpendicular to the chamber axis (left picture of figure 3.4).

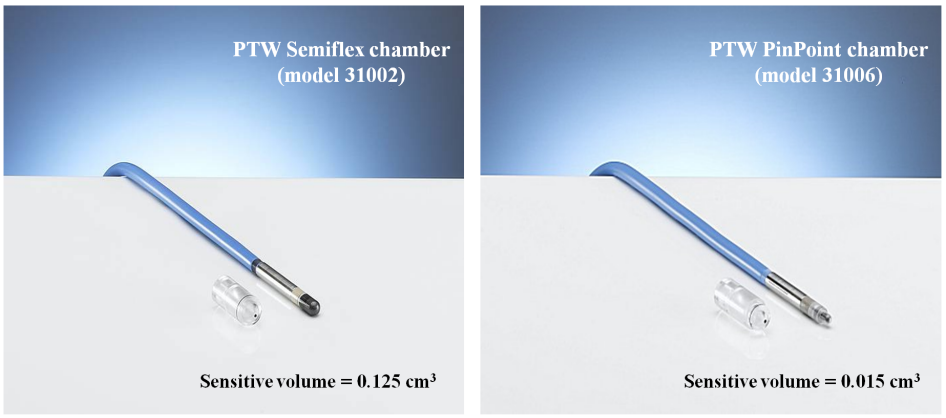

Figure 3.4: PTW Semiflex chamber of 0.125 cm^3 (left) and PTW PinPoint chamber (right) (figures from www.ptw.de).

- **Roos parallel-plate chamber (model PTW 34001)**: The Roos chamber is the chamber recommended for high precision absolute dose measurements in high-energy electron beams. However, it is also well suited for measurements of high-energy photon depth-dose curves up to 2.5 mm depth below the water surface. The Roos chamber consists of a flat cylinder with a radius of 7.5 mm and a height of 2 mm. It has a sensitive volume of approximately 0.35 cm^3. The waterproof design of this chamber makes it suitable to be used in water as well as in solid water phantoms (right picture of figure 3.5).

- **Advanced Markus parallel-plate chamber (model PTW 34045)**: The Advanced Markus chamber is also a well-recommended chamber for dose measurements in high-energy electron beams. The chamber has a small sensitive volume of 0.02 cm^3 (radius of 2.5 mm and 1 mm depth), which makes the chamber ideal for dose distributions measurements with a good spatial resolution. The chamber can be used both in solid water and water, although in the last case, it is necessary to use the protective cap (left picture of figure 3.5).

[3]Output factors are derived by performing relative dose measurements for various field sizes and then normalizing the results to a reference field size, normally 10 x 10 cm^2.

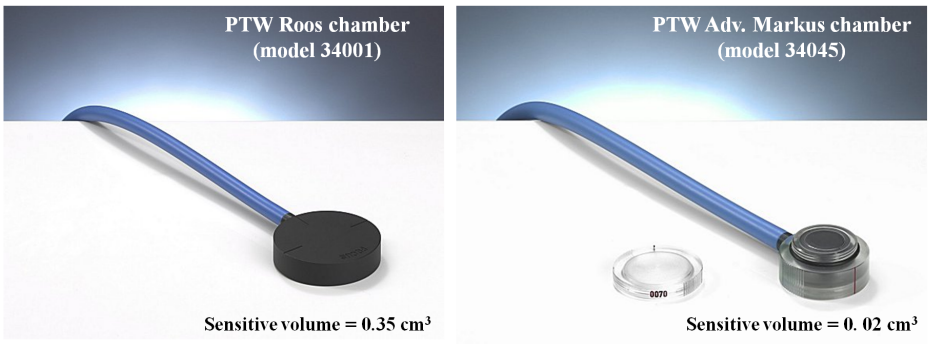

Figure 3.5: PTW Roos parallel-plate chamber (left) and PTW Adv. Markus chambers (right) (figures from www.ptw.de).

Dosimetry protocols with ionization chambers

When measuring absorbed dose with an ionization chamber several corrections need to be made to ensure that the measurement of absorbed dose gives the same result regardless of operational conditions such as radiation quality and dose rate. The International Atomic Energy Agency (IAEA) and other institutions such as the American Association of Physicist in Medicine (AAPM) have published dosimetry protocols to be used for the dose determination in external radiation therapy. These protocols define all the different correction factors needed to achieve a clinically relevant accuracy of the measurements of absorbed dose.

The **IAEA TRS-398** code of practice [And00] has been taken as a reference for the dosimetric measurements performed in present work. A brief description of the methodology and recommendations given by this protocol are given next.

Ionization chambers for absolute dosimetry are usually calibrated in secondary standard laboratories by national radiation authorities using reference conditions under a known field of radiation, usually a ^{60}Co beam. The calibration is based on determined absorbed dose in water by international primary standard laboratories in so-called standard conditions of pressure 101.3 kPa and temperature 20 °C. In order to use the ionization chambers in other conditions as those of the chamber calibrations, it is essential to consider many issues concerning either the chamber or the measurement circumstances and correct the measured signal for the specific conditions.

The IAEA TRS-398 code of practice is based on a calibration factor N_{D,w,Q_0} in terms of absorbed dose to water for a reference beam of quality Q_0 (usually a ^{60}Co beam) and is applied to photon beams generated by electrons with energies in the range of 1 MeV to 50 MeV. According to this

code, the absorbed dose in water for a megavoltage beam is given by:

$$D_{w,Q_0} = M_{Q_0} \cdot N_{D,w,Q_0} \tag{3.1}$$

where the N_{D,w,Q_0} *calibration coefficient* has been traceable from the standards laboratory and relates the reading of the dosimeter M_{Q_0}, formed by the ionization chamber and the electrometer, to dose to water D_{w,Q_0} in a reference field under reference conditions. These reference conditions are air pressure, temperature, field sizes, measurement depth, phantom size and quality index Q directly linked to the energy of the irradiation beam.

In general, when a ionization chamber is used for clinical dosimetry, only a few of the defined reference conditions can be usually reproduced. Thus, deviations due to several *influence quantities* need to be accounted for by the application of a product of multiplicative factors of two classes. The first class of corrections accounts for changes in the beam quality compared to the reference beam quality Q_0. These corrections are represented by the *beam quality correction factor* which is denoted as k_{Q,Q_0}. This factor corrects all departures from the ideal conditions of the Bragg-Gray cavity theory and includes the following parameters:

- p_{wall}: Correction for the non-medium equivalence of the chamber wall and the surrounding water where the chamber is placed.
- p_{cav}: Correction for scattering differences between the air cavity and the surrounding material, usually water.
- p_{cel}: Central electrode perturbation correction accounting for the central electrode in a thimble ionization chamber.
- p_{dis}: Factor accounting for the fact that the air cavity of a cylindrical chamber causes less attenuation or build-up than the water displaced by it and causes the upstream shift of the effective point of measurement. The effective point of a chamber is usually shifted from the position of the center towards the source by a distance which depends on the type of beam and chamber.
- $s^{\Delta}_{w,a}$: Restricted stopping power ratio of water to air considering the fraction of the total collision stopping power that includes all the soft collisions and those hard collisions resulting in δ-rays with energies less than a cutoff value Δ.

Extending these corrections to a function of beam quality leads to:

$$k_{Q,Q_0} = \frac{N_{D,w,Q}}{N_{D,w,Q_0}} = \frac{\left(s^{\Delta}_{w,a} \cdot p_{cel} \cdot p_{wall} \cdot p_{cav} \cdot p_{dis}\right)_{Q}}{\left(s^{\Delta}_{w,a} \cdot p_{cel} \cdot p_{wall} \cdot p_{cav} \cdot p_{dis}\right)_{Q_0}} \tag{3.2}$$

The second type of corrections relates to the reading of the electrometer and include:

- k_{elec}: Calibration factor of an electrometer.
- $k_{P,T}$: Temperature and pressure correction for the varying density and humidity of the air in the user facility with respect to the conditions specified by the standards laboratory.
- k_{pol}: Polarity correction for the effect of altering the measured charge.
- k_s: Recombination correction for ions that recombine before they reach the electrodes, leading to the incomplete collection of charge in the chamber.

In summary, the absorbed dose to water $D_{w,Q}$ in a user's beam, measured with an ionization chamber dosimeter, is determined by:

$$D_{w,Q} = M_C \cdot N_{D,w,Q_0} \cdot k_{Q,Q_0} \tag{3.3}$$

where M_C is the reading of the electrometer corrected for the various influence factors previously mentioned:

$$M_C = M \prod k_i = M \cdot k_{elec} \cdot k_{P,T} \cdot k_{pol} \cdot k_s \tag{3.4}$$

The factor N_{D,w,Q_0} is a calibration factor valid under reference conditions for the quality Q_0 and it is obtained at a standards dosimetry laboratory under a set of well-established reference conditions.

All this factors are generally provide by the protocol or the chamber manufacturer for the various ionization chambers and beam qualities, requiring to maintain the geometrical reference conditions.

3.2.2 Film dosimetry

Film dosimetry has been used extensively as a convenient and rapid mean of measuring dose distributions of therapeutic electron and photon beams. In radiation dosimetry, there are numerous

problems associated with the measurements of two-dimensional dose distributions or depth-dose distributions in high-gradient dose regions, where automated dosimetry systems using ionization chambers cannot easily be employed. Dosimetry with films have resulted in a suitable solution to overcome these difficulties due to features such as their high spatial resolution. The films is easy to develope and gives a permanent record of dose distributions with an acceptable accuracy and precision.

In film dosimetry, the effect produced in the film by the radiation is measured in terms of light opacity of the film using a densitometer. Opacity is defined as I_0/I, where I_0 is the light intensity measured in the absence of the film and I the intensity through the film in a direction perpendicular to its plane. Based on this relation of intensities, the optical density (OD) is defined as:

$$OD = -log_{10}(\frac{1}{T}) = log_{10}\Big(\frac{I_0}{I}\Big) \tag{3.5}$$

where T is the transmittance defined as I/I_0.

A relationship between the OD and the dose is generally defined for each combination of film and densitometer or scanner. This relation is known as *sensitometric curve* or H&D curve (which stands for its inventors Hurter and Driffield) and it provides the characteristics of a film. This type of curves are also an important tool for quantifying contrast and dynamic range of a radiographic film and depend strongly on the processing conditions.

Currently, there are two different types of films used for dosimetry: radiographic and radiochromic film. The properties and features of both films are slightly different and these are summarized below.

3.2.2.1 Radiographic film

A radiographic film consists of a radiation-sensitive emulsion coated by a transparent polyester base. The emulsion consists of silver halide crystals (typically 95% silver bromide and 5% silver iodide) embedded in gelatine. The exact composition of emulsions varies with the manufacturer and is a closely guarded industrial secret.

The ionization of AgBr grains, as a result of radiation interaction, forms a latent image in the film. The latent image is defined as the radiation-induced change in a grain of silver-halide crystal that renders it susceptible to the chemical action of a developer. This image only becomes visible (film blackening) and permanent subsequently to processing. After the proper developing and fixation of

the film, the image can be seen and analyzed with a densitometer or scanner. More details about this process can be found in [Pai07].

The useful dose range of radiographic film is quite limited and the energy dependence is pronounced for lower energy photons. Due to the high atomic number of emulsion components such as silver (Ag), bromine (Br) or iodine (I), film's dose response will depend strongly on the relative contributions of photoelectric interactions, and thus on the photon energy. This fact causes serious problems in the dosimetry of kilovoltage beams but to a lesser degree in megavoltage beams.

The response of the film depends on several parameters, which are difficult to control. Consistent processing of the film is a particular challenge in this regard.

Typically, film is used for qualitative dosimetry, but with proper calibration, careful use and analysis, film can also be used for dose evaluation.

Two types of radiographic films, namely the Kodak XOMAT-V and EDR2 (Extended Dose Range) manufactured by Kodak, Inc. (Rochester NY and Europe), are used in this work. These films are very different in their response to dose. The difference between the two films originates from their differences in the content of silver bromide crystals and grain size. The grain size of EDR2 film is smaller than that in the XOMAT-V. Both films are manufactured with typical dimensions of 25.4 cm x 30.5 cm (for smaller size) and 35.0 cm x 43.0 cm (for larger size). They are ready packed, i.e. each single film has a light-tight paper envelope and can be easily handled in the irradiation room at normal illumination.

Radiographic film XOMAT-V

The film emulsion of XOMAT-V is composed of AgBr (I) grains of an irregular shape with an average grain size of about 2 μm. In densitometry, the maximum light absorption in the film occurs between 380 to 420 nm. It saturates at about 3.0 Gy of irradiation. The XOMAT-V film is the one most frequently used to measure relative dose distributions for IMRT; it is everywhere available and is highly demanded for clinical duties. The main disadvantage of XOMAT-V is the saturation at a relative low dose. For IMRT verification, a typical patient dose of 2 Gy should be used; therefore for film dosimetry the dose must be scaled, and that can be achieved by reducing the number of monitor units per segment. Some research [Pai07] has proved that the sensitivity of XOMAT-V films is neither energy dependent nor field size and depth dependent for field sizes below 10 x 10 cm^2 at 10 cm depth.

Radiographic film EDR2 (Extended Dose Range)

The film EDR2 is composed of cubic silver grains of approximately 0.24 μm diameter. The response curve of the EDR2 film is extended across a large range of radiation dose. This has been the reason for the term ”extended dose range”. The maximum light absorption in the film occurs around 375 nm. The response of the EDR2 film is almost linear over a wide range (from 0.25 Gy to 4 Gy), and it saturates at 7 Gy. The concentration in silver for EDR2 is about 50 % compared with that for XOMAT-V, implying a lower sensitivity. The fact that it is possible to expose EDR2 film to doses higher than 3 Gy is an advantage for IMRT field. The complete dose per fraction of the patient can be delivered to the film without a need for rescaling the monitor units.

Response curves of both radiographic films

The calibration curves for the two radiographic films used in this investigation are shown in figure 3.6. Included in this plot are the data for a 6 MV photon beam for a 10 x 10 cm^2 field size at a fixed depth of 5 cm within the solid water phantom.

In general, the typical response curve of radiographic film for film screen systems has a sigmoid shape and is divided into three different regions: a toe region or region of low gradient at low exposures, a region of relatively steep increase in density for minimal exposure increase (slope region) and finally, a third relatively flat region called the shoulder region at high exposures where the response follows a flat behavior.

The slope is an important factor of radiographic film dosimetry since it describes the sensitivity of a film. Based on the slope of the sensitometric curve, radiographics films can be categorized into ’*fast*’ films, as those films with a steep response curve, and ’*slow*’ films as those films showing a smaller slope in the dose response curve.

In dosimetry, the dose response curve should be approximately linear with dose and approximately independent of the dose rate and radiation energy.

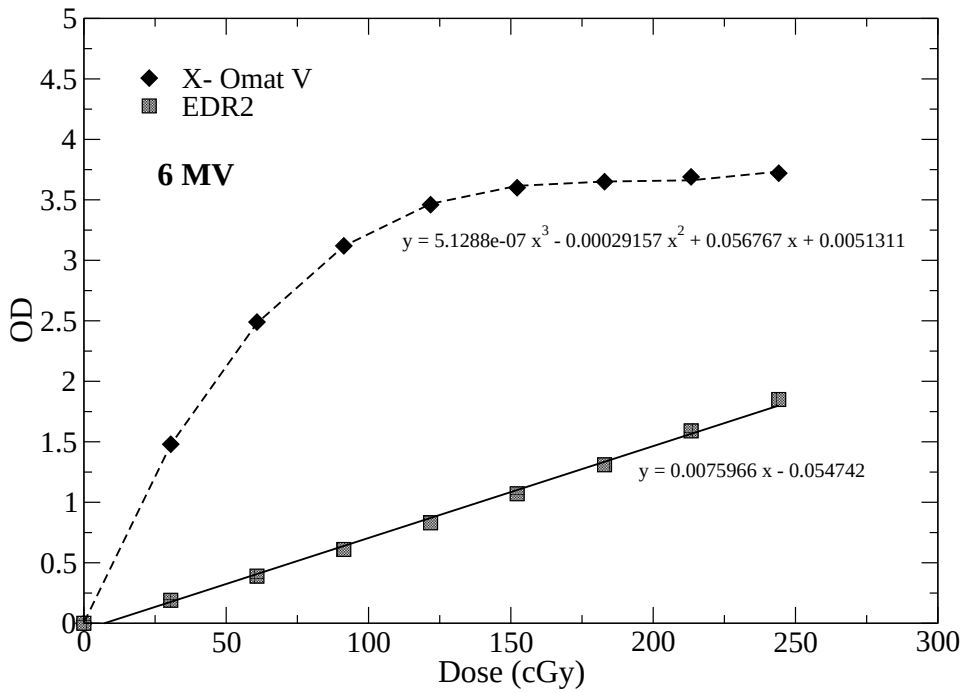

Figure 3.6: Typical response curve, i.e. net optical density versus dose curves of radiographic films X-OMAT V and EDR2 for direct x-ray exposure. Films were irradiated perpendicularly at a depth of 5 cm by a 6 MV photon beam with a 10 x 10 cm^2 field size. The cubic and linear interpolation between the measured data is depicted with solid and dotted lines for XOMAT-V and EDR2 film, respectively.

As seen in figure 3.6, the sensitometric response of Kodak X-Omat V film is seen to increase linearly with dose until approximately 80 cGy, beyond which the curve appears to deviate from linearity. Above this dose value, the gradient of the sensitometric curves decreases. Kodak EDR2 film response is quite different from that of X- Omat V films. Kodak EDR2 shows a linear response along the entire dose range, resulting in an increased sensitivity at higher doses.

It is important to mention that the shape of the curves may vary due to the use of different chemical reagents or the use of different types of film processors. Also, the type and model of the scanner used may affect the final response curve. The curve may also vary if the condition of the film processor changes or the scanner light source wears out.

3.2.2.2 Radiochromic film

Radiochromic film is a new type of film for radiotherapy dosimetry. The introduction of radiochromic films (based on polydiacetylene) has solved some of the problems associated with conventional 2D radiation detectors. The high spatial resolution, weak energy dependence and near tissue-

equivalence of radiochromic films make them more suitable for measurement of dose distributions in radiation fields with high dose gradients than previous radiographic films.

There are many different types of radiochromic films in the market, but the most commonly used is the Gafchromic film. This film shows also a large variety of models, such as HS, XR-T, MD-55, EBT, among others, differing basically in the composition and dose response and sensitiviy. Here the recently introduced radiochromic Gafchromic external beam therapy (EBT) film is used and thereby briefly discussed.

According to the manufacturer ISP (International Specialty Products: www.ispcorp.com) the GafChromic EBT film is composed of two active layers, which are 17 μm thick and separated by a 6 μm surface layer. All three layers are coated with two clear polyester sheets with a thickness of 97 μm, as it is presented in figure 3.7.

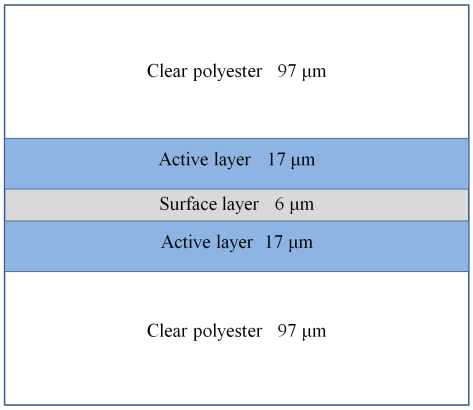

Figure 3.7: Composition of a Gafchromic EBT film.

Unlike silver-halide based radiographic films, the active component of EBT film is nearly tissue-equivalent with an atomic number Z_{eff} of 6.98. Its overall atomic composition is H (39.7 %), C (42.3 %), O (16.2 %), N (1.1 %), Li (0.3 %) and Cl (0.3 %). GafChromic EBT films are grainless and therefore have a high spatial resolution. The uniformity of this EBT model is better than 1.5 %. Furthermore radiochromic films are independent of the energy of the ionizing radiation and self-developing. These kind of film contains a special dye that is polymerized upon exposure to radiation. The polymer absorbs the light and the transmission of light through the film is measured with a densitometer. As consequence, neither a developer, nor a heater is required for analyzing these films.

GafChromic EBT films are stored in an opaque envelope provided by the manufacturer and should be only removed while irradiation and scanning. The films do not change their color due to artificial light, but UV-light can cause the polymerization of the active surface layer and change the color of the film. Besides, the films must be kept at constant temperature and handled with cotton gloves to avoid scratches and stains on the surface of the film and therefore make sure that the accuracy of a verification will not be reduced. More details about the properties of EBT Gafchromic film can be found in the literature [Buts03, Nir98, Mar08].

The dosimetry with radiochromic films has several advantages over radiographic films, such as ease of use, elimination of the need for darkroom facilities and film processing, dose rate independence, better energy characteristics and insensitivity to ambient conditions. All these advantages have subsequently consequences in the accuracy and precision of the dosimetry performed using these films. Compared with radiographic films that can produce dose inaccuracy higher than 5 %, the statistical uncertainty using radiochromic films can be reduced to 2 - 3 %.

A critical component for the GafChromic dose measurement process is the densitometer used for the films optical density readout.

In this work, all radiochromic films have been scanned using the Epson Expression 10000 XL commercial scanner. The subsequent analysis of the data was performed with the software Omni'Pro IMRT. The procedure followed in present work for the digitalization and analysis of irradiated EBT films has been based on previous published work by Ferreira et al (2009) [Fer09].

Chapter 4

Monte Carlo simulation techniques in radiation therapy

In this chapter, an overview of the fundamental principles of the Monte Carlo technique is done on a first approach. The application of this technique to radiotherapy is then briefly discussed. Afterwards, it is presented a short description of the MC simulation of electron and photon transport. This is followed by the introduction of the general - purpose EGSnrc code as well as the EGSnrc-based user codes, BEAMnrc and DOSXYZnrc, which are the underlying Monte Carlo codes used for the dosimetric studies developed in the present thesis. Variance reduction techniques of particular importance in simulations of linacs and dose calculations are also reviewed.

4.1 General fundamentals of the Monte Carlo method

The Monte Carlo (MC) method was originally proposed by Stan Ulam and John von Neumann during the Second World War with the aim of developing atomic weapons [Eck87]. The first application of the method was idealized by Wilson in 1952 for the study of the production of electromagnetic cascades in the area of high energy physics [Wil52]. It was this study which established the base for the development of MC codes focused on the simulation of radiation transport. Since then, the method have been evolved into many different areas (high energy physics, nuclear reactor analysis, medical imaging, radiation shielding, etc.) as an alternative of experimental approaches.

In the 1970s and early 1980s, the application of MC method to the field of medical physics

made a slow entry [And91]. Only simulation of simple radiation geometries such as point sources irradiating homogeneous water phantoms could then be modeled. For the last years, the use of the Monte Carlo method has been widely increased and, currently, it shows numerous applications in the medical physics field, namely the simulation of detectors of nuclear medicine, the calculation of absorbed dose in radiotherapy or the modeling of the interaction of ionizing particle with the structures such as the DNA molecule in micro or nanodosimetry.

Regarding to the particular case of radiotherapy problems, the issue of large computing times has traditionally led to the MC method being viewed as a clinically unfeasible approach. However, due to the most recent improvement in computer technology and development of faster codes optimized for radiotherapy calculations, the method has become now an excellent alternative to the analytical solving of complex transport equations or to the widely use of crude macroscopic algorithms. In fact, clinical treatment planning systems (TPS) based on the MC method are being recently implemented for the dose calculations at many radiotherapy departments.

Typically, "Monte Carlo" represents a generic name for all calculation methods that use random numbers. The general idea of MC analysis is to create a model, which is as similar as possible to the real physical system of interest, and to create interactions within that system based on known probabilities of occurrence, using **random sampling** of the probability density functions (PDFs).

In the context of modeling radiation transport, Monte Carlo is a stochastic method which simulates individual trajectories in an arbitrary geometry employing a sequence of random numbers in a sampling process based on the probability distributions governing all the physics process involved in the radiation interactions with matter.

In the MC approach, the transport of an incident particle and all of its progeny particles subsequently set in motion is referred as "*particle history*". By simulating a large number N of histories, reliable average values of different macroscopic quantities of interest (absorbed dose, fluence, etc.) can be obtained. Since the result is an average value, it is associated with a standard deviation that expresses the uncertainty due to the fact that the simulated number of histories is not infinite. In fact, the statistical uncertainty of a simulation depends on the number of considered histories N and usually decreases as $N^{-1/2}$.

As stated before, for any MC simulation it is necessary to be able to reproduce randomness. The first and major essence of any Monte Carlo simulation is therefore an infinite sequence of **random numbers**. A random number is a particular value of a continuous variable uniformly distributed on

the unit interval $[0, 1]$. A high quality random number sequence is a long stream of numbers with the characteristic that the occurrence of each number in the sequence is unpredictable. Although databases of real random numbers can be found, their use is limited due to the large size, making the simulation process very slow. Thus, mathematical algorithms for the generation of 'pseudorandom numbers' have been introduced, the so-called random number generator (RNG). The outputs of the RNG can not be considered exactly random; they only approximate some of the properties of random numbers. Hence, a careful mathematical analysis is required to ensure that the generated numbers are sufficiently 'random' for the particular simulation. The length of the period of a RNG must be long enough to avoid repetitions in the sequence of numbers used during the simulation process, as otherwise correlations can be produced.

The selection of a random value of a specific quantity, from a continuous probability density function is realized in MC simulation through **sampling methods**. The general basis of sampling is not a easy task. However, a large number of works has been done regarding this subject and nowadays accurate and efficient algorithms exist for sampling from all frequently used distributions. A more detailed discussing of sampling methods does not lies on the scope of this thesis. A general introduction to sampling methods and a review of all typical sampling algorithms utilized in the Monte Carlo codes can be found in [Biel01].

4.2 Why use Monte Carlo in radiotherapy?

All physics processes involving the transport and interaction of radiation with matter have a random nature, where the probability distribution governing the event is known. Because of this stochastic behavior of the radiation, the MC method represent an excellent tool not only to the modeling of these processes, but also to be used in practical applications in radiotherapy. In particular, the MC method has become now an accurate alternative to the analytical (conventional) algorithms which are extensively implemented in the majority of the TPSs for the dose calculation in arbitrary geometries, e.g. pencil beam and superposition/convolution algorithms.

Unlike of analytical methods which apply formulas for explicit calculation of the macroscopic energy deposition in material, the MC algorithm acts at a microscopic level and considers the trajectory of each individual particles composing the irradiation beam. Along their trajectories in matter, the particles loose energy or undergo interactions that give rise to secondary particles, which in turn

also deposit energy in material. The sum of the microscopic energy looses in a small volume unit gives the macroscopic dose.

Most of the conventional algorithms have been developed based on the assumption that the human body is made up of water-equivalent tissues. This assumption is roughly valid since 50 - 80 % of the human body is water. However, the body presents some heterogeneous regions containing air cavities, bones or lung tissues. As it has been widely investigated, the effect caused by these inhomogeneities can lead to significant changes on the dosimetric output of radiotherapy treatments [Leal03, Sec05, Yang05, Reyn07] and they need to be taken into account. Generally, it has been found that most of the conventional dose calculation algorithms are able to predict the dose with acceptable precision in homogeneous water phantoms, but they fail in the vicinity of tissue inhomogeneities. In order to account for the influence of inhomogeneities, conventional algorithms introduce some correction methods to account for density related fluence and particle range changes caused by inhomogeneities. Typically, the procedure to obtain the dose distribution within an inhomogeneous geometry is based on the modification of the dose calculated within an homogeneous water medium through the application of a factor, the so-called ”inhomogeneity correction factor”. Several methods to determine this factor have been developed, including the low tissue-air ratio (Batho) law, Modified Batho Power Law, equivalent tissue-air ratio (ETAR), among others [AAPM85]. Although all these methods are able to calculate the effect of inhomogeneities on photon fluence, they have still some limitations to calculate the perturbation of the electron fluence. In fact, most of these methods are not able to calculate dose with the required accuracy in all cases.

As stated in chapter 1, the degree of accuracy for the delivery of dose in radiotherapy treatments is recommended to be less than 5 % [ICRU24]. To satisfy this requirement, higher accuracy (2 - 3 %) and quality is required for the calculation of dose distributions in order to increase the success probability of the treatment and to avoid clinical effects. The above-mentioned limitations of the conventional algorithms in the presence of inhomogeneous regions may result in an increase of uncertainty in the dose calculation and thus affect the accuracy of the treatment. Only Monte Carlo algorithms that use the photon interaction probabilities and have the potential to model the electron transport can account explicitly for density inhomogeneities. This method has shown a high potential in these situations, allowing to meet the 3 % requirement for accurate radiotherapy [AAPM85, ICRU24].

There is also an additional aspect in which the application of Monte Carlo method to the radio-

therapy have shown more advantages over, not only the analytical algorithms, but also measurements. Recently, more sophisticated radiotherapy techniques such 3D-conformal or IMRT are being implemented at more radiotherapy centers. As previously mentioned, these techniques consist in the dose escalation delivery to tumor cells by conforming the dose distributions to the three-dimensional shape of the tumor volume. In order to achieve the desirable conformity and modulation of the beam, the use of more complex plans using, for example, non-coplanar beams or including auxiliary conformation devices such as a multileaf collimator may be involved. Given the complexity of the plans, the potential for local control is increased and thereby it raises the need of increasing the accuracy of dose calculation algorithms. In general, an essential prerequisite for the high dose accuracy is the precise knowledge of the characteristics of the radiation field. The introduction of multileaf collimators in these techniques results also in major challenges for dose measurements in photon beams. Again, the MC method appears as the most accurate method to deal with these situations, since it allows a precise modeling of the geometry of individual linacs and beam shaping devices.

At present, several general-purpose Monte Carlo codes exits in widespread use for radiation transport simulation, as the MCNP (Monte Carlo N-particle) system (Los Alamos National Laboratory) [Brie00], GEANT4 (Cern, Switzerland / France) [Ago03], Penelope (Barcelona, Spain) [Fern95] and EGSnrc (National Research Council of Canada) [Sieb02]. From all of them, it is well known that the EGSnrc code system is a very well documented code and addressed to radiotherapy applications. This code has been well benchmarked in the energy region of dosimetric interest [Rog95, She00, She00, Mor99] and it is the underlying code used for the present work.

4.3 Simulation of Photon and Electron Transport

The physical processes of electron and photon interactions with matter are well established as described in previous section 2.1. Although this process can be described mathematically by a coupled set of integro-differential transport equations, the equations are so complicated that it is very difficult to develop analytical expressions except under severe approximations. This difficulty is mainly due to the complex modeling of the interaction process which involves the generation of secondary particles, such as δ-ray and bremsstrahlung photons, and the scattering process.

As previously mentioned, for the MC modeling of radiation transport, *random numbers* and *probability distributions* are two essential elements used to simulate each step of the particle trajectory.

Basically, the choice of the interaction type at each transport step and the determination of the particle state (energy and direction) is performed using both elements.

In a general way, the MC simulation of the radiation transport can be summarized as a process consisting of four main steps:

1. selection of distance to next interaction,
2. transport to interaction point taking geometry into account,
3. selection of interaction type and,
4. simulation of selected interaction.

These steps are repeated until particles have left the defined simulation geometry or if their energy falls below a specified energy which is the energy where particles are assumed to be stopped and locally absorbed in the medium.

As photons and electrons interact differently with matter, the MC modeling is done differently. A separated description of the transport of both particles is given next.

Transport of photons

Due to its neutral characteristic, photons undergo, on average, a low number of interactions as they travel in a medium. It is adequate that the Monte Carlo simulation of photon transport includes all the interactions with surrounding matter. This simulation methodology is often referred to as *analog* Monte Carlo or ”event-by-event” technique and it is characterized by the explicit simulation of all particle interactions with surrounding material, including those secondary particles created in the collisions. Analog simulations are suitable for the transport of neutral particles (photons or neutrons) and other particles with low cross section and a high mean free path length.

The first step of the photon transport process is based on the knowledge of the *mean free path length*, λ, which characterizes the probability density distribution of the distance *t* traveled by the particle between two consecutive interactions and it is given by:

$$Prob \approx exp\left(\frac{-t}{\lambda}\right) \tag{4.1}$$

with

$$\lambda = \frac{A}{N_a \rho \sigma_{total}} \tag{4.2}$$

where A, N_a and ρ are the atomic mass number, the Avogadro's number and the material density, respectively, and σ_{total} is the total cross section which is proportional to the interaction probability.

Based on the probability distribution of equation 4.1, the distance t can be determined by $t = -\lambda ln(\xi)$, with ξ being a pseudorandom number sampled in the interval]0, 1].

Afterwards, the simulation follows with the transport of the photon to the next interaction point, taking into account the different materials found. Once the photon reaches this point, the interaction type is sampled using a second randomly generated number ξ_2. In particular, the choice of the interaction type is selected through the sampling of the relative probabilities of each interaction mechanism, i, in relation to the total cross section ($\sigma_{total} = \sum \sigma_i$) as follows:

$$\frac{\sigma_i}{\sigma_{total}} \tag{4.3}$$

In the range of interest of external beam radiotherapy, photons interact with matter via four main process: photoelectric effect, incoherent (Compton) scattering, pair production and coherent (Rayleigh) scattering (section). The total cross section takes thus into account all of these processes.

If a secondary particle is generated by inelastic scattering, the kinematic characteristics of the new particle are obtained in the vertex by sampling the respective differential cross section in energy and angle. Then, the transport of the secondary particle is effectuated independent from the primary particle, whose energy and angle is subsequently readjusted.

The entire procedure is repeated until the photon reaches its final destiny, usually an energy limit (cutoff) or a discard boundary, being then absorbed in the medium.

Transport of electrons and positrons

The simulation of charged particles transport by analog Monte Carlo techniques is incompatible for most applications. Unlike photons, which deposit their energy at discrete points along their path, electrons and positrons loose their energy in a near continuous set of interactions. As known, they have a considerably smaller mean free path length and undergo an enormous number of interactions

with the electrons and atomic nuclei in the medium until they are locally absorbed. As example, a relativistic electron can typically undergo around 10^4 - 10^5 elastic interactions and 10^5 - 10^6 inelastic collisions. Therefore, an event-by-event simulation of electron transport is not a suitable technique, since it would lead to unacceptable long simulation times in order to reach an acceptable statistical uncertainty of the calculated quantities. To solve this difficulty, it was developed a more elaborated modeling technique of the transport of electrons (positrons).

In 1963, Berger established the known method of *condensed history*, which is now the fundamental element of the algorithms which simulate the transport of electrons by Monte Carlo methods [Ber63]. Motivated by the fact that most electron collisions are elastic or semi-elastic, in this method, the electron trajectory is broken into a series of steps, usually known as *condensed steps* or *multiple scattering steps*. In each step, electron interactions which lead to very small changes in the electron energy and/or direction are statistically grouped (figure 4.1).

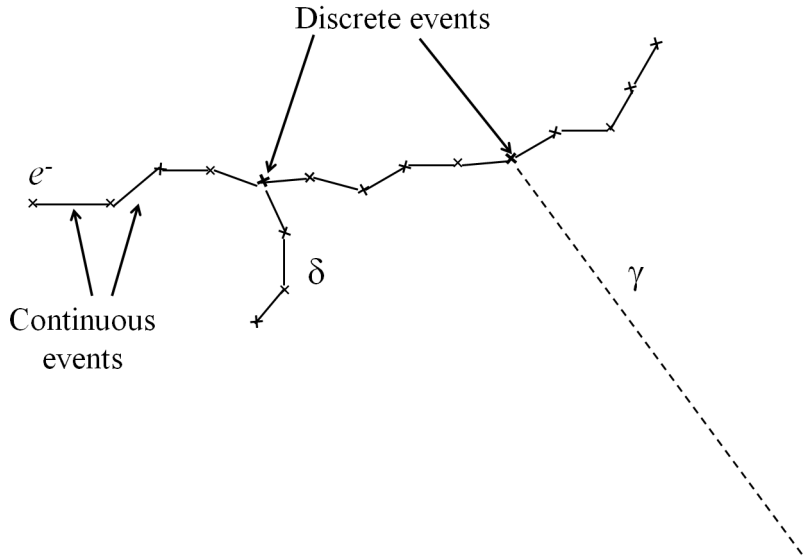

Figure 4.1: Schematic representation of the MC simulation of an electron by successive steps of *condensed history* between points of discrete events resulting in a δ-ray and a bremsstrahlung photon.

Each of this condensed step takes into account the combined effects of individual interactions occurring during the course of the step, including the angular scattering due to elastic interactions and energy loss associated to inelastic interactions. Specifically, these interactions, sometimes referred as *soft collisions*, include Coulomb elastic scattering, atomic excitation and, finally, the

production of δ - ray (Mϕller scattering) and bremsstrahlung photons with an energy below some defined threshold, Δ . The cumulative energy loss and angular deflection are sampled once per each condensed step from appropriate distributions. In particular, the losses are evaluated within the Continuous Slowing - Down Approximation (CSDA), using the restricted Δ stopping powers. On the other hand, the angular deflections caused by the elastic scattering are combined for each step using a multiple-scattering theory such as the Moliére or Goudsmit and Saunderson theories[Kaw00a, Kaw00b].

All the remaining interactions including the δ - ray and high-energy bremsstrahlung production, involving the production of secondary particles above some defined threshold energy Δ, are considered *catastrophic interactions*. These interactions are modeled in a discrete way and independent form the simulation of the primary particle.

This approach for the electron(positron) transport increases the simulation efficiency by a factor of three or four relative to the analog simulation.

According to the different methodologies which are adopted by the Monte Carlo algorithms for the simulation of catastrophic events, Berger defines two different implementations of the condensed history scheme (figure 4.2):

- **Class I** - The effects on the primary particle caused by *all* interactions (soft and catastrophic) are grouped together for each condensed-history step. When a secondary particle is generated, the primary particle step does not depend directly on the parameters of the secondary particle, although a relation through the cross sections is obviously present (conservation of energy and momentum on a macroscopic scale).

- **Class II** - The effects on the primary particle due to catastrophic events are counted in the interaction vertex by the generation of an explicit secondary particle. When a secondary particle is generated, a new energy and angle are selected for the primary particle in correlation with the parameters of the secondary particle (conservation of energy and momentum on a microscopic scale).

In class I models, the distribution for the sampling of energy loss of primary particles include energy loss caused by the production of secondary electrons, since the catastrophic events are grouped in the condensed-history step. The probability distributions are hence values of total collision energy loss incorporating statistical fluctuations (energy straggling) described by theories such

as Landau or gaussian distribution. At the end of each step, s, the energy of the primary particle is given by:

$$E_{final} = E_{inicial} - \Delta E(s) \tag{4.4}$$

with $\Delta E(s)$ being the energy loss along the step caused by continuous and catastrophic events. In this class, the simulation of a δ-ray does not imply the energy change of the primary particle and the final state of this particle is not directly related with the generated particle, which can be emitted at any point along the step.

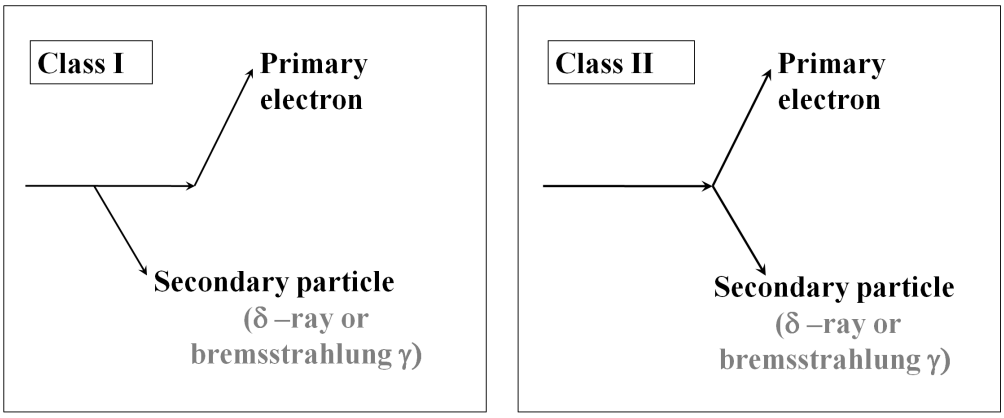

Figure 4.2: Different ways to perform a sampling of electron energy loss, Class I (left) and Class II (right) algorithms.

In MC algorithms of class II, the production of secondary electrons and photons above a defined threshold energy Δ are simulated explicitly. The final state of the primary particle is now well defined and it is related with the kinematic quantities of the created secondary particle. Below the production energy threshold, the inelastic and elastic collisions are grouped statistically in each condensed step. Along the step, the energy loss of the δ-rays are obtained from the distributions of the restricted collision stopping power, being therefore the final energy of the primary particle the following:

$$E_{final} = E_{inicial} - s\left(\frac{dE}{dx}\right)_{col,\Delta} - E_{\delta} \tag{4.5}$$

with $\left(\frac{dE}{dx}\right)_{col,\Delta}$ the restricted stopping power which corresponds to the value of energy loss by length

unit for secondary particles with energies below the production energy threshold, Δ. The value E_δ is the energy of the created δ -ray.

A similar expression may be written for bremsstrahlung production with $\left(\frac{dE}{dx}\right)_{rad,\Delta}$ replacing $\left(\frac{dE}{dx}\right)_{col,\Delta}$ and E_γ replacing E_δ.

In spite of the fact that the MC simulation of electron transport includes the condensed history technique, it is possible to state that, in a general way, the transport of electrons follows a methodology similar to that described for photon transport. In a first step, the distance between two catastrophic events is sampled based on the total cross section of inelastic and radiative processes. The electron is then transported in condensed steps until it reaches this point. In each condensed step, the particle position, direction and energy is modified. Once at the next discrete interaction site, the interaction type (δ-ray or bremsstrahlung above defined energy threshold Δ) is selected and the energy and angular changes are sampled from the appropriated differential cross sections. This procedure is repeated until the electron comes to rest or it leaves the simulated geometry.

At the end of each condensed step, the angular deviation of the particle due to multiple scattering is selected based on theories of multiple scattering, such as Molière, Fermi-Eyges or Goudsmit-Saunderson [Kaw00a, Kaw00b]. The angular distribution after the step characterizes the direction of the electron, but it does not give information about the spatial distribution of the electron.

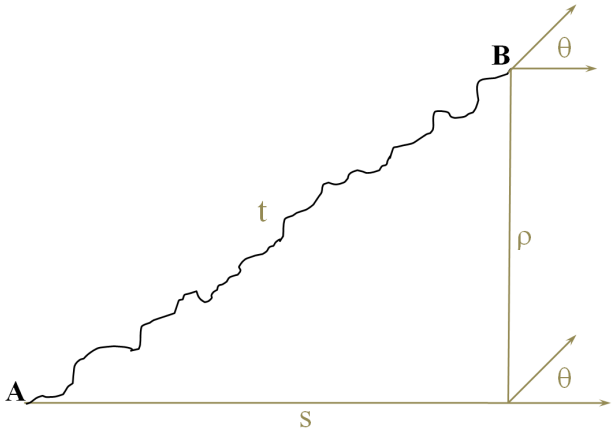

Figure 4.3: Schematic representation of the electron pathlength correction in a MC simulation: *t*, total (curved) path length of the step; *s*, the component of transport distance along the initial direction; ρ, the lateral displacement; θ, the multiple-scattering angle.

The condensed history technique uses straight steps for the electron transport, since as previously mentioned, this steps are based on the CSDA theory. This approximation is however in contradiction to nature, where electrons follow curved paths (figure 4.3). Thus, some corrections of the condensed step, s, are therefore required for the calculation of the true and real curved trajectory of the electron. Additionally to the correction of the *path length curvature*, the *lateral displacement* ρ of the electron due to multiple scattering must be taken into account.

One important question is the selection of the size of each electron step for a particular MC simulation. The size of the step can affect dramatically both the accuracy and the computation time. A reduction in the electron step size can result in accurate results, since in this case all the corrections required for the calculation of the true curved trajectory of the electron would be avoided. However, the calculation time would increase dramatically. On the other hand, reducing the step size can also lead to the violation of fundamental constraints of the multiple-scattering theories.

Anther special aspect is the presence of interfaces between different materials and/or scoring regions. In this situation a boundary crossing algorithm must be used. As the condensed history technique relies on the multiple scattering theory of Molière, Fermi-Eyges or Goudsmit-Saunderson, it is limited by the fundamental constraints of these theories, namely their strict application in infinite or semi-infinite geometries. The presence of a boundary, dividing two different regions, two regions composed of different materials, can result in incorrect energy deposition calculation. This situation is illustrated in figure 4.4. The straight line AB represents a simulated condensed history electron step, whereas ACB and ADB are electron paths that could be observed in reality.

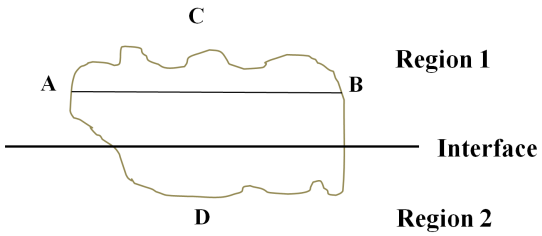

Figure 4.4: Schematic drawing of the boundary problem in the condensed-history method for the simulation of the electron transport.

An electron starting at point A could pass through region 2 before ending at point B. If the medium in region 1 differs from the medium in region 2, this would affect the whole particle history.

More details about all these simulation aspects have been described in detail by A. Bielajew in [Biel01]. Additionally, the manual of the Monte Carlo codes includes further information about each specific algorithm and approximation which are used.

4.4 The EGSnrc Code System

4.4.1 General Description

The EGSnrc, an acronym of Electron-Gamma Shower, is a general-purpose package of Monte Carlo codes used for the simulation of the coupled transport of electrons and photons through an arbitrary geometry and for particle energies ranging from a few tens of keV up to a few hundred GeV [Kaw03]. This code is the most recent in the family of the EGS Monte Carlo codes and it is substantially improved from its predecessor, the EGS4 version originally developed at Stanford Linear Accelerator Center (SLAC) [Nel85]. The first code (EGS3) was developed in 1978 for the simulation of electromagnetic cascades for high energy physics. Later, the algorithms of transport were extended to lower energies to answer the increasing demand of the medical physics area.

Basic EGSnrc simulation parameters and features

The EGSnrc code is written in the MORTRAN programming language, which is a string preprocessor for the FORTRAN language. In this code, the transport of photons is performed in a analog manner. Regarding to the electron and positron transport, the EGSnrc code uses a class-II scheme based on the condensed history model. The mechanisms considered by EGSnrc for the simulation of *catastrophic* interactions generating secondary particles above a defined threshold Δ are: bremsstrahlung production, Mϕller scattering for electrons and Bhabha scattering for positrons.

In EGSnrc, the energy thresholds for the production of secondary electrons and photons are referred as *AE* and *AP*, respectively. These values are selected by the user. Their choice depends on the problem and it has a high influence on the speed of the EGSnrc calculation. Typically, the recommended value for AP is 0.01 MeV [Wal05], which means that all bremsstrahlung events are practically simulated as discrete events. The selection of the best value for AE is more complex because its choice can affect significantly the computing time due to the high probability of interaction of electrons and positrons. In addition, the choice of AE can also have influence on the statistical fluctuations of the energy loss (energy straggling). A reduction of AE results in a more realistic

energy straggling modeling [Wal05]. The two recommended values for AE are 0.521 MeV and 0.700 MeV (including rest mass energy of electron/positrion).

Additionally to the threshold of discrete events, the code have others energy threshold which can affect the speed and accuracy of the simulations. These parameters are ”the cutoff energies” *ECUT* and *PCUT* for electrons/positrons and photons, respectively. This cutoff energies represent the energy below which the transport of the particle is terminated and the energy is locally deposited. Similarly to AE and AP values, ECUT and PCUT also have influence on the accuracy and time consuming of a simulation. In general, the value of ECUT equal to 0.700 MeV and PCUT of 0.01 MeV are appropriate for most situations. A exceptional situation occurs for example for dose calculation is focused on surface regions, where the ECUT value should be decreased.

Prior to all simulations the cross section databases for photon and electron interactions are initialized. The data sets are provided in look-up tables for the materials found in the simulation geometries. These tables can be generated with the **PEGS4** program, the cross section data preprocessor for EGSnrc. Specifically, PEGS4 generates energy dependent photon attenuation coefficients and electron stopping powers based on experimental data and theoretical cross section calculations. By specifying elemental composition, density and energy range, data tables are generated for use in the EGS simulation.

The EGSnrc code includes a specific electron-transport algorithm which selects automatically the optimum step-size, saving time to the user. This algorithm is called PRESTA, an acronym that stands for Parameter Reduced Electron-Step Transport Algorithm [Biel87]. Such algorithm may allow the use of fewer, larger electron steps, increasing the speed of the simulation without compromising the accuracy of a simulation. It has been shown that the original PRESTA underestimates lateral deflections and longitudinal straggling and produces a singularity in the distribution describing the lateral spread of electrons in a single condensed history. Even though the original PRESTA may be accurate enough for high energies (where elastic scattering is weak), it is not recommended for low energy applications. The code includes now a new version of this algorithm, the PRESTA-II, to overcome this limitations.

The size of the condensed step is controlled by the parameter ESTEPE which limits the fractional loss of energy for the continuous process. In order to ensure the convergence for the correct spacial distribution, the condensed steps may be of small sizes, corresponding to values of ESTEPE within 1 and 4 % using the original PRESTA algorithm and 25 % for the PRESTA-II algorithm.

To address the problem of interface artefact, EGSnrc uses two boundary crossing algorithms, PRESTA and EXACT [Sieb02]. It has been shown, however, that PRESTA is not adequate for simulating the dose deposited in a small air cavity or in the neighborhood of high-Z interfaces. This led to the introduction of a new algorithm, EXACT, which allows the user to revert to a single scattering model in the close neighborhood of boundaries, thereby reducing the minimum path length to very small values. This appears to resolve the problems observed in the above-described circumstances.

In EGSnrc, statistics are handled by grouping scored quantities on a history by-history basis [Wal02]. Uncertainties ($s_{\overline{X}}$) at the 1σ level are determined for each scored quantity X_i (energy fluence or dose to a voxel) as statistically independent events, such that

$$s_{\overline{X}} = \sqrt{\frac{1}{N-1}\left(\frac{\sum_{i=1}^{N} X_i^2}{N} - \left(\frac{\sum_{i=1}^{N} X}{N}\right)^2\right)} \tag{4.6}$$

where N is the total number of independent events and is always equal to the total number of primary histories. Using this method, a statistical dose uncertainty for each voxel can be calculated as a function of initial history number. For phase space sources generated using BEAMnrc, there is potentially more than one particle in the file that may be traced back to the same initial primary history. Therefore, to account for a common initial history, the history-by-history technique groups all particles according to the primary history that generated each and calculates the uncertainty accordingly.

A set of readily implemented user codes is available [Rog11], which allows the definition of a geometry, set-up of various particle sources (e.g. parallel beam of photons with certain spectral distribution), and the scoring of quantities sufficient for most problems. For example, the SPRRZnrc code allows the calculation of stopping power ratios, the FLURZnrc calculates fluences and particle spectra and the DOSRZnrc code scores dose in an arbitrary geometry composed of cylinders (RZ-geometry). On the other hand, the BEAMnrc code [Rog05] can be employed to calculate the passage of particles through the head of a linear accelerator (see below). It incorporates its own geometry functions, organized in a set of modules as jaws or a flattening filter. Finally, the DOSXYZnrc code [Wal02] calculates dose to rectilinear voxels of a homogeneous or heterogeneous geometries.

General description of EGSnrc implementation

The EGSnrc code consists basically of a set of two distinct components: the *USER* code where

user specific parameters (geometry, output variables) are set and the *EGS* code which handles the simulation of the physical processes that are independent of the user setup. The general structure of the code is illustrated in figure 4.5.

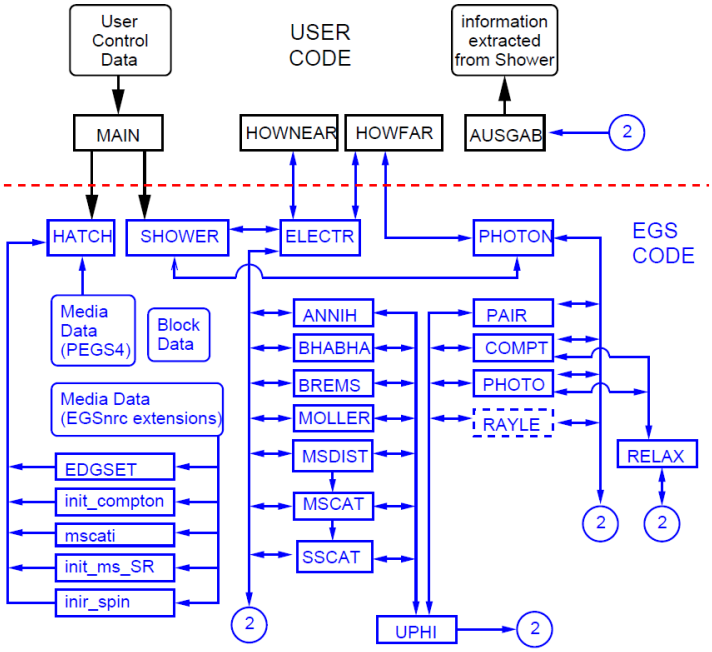

Figure 4.5: The structure of the EGSnrc code system (figure by [Kaw03]).

The USER code is responsible for writing four routines: MAIN, HOWFAR, HOWNEAR and AUSGAB. The MAIN subroutine performs any initialization necessary for the simulation, including the media to be used, particle parameters and cut-off energies. This subroutine also interfaces with the EGS code through the HATCH and SHOWER subroutines.

The necessary material data (cross section and loss energy distributions data) is set up for the HATCH subroutine, which relies on pre-generated data from the separate pre-processor program PEGS4.

Having called HATCH, MAIN then repeatedly calls SHOWER once for each incident particle. The SHOWER subroutine simulates the particle and its progenitor until they leave the region of interest, reach the end of their track or are locally absorbed. The subroutines HATCH and SHOWER call the other subroutines in the EGS code. If the transported particle is an electron or a positron, the sub-

routine ELECTR is called for the selection of the physical process at the end of each step: multiple scattering (MSCAT), bremsstrahlung (BREMS), electron-electron scattering (MOLLER), positron-electron scattering (BHABHA) and anniquilation (ANNH). In contrast, the photon transport is performed by the PHOTON subroutine, which calls the subroutines for simulation of Compton scattering (COMPT), photoelectric effect (PHOTO) and pair production (PAIR). The process of elastic (Rayleigh) scattering is optional and it is controlled by the subroutine RAYLE.

The radiation transport through geometries consisting of different volumes and materials need the knowledge of, on one side, the electron and photon position at the end of each step and, on the other hand, the distance until the boundary. Based on the material which is traversed during the transport, it is possible to modify the cross section and the probability of occurrence of the different mechanism of interaction. The tracking and geometrical transport of the particle is made by the subroutine HOWFAR, where the geometry of the simulation is defined. Moreover, HOWFAR calculates the distance-to-intercept (DTI) of a particle to a geometric surface along a given trajectory.

The EGSnrc code also includes the subroutine HOWNEAR which aids in electron transport and boundary crossing; specifically, this routine calculates a particle's distance to the nearest boundary.

The kinematic characteristics of each simulated history is stored by the subroutine AUSGAB, where the user can also define quantities of interest for the subsequent analysis.

4.4.2 BEAMnrc: A linac modeling tool

The BEAMnrc code [Rog05] is a Monte Carlo simulation tool for the modeling of radiation beams from any radiotherapy units, including orthovoltage units, ^{60}Co units and linear accelerators. The first version of this user interface, BEAM/EGS4, was released as part of the OMEGA project in 1995; now it has been upgraded to BEAMnrc/EGSnrc.

One important feature of BEAMnrc is that each part of a linear accelerator is considered to be a single component module (CM). Each component modules are re-usable and operate completely independent of each other. This feature is very useful to model different accelerators. In fact, due to the modular design of a linear accelerator, the whole treatment unit can be thereby composed of many such component modules according to the technical drawing of the treatment unit. Furthermore, the independence's feature of each component of the geometry package allows each CM to be tested and debugged separately.

Typical component modules used in medical accelerator modeling are: SLABS for X-ray target,

CONESTAK for primary collimator, FLATFILT for flattening filters, CHAMBER for ionization chambers, JAWS for photon jaws, etc.

The primary output of a BEAMnrc simulation is the so-called **phase-space file** (PSF). This file contains information on all particles crossing the xy-plane located at a fixed point along the z-axis. The xy-plane is referred to as a scoring plane and an arbitrary number of scoring planes can be defined and located at the back of each component module. In particular, a phase-space file contains the following information of each crossing particle: energy, xy-position, direction cosines with respect to the x- and y-axis, the direction cosine of the angle with respect to the z-axis, the particle weight, the charge, the number of times the particle has crossed the scoring plane and other particle history information (LATCH). All these informations are scored in an arbitrary number of circular rings or concentric square rings of arbitrary width and may be then used subsequently as input for further linac head simulations or to calculate the dose distribution in a phantom with the DOSXYZnrc code [Wal02].

Additionally, the ability to score particle characteristics in a phase space file (PSF) allows also the stopping/restarting of simulations, analysis of particle characteristics, modification of particle characteristics, etc.

One of the major advantages of the MC technique is that it allows to know detailed information about each particle's history. For this purpose, BEAMnrc includes a general technique built upon the LATCH feature of EGS4. LATCH is a variable which indicates the positions where the particles have interacted or have been created. With LATCH it is possible to keep track of each particle history and it is used in the analysis of the relative dose distributions from various accelerator components.

Full phase-space files can be analyzed using beam data processing software BEAMDP (BEAM Data Processor) [Ma09]. This is an interactive program, developed for the OMEGA (Ottawa Madison Electron Gamma Algorithm) project, which allows to derive the beam characteristics obtained by the Monte Carlo simulation of the coupled transport of photons and electrons in a clinical accelerator. This program can be also used to derive the data required by the simplified sub-source models of these electron beams for use in Monte Carlo radiotherapy treatment planning.

4.4.3 DOSXYZnrc: Phantom dose calculation tool

The DOSXYZnrc [Wal02] is an EGSnrc-based code dedicated to the calculation of dose distributions within phantoms consisting of rectilinear volume elements (voxels) which contain a specific physical

density and material. Voxel dimensions are independently variable in all 3 directions (X, Y and Z).

The code allows to select between different source types, including monoenergetic diverging or parallel beams, phase-space data generated by BEAMnrc simulations, or a model-based beam reconstruction produced by the BEAMDP software.

One important feature of the DOSXYZnrc is the calculation of dose distributions within phantoms derived from a CT dataset. The available information contained in a pixel of a CT-image is called CT-number. This number is expressed in Hounsfield units (HU) in honor of Godfrey Hounsfield and is formally given by:

$$CT = \left(\frac{\mu}{\mu_{water}} - 1\right) \times 1000 \tag{4.7}$$

where μ is the linear attenuation coefficient at the pixel position, which are dependent on the x-rays spectra of the CT-machine. In general, the CT numbers range between +1000 HU and -1000 HU for bone to air, respectively, while, by definition, the water has a CT number of 0 HU.

The CT numbers are not suitable yet for use in Monte Carlo dose calculations code. In these codes, the dose deposition in the simulated geometry is calculated as a final stage of the particle transport. The geometry may include different media, which are specified with a density and a composition.

In order to calculate dose in real conditions, it is thus necessary to transform the CT number to density and chemical composition. For this purpose, the stand-alone program, CTCREATE, was developed and included in the DOSXYZnrc code.

Using this program, a CT data set can be converted into the appropriate voxel geometry for DOSXYZnrc calculations. The material type (composition) and mass density data within each voxel are derived from the Hounsfield number exported from the patient CT using a CT conversion ramp. The default ramp for converting CT to material and density in CTCREATE is shown in figure 4.6. The ICRU standardized materials used to characterize this ramp are ”Air”, ”Lung”, ”Tissue” and ”Bone” where material densities between the fixed points are linearly interpolated. The corresponding range values of CT number and density are summarized in the table 4.1. Note that the CT numbers presents a shift of 1000 with respect to the standard definition of the Hounsfield number.

Table 4.1: CT numbers and density range for the four materials used in the ramp for converting CT numbers to material parameters (composition and density).

	Air	Lung	Tissue	Bone
CT number range	0 - 50	50 - 300	300 - 1125	1125 - 3000
Density range	0.001 - 0.044	0.044 - 0.302	0.302 - 1.101	1.101 - 2.088

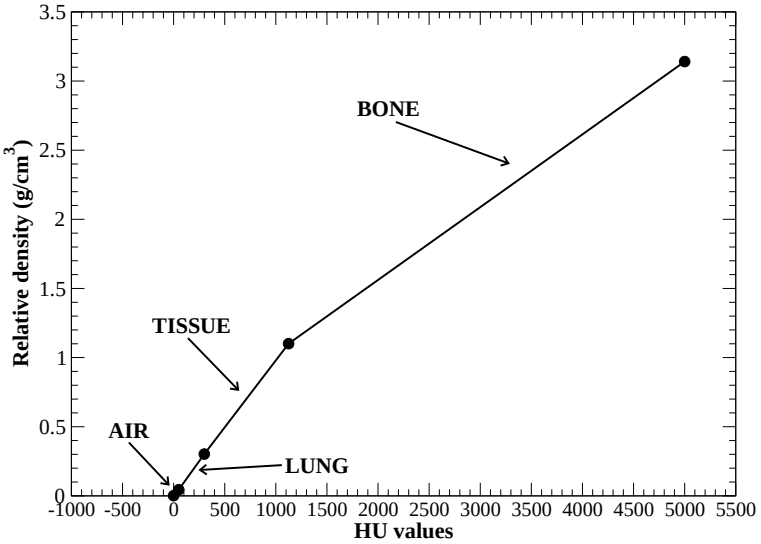

Figure 4.6: The DOSXYZnrc default ramp for converting CT-number to material density [Wal02]. Indicated in the figure are the ICRU standardized points for ”Air”, ”Lung”, ”Tissue” and ”Bone”. Note that the CT numbers considered for the DOSXYZnrc presents an offset of 1000 with respect to the standard definition of Hounsfield number ([-1000, 1000]).

When phase-space files are used as input of the DOSXYZnrc, the phase-space file may be re-sampled in order to increase the number of particles simulated in a run. NRCYCL is an input parameter used to define the number of times each particle in a phase-space file will be re-used or recycled. Recycling incident particles NRCYCL times is equivalent to use a total of NRCYCL+1 times the particles. Along with particle recycling, ISMOOTH is used to redistribute the recycled particles about the central axis of the accelerator beam. As long as the simulated linear accelerator geometry and field size are symmetric, and centered on the central beam axis, the ability to redistribute the phase-space file allows for a reduction of systematic uncertainties in small data sets (particularly important for small field sizes). The ability to recycle phase space-data is important as calculation time is clinically relevant. However, it is important to point out that the recycling of particles can have significant effect on the final statistical uncertainty of the dose [Wal02]. Recycling incident particles may introduces correlations between particles in the phase-space file. The failure in considering

these correlations can lead to a significant underestimate of the uncertainty, basically because the statistical fluctuations inherent in the phase-space file are ignored. Sempau *et al* [Sem01] introduced the term ”latent variance of a phase-space file” to distinguish between the uncertainty in a dose calculation due to the random number of the transport in the phantom from that uncertainty due to the statistical fluctuations in the phase-space file. According to this work, even if particles are recycled many times, the uncertainty will always reflect the uncertainty in the phase-space file itself.

Whereas, for photon beams, the use of a high number of recycling times (27 times) has little effect on the uncertainty, for electron beams, the recycling of 3 times may introduce an increase of a factor of 5 in the uncertainty [Wal02]. In the present thesis, a maximum recycling of 3 and 20 times for electron beams and photon beams, respectively, has been used in the dose calculations.

4.4.4 Variance Reduction Techniques and Efficiency Improvements

The efficiency of a Monte Carlo code is a very important factor, as it takes into account both the simulation time T and the statistical uncertainty s. The efficiency is defined as

$$\epsilon = \frac{1}{\sigma^2 T} \tag{4.8}$$

where σ^2 is the variance of the simulated result and T the CPU simulation time needed to reach this variance. The time T is directly proportional to the number of simulated histories N, while the variance is inversely proportional to N. Thus, the efficiency is independent of the number of histories N.

There are two different ways to improve the efficiency of a given calculation: either decreasing σ^2 for a given T or decreasing T for a given N without changing the variance. Several techniques, often referred to as **variance reduction techniques**, has been developed to increase the efficiency, not necessarily reducing only the variance, but also decreasing the time to achieve it. One first example of this technique can be considered the mentioned condensed history technique for the transport of electrons and positrons.

Additionally, two general classes of variance reduction techniques can be defined that increase the efficiency. The first class increases the efficiency by making approximations to the transport simulation. Certain energy thresholds can be defined, so that a particle is discarded and its energy is deposited locally, whenever it falls below the threshold. It is clear that increasing the threshold

reduces the simulation time, but introduces a bias. Changes on the values of ECUT and PCUT for electron (positron) and photon transport are an example of this first class.

Another example is the so called **Range rejection**. This technique implemented in the BEAMnrc code allows the user to terminate the history of an electron when its residual CSDA range is such that it cannot possibly reach some region of interest and deposit its energy there. However, by terminating an electron's history preliminary, the possibility of a bremsstrahlung photon being created and escaping from the region is eliminated. This may lead to underestimation of the dose for high Z materials and high energies. Thus, an energy threshold is defined, ESAVE, above which no range rejection is done. An intelligent choice of this energy must depend on Z and is essentially made based on the approximate fraction lost to bremsstrahlung in a specific medium. Furthermore, this value may vary from region to region depending on the type of range rejection used. This energy has to be chosen so that bremsstrahlung production at lower energies has a negligible effect. In the present work, all BEAMnrc simulations use range rejection with ESAVE of 1 MeV. As studied by [Rog95], this value has been shown to provide the best compromise between simulation speed and accuracy.

The variance reduction techniques of second class are considered real variance reduction techniques because they do not introduce any bias. Two commonly techniques usually used in conjunction in the BEAMnrc are **photon splitting** and **charged particle Russian Roulette**. Generally, splitting leads to N particles with a statistical weight reduced to 1/N. Thus, a splitted particle contributes to only 1/N to a scored quantity such as dose, but the probability for the dose deposition is increased due to the larger number of splitted particles. The splitting can be applied in three different ways: uniform bremsstrahlung splitting (UBS), selective bremsstrahlung splitting (SBS) and directional bremsstrahlung splitting (DBS). The USB technique is based on the original concept of the photon splitting technique where the photon are splitted uniformly along the initial photons path with a value NBRSPL. Selective bremsstrahlung splitting (SBS) is more efficient than UBS. This technique uses a variable splitting number, NBR, which reflects the probability that a bremsstrahlung photon will enter the field defined by a given and specific field size (FS) and distance from the bremsstrahlung target at which the above FS is defined (SSD). This last technique is however nowadays superseded by the recently-implemented directional bremsstrahlung splitting. DBS technique is a refinement of this technique which only splits those photons if they are aimed into a field of interest, saving further calculation time by ignoring those that are unlikely to reach the scoring region.

Further details about both techniques are found in [Rog05].

The game of Russian Roulette (RR) can reversely reduce the number of particles simulated and thus the time needed to simulate their transport. Following the whole track of the secondary charged particles created by the split photons may increase significatively the CPU time required for simulations. If the primary interest is in secondary electrons or their effects, the extra computing time is obviously acceptable. When the main interest is in the bremsstrahlung photons themselves, one can reduce the CPU time while still preserving the variance reduction advantages of Bremsstrahlung splitting applying the Russian Roulette technique to any charged particle generated by the split photons. If a particle survives the game, it carries a statistical weight, increased by the inverse probability to survive the game. The surviving particle, often referred as fat particle, contribute to scored quantities with their increased weight.

In the context of present work, all BEAMnrc simulations use an uniform bremsstrahlung splitting with a splitting factor of 20 along with the Russian Roulette option. The choice of these options is based on the previous experience of several authors, which performed calculations with realistic photon beams [Rog95, Deng99, Mor01].

Comparable to the splitting technique, BEAMnrc also offers an option which allows the user to force photons to interact with specified component modules within a simulation and at the same time to reduce the weight of secondaries accordingly without introduction of a bias. This option is useful for improving the statistics of scattered photons when photon interactions are very sparse as in thin slabs of material or in materials with low density. This technique has not been used in the present work.

Part III

ELECTRON BEAM RADIOTHERAPY APPLICATION

Chapter 5

Dosimetric effect of shallow air cavities in high energy electron beams

5.1 Motivation

The presence of air cavities in regions irradiated with radiotherapy beams is very common in clinical applications, especially in the head and neck. Over the last years, the evaluation of the impact of air inhomogeneities on the absorbed dose has been a subject of many investigations either by experimental measurements or by using Monte Carlo simulations [Klein93, Nir94, Beh06, Li00, Kan98, Pael03, Nuss75, Shor86, Zar07, Chow10]. All previous works reported that the perturbation caused by the air inhomogeneity near the tissue-air interfaces can be responsible for significant overdosing and underdosing, whose magnitude can be of clinical interest in some cases. Accurate knowledge of this effect becomes critical for treatment planning dose calculations in order to reduce the dose to healthy tissue and to avoid posterior complications in the radiotherapy treatment.

In the early 70s, a systematic study was performed to assess the air effect with the variation in cavity dimension and energy beam by using experimental measurements [Nuss75]. This was performed for electron beams produced by a Siemens Betatron with energies of 10 and 42 MeV and it reported a significant effect (up to 60 %) caused by the presence of the air (1 cm radius and 2 cm height at 1 cm depth from the surface).

Experimentally the evaluation of the dose perturbation in the presence of air is however a com-

plex task due to the difficulty of measuring accurately the air-tissue interface effect. In contrast, Monte Carlo simulations are ideally suited for these cases as they provide a better assessment of interface doses.

With the recent implementation into the clinical practices of Monte Carlo treatment planning systems (MCTP) for electron beams and for combined electron-photon beams, it becomes thus important to assess precisely the perturbation caused by the presence of air inhomogeneities. To date, a large number of works has been published about the influence of air cavities as function of beam energy or cavity configuration for radiotherapy photon beam [Klein93, Nir94, Beh06, Li00, Kan98, Pael03]. However, there is a lack of studies accounting for the dependence of the air cavity effect on its geometry, position and energy for electron beams [Zar07, Chow10]. Most of the published studies for electron beams [Cyg04, Ding06] were focused on benchmarking the accuracy of a commercial treatment planning system incorporating Monte Carlo dose calculation. Although the results of these previous works indicated a dosimetric effect, both experimentally and with Monte Carlo simulations, in air cavity phantoms for different energy of electron beams, the magnitude of the dose perturbation depending on the geometry and location of the cavity was not reported.

Recently, Chow *et al* (2010) [Chow10] published an extensive investigation of the impact of an air cavity on the dose distribution for electron beams by using Monte Carlo calculations. They also included an experimental validation of the Monte Carlo calculations, but it was restricted to one specified inhomogeneous phantom. This work evaluated the variation of the dosimetric effect versus beam energy as well as size and position of the cavity, considering always the cavities located at depths deeper than 5 mm. Shallower air inhomogeneity was not considered although they can affect the clinical result in several radiotherapy treatments [Cyg04, Ding06, Salg09].

In the present work, a systematic study assessing the air cavity perturbation on electron dose distributions has been carried out by using both Monte Carlo simulations (EGSnrc code) and experimental measurements (Gafchromic EBT films) for beams of 10 x 10 cm^2. For this field, the dependence of the effect on cavity size (area and thickness) and beam energy is evaluated for air cavities located at shallow depths (2 mm depth). The impact caused by the presence of the air is also analyzed through the electron energy and angular spectra calculated below the cavity.

The air cavity effect has been also investigated for real treatment fields defined using cerrobend cutouts for the collimation. For this case, Monte Carlo dose calculations in homogeneous and het-

erogeneous phantoms containing an air cavity of different dimensions were compared for a 12 MeV electron beam. The influence of the cavity on these dose distributions was assessed using depth-dose and lateral dose profiles. The use of the cerrobend cutouts is still a frequent practice in electron radiotherapy. Hence, the present study could provide useful guidelines in the context of this treatment modality.

5.2 Material and Methods

After describing the geometry of the heterogeneous phantoms used for the present work (Sec. 5.2.1), details about the Monte Carlo phantom calculations as well as a characterization of the electron beams are discussed in the section 5.2.2. The procedure for experimental measurements, including a short description of the phantom built specifically for the measurements, is described in section 5.2.3. Finally, the results and a brief discussion are presented.

5.2.1 Air cavity phantom

Heterogeneous phantoms containing a three-dimensional inhomogeneity of air were used for this investigation. Specifically, the phantoms consisted of tissue-like medium (water or PMMA) with an rectangular air cavity of area S and thickness L in the center (Table 5.1). The total dimensions of the phantoms were 15 x 15 x 12 cm^3 for the study using the 10 x 10 cm^2 field and 25 x 25 x 12 cm^3 for the cerrobend field application. The axis of the cavity was parallel to the beam axis and the top of the cavity was located 2 mm deep from the surface phantom.

Square area S (cm^2)	Thickness L (cm)
3.8 x 3.8	1.8
1.8 x 1.8	1.8
1 x 1	1.8
1 x 1	2.8
1 x 1	0.8

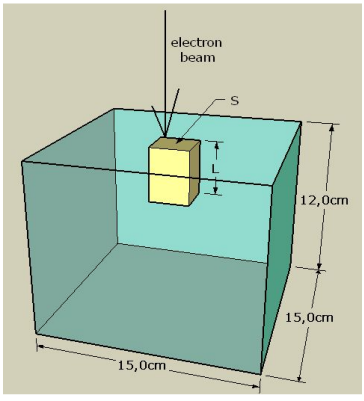

Table 5.1: Variations of the thickness L and square area S of the air cavities considered in the study (left side). The figure shows a schematic diagram of the heterogeneous phantoms (right side).

The dimensions of the cavities were chosen as representative geometries of cavities presented in the head and neck region, in particular in the nasopharynx region where small and irregular cavities around 1 - 3 cm of diameter can be found [Kan98, Cyg04].

Table 5.1 summarize the variations in thickness and area of these cavities.

5.2.2 Monte Carlo simulations

In the present sections, details about the phantom calculations are presented. Subsequently, it is performed a characterization of the electron beams through the analysis of the energy spectra, angular distribution, fluence profiles and mean energy profiles of the incident particles at the phantom surface. Finally, the accuracy of the linear accelerator model is evaluated by comparing Monte Carlo simulations against experimental measurements in a homogeneous water phantom.

DOSXYZnrc phantom calculations

Monte Carlo dose calculations were performed in the above described heterogeneous geometries using the DOSXYZnrc/EGSnrc system code [Kaw03, Wal05]. For this purpose, previous BEAMnrc/EGSnrc simulated phase-space files [Salg09, Salg10] for the Siemens Primus linear accelerator installed at the *Virgen Macarena Hospital* in Seville (Spain) were used as input of the DOSXYZnrc phantom calculations.

These phase-space files correspond to the surface of the phantom (SSD of 100 cm) for a 10 x 10 cm^2 electron beam with nominal energies of 12 and 18 MeV. Approximately 11 and 7 million of particles were collected in these files for the 12 MeV and 18 MeV electron beam, respectively. The uncertainty in the calculated electron fluence on the central axis ($0 < r < 4$ cm) is about 0.35 % for the 12 MeV beam and 0.3 % for the 18 MeV beam.

Monte Carlo phantoms were built using the same dimensions as above described in section 5.2.1 including the cavities whose dimensions are summarized in table 5.1. Phantoms of PMMA were considered for the evaluation of the air cavity effect.

The relative numbers of elemental compositions of PMMA (H=8, C=5 and O=2) and density of 1.19 g/cm^3 were considered by the PEGS4 [Kaw03] data-preprocessing code to create the data files containing information of material cross section and branching ratios. The low energy thresholds for

the production of knock-on electrons was set to AE = 0.521 MeV (total energy) and the threshold for bremsstrhalung events was set to AP = 0.010 MeV.

In all DOSXYZnrc calculations, the global electron energy cut-off (ECUT) and the global photon energy cut-off (PCUT) were set to 0.561 MeV and 0.01 MeV, respectively and the default parameters for PRESTA were used, e.g. PRESTA-II for the electron-step algorithm and PRESTA-I for the boundary crossing algorithm. The low energy thresholds for the production of knock-on electrons and bremsstrahlung events are set to AE = 0.521 MeV (total energy) and AP = 0.010 MeV. Auxiliary simulations considering an ECUT of 0.521 MeV were also performed in order to analyze the impact of this parameter on the results. No significant dose differences were observed, whereas the simulation time was approximately halved reduced.

The calculation dose-scoring voxel was set to 0.3 cm in X, Y direction and 0.2 cm along Z direction for the simulations performed in the homogeneous phantoms for both energies. For the heterogeneous phantoms, the same voxel size as used for the homogeneous phantom was set (0.3 x 0.3 x 0.2 cm^3) in the lateral regions out the edges of the cavity. Inside and below the cavity (i.e. the acrylic region along the Z axis limited by the cavity edges), the voxel size was set to 0.2 x 0.2 x 0.2 cm^3 in order to reproduce accurately the details of the dose profiles in the immediate vicinity of the cavity. The choice of this voxel was based on previous findings reported by Mora *et al* (2000) [Mor00] and Cygler *et al* (2004) [Cyg04].

A total of 4.4 x 10^7 and 3.4 x 10^7 histories were run for all the dose calculations using the phase space files for 12 MeV and 18 MeV beams, respectively. In each calculation, the phase space files were recycled 3 (12 MeV) and 4 (18 MeV) times based on the study published by Walters *et al* (2002) [Wal05] in order to minimize introducing any bias in the dose calculation.

In order to asses the effect of the particle recycling on the uncertainty as reported by previous authors, a set of DOSXYZnrc calculations were performed in a homogeneous water phantom by recycling the particles of the phase-space files from 1 time to 24 times. Figure 5.1 illustrate the effect of the recycling on the relative uncertainty of the central-axis dose as a function of the depth for a simulated 12 MeV beam with a field of 10 x 10 cm^2.

The figure clearly indicates that the relative uncertainty is mostly constant with the depth if the particles are not recycled. Recycling the particles, however, changes the constant behavior of the uncertainty. In these cases, the relative uncertainty keeps approximately the same value at the surface but decreases for deeper depths. For example, recycling 24 times leads to an uncertainty

of 2.8 % at 2 mm from the surface and 0.8 % at the depth of maximum dose (2.7 cm). This effect is shown to be more relevant for a larger number of recycling times. Note that the uncertainty at the surface is dominated by the latent variance of the phase-space files and thus no matter how often the particle is recycled, this value would only decrease to a fixed value, reflecting the latent variance.

At depths deeper than 3 cm, the fluence of the electrons on the central axis is significantly reduced, due to the attenuation and scattering undergone by the electrons traveling through the water. The reduction of the electron fluence will lead thus to an increase of the relative uncertainty, as it can be confirmed in the figure. As expected, this increase of the relative uncertainty with depth decreases with the number of recycling times due to the increase of the simulated histories.

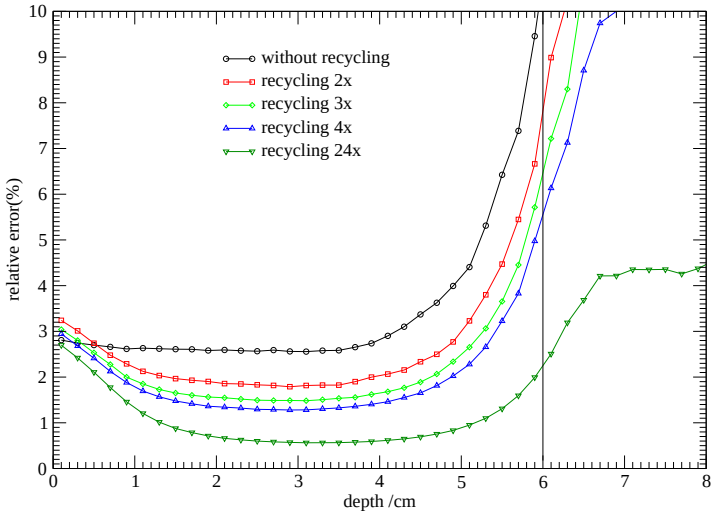

Figure 5.1: Effect of the particle recycling on DOSXYZnrc dose calculations performed in a homogeneous water phantom irradiated with a 12 MeV beam of 10 x 10 cm^2 field size. The vertical line placed at 6 cm represents the range of electrons calculated based on the CSDA approximation.

The statistical uncertainty of calculated dose distributions yielded 1 % (12 MeV) and 1.7 % (18 MeV) at the maximum dose value for the homogeneous phantom. For the heterogeneous phantoms, the statistical uncertainty at the position of the maximum dose increased up to 1.7 % (12 MeV) and 2.2 % (18 MeV); whereas inside the cavity, the average uncertainty was about 3 and 4 % for 12 MeV and 18 MeV, respectively.

The effect of the air cavity on dose distributions for fields conformed using cerrobend blocks was also evaluated for a 12 MeV electron beam using MC calculations (figure 5.2). The phase-space file resulting from the BEAMnrc simulation with about 4.9 x 10^6 particles was used for subsequent dose calculations in a PMMA homogeneous phantom and two different air heterogeneous phantoms using

the DOSXYZnrc code. In particular, a field of 27 cm (X axis) defined by the jaws was conformed with a cerrobend block located below an electron applicator of 25 x 25 cm^2. The final field had a size of about 14 x 14 cm^2 at a SSD of 100 cm. Two heterogeneous phantoms containing an air cavity of 1 x 1 x 2.8 cm^3 and 3.8 x 3.8 x 1.8 cm^3 at the position of x = -5.0 cm and y = -5.0 cm were used for this investigation. The top surface of the cavities was located at 0.2 cm depth from the phantom surface. The simulated phantoms had a total dimension of 25 x 25 x 12 cm^3 and the dose was scored in voxels with the same size as those considered for previous calculations using a 10 x 10 cm^2 field. A total number of about 2 x 10^7 histories was used for each calculation with the phase-space file recycled 3 times. The final statistical uncertainty was about 2 % at the values of maximum dose.

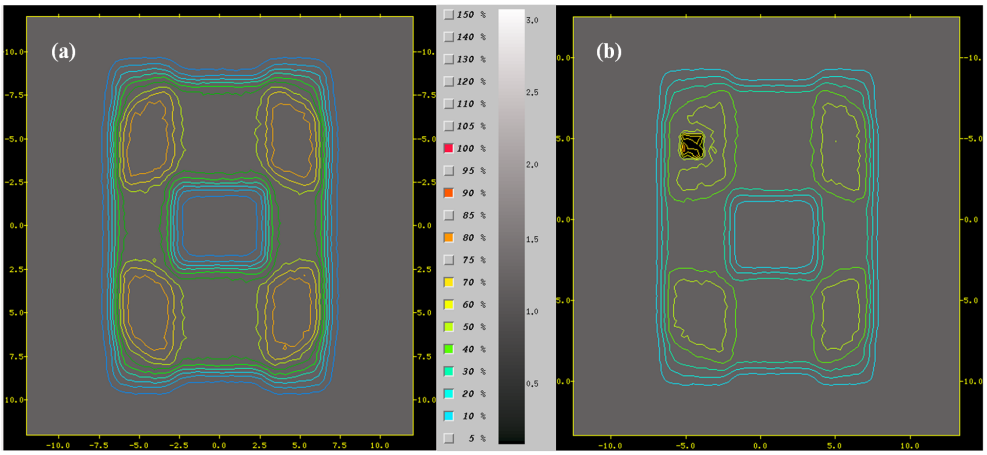

Figure 5.2: Isodose distribution calculated for a 12 MeV electron beam shaped by a cerrobend block in an (a) homogeneous PMMA phantom and (b) an heterogeneous PMMA phantom containing an air cavity of 1 x 1 x 2.8 cm^3 at a position of (-5.0, -5.0) cm. The isodoses were plotted at a depth of 2.7 cm (d_{max}) for the homogenous phantom and 2.2 cm for the heterogeneous ones. The color scale represents the isodose levels normalized to the respective maximum dose of each distribution. The gray scale indicate the density of materials included in the phantoms. The slice views were obtained using the dose visualization dosxyz_show included as part of the BEAM distribution.

BEAMnrc phantom simulations (CHAMBER CM) for the spectral analysis

Electron energy spectra, fluence profiles, angular distribution and mean energy distribution were also calculated at different depths in the PMMA phantoms using beams of 10 x 10 cm^2 field size. For this purpose, phantoms with and without air cavity of same dimensions as those described previously for dose calculations were modeled using the EGSnrc- based BEAMnrc code [Rog05].

Two scoring planes were placed at depths where dose profiles were evaluated (3.3 and 4.2 cm). The output phase-space files for each scoring plane were analyzed using the data processor BEAMDP [Ma09] to obtain the above mentioned spectra.

5.2.2.1 Benchmark of linear accelerator model

The accuracy of the simulated beams was validated by the agreement between the Monte Carlo calculated dose distributions and experimentally measured dose in an homogeneous water phantom. The validation was carried out for electron beams of 12 and 18 MeV with a field of 10 x 10 cm^2.

For the experimental measurements, depth ionization curves and lateral profiles were measured with a PTW 34045 Adv. Markus plane parallel ionization chamber in water using the 12 and 18 MeV electron beams. The sensitive volume of this chamber is 0.02 cm^3 and it has a radius of 2.5 mm. Following recommendations of the IAEA TRS-398 code of practice [And00], the depth ionization curves were converted to depth dose curves by correcting for changes in water-to-air stopping power ratios ($s_{w,air}$) with depth (figure 5.3). MC calculations of the $s_{w,air}$ as a function of the the depth were additionally performed in this part of the work for electron beams of 12 and 18 MeV produced by the simulated Siemens Primus linear accelerator. The calculations were made by using the EGSnrc user-code SPRRZnrc [Rog01]. Previous phase-space files of electron beams obtained for a field of 10 x 10 cm^2 at 100 cm SSD were used as input of this code. The Spencer-Attix $s_{w,air}$ were then calculated on water along the central axis of the beam in a cylindrical region of 0.2 cm thickness and 2 cm radius. The relative statistical uncertainty was within 0.03 %. The calculated stopping power ratios were compared with the corresponding values given by the TRS-398 protocol, as illustrated in the figure 5.3. As shown, differences between calculated and currently recommended ratios of about 1 % were found for both beam energies along all depths, except to the region between the phantom surface and 2 cm depth where larger differences (about 2 %) were observed for the 18 MeV beam.

The effective point of measurement of the chamber was also taken into account in order to correct for the displacement effect, as recommended by the IAEA protocol. In particular, for the Adv. Markus chamber, the effective point was positioned at the front surface of the chamber. The perturbation factor (p_Q) was considered equal to 1 for all depths, since for well-guarded plan-parallel ionization chamber, the variation of this factor is not observed, as reported in the TRS-398 protocol. The statistical uncertainty considered for the measurements was 2 %.

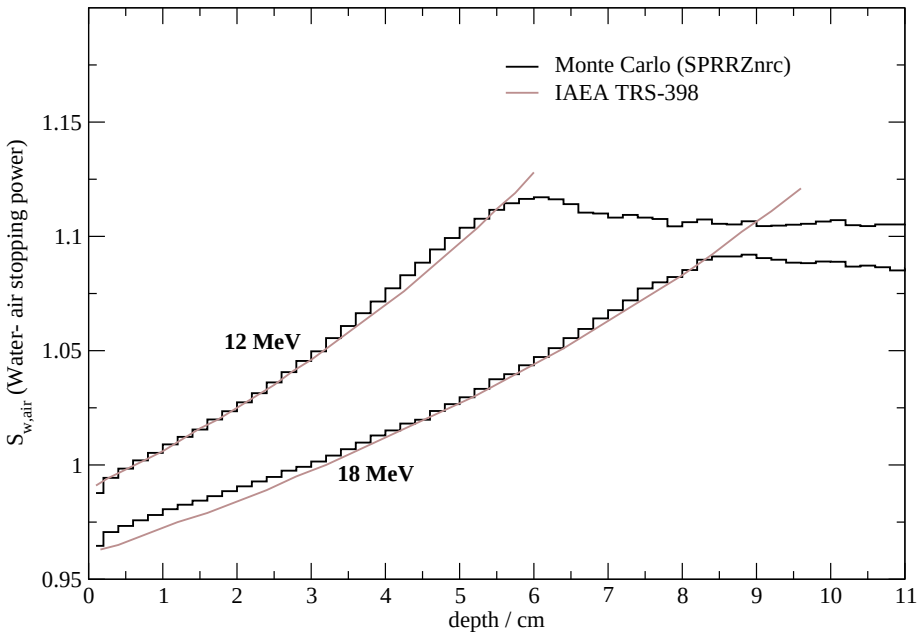

Figure 5.3: Comparison of the water-air stopping power ratio given in the IAEA protocol (TRS-398) and those calculated for realistic Siemens Primus electron beams of 12 and 18 MeV using the SPRRZnrc code. The incident beam used in the calculations as 10 x 10 cm^2 at SSD = 100 cm. The ratios were calculated in water along the central axis in a cylindrical region of 0.2 cm thickness and 2 cm radius.

The experimental data were compared to Monte Carlo calculations carried out in water using previously analyzed phase-space files as inputs of the DOSXYZnrc code. A rectangular phantom with dose-scoring voxels set to 0.2 cm in X, Y and Z axis was employed. The PRESTA electron transport algorithm and cutoff energies of 561 keV for electrons and 10 keV for photons were considered for these calculations.

Results of the comparisons are illustrated in figures 5.4a and 5.4b. It can be seen that the MC data, with an overall uncertainty less than 2 % (both energies), matches the measurements within 2 % at depths beneath maximum dose.

The main discrepancies between the calculated and experimental depth-dose curves are observed at shallow depths (2 -4 mm beneath the phantom surface). These differences are probably due to a wrong readout of the chamber, since the measurements at these shallow depths are being made in a region with a high dose gradient, where half of the sensitive volume of chamber is outside the phantom.

Figures 5.4c and 5.4d present the comparison of calculated and measured lateral profiles along the X axis at different depths, e.g. 2.7 cm (d_{max}) and 4.1 cm for 12 MeV and 2.5 cm (d_{max}) and 6.24 cm for 18 MeV. An excellent agreement ($\sim$ 1 %) is found between the curves along the central axis,

but it worst in the shoulders of the curves where larger differences (about 2 %) are reached.

In overall, it can be considered that the geometric modeling of the Siemens Primus accelerator can accurately represent the output of the accelerator used for experimental measurements (Siemens Oncor) for the two studied energies and a 10 x 10 cm^2 field.

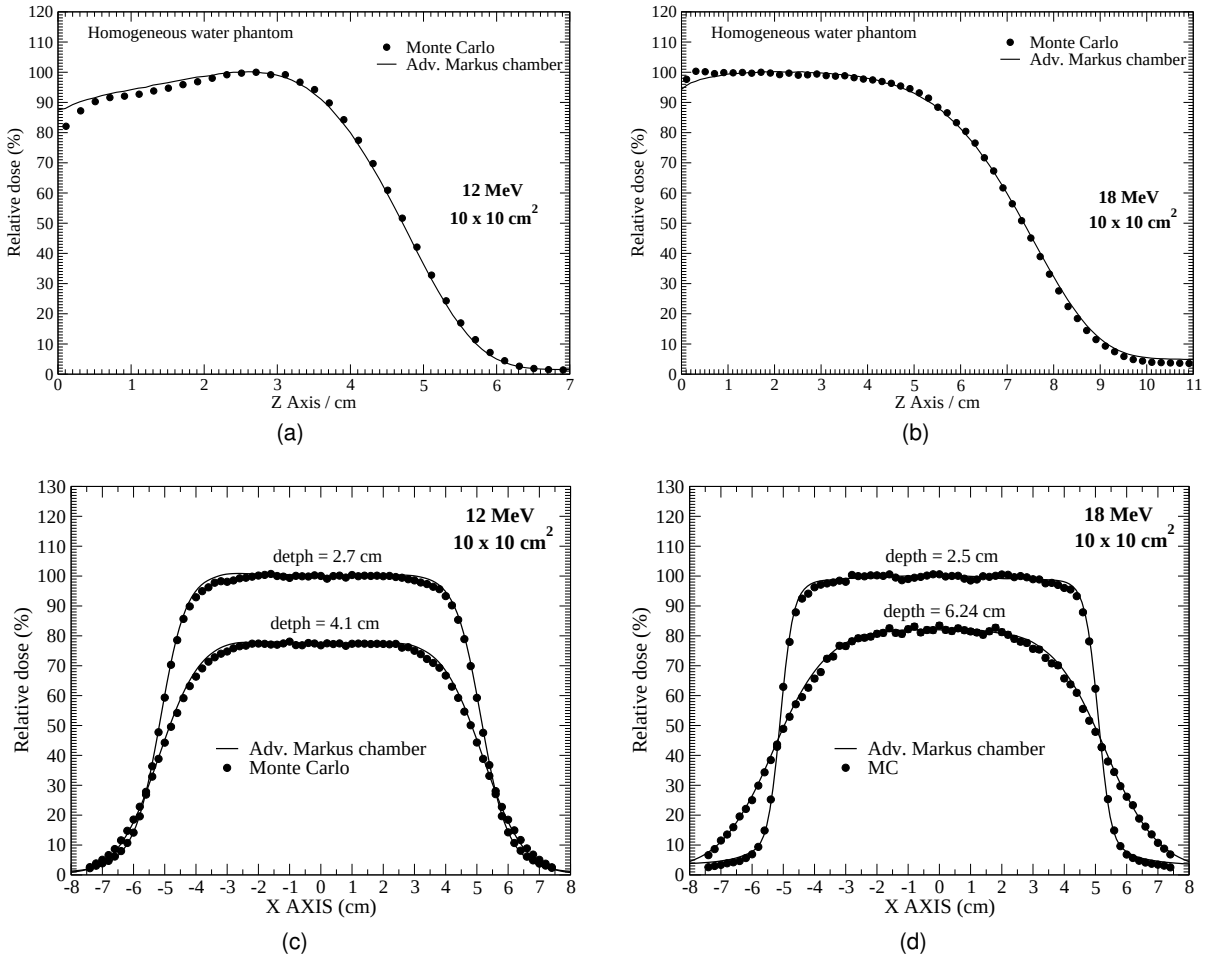

Figure 5.4: On-axis depth dose in a water phantom relative to the dose maximum (a - b) and lateral profiles at depths below the water surface indicated in the insets (c - d) for the 12 and 18 MeV beams from Siemens Primus with 10 x 10 cm^2 field defined at 100 cm SSD. Symbols represent DOSXYZnrc results and full curves correspond to ion chamber measurements.

5.2.2.2 Electron Beam Characterization

For over 50 years, electron beams have been an important modality for providing an accurate dose of radiation to superficial cancers and disease and for limiting the dose to underlying normal tissues and structures. Currently, with the implementation of new treatment modalities using electron beams,

such as modulated electron radiation therapy (MERT), electron beams still represent an important therapy option.

The precise knowledge of radiotherapy beams, using either photons or electrons, is always essential for dosimetry, quality assurance, design of an accelerator as well as accurate dose calculations. The energy and angular distributions of the beam particles produced by medical linear accelerators are the most important characteristics of the beams, because, as known, the dose distributions depend on them. It is very difficult to obtain such detailed information using an experimental approach due to limitations in the clinical environment and detectors and, alternatively, Monte Carlo methods are recognized nowadays as a powerful mean of obtaining such spectra.

In the present work, characteristics of simulated 12 and 18 MeV electron beams from the Siemens Primus with a 10 x 10 cm^2 field at SSD of 100 cm were analyzed using the data processing program BEAMDP [Ma09]. The most representative spectra are displayed in figures 5.5 and 5.6.

As seen from figures 5.5a and 5.5b, electrons leaving the accelerator head show a very broad energy spectra centered on 11.5 MeV and 18 MeV energy for 12 MeV and 18 MeV beams, respectively.

Although the electrons emanating from the waveguide of the linear accelerator are fairly monoenergetic, before reaching the phantom surface they have undergone many interactions with the air volume and the various head components (scattering foils, exit window, collimators, etc.), resulting in the broadening of the electron energy spectrum. Additionally, the interactions of electrons with the head components, primarily containing W and Au, lead to the production of bremsstrahlung photons. As also illustrated in these figures, the spectra of the photons have the higher contribution at the lowest energy range of the beam spectra and present a peak around 250 keV for both beams. Moreover, it is interesting to point out that the number of the contaminant photons exceeds in a factor of 2.5 and 6 the maximum value of electron fluence for 12 and 18 MeV beams, respectively. As expected, the higher the energy of the electron beam is, the higher the contaminant photon dose due to the increase of bremsstrahlung probability.

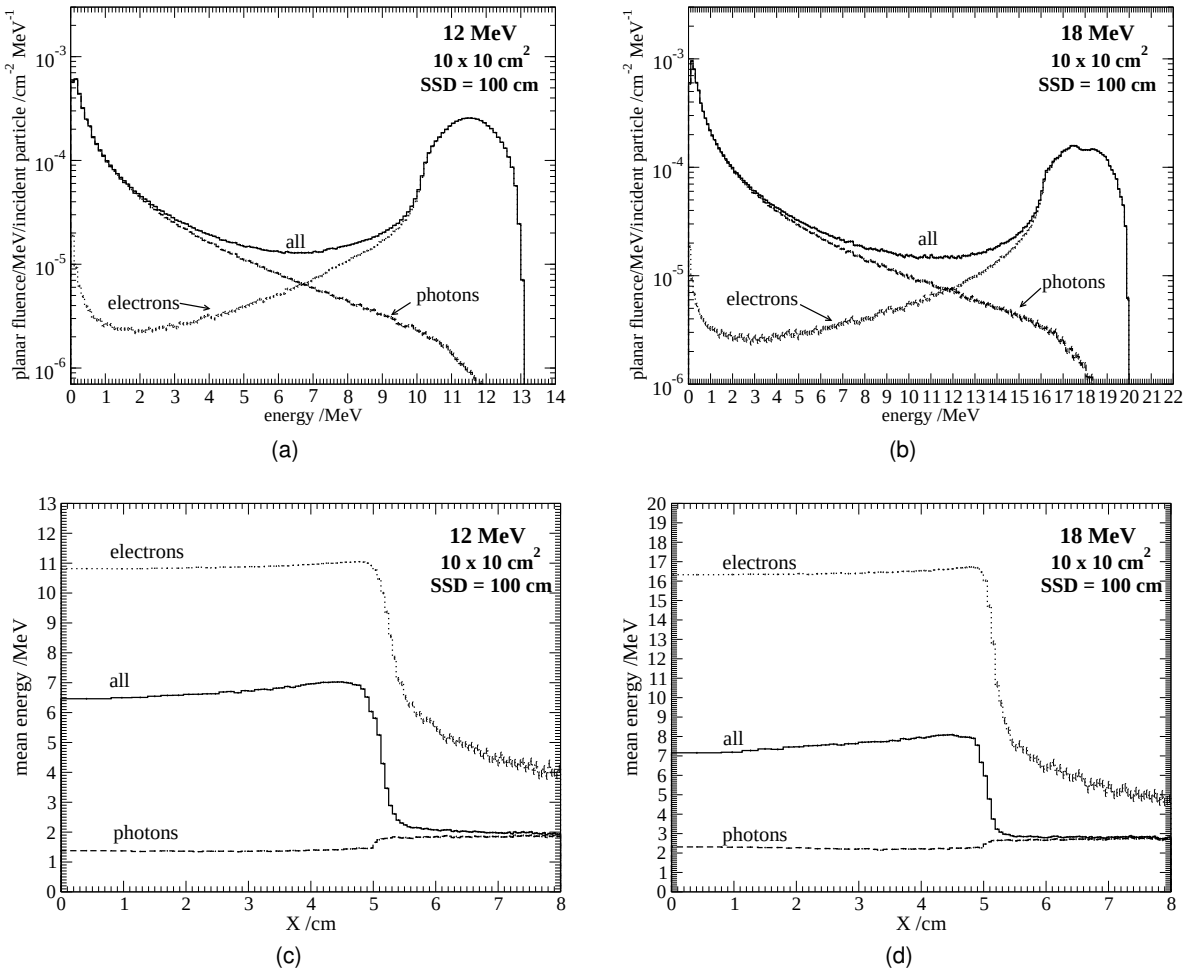

Figure 5.5: Energy distributions (a - b) and mean energy profiles (c - d) of electrons and photons present in the 12 and 18 MeV beams from Siemens Primus with 10 x 10 cm^2 field defined at 100 cm SSD. Same spectra for the contribution of "all" particles is also included for comparison. The energy spectra are calculated in a central region of 5 x 5 cm^2 using bins 200 keV wide.

As shown on the plot of mean energy against distance from the beam axis in figures 5.5c and 5.5d, the spectral distribution is weakly dependent on the position of the particle across the treatment field. The mean energy of electrons in the central part (between 0 and 5 cm) stays approximately constant at 11 MeV and 16.5 MeV for the beams with nominal energy of 12 MeV and 18 MeV, respectively. Outside the field, this mean energy varies considerably with distance from the field edge, decreasing up to 4 MeV (12 MeV beam) and 5 MeV (18 MeV beam) at 8 cm from the central axis. In contrast to electrons, the mean energy of contaminant photons remains relatively flat away from the central axis, although with lower values than that of electrons, around 1 - 2 MeV for the 12 MeV and 2-3 MeV for the 18 MeV beam.

Figures 5.6a and 5.6b show the fluence of electrons and contaminant photons as function of the

distance to the central beam axis. These profiles were calculated in a square region of 8 cm half-side. For both electron beams, the electron's fluence remains relatively constant until the field edge and then decreases sharply. For contaminant photons, the fluence has a maximum in the central axis and gradually decreases across the field. After the field edge, it does not change so sharply as for electrons.

Moreover, it is interesting to see from the fluence profiles how the contaminant photons contribute significantly to the beam for both beam energies, being even higher for the higher-energy beam (18 MeV) where the photon fluence presents a contribution of up to 80 % higher than that electron fluence at the central axis.

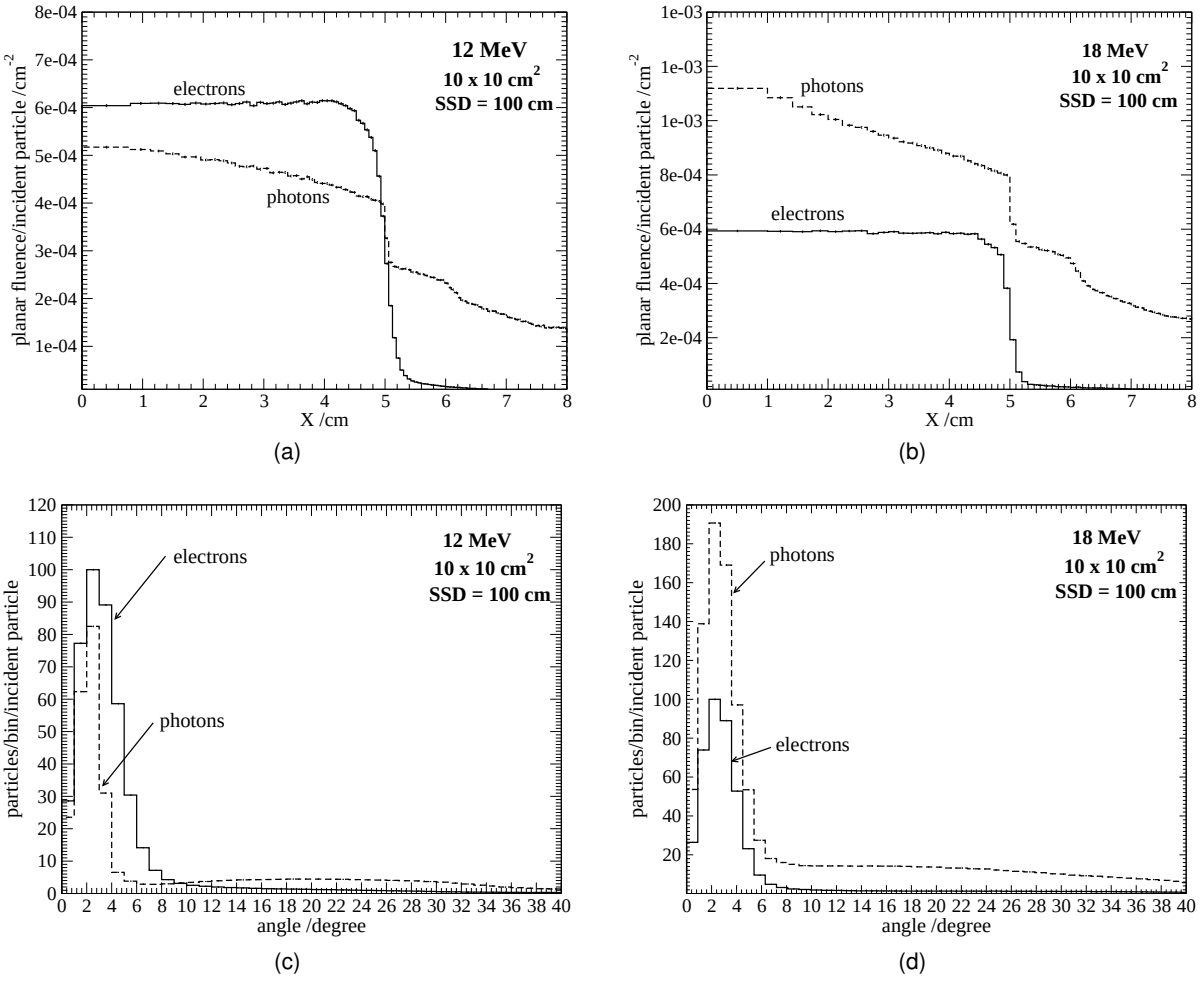

Figure 5.6: Fluence profiles (a - b) and angular distributions (c - d) of electrons and photons contained in the 12 and 18 MeV beams from Siemens Primus with 10 x 10 cm^2 field defined at 100 cm SSD. The fluence spectra are calculated in a square region of 8 cm half-side. Angular distributions were scored in a region of 5 cm radius and using bins 1° wide.

Finally, the angular distributions of electrons and contaminant photons are plotted in figures 5.6c and 5.6d. As seen, both electrons and photons show a very narrow angular spread centered around 2.5° for both electron beams. As expected for the higher electron beam (18 MeV), it can be also noted how the photon distribution is more forward-peaked than for the 12 MeV case.

5.2.3 Measurements

5.2.3.1 Home-built PMMA phantom

An air cavity phantom of PMMA was specifically built for this investigation (figure 5.7d).

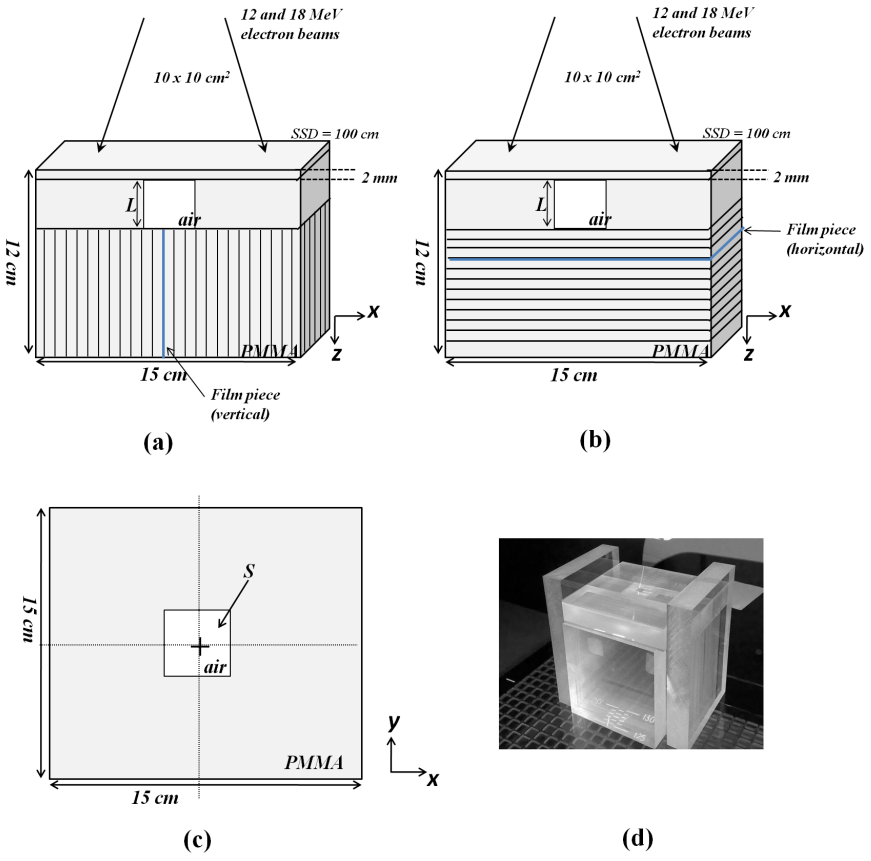

Figure 5.7: Scheme of sagittal (a-b) and transverse (c) views of the home-built PMMA phantom (d) including an air cavity with area S and thickness L used for experimental measurements and modeled for MC dose calculations (drawings not in scale). The cavities were located at 2 mm depth from the phantom surface. The blue line indicates the position of the radiochromic film during experimental measurements. The electron beam was directed perpendicularly to the phantom surface, but a beam gantry angle of 2° in respect to the film axis was applied for experimental acquisition of depth dose distribution to avoid the self-attenuation of the film for the (a) configuration.

The phantom with an area of 15 x 15 cm^2 and a total height of 12 cm consisted of two parts: a) a PMMA block (15 x 15 cm^2 area and 2.8 cm thickness) containing an air cavity of 3.8 x 3.8 x 2.8 cm^3 at the centre and b) 30 PMMA slabs (15 x 15 cm^2 area) with thickness of 0.3 cm placed below the previous part (a). Inside the 3.8 x 3.8 x 2.8 cm^3 cavity, air cavities with varying areas S and thicknesses L (figure 5.7a-c) were carefully arranged using small blocks of PMMA. For all phantom configurations, a PMMA plate (15 x 15 cm^2 area) with thickness of 0.2 cm was located at the top of the phantom block with the cavities. Four thick PMMA pieces were inserted around the phantom to press tightly together the structure and avoid possible air gaps between PMMA slabs or between the small pieces building each arranged cavity.

Two different set-ups were applied to perform the dosimetric measurements as illustrated in figures 5.7(a) and 5.7(b). In one case, the 0.3 cm thickness slabs were positioned parallel to the beam axis in order to acquire the depth dose curve (figure 5.7(a)). In the other case, the slabs were positioned perpendicularly to the beam for the acquisition of the transversal dose profiles [figure 5.7(b)]. In both cases, the total thickness below the cavity was about 10 cm in order to consider the backscatter contribution. Further details of the experimental set-ups are described in the next section *"Radiochromic film dosimetry"*.

5.2.3.2 Radiochromic film dosimetry

Radiochromic films type Gafchromic EBT were irradiated to determine the depth dose curves along the central axis and dose profiles at various depths for homogenous and heterogeneous geometries. The choice of the film was influenced by its favorable performance in several aspects such as spatial resolution, low spectral sensitivity, tissue equivalence, dose range, and others [Fer09, Chi07, Such01, Suth10, Bou09].

Measurements were carried out for electron beams with energies of 12 MeV and 18 MeV produced by the Siemens Oncor accelerator installed at the *"Hospital de Santa Maria"* in Lisbon. These measurements were performed in the home-built PMMA phantom previously described in section 5.2.1 using the standard 10 x 10 cm^2 applicator size at a SSD equal to 100 cm. For this field, the jaws were set to define a field of 19 x 19 cm^2.

For the depth dose curves acquisition, pieces of radiochromic films (12.5 x 10 cm^2) were individually exposed parallel to the central axis of the incident beams (150 UM) between two central

PMMA slabs of 0.3 cm thickness, which were vertically placed as illustrated in the figure 5.7(a). Depth dose curves were measured at depths below the PMMA block containing the cavity, i.e. beyond 3 cm (figure5.8a). A beam gantry angle of 2° respect to the film axis was applied in order to avoid the self-attenuation of film and to reduce the effect of possible gaps between the phantom slabs [Khan90]. For measurements of depth dose curves in an homogeneous phantom, the PMMA block with the air cavity as well as the 2 mm thick plate were removed. Thus, a total depth dose distribution from the top surface of the phantom was registered in this case. Film samples were exposed following the same conditions described above for the heterogeneous phantom.

For transverse dose profile measurements, film samples (12.5 x 10 cm^2) were irradiated horizontally on the central beam axis with 150 UM, supported between two PMMA slabs, at 3.3 cm and 4.2 cm depths (figure 5.8b). Dose calibration curves of the film were obtained for both electron beam energies, 12 and 18 MeV, in order to evaluate the energy dependence of the film reported by previous studies [Chi07, Suth10]. Twelve pieces (8.3 x 10 cm^2) of the film were used for each calibration curve.

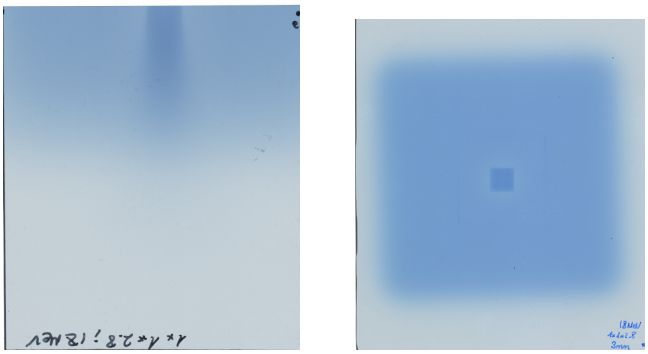

(a) (b)

Figure 5.8: EBT film samples exposed by the 18 MeV electron beam in a heterogeneous phantom containing the cavity of 1 x 1 x 2.8 cm^3: PDD (a) profile at 3 mm depth below the cavity (b).

An Epson 10000 XL Expression flatbed scanner was used to study the films response. After irradiation, the films were left for a period of 24 hours before the scanning. During the scanning process, each film sample was placed on the center of the scan bed always with a landscape orientation, e.g. with the short film side coinciding with the large glass plate side. The software package ”EPSON scan” was used with all filters switched off. The images were scanned in transmission mode with a resolution of 72 dpi (0.35 mm/ pixel) in the 48 bit RGB uncompressed tagged image file format TIFF. Therefore, the red component was extracted in all images, since the greatest response of EBT films

are in the red color channel / red wavelength band of the visual spectrum. Scanner warm-up effects were reduced by doing five successive pre-scans before the final reading of the film [Fer09]. The dosimetric analysis of scanned images were carried out using the OmniPro-I'MRT software.

In addition to the cares mentioned above, other reported guidelines and precautions about EBT radiochromic dosimetry [Buts03, Khan90] were taken into account to ensure maximum reproducibility and accuracy of the results. All films used in this study were from the same batch to remove any variability between batches. They were always handled with gloves, and care was taken to avoid mechanical strain where possible. Furthermore, the film pieces were cut 1 day prior to irradiation to allow for disturbances around the edges. While not in use, films were stored in light-tight envelopes under constant atmospheric conditions. For the procedure followed in the study [Klev92, Suth10, Mar08, Van07], our statistical uncertainty of film dosimetry is estimated to be about 2 % - 2.5 %.

Sensitometric curve

Dose calibration curves of the film were obtained for both electron beam energies, 12 and 18 MeV, in order to evaluate the energy dependence of the film reported by previous studies [Chi07, Suth10]. Twelve pieces (8.3 x 10 cm^2) of the film were used for each calibration curve. As recommended by H. Bouchard *et al* (2009) [Bou09], the choice of 12 point for the characterization of the sensitometric curve provides a sufficient precision for the uncertainty estimation. Each piece was placed horizontal in a Solid Water phantom (PTW RW3 plate phantom) at the depth of maximum dose and irradiated separately with a 10 x 10 cm^2 field to doses ranging from 0 to 500 cGy. A source-to-surface distance of 100 cm was used. The specified absolute dose at the center of each film piece was determined with a parallel-plane ionization chamber PTW Adv. Markus with a sensitive volume of 0.02 cm^3. These absolute doses were determined from the ionization chamber signal according to the IAEA TRS 398 protocol [And00] with the appropriate correction factors for beam quality and environmental conditions. Additionally, an unexposed film sheet (0 cGy) was used as a zero-dose point and also to derive the background correction of the batch.

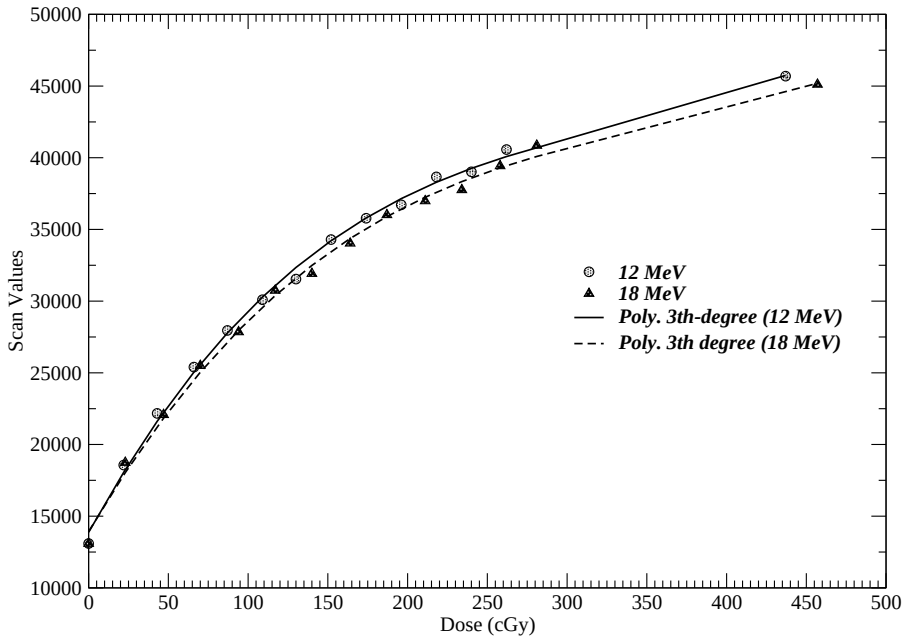

Figure 5.9: Energy dependence of the calibration curve for Gafchromic EBT film. Solid and dashed lines represent a third order polynomial fitting curve for 12 MeV and 18 MeV electron beams, respectively.

Figure 5.9 presents the variation of measured scan values with dose (symbols) for the two energies studied. A polynomial function of the third degree was applied to fit the experimental points as shown in figure 5.9. No significant variation of measured scan values was observed for doses lower than 100 cGy. However, the average separation between curves increases up to 2.5 % with increasing dose, which still results in a weak energy dependence of the film sensitivity. In addition, these results are consistent with those previously published by Su Fan-Chi *et al* (2007) [Chi07]. To minimize this dependence, results of all later sections were obtained by using the corresponding calibration curve for each energy.

5.3 Results

5.3.1 Air cavity effect for standard 10 x 10 cm^2 field

5.3.1.1 Central-axis PDD variation due to the presence of air cavity

Figures 5.10 and 5.11 compare the calculated central-axis PDD curve with the measured PDD curve for heterogeneous phantoms irradiated by electron beams of 12 MeV and 18 MeV. The heterogeneous phantoms included an air cavity of varying size of thickness L or area S, as summarized in

table 5.1. The beams were incident perpendicular to the phantom surface with a field size of 10 x 10 cm^2 at a SSD of 100 cm. In addition, the PDD curve for the homogeneous phantom without air cavity (labeled as *"without cavity"*) is also shown in these figures.

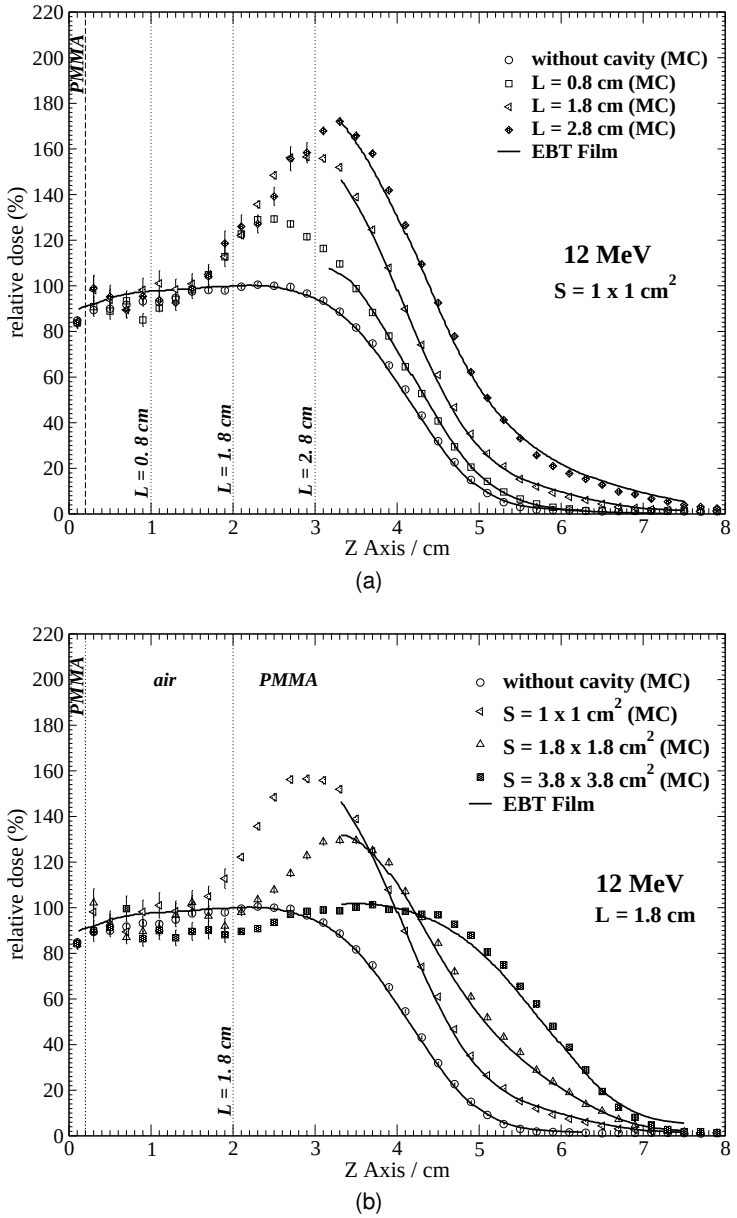

Figure 5.10: On-axis PDD curves measured (solid line) and MC calculated in heterogeneous phantoms including (a) a 1 x 1 cm^2 air cavity with different thickness L and (b) a 1.8 cm thick air cavity with different area S. The top of 300 the air cavities was located at 2 mm depth. An electron beam of 12 MeV (10 x 10 cm^2) was incident perpendicular to the phantom surface at a SSD of 100 cm. The PDD curve for the homogeneous phantom (labeled as "without cavity") is also shown. Both MC calculated and experimental PDD curves are normalized to the maximum dose value of the PDD for the homogeneous phantom. The vertical lines show the position of the air cavities.

All curves were normalized to the dose at the depth of dose maximum in the homogeneous phantom, i.e. 2.3 cm for 12 MeV and 2.7 cm for 18 MeV. Note that the position of the cavities is kept at the same depth (2 mm from phantom surface) while the dimensions S or L vary.

In figures 5.10a and 5.11a, it can be clearly seen that the PDD is strongly dependent on the thickness L of the cavity for both energies. As shown in figure 5.10a for 12 MeV electron beams, the presence of an air cavity of 2.8 cm thickness leads to an enhancement of about 72 % of the maximum dose with respect to the *"without air cavity"* curve. This increase is a consequence of the electron disequilibrium caused by the lack of scattering in air. Because of the small area of the cavity (S = 1 x 1 cm^2), electrons scattered from the two PMMA sides surrounding the cavity can scape from the air cavity and contribute to the electron on-axis fluence at the first centimeters depths beyond the air-PMMA interface. As the cavity thickness decreases, the scatter contribution from the PMMA adjacent to the cavity decreases and hence the perturbation of the maximum dose reduces along the central axis. For instance, the increase of maximum dose is only about 27 % for the cavity phantom of L = 0.8 cm irradiated by a 12 MeV beam.

It can be also seen from figure 5.10a that the presence of the air cavity with varying thickness causes a shift of the PDD curve to the downstream direction.

The reduced attenuation of electrons passing through the air compared to those through water results in higher energy and forward electrons, as revealed by the spectral distribution in the next section *"Influence of air cavity on spectral distributions"*. This higher energy electron contribution increases the penetrating power of the beam and hence moves the maximum dose to deeper positions.

As expected, the depth dose displacement becomes much pronounced for a larger cavity thickness. As seen in figure 5.10a, the position of the maximum dose changes from 2.3 cm to 3.3 cm for the cavity of larger thickness (L= 2.8 cm), whereas a small shift (about 2 mm) occurs for the cavity with thickness of 0.8 cm.

Similar cavity effects on the PDD curves with the cavity thickness are also observed for the electron beam of 18 MeV, as illustrated in figure 5.11a for the cavity of 1 x 1 x 2.8 cm^3. However, it is evident from this figure that the effect on the dose maximum is not so strong as those observed for the previous energy. In particular, the enhancement of the dose maximum due to the air cavity is reduced about 6 % compared to 12 MeV case for all heterogeneous phantoms. This reduction is probably due to the contribution of the electrons scattered from the PMMA sides surrounding the

cavity to the on-axis electron fluence decreases with the energy of the electron beam.

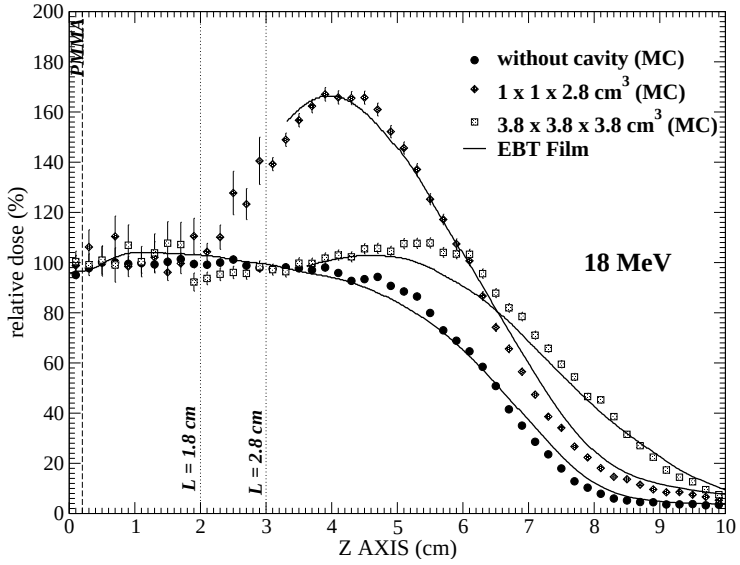

(a)

Figure 5.11: On-axis PDD curves measured (solid line) and MC calculated in heterogeneous phantoms including a 1 x 1 x 2.8 cm^3 (left triangle) and a 3.8 x 3.8 x 1.8 cm^3 (up triangle) air cavity. The top of the air cavities was located at 2 mm depth. An electron beam of 18 MeV (10 x 10 cm^2) was incident perpendicular to the phantom surface at a SSD of 100 cm. The PDD curve of the homogeneous phantom (labeled as "without cavity") is also shown. Both MC calculated and experimental PDD curves are normalized to the maximum dose value of the PDD for the homogeneous phantom. The vertical lines show the position of the air cavities.

Figures 5.10b and 5.11a show the dependence of the perturbation of depth dose on the variation of the square area S of the cavity for 12 and 18 MeV electron beams, respectively. As seen, the presence of these air cavity configurations results in an increase of maximum dose as well as a shift towards larger depth values, analogously to the previous effect of cavities with varying thickness.

In particular, it is observed that the perturbation on the dose maximum value is reduced with the area of the cavity. For the 12 MeV electron beam, the dose maximum increases about 57 % for the cavity of S = 1 x 1 cm^2. This increase is smaller for higher values of S, attaining 32 % for S = 1.8 x 1.8 cm^2 (figure 5.10b) and about 1 % for the wider cavity (3.8 x 3.8 cm^2). This is because the contribution at the central axis of the electrons scattered from the two PMMA lateral boundaries of the cavity is reduced significantly as the area increases.

On the other hand, it can be also noted that when the energy of the electron beam is increased to 18 MeV, the dose maximum perturbation for the cavities of 1 x 1 and 1.8 x 1.8 cm^2 is less pronounced (6-10 %) than that for the 12 MeV beam. This behavior changes however for the largest cavity (3.8 x 3.8 cm^2) where the dose maximum leads to an increase of 6 % of the maximum dose in comparison

with the increase of 1 % previously obtained for the beam energy of 12 MeV.

Comparing the dose curves for homogeneous and heterogeneous phantoms in figures 5.10b and 5.11a, it is observed a shift of the PDD to deeper positions of the phantom caused by the presence of air cavities with varying area and this displacement of the PDD increases with the area of the cavity and the energy. So, for the 12 MeV electron beam, a change of about 1.4 cm in the maximum dose position is observed when an air cavity of 3.8 x 3.8 cm^2 is embedded in the phantom with respect to that dose maximum position for the homogeneous phantom. Larger displacement (about 2.4 cm) of dose maximum is found for 18 MeV electron beam due to the longer range of the electrons for this energy.

The agreement between calculated and measured central-axis PDD is within 2 % for all heterogeneous phantoms irradiated by a 12 MeV electron beam as seen in figures 5.10. However, for 18 MeV, a worst agreement is found, where discrepancies between the measured and calculated values reach up to 6 % along the high-dose gradient region below each respective maximum dose value in the heterogeneous phantoms (figure 5.11a).

5.3.1.2 Off-axis dose variation due to the presence of the air cavity

Figures 5.12 and 5.13 show dose profiles calculated along the cross-plane (X axis) of the PMMA phantoms including an air cavity (table 5.1) and irradiated with electron beams of 12 and 18 MeV, respectively. The profiles are presented below the cavity at two depths, 3.3 and 4.2 cm, for all sizes of cavity. The figures include also the experimental profiles measured in the home-built PMMA phantom using EBT films at the same location as the calculated profiles. All curves were normalized to the dose value at 3.5 cm, an off-axis point located out of the cavity perturbation region.

For 12 MeV, it is clearly seen that two small dips and peaks appear on the dose distribution near the lateral edge of the cavity with 3.8 x 3.8 cm^2 area and 1.8 cm thickness at the depth of 3.3 cm (figure 5.12a). This effect is caused by the existence of fewer electrons scattered from the air cavity into the surrounding PMMA than scattered into the air from the PMMA. For the other heterogeneous phantoms, it is observed a unique sharp peak along the central axis. For these cases, the decrease in cavity area leads to the increase in the fluence along the central axis of electrons scattered from the lateral cavity boundaries, as mentioned above in the previous analysis for the depth-dose curves. The largest dose increase at the central axis is caused by the presence of the largest thickness, L = 2.8 cm, as exhibited previously by the PDD curves.

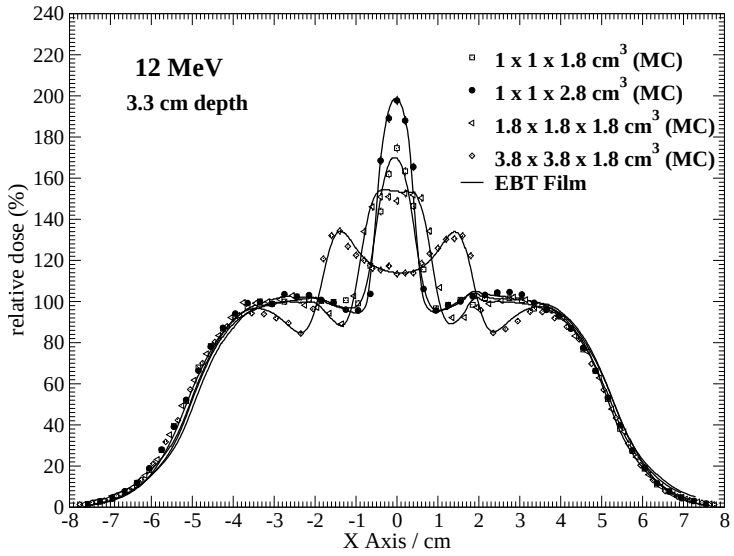

(a)

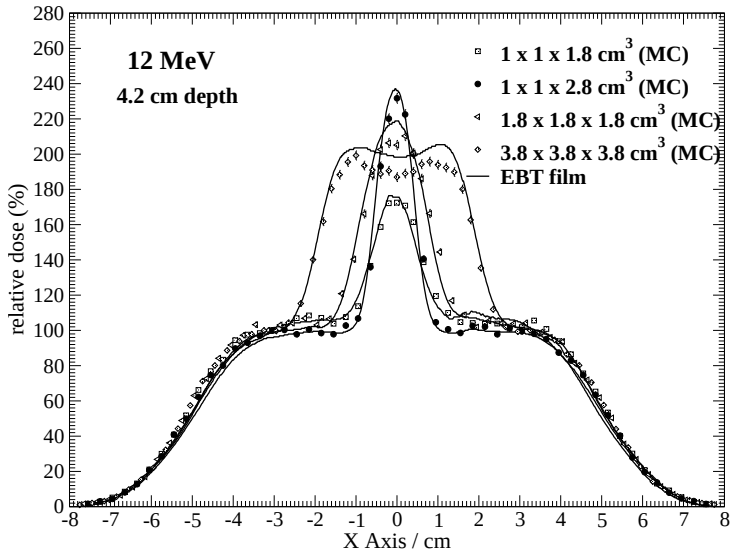

(b)

Figure 5.12: MC calculated (symbols) and measured (lines) cross-plane dose profiles (X axis) at (a) 3.3 cm and (b) 4.2 cm depth in heterogeneous phantoms containing an air cavity of different area S and thickness L. An electron beam of 12 MeV (10 x 10 cm^2) was incident perpendicular to the phantom surface at a SSD of 100 cm. Both MC calculated and experimental dose profiles are normalized to the dose value at the off-axis position of 3.5 cm.

The effects of the electron disequilibrium caused by the air become less dramatic at greater distances below the cavity as shown in figure 5.12b for 12 MeV.

At 4.2 cm depth, the characteristic dip and peak just around the cavity edges are significantly reduced and a sharp dose peak is clearly seen for all heterogeneous phantoms as a result of the increase of electron fluence at the center due the reduced attenuation of the electrons passing

through the air cavity.

For 18 MeV, a similar behavior as previously mentioned for 12 MeV is observed for the dose profiles at the depth of 3.3 cm in figure 5.13a.

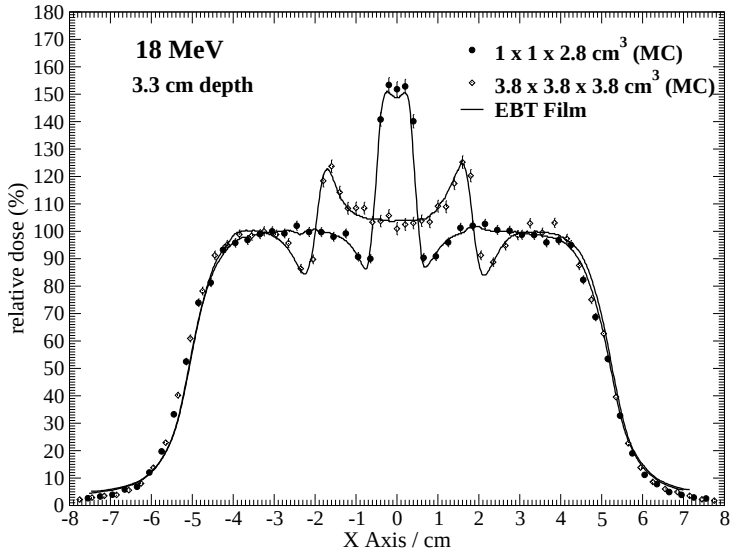

(a)

Figure 5.13: MC calculated (symbols) and measured (lines) cross-plane dose profiles (X axis) at 3.3 cm depth in heterogeneous phantoms containing a 1 x 1 x 2.8 cm^3 and 3.8 x 3.8 x 1.8 cm^3 air cavity for a 18 MeV electron beam. An electron beam of 18 MeV (10 x 10 cm^2) was incident perpendicular to the phantom surface at a SSD of 100 cm. Both MC calculated and experimental dose profiles are normalized to the dose value at the off-axis position of 3.5 cm.

From figures 5.12 and 5.13, it is also remarkable that experimental results show well the fine details of the dose near the interface of the cavity. For both energies, the agreement between measured and calculated is within 3 % for all cavity sizes at both considered depths, except for the case of the 3.8 x 3.8 x 1.8 cm^3 cavity at 12 MeV, where the difference between experimental and calculated profile at 4.2 cm depth reaches up to 8 %.

5.3.1.3 Influence of air cavity on spectral distributions

In this section, we pretend to explain the previously observed dose perturbation in the air cavity phantom based on the variation of the electron spectra due to the air cavity. For this purpose, we present the on-axis energy spectra of the electrons for the phantom configurations used for dose calculations and measurements (table 5.1). The angular distribution of the electrons for each case is also reported.

Energy spectra

Figures 5.14 compare the calculated electron energy spectra of electrons in a homogeneous PMMA phantom with those spectra calculated for the different heterogeneous phantoms. These heterogeneous phantoms included an air cavity with varying area S and thickness L and they were irradiated by single beams with energies of 12 MeV (figure 5.14a and 5.14b) and 18 MeV (figure 5.14c and 5.14d). In all cases, an applicator field of 10 x 10 cm^2 was used at a SSD of 100 cm. The spectra were calculated in a scoring plane of 2 cm radius for both phantom configurations (homogeneous and heterogeneous). The scoring plane was located at 3.3 cm depth, just beneath the air cavity. Energy bins 200 keV wide were used. The values of the electron fluence calculated in each heterogeneous phantom were normalized to the value of the maximum electron fluence calculated in the homogeneous phantom, labeled as *"without cavity"*.

For the 12 MeV electron beam, the energy spectra of electrons present a fluence peak at about 4 MeV for the homogeneous phantom configuration as shown by the continuous black line in figures 5.14a and 5.14b. In Fig. 5.14a, it is noted that the position of this does not change in the electron energy spectra calculated for the cavity phantoms with different values of thickness L. However, the relative fluence of the electrons at this peak decreases with the variation of this dimension. Inserting an air cavity with 1.8 cm thickness causes a reduction of the electron fluence of about 8 % relative to the fluence observed for the homogeneous phantom.

It can also be seen in figure 5.14a that there is an increase of the on-axis electron fluence in the high-energy range ($>$ 7 MeV) for cavity phantoms of varying thickness L. This enhancement is mainly caused by the electrons passing through the air cavity, which are more forward scattered and hence higher in energy. The effect is clearly more evident in the electron energy spectra for cavities with larger thickness, 1.8 and 2.8 cm, where peaks at around 8 MeV and 10.5 MeV are observed. The contribution of the electrons at these peaks represents 13 % of the maximal on-axis electron fluence for the homogeneous phantom. This electron contribution of higher energy ($>$ 7 MeV) causes the increase and displacement forward of the PDD curves compared to the homogeneous phantom. In particular, these effects are more pronounced for larger thickness of the cavity; where the largest fluence of electrons with energy $>$ 7 MeV and the highest electron energy are responsible for the largest increase and shift of depth dose curve as observed in the previous section assessing the cavity effect on the PDD distributions.

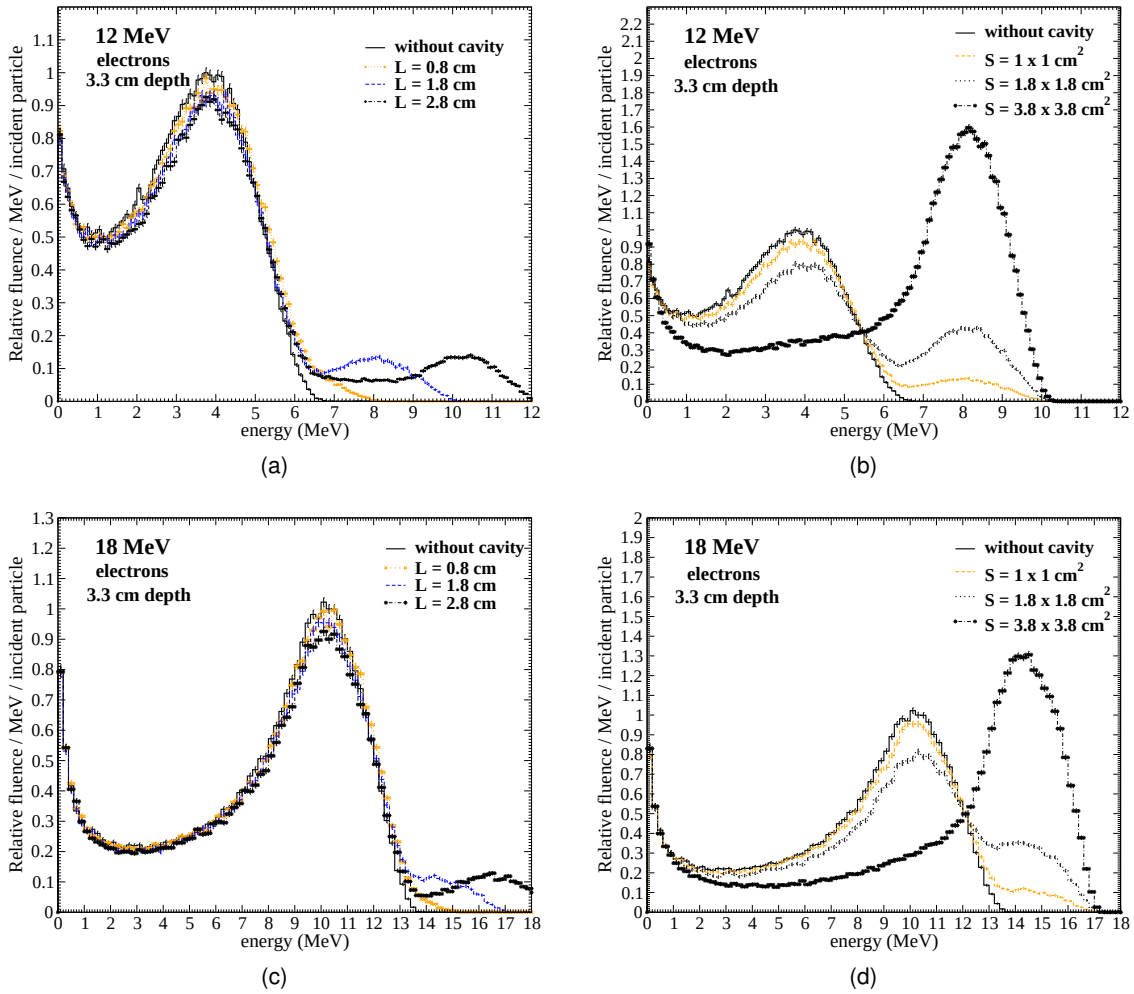

Figure 5.14: Electron energy spectra calculated at a depth of 3.3 cm in a PMMA phantom with and without an air cavity of varying dimensions, thickness L (a-c) or area S (b-d), irradiated by 12 MeV (top) and 18 MeV (bottom) electron beams. The applicator field was 10 x 10 cm^2 for a SSD of 100 cm. The spectra are calculated in a scoring region of 2 cm radius. Energy bins are 200 keV wide.

Figure 5.14b presents the perturbation caused on the electron spectra by air cavities of different square areas using a 12 MeV electron beam. As shown in this figure, the presence of cavity with varying area S result in a reduction of electron fluence in the energy range below 7 MeV. This variation depends on the cavity area and become more significant with increasing area. At the same time, additional electron contribution in a high-energy range (> 7 MeV) is observed for these heterogeneous phantoms. These contributions correspond to the electrons going through the cavity and attenuated subsequently in 1.3 cm of PMMA, i.e. from the end of the cavity (at 2 cm) to the scoring plane at 3.3 cm. Since the thickness for these cavity phantoms is maintained (L = 1.8 cm) and only the area is varied, the position of the maximal electron fluence in the high-energy range will

occur at the same energy (around 8.3 MeV). However, the relative on-axis electron fluence changes with the cavity area since the electron beam area corresponding to electrons traveling through the air is higher as the cavity area increases.

For a cavity of 3.8 x 3.8 cm^2 area, these electrons with high energy are responsible for the increase of up to 60 % of the on-axis fluence of electrons compared to the maximal electron fluence for the homogeneous phantom. This would explain the highest shift of the depth dose curve observed for the wider cavity in previous figures 5.10 and 5.11.

Similar changes of electron energy spectra due to the presence of an air cavity are found for the 18 MeV electron beam as shown in figures 5.14c and 5.14d. For this energy, the homogeneous spectrum presents a peak at the energy of around 10 MeV. The on-axis electron fluence at this peak decrease with the thickness L and the area S of the cavity as previously observed for the 12 MeV beam. However, this reduction becomes less significant because of the increased range of the electrons for 18 MeV compared to the 12 MeV electron beam. At the same time, a contribution of electrons with energies higher than the maximum value of energy for the homogeneous spectrum (14 MeV) appears again for heterogeneous phantoms as consequence of the reduced attenuation of electrons traveling through the air. The trends seen in these figures confirm the less pronounced (about 6 %) perturbation of depth dose curve for higher beam energy (figures 5.11).

Angular distributions

The angular spread of electrons reaching the plane at 3.3 cm depth in homogeneous and heterogeneous phantoms is plotted for the 12 MeV and 18 MeV electron beams in figures 5.15. The angular distribution was recorded over a region of 2 cm radius using an angle bin 1° wide. Figure 5.15b shows the variation of the angular spread as a function of the area of the cavity inserted in the phantom for the 12 MeV electron beam. Comparing the curves in this figure, it can be seen that the variation of angular spread between homogeneous and heterogeneous phantom occurs in the lower angle range from 0° to 25°. The largest discrepancy between the homogeneous and heterogeneous phantoms occurs for the cavity of largest thickness, where an increase of about 8 % and a shift of 5° to lower angle appear. These differences represent the contribution of electrons with high energy, as previously discussed in the energy spectra, which travel through the air where the lateral scattering decreases in comparison to water.

When the area S of the cavity increases, the maximum on-axis fluence of electrons for homo-

geneous phantom (at around 25°) is shifted to lower angle and is also enhanced significantly as illustrated in Fig. 5.15b for the 12 MeV electron beam. As shown, the presence of the wider cavity (S = 3.8 x 3.8 cm^2) produces a displacement of 10° to lower angle as well as an increase of about 150 % whit respect to the homogeneous case. Again, this fact is due to the large contribution of electrons crossing the cavity which are significantly less scattered than those electrons traveling in the homogeneous phantom without air cavity.

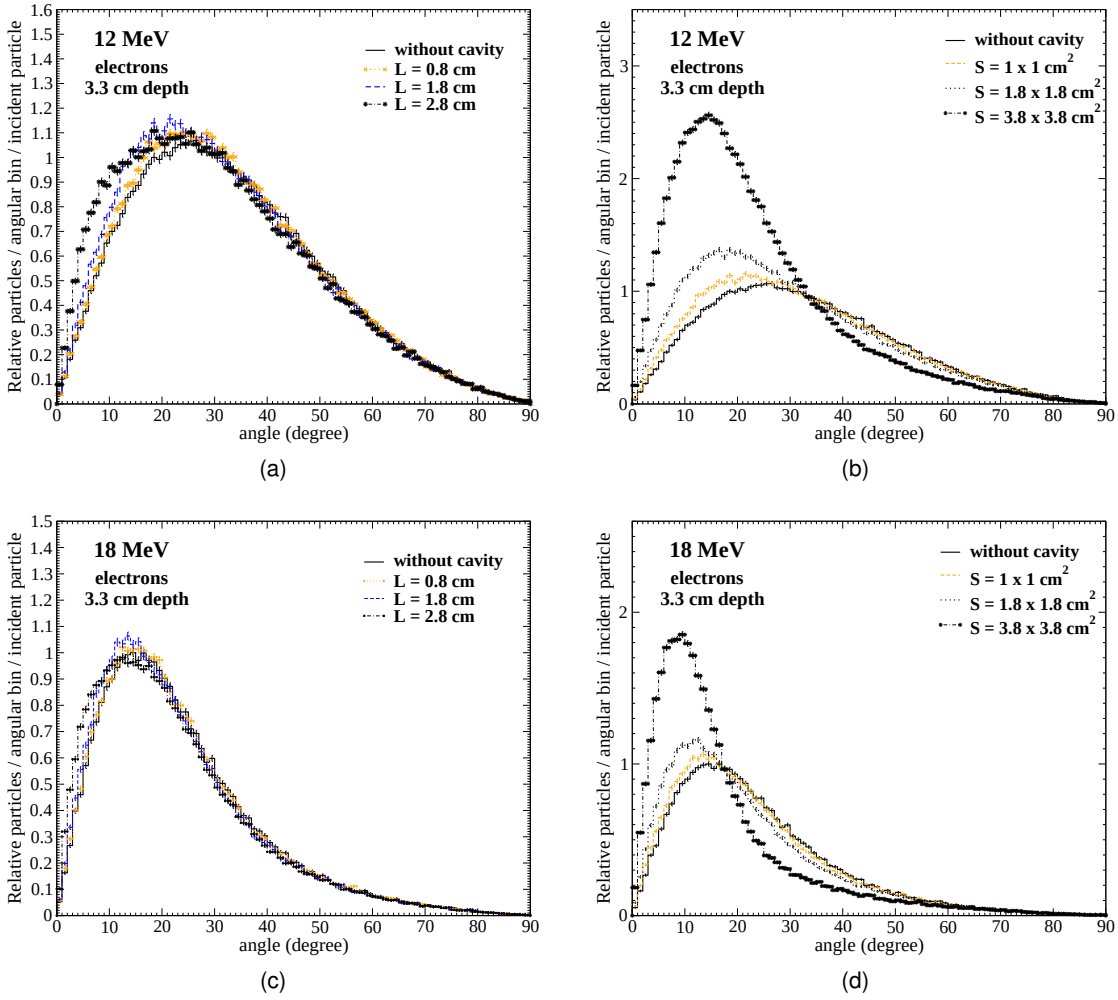

Figure 5.15: Angular spectra of electrons calculated at a depth of 3.3 cm in PMMA homogeneous and heterogeneous phantoms with an air cavity of varying thickness L (a-c) or area S (b-d), irradiated by 12 MeV (top) and 18 MeV (bottom) electron beams. The applicator field was 10 x 10 cm^2 for a SSD of 100 cm. The scoring region has a radius of 2 cm and angle bins 1° wide.

Figures 5.15c and 5.15d present the perturbation of the angular distribution caused by the presence of the air cavity, but for the 18 MeV electron beam. It is seen that there is an increase of electron fluence at lower angles (0-15°) as a cavity is inserted in the phantom. This enhancement is

more pronounced for the cavities of largest thickness (2.8 cm) and area (3.8 x 3.8 cm^2). However, the variation of the angular maximum becomes less accentuated than for the 12 MeV case due to the higher electron range of the 18 MeV beam.

5.3.2 Air cavity effect for fields shaped by Cerrobend blocks

This section evaluates the dosimetric effect caused by the presence of an air cavity for electron beams shaped using a cerrobend block.

Figures 5.16 present the comparison of MC calculated PDD curves in a PMMA homogeneous and two different heterogeneous phantoms for an electron beam of 12 MeV shaped by a cerrobend block.

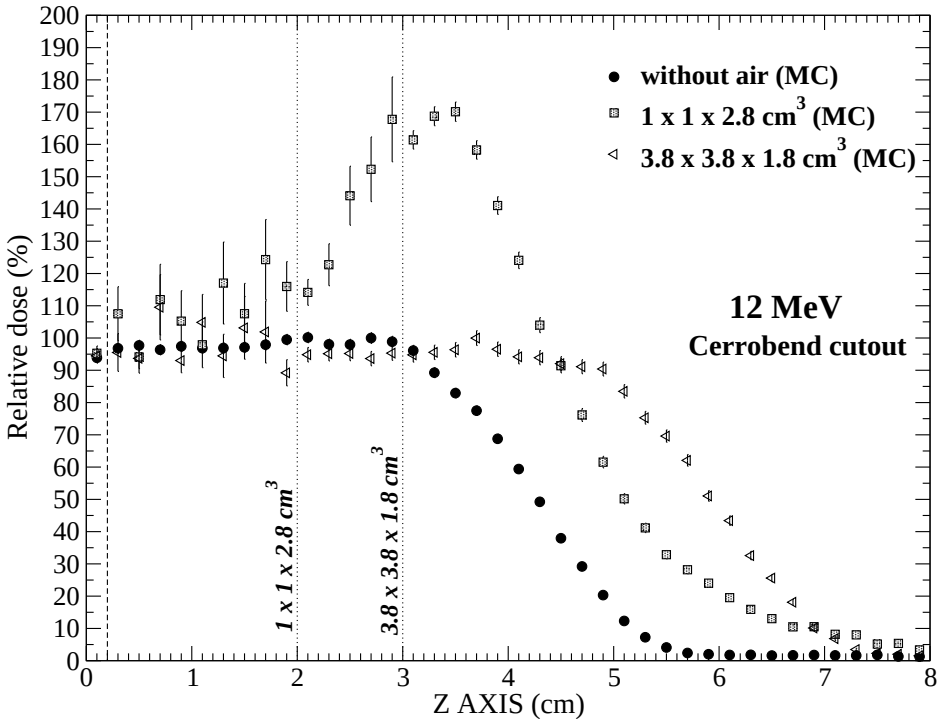

(a)

Figure 5.16: MC calculated PDD curves in heterogeneous phantoms containing an air cavity of 1 x 1 x 2.8 cm^3 (square) and 3.8 x 3.8 x 1.8 cm^3 (triangle) and irradiated with an electron beam of 12 MeV collimated using a cerrobend cutout. The curves were plotted along the central axis of the cavities, i.e. at x = -5.0 cm and y = -5.0 cm. The vertical lines show the edges along the Z axis limited by the corresponding cavity. The PDD calculated in an homogeneous phantom is also illustrated (circles). PDD curves were normalized to the maximum dose value calculated in the homogeneous phantom (labeled as "*without air*").

The heterogeneous phantoms used in this part of the study contained an air cavity of 1 x 1 x 2.8 cm^3 and 3.8 x 3.8 x 1.8 cm^3. The position of the cavities were set to x = -5.0 and y = -5.0 cm,

corresponding to a field region of maximum dose. PDD curves were normalized to the depth of maximum dose obtained for the homogeneous phantom, i.e. at 2.7 cm.

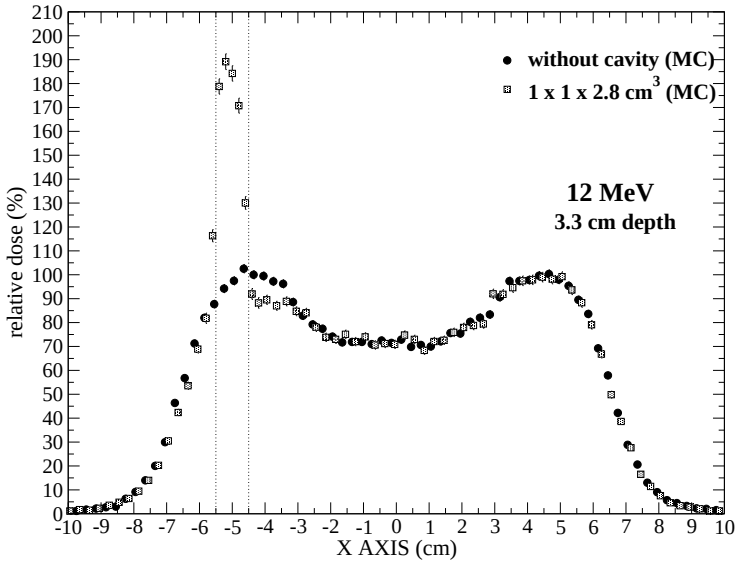

(a)

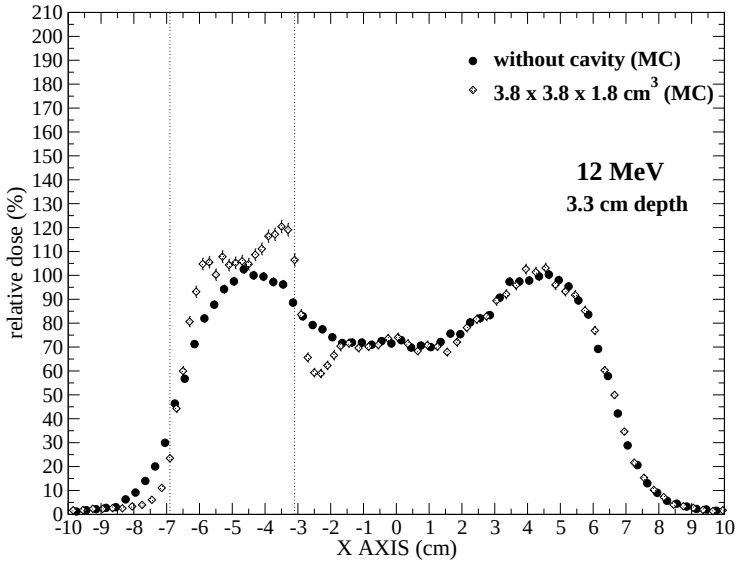

(b)

Figure 5.17: MC calculated dose profiles across the X axis in heterogeneous phantoms containing an air cavity of (a) 1 x 1 x 2.8 cm^3 and (b) 3.8 x 3.8 x 1.8 cm^3 and irradiated with an electron beam of 12 MeV shaped using a cerrobend cutout. The cavity surface was 2 mm below the phantom surface and the position of the cavity were in the upper left region of the field (see figure 5.2).The profiles were plotted at y = -5.0 cm and a depth of 3.3 cm. The vertical dashed lines show the region containing the air cavity. The dose profiles calculated in homogeneous phantoms are also illustrated (circle). The normalization of the profiles was at the maximum dose in the homogeneous phantom (at x = - 5.25 cm).

As it is observed from this figure, the presence of the cavity caused a similar effect on the PDD

curve as those observed previously for a 10 x 10 cm^2 field. In particular, the maximum dose value increased up to 70 % due to the presence of an air cavity of 1 x 1 x 2.8 cm^3.

At the same time, the position of the maximum dose was shifted towards ($\sim$ 0.6 cm) with respect to the maximum dose for the homogeneous case. For the cavity of 3.8 x 3.8 x 1.8 cm^3, the maximum dose did not increase significantly, however, the position of this value changed from 2.7 cm to about 4 cm.

Figures 5.17 show the comparison of MC calculated lateral profiles (X axis) for both homogeneous and heterogeneous phantoms irradiated by the electron beam using a cerrobend block. The profiles were plotted crossing the center of the cavities (y = -5.0 cm) at a depth of 3.3 cm from the phantom surface. The normalization of the profiles was at the maximum dose in the homogeneous phantom (at x = - 5.25 cm).

For the cavity of 1 x 1 x 2.8 cm^3 (figure 5.17a), it is observed a unique sharp peak at the position corresponding with the center of the cavity. This peak represents an increase of about 90 % of the dose compared to the dose value for the homogeneous phantom at the same position (x = -5.0 cm). For this cavity, a decrease of about 10 % is observed at the right side outside the cavity edge, around x = - 4.0 cm. From figure 5.17b, it is clearly seen that a two dose peaks appear on the dose distribution near the lateral region inside the cavity. The magnitude of this peak is about 70 % smaller than the peak observed for the previous case (figure 5.17a). A dose decrease of about 20 % relative to the dose value for the homogeneous phantom is observed at the right region of the cavity edge (x $\sim$ -2.5 cm). This decrease is less pronounced (about 10 %) at the left region of the cavity (x $>$ -6.9 cm). It is therefore important to point out that the dose peak and dip located close to the cavity edge at -3.1 cm was found higher than those located at the other edge at -6.9 cm. This is probably caused by the asymmetry of the field present in the region where the cavity was located.

Overall, the results observed using cerrobend cutouts for the collimation are consistent with the behavior previously observed for the 10 x 10 cm^2 field.

5.4 Conclusions

Experimental measurements and Monte Carlo simulations were used to evaluate systematically the dosimetric effect of a shallow air cavity embedded in a PMMA phantom as irradiated by electron beams of 12 and 18 MeV.

The influence of this effect as a function of the cavity geometry and beam energy was specifically investigated using both methods. Additional MC simulations using a cerrobend block for the collimation of a 12 MeV beam was also carried out in order to asses similar influence under this specific field.

Significant dose enhancements up to 70 % were observed at depths below the cavities for both beam energies and a 10 x 10 cm^2 field with respect to the homogeneous phantom. In addition to this dose perturbation, there was a shift on the depth-dose curve to larger depths which depends on the cavity geometry. In particular, our results using the 10 x 10 cm^2 field indicate that the variation and shift caused by the presence of the inhomogeneity were more pronounced for lower electron energy (12 MeV), larger cavity thickness and smaller cavity area.

On the other hand, the shape of dose transversal profiles changes dramatically due to the presence of the air cavity. In comparison to the homogeneous profile obtained for the phantom without air cavity, two small dips and peaks (about 10 - 20 %) for heterogeneous phantoms appear on the dose distributions near the lateral edge of the cavity.

Analysis of electron energy spectra showed also that the magnitude of the air cavity effect depend on the above parameters and confirmed the observed perturbation on the dose distributions.

The agreement between the Monte Carlo calculations and EBT film measurements performed for the 10 x 10 cm^2 field was about 2 % for the depth-dose curves and off-axis profiles except for the 18 MeV electron beam where differences in depth-dose curves were up to 6 % for some heterogeneous phantoms.

The influence of the air cavity on dose distributions calculated using cerrobend fields showed a similar behavior as that observed for the field of 10 x 10 cm^2. The cavity caused an increase of the maximum dose and a shift of the PDD curve relative to the homogeneous phantom. On the other hand, characteristic peak and dip were also observed on the lateral dose profiles due to the electron disequilibrium caused by the air inserted in the PMMA phantom. In particular, a sharp increase of the dose (about 90 %) in the central region inside the cavity edge is observed for the cavity of large thickness (1 x 1 x 2.8 cm^2) relative to the profile for the homogeneous phantom. For a cavity with large area (3.8 x 3.8 x 3.8 cm^2), an increase of about 20 % is found in the dose values located in the inner side close to the cavity edge. Additionally, a decrease of about 20 % in the dose values at the outer side close to the cavity edge is also observed for this cavity.

In conclusion, the perturbations in the dose presented in this work due to the presence of shallow

cavities, should alert radiophysicists, using treatment planning based on pencil beam algorithm, for cases of head and neck and others treated with electron beams, that underestimation and overestimation of the dose is expectable. Monte Carlo verification as a quality assurance protocol is strongly recommended for these situations.

Part IV

PHOTON BEAM RADIOTHERAPY APPLICATION

Chapter 6

Monte Carlo modeling of a 6 MV Varian 2100C/D medical accelerator

The following chapter is focused on MC modeling of a clinical Varian Clinac 2100C/D accelerator producing a 6 MV photon beam. The detailed description of the basic components of the accelerator is presented in the first section (section 6.1). The accurate determination of the parameters (energy and radius) for the primary electron beam hitting on target is described in the section 6.2. This latter section presents also the validation of the accuracy of the accelerator model by comparing simulated depth-dose and lateral dose profiles against experimental data. Finally, the characterization of the produced beam through the evaluation of typical spectral distributions is shown in the last section 6.3.

6.1 Linear accelerator model

The modeling of a linear accelerator has been an important research topic over the last years. The knowledge of the clinical photon beam characteristics has shown to be an important prerequisite for high accuracy dose calculation planning of any radiotherapy treatment. Detailed information including the energy, angular and spatial distributions of the particles forming part of the beam (photons and electron contamination) are very important for its characterization, because any variation of these distributions is reflected by a change in the subsequent dose distributions obtained in the patient [Mor99]. Additionally, the knowledge of this spectral information can also improve the radio-

therapy treatment planning and contribute to the development of new accurate treatment planning systems.

Several experimental investigations to obtain photon energy spectra has been reported [Lev76, Hua83, Dea96, Jal06, Jus08]. However, the high intensity photon beams used for therapeutic purposes makes the direct measurement of energy spectra very difficult, as consequence, for example, of the saturation of the detector under so high intensive radiation field. To overcome this limitations, some methods based on the reconstruction from measured beam transmission data or the spectroscopy of Compton scattered photons have been described in the literature [Jal06, Jus08]. However, the results of these studies are not entirely reliable.

Alternatively, one additional approach, adopted extensively during the last years to characterize clinical photon beams, has been to perform a full MC simulation through the linac head. After the modeling, it is also required to perform a fit of some critical parameters of the component modules (e.g. dimensions, materials and densities of the bremsstrahlung target and flattening filter) and incident electron beam until a sufficiently good match with the experimental data is obtained. The construction of a complete model of a linac head is not an easy task because of its complexity and the necessity of a detailed modeling approach to obtain accurate dose calculation. Although the process of the simulation is quite time consuming and involves some trial and errors, the effort is worthwhile because, once the MC simulation is validated, it will provide the most accurate prediction of dose, particularly in situations which have material inhomogeneity and irregular geometry, such as patients.

In addition to this, MC simulations can be also used to obtain angular and energy distributions or even other quantities which can not be measured experimentally. Moreover, the spectrum can be generated, not only for the primary photons of the beam, but also for the scattered photons and electrons produced by the interactions of the photons with the different components of the treatment head. The evaluation of the scatter contribution from each part of the linac is essential to asses the beam spectral quality, especially in the case of complex radiotherapy techniques as Intensity Modulated Radiotherapy (IMRT), where the addition of new dynamic devices for the conformation and modulation of the beam (e.g. multileaf collimators) can introduce changes in the characteristics of the incident photon beams.

With the most recent improvements in computer technology, MC simulations have shown to be a suitable approach for modeling realistic photon and electron beams from medical linear accelerators

and, currently, the MC method is recognized as the most accurate method of modeling radiotherapy beams.

The modeling of external radiotherapy photon beams using Monte Carlo technique has been extensively reported in detail in the literature for the last years. A detailed review was published by Verhaegen and Seuntjens [Ver03].

The accuracy of the simulations depends heavily on an appropriate selection of certain parameters regarding the geometry or composition of the linac components and the parameters defining the radiation source. Only in a very few occasions the linac user can be provided with a very detailed description of the geometry of the linac head and even of the parameters of the initial electron beam exiting the accelerator (energy spectrum and radial distributions). Even when all the specifications of the geometry and initial electron beam are known, this information may be subject to user misinterpretations or they may not document the most updated geometry version of the accelerator. For this reason, it becomes essential to simulate each specific accelerator head implemented at each particular department, validating subsequently the accuracy of the proposed model against experimental data.

A large number of MC studies modeling the clinical treatment heads produced by the three major manufacturers (Varian, Elekta and Siemens) have been carried out [Deng99, She02a, She02b, Ding06, Pena07, Van03]. Some of these works [Deng99, She02b, Ding06] were focused on the characterization of the produced beam, evaluating a set of spectral distributions for different energies of the beam. Other studies [She02a, Pena07] were aimed to analyze the sensitivity of the MC simulations to the characteristics of the electron beam incident on the target (energy and radius), as well as, to other treatment head parameters (flattening filter and primary collimator characteristics).

Even though some of previous works were performed using the same accelerator head as considered for this dissertation, the differences reported between these works in terms of, for example, energy and radius of primary electron beam, lead to the necessity of modeling explicitly the geometry of our specific linac as well as the explicit determination of parameters for our particular primary electron beam. As stated above, an accurate beam model of the accelerator will allow us to guarantee an accurate dose calculation within the patient in the subsequent phase of the work where MC simulations of IMRT treatment plans are performed (chapter 9).

Description of Monte Carlo model of treatment head

The linear accelerator Varian Clinac 2100C/D (Varian Medical Systems, Palo Alto, CA) installed at the *Centro Oncológico Dra. Natália Chaves* in *Carnaxide (Lisbon)* was accurately modeled by using the Monte Carlo EGSnrc code for the photon mode with an energy of 6 MV.

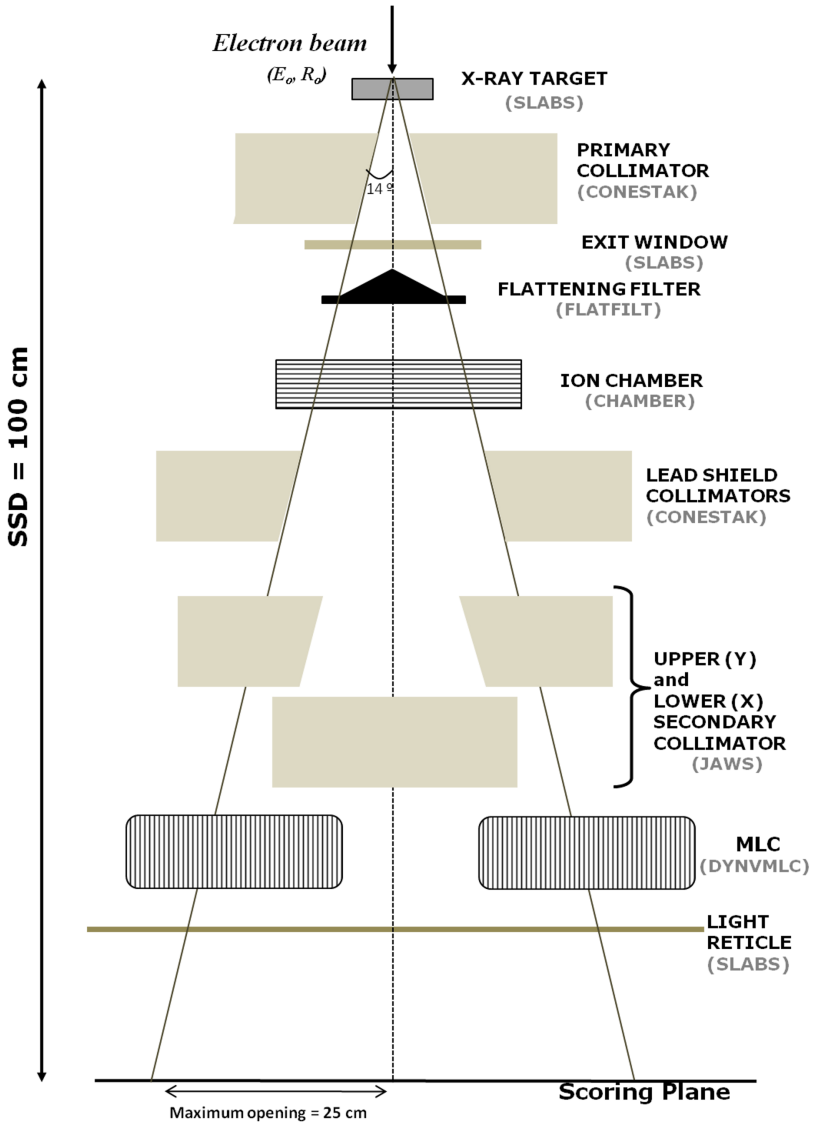

Figure 6.1: Schematic drawing of Varian 2100C/D linac components modeled in Monte Carlo simulations (figure not to scale). The names of each CM used in the BEAMnrc code for the linac modeling are indicated in gray.

In particular, the geometries of the accelerator's components were defined in the software package BEAMnrc [Rog05] through the design philosophy of this code, i.e. the use of components modules (CMs). As it has been already mentioned in chapter 4, these CMs operate completely independently of the other component models and are located perpendicular to the beam axis. An overview of the complete Varian Clinac 2100C/D head producing the 6 MV photon beam is displayed in figure 6.1. The figure includes also the name of the CMs used in the BEAMnrc code for the modeling.

Specifically, the CMs used in the present study were: *SLABS* for the bremsstrahlung target, *CONESTAK* for the primary collimator, *SLABS* for the exit window, *FLATFILT* for the flattening filter, *CHAMBER* for the monitor ionization chamber, *JAWS* for the movable secondary collimators (X1, X2, Y1 and Y2), *DYNVMLC* for the MLC and finally, *SLABS* for the light reticle and the air gap between the reticle and the phantom surface located at SSD = 100 cm.

For each CM, the physical dimensions and material involved are set to match the specific components given by the manufacturer's specifications. In our specific case, the information given by the manufactures just included a scheme of the accelerator, without including each specific geometrical detail of the component of the linac, except for the multileaf collimator for which the specifications included all the details. In order to overcome this drawback, all the details considered in our specific model and regarding to the geometry (dimensions, material and density) of each specific component were set using the information of previously modeled Varian 2100C/D accelerator by [Mor01] for a 4 MV photon beam. Small adjustments of this model had however to be performed for the bremsstrahlung target and flattening filter, since the energy considered for the present studied (6 MV) do not correspond with the previous case and the characteristics of both components change with the energy of the photon beam. As it is further discussed, the accuracy of the proposed model is validated against measurements.

The *target* for the 6 MV photon beam consisted on two slabs: a first thin slab (around 1 mm) of tungsten followed by a thicker slab of copper (figure 6.2a). As discussed in section 3.1, the tungsten is responsible for the larger fraction of produced bremsstrahlung photons, whereas the copper works just as a cooling system of the tungsten, reducing also the production of secondary electrons.

To analyze the characteristics of the bremsstrahlung photon beam produced by this particular target, an additional simulation of an parallel electron beam of 6.0 MeV and 1 mm radius hitting on the top surface of the target (z = 0.0 cm) was performed using BEAMnrc. No additional CM

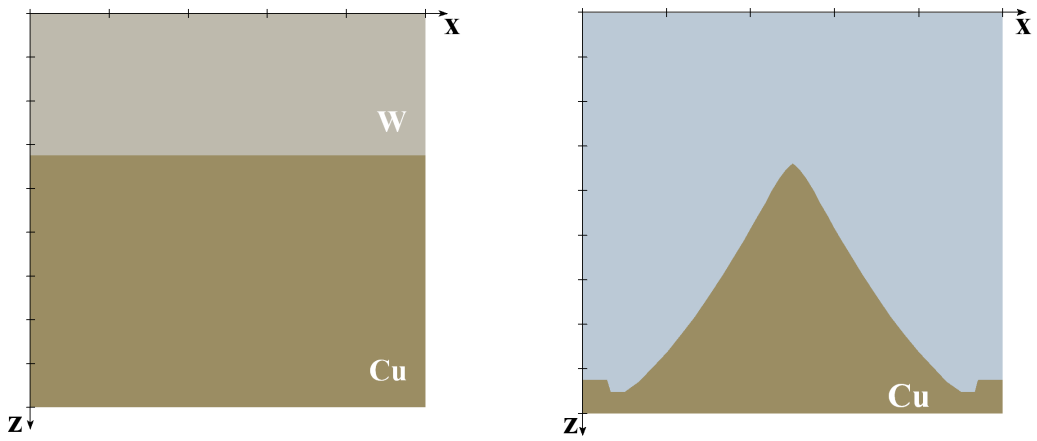

(a) (b)

Figure 6.2: Schematic draw of (a) bremsstrahlung target of W/Cu and (b) flattening filter geometry inserted in the Varian 2100C/D accelerator for 6 MV photon beam.

was incorporated for this particular simulation. The energy cut-off ECUT and PCUT were set to 0.7 MeV and 0.01 MeV and no variance reduction techniques were used. The characteristics of the particles (energy, position, angle, etc.) generated by the interactions on the target were scored immediately below the target (z = 0.246 cm). It is important to point out here that the use of a parallel and monoenergetic electron beam is a good approximation. As it will further discussed, there are several works reporting weak sensitivity of the dose distributions on the energy and radial distributions of the beam [She02a, Jut05].

Figures 6.3b and 6.3a present the characteristic distributions of the bremsstrahlung photon beam resulting from this simulation; namely, the energy fluence spectra and the fluence distribution as function of the distance to the beam axis. From these figures, it is clear that the resulting photon beam present a strongly forward-peaked distribution. As seen in figure 6.3a, about 50 % of photons leave the target inside a square region of 1 mm half-width. On the other hand, the energy spectra shows a continuous distribution of photons along the energy range from 0 to a highest energy of 6.0 MeV, which is the kinetic energy of electrons incident on target. As it is also shown in these spectra, there exists a very low contribution (4 %) of incident electrons exiting the target with energies ranged from 700 keV (the electron cut-off considered for the simulation) to about 2.5 MeV.

After leaving the target, the photon beam is then collimated with a tungsten collimator, frequently named as *primary collimator*. This collimator is designed with a conical opening of 14° which allows the definition of a field of 50 x 50 cm^2 size projected at 100 cm distance from the top surface of the

target (SSD). The primary collimator is one of the linac components with a potential to influence the beam, as it will be shown in the spectral characterization of the beam in section 6.3. The photon beam after the primary collimator exits the evacuated transport system through a thin window made of beryllium, called exit window.

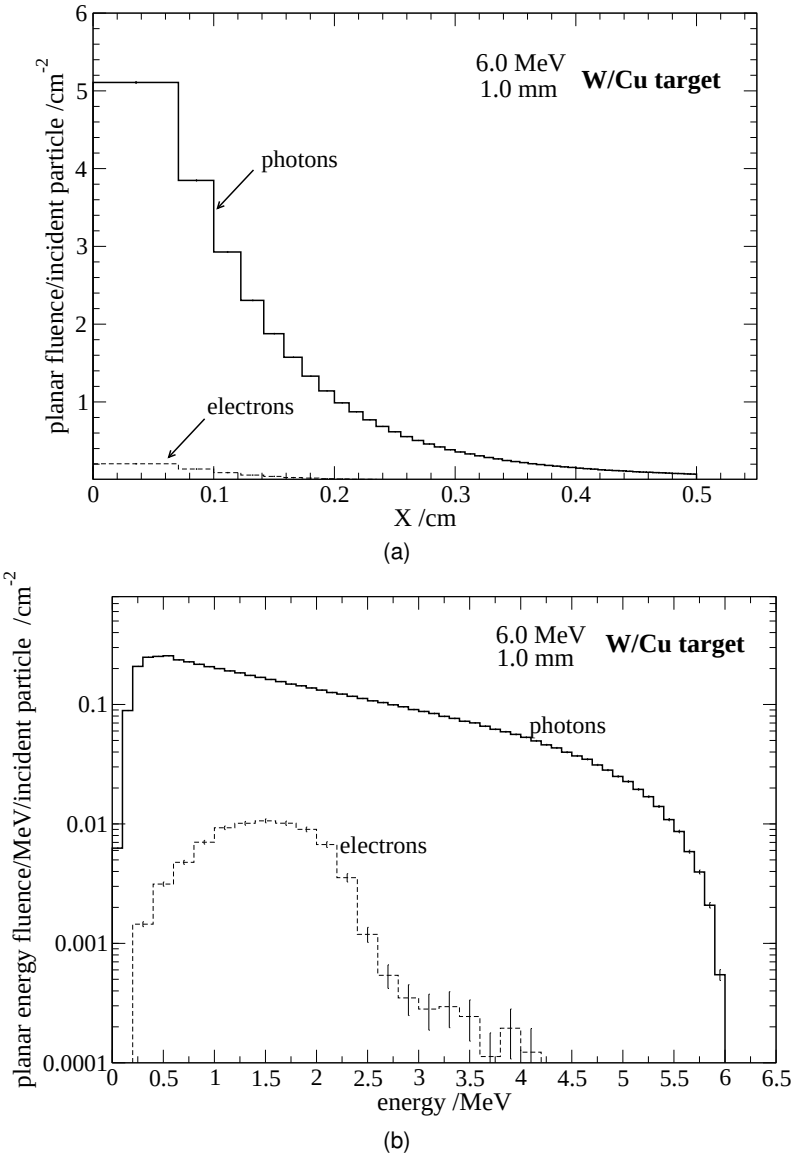

Figure 6.3: Monte Carlo simulated bremsstrahlung spectra from the W/Cu target hit by a 6.0 MeV electron beam: (a) fluences as function of the distance to the beam axis and (b) energy fluence spectra. The electron beam was incident perpendicularly on target with a radius of 1.0 mm. Spectra were scored just below the bottom surface of the target. The fluence spectra is defined in an area of 0.5 cm half-width divided in 50 square bins. The energy spectra was scored in an area of 0.5 cm with energy bins 100 keV wide for photons and 200 keV wide for electrons. The overall statistical uncertainty of photon spectra is within 0.5 % at the maximum energy (E=0.5 MeV), while for electrons is about 4 % due to the lack of electron fluence.

The next component below the target having a high influence on the beam is the *flattening filter* (Figure 6.2). This component is designed as a single cone in order to flatten the fluence of photons emitted from the target with a strong forward-peaked distribution. Duo to this form, the filter tends to attenuates strongly the beam in the central part. For the energy of 6 MV photons, the filter is made out of copper (Z = 29). It removes low energy photons below a few hundred keV through photoelectric effect without changing the spectral shape of the higher energies. As a result of filter shape and material composition, the beam leaving the filter shows a flat shape across the field with a significant spectral hardening due to the removed low-energy photons.

After the flattening filter, the beam traverses the *monitor ionization chamber*. The chamber is made out of a layer of kapton and copper alternated with air. As stated before in chapter 3.1, the function of this chamber is mainly to monitor the dose output, symmetry and flatness of the beam.

Two fixed collimation systems are mounted below the monitor chamber to prevent scatter radiation coming from other parts of the linac (*shield collimator*). These systems are made from tungsten and lead and they are designed with the same conical opening as the primary collimator in order to avoid the contribution to the beam of additional scattered photons or electrons.

Secondary beam collimation occurs on the flattened beam using a paired set of tungsten blocks, usually known as *jaws*. In particular, the Clinac 2100C/D contains 2 sets of parallel opposed JAWS capable of collimating the beam into rectangular fields in X and Y direction with a maximum size of 40 x 40 cm^2 projected at a distance of 100 cm from the target. It is important to point out that these collimator systems play an important role as a source of scatter or particle generation to the primary beam, as it will be evaluated later in section 6.3. Other particular aspect of the jaws collimator is the influence on the signal of the monitor chamber, especially for small fields where a high number of backscattered particles from the collimators occurs [Ver00, Liu00].

The last important linac component included in our model is the *multileaf collimator* (MLC). This device consists of a set of movable leaves of tungsten which allow to create irregular field shapes. Contrary to the jaws, the backscatter from MLC is negligible at the level of the monitor chamber due to the large distance of the MLC to the monitor chamber [Ver00]. However, the influence on the final beam through the production of scattered photons and electron contamination can be significant in some cases as it will be later evaluated in chapter 7. The detailed evaluation of this linac component is essential for this work, since its characteristics (geometrical and dosimetric) have a large influence on the dose distributions and it may therefore affect the accuracy of the dose calculations of complex

cases of IMRT treatments. Further details about the MLC modeling are presented in the next chapter 7.

Finally, a thin slab of mylar is located below the MLC (z = 55.5 cm). This slab is used as a reticle of the light field to adjust the radiation isocenter for a given field. After the reticle, the air column between the reticle and the phantom surface is placed. The thickness of this air column will depend on the SSD considered for each particular field. In this chapter, the air column was added to the BEAMnrc simulations using a SLAB CM. In addition to this final air gap, the simulation of the entire treatment includes also the air columns between the considered CMs of the linac model.

6.2 Determination of primary electron beam parameters

As it was discussed above, accurate modeling of the accelerator head is essential in the calculation of dose distributions for radiotherapy. One of the factors influencing the MC modeling of a linear accelerator is the information about some particular components incorporated in the treatment head (dimension, material and density). Several authors [She02a] have pointed out that small changes in the primary collimator upstream opening, as well as the flattening filter material and density can alter significantly the simulations results. As an example, the use of copper (Cu) instead of tungsten (W) in the flattening filter for a 15 MV photon beam can reduced the in-air off-axis ratios (a ratio of dose-to-air at a certain lateral distance to the dose-to-air on the central axis) up to 50 %. Although the MC calculated results have shown to be sensitive to some geometrical details of the linac, these details are mostly supplied by the manufacturers.

In general, the less known parameters are the properties of the radiation source, i.e. energy and radius of the electron beam incident on the target. Manufactures usually specify the nominal energy of the electron beam, but, in most of the cases, this nominal value can only be taken as a first estimate and it must be adjusted in the simulations [She02a, Pena07]. Regarding the electron beam radius, most manufactures do not provide an accurate description of this parameter. As it was described by Sheikh-Bagheri and Rogers [She02a], these parameters can have a high influence on the MC dose distributions and their determination is thus crucial for an accurate model of the linac using Monte Carlo methods.

In the following subsections it will be checked the accuracy of the above modeled linac thought the comparison of calculated dose distributions (depth dose curves and transversal profiles) with ex-

perimental measurements. At the same time, this comparison will allow us to define the energy and radius of the incident electron beam which provided the best agreement between MC calculations and measurements.

Monte Carlo simulations

As previously mentioned, the primary radiation source to produce a photon beam by a medical linac is an electron beam impinging on a bremsstrahlung target. The exact characteristic of this primary electron beam (i.e. energy and radius) are rarely known and they are very difficult to be determined experimentally. However, the determination of these parameters is critical to the future development of an accurate MC calculation.

Sheikh-Bagheri and Rogers [She02a] studied the sensitivity of photon beam simulations to the initial electron fluence parameters. Their study concluded that the mean energy and radial intensity distribution of the incident electron beam were the two most important parameters for simulating photon radiotherapy beams. On the one hand, they found that the electron beam radial intensity distribution had influence on the off-axis ratios to a great extent; the greater the width of the electron-beam radial intensity distribution, the more intense is the photon beam on the central axis. The calculated profiles are observed to be quite sensitive to the electron energy. On the other hand, the central axis depth dose curves are also strongly influenced by the electron energy. However, the central-axis depth-dose curves are quite insensitive to variation in the radial intensity distribution of the electron beam striking the target, because the dose along the central axis is deposited primarily by particles in the vicinity of the central axis.

In the present thesis, the energy of the electrons (E_i) and the radius of beam spot (R_i) was determined using an iterative process based on the observations of previous work [She02a]. A brief description of the procedure is represented by the flowchart in figure 6.4. Further details are given next.

In this process, the MC simulations involved two stages:

1. The simulation of the linear accelerator head using the BEAMnrc code
2. The dose calculation in the homogenous water phantom using the DOSXYZnrc code.

For the first stage, the full accelerator head was simulated in one unique step, i.e. particles traveling by the accelerator head and interacting with all the different accelerator's components were

simulated until they reached the phase-space plane located at 100 cm from the target. For this specific case, the MLC was omitted during these simulations and only the JAWS collimators were used as beam modifiers.

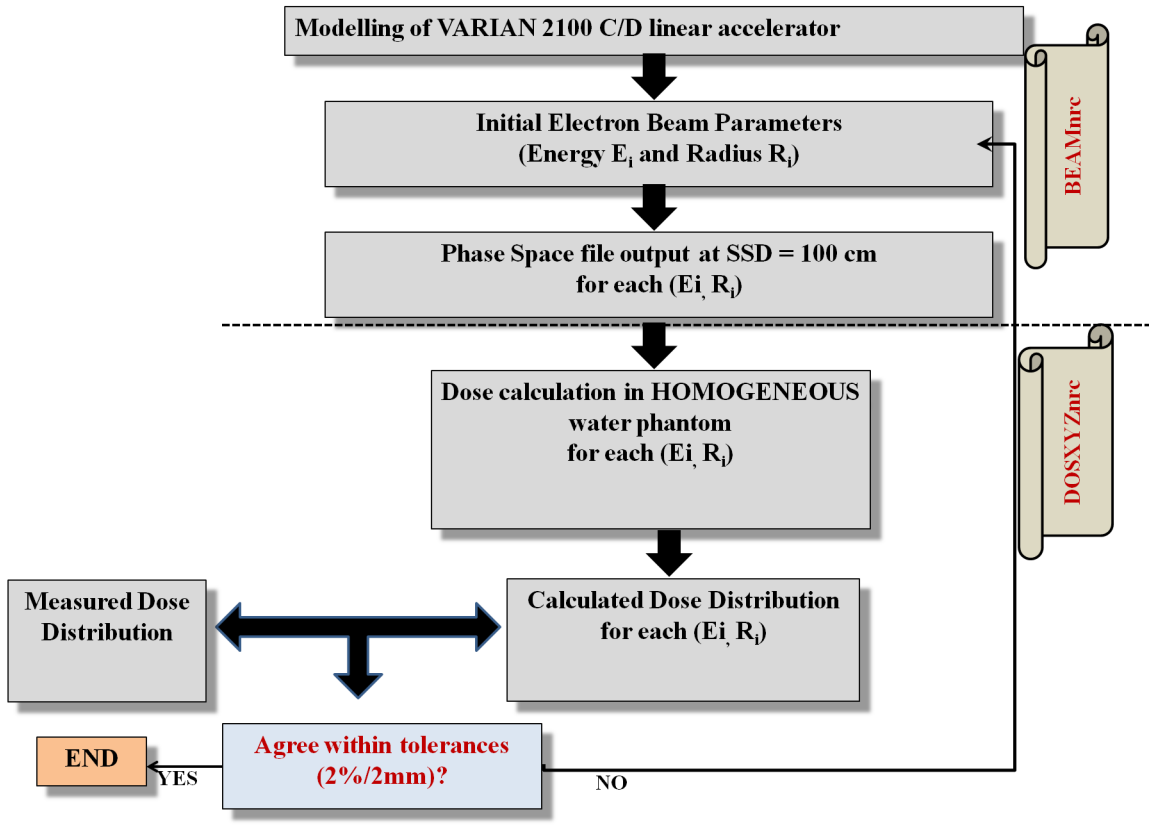

Figure 6.4: Flowchart of the procedure to find the accurate description of the incident electron beam at the target, namely electron energy E_i and radius R_i.

The electron beam hitting the target was assumed to be parallel and monoenergetic. For this purpose, the ISOURCE = 0 source type available in the BEAMnrc code was used. The electron beam energies and radius considered in the selection process are summarized in table 6.1.

Table 6.1: Energies and radius combinations considered for the electron beam incident on the bremsstrahlung target. The electron beam was assumed to be parallel (ISOURCE = 0) and monoenergetic.

Nominal potential (MV)	e^- beam **ENERGY** (MeV)	e^- beam **RADIUS** (mm)
6	6.0, 6.2, 6.4	1.0, 1.5

In general, the actual shape and spectra of the incident electron beam are rarely known. In a previous work [She00], it was experimentally observed that the radial distribution of the electron beam has an irregular and Gaussian shape with an given FWHM (Full Width at Half Maximum). However, the results reported by [Jut05] shows that the use of an uniform circular distribution instead of a Gaussian distribution did not affect the final transversal dose profiles. According this study, only the size of the radius and the FWHM affect the final dose output. Based on this, a circular and uniform beam was simulated for simplicity.

On the other hand, the assumption of a monoenergetic beam is a good initial approximation. According to previous work [She02a], the energy distribution of the electron beam shows a weak influence (1 %) on the relative depth dose curves.

Linac simulations were carried out for a variety of field sizes: 4 x 4, 10 x 10, 20 x 20 and 30 x 30 cm^2 at SSD = 100 cm. A total of 10^9 electron histories were simulated for the three first fields (4 x 4, 10 x 10 and 20 x 20 cm^2), whereas for the 30 x 30 cm^2 field, a smaller number of electron histories (5 x 10^8) was considered. The number of particles collected at the scoring plane (SSD = 100 cm) varies from ~3.44 x 10^6 for the smaller field size to ~2.20 x 10^8 for the larger field. For both field sizes, the photons represent about 99.98 % of the total number of particles reaching the scoring plane, whilst the remaining particles are electrons and positrons. The average time required for these simulations was about 31 - 32 hrs in a single 2.2 Ghz processor, being longer for the simulation of the largest field (30 x 30 cm^2) as it can be seen in table 6.2. The typical size of each phase-space file generated for the same number of primary electron histories hitting on the target ranges from about 0.1 to 7.5 Gbytes as the field size increases from the smallest to the largest one.

Table 6.2: Summary of the number of particles scored in the phase space file and the CPU time used for the BEAMnrc simulations of the linac for various field sizes using an electron beam of 6.2 MeV and 1.5 mm radius impinging on the bremsstrahlung target. Simulations ran on a single AMD Opteron machine with 2.2 GHz processor. Details about the transport parameters and variance reduction techniques used for these simulations are summarized in table 6.3.

Field size (cm^2)	number of incident e^-	number of particles in phase space file	CPU time (hrs)
4 x 4	5 x 10^8	~3.44 x 10^6	31.77
10 x 10	5 x 10^8	~22.3 x 10^6	31.68
20 x 20	5 x 10^8	~93.5 x 10^6	31.97
30 x 30	5 x 10^8	~220.4 x 10^6	32.94

Dose distributions were calculated with DOSXYZnrc code using a water phantom of dimensions

35 x 35 x 35 cm^3 positioned at 100 cm SSD. For depth-dose calculations, the dose was scored in voxels with dimensions of 0.3 x 0.3 x 0.3 cm^3 along the X, Y and Z direction, respectively. For the lateral profiles, it was considered a resolution of 0.5 x 0.5 x 0.5 cm^3 for all fields, with exception of the 4 x 4 cm^2 field where the voxel size was the same as for depth-dose calculations to increase the resolution inside the field and in the penumbra region. Auxiliary simulations using different voxel sizes along the X and Y axis were performed in order to asses the influence of the dose calculation resolution on the final dose outputs. It was found thus that the choice of voxel size for the lateral profiles allowed to reach a better uncertainty in a lower calculation time without introducing any difference on the dose profiles. The number of simulated histories in these calculations ranged from 8 x 10^7 for the 4 x 4 cm^2 field size to 2 x 10^9 for the 30 x 30 cm^2 field size. For these fields, the typical CPU time on a 2.2 Ghz processor for the dose calculations was about 2 h and 62 h, respectively, with the voxel size set to 0.3 x 0.3 x 0.3 cm^3. The increase of the voxel size reduced the calculation time by a factor of about 1.5.

The relative statistical uncertainties (1σ) for all studied field sizes was within 1% at the depth of maximum dose (D_{max}) for the resolution of 0.3 x 0.3 x 0.3 cm^3, whereas it was reduced to 0.7 % at D_{max} using larger resolution of 0.5 x 0.5 x 0.5 cm^3. For all dose calculations, the particles scored in phase-space files were reused between 10 - 20 times without introducing any bias in the form of spurious peaks along the curves. This was possible due to the low latent variance of the produced phase-space files [Sem01].

In both steps of MC simulations, cut-off energies for transport and production thresholds have been set to ECUT = AE = 700 keV for electrons and PCUT = AP = 10 keV for photons. The maximum fractional energy loss per electron step (ESTEPE) was 0.25 and the electron step algorithm chosen was PRESTA-II.

Two different variance techniques were employed during the linac simulation in order to increase the efficiency of the simulations: uniform bremsstrahlung splitting in conjunction with the Russian Roulette and the electron range rejection [Deng99]. The uniform bremsstrahlung splitting with a splitting factor (NBRSPL) equal to 20 allows generating multiple photons from each bremsstrahlung interaction, with the photon weight being reduced proportionally to NBRSPL. Coupled with uniform bremsstrahlung splitting, the Russian Roulette technique was employed for secondary electrons resulting from split photons, where based on a random process, each secondary electron with a given survival threshold (1/NBRSPL for uniform splitting) is evaluated and it is decided if the electron

Table 6.3: Summary of run parameters and variance reduction techniques for the BEAMnrc and DOSXYZnrc simulations performed for the commission of the 6 MV photon beam from the Varian 2100C/D accelerator.

Electron/Photon transport parameter BEAMnrc and DOSXYZnrc	
ECUT	700 keV
PCUT	10 keV
Electron-step algorithm	PRESTA - II
Maximum fractional energy loss/step (ESTEPE)	0.25
Variance reduction techniques BEAMnrc	
Uniform Bremsstrahlung splitting	NBRSPL = 20
Electron range rejection	ESAVE = 1.0 MeV
Russian Roulette	ON
Photon forcing	OFF

is kept or discarded. Electron range rejection was also used with the ESAVE parameter, which is the energy threshold to turn on the range rejection, set to 1.0 MeV. Thus, any electron below this ESAVE value was estimated to determine wether its range within the CM was short enough to terminate its transport. No variance reduction techniques have been used in the phantom calculations. A summary of transport simulation parameters is presented in table 6.3.

Measurements

Measured data for relative depth dose and lateral profile comparisons were taken using a semiflex ionization chamber (PTW 31001) for the same conditions as the calculated ones. The active volume of this chamber is 0.125 cm^3 and it has an inner diameter of 5.5 mm. The chamber was mounted on a computer controlled scanning system placed in an automatic water tank PTW FREIBURG (model 41006) with a scanning volume of 48.0 x 48.0 x 48.0 cm^3. Central axis depth ionization curves and transversal ionization profiles were acquired using the PTW software Memphysto mcc software. For depth ionization curves the acquisition was made in steps of 0.1 cm up to 2 cm depth and 0.5 cm beyond 2 cm depth. Transversal profiles (X and Y axis) were scored in steps of 0.25 cm in the central (homogeneous) region of field, being reduced to 0.1 cm for the acquisition of dose values in the penumbra and umbra region of the profiles.

As discussed in section 3.2, the absorbed dose measured with an ionization chamber and following the recommendations of the IAEA TRS-398 code of practice [And00] can be derived from the

ionization readout of the chamber corrected by using the calibration factor and several correction factors for different influence quantities (Eq. 3.3 and 3.4). Based on that, the ionization readout obtained for the present measurements were firstly corrected for the influence of changes in ambient temperature and pressure of the air $k_{P,T}$, effects due to the applied chamber polarity k_{pol} and also due to the ion recombination on the chamber k_s. The calibration factor of the electrometer, k_{elec}, was also taken into account.

The correction of the effective point of measurement was considered before the acquisition of the profiles and, therefore, it was included already in the ionization profiles. The effective point of measurement for the chamber PTW 31001 was 2 mm upstream from the chamber center. The additional correction factors regarding the beam quality may be assumed to to be independent of depth according to the protocol and, therefore, they were not considered to convert the relative ionization profiles to dose profiles. Finally, the overall accuracy of the ionization chamber measurements was estimated to be within 2 %.

Determination of initial electron beam parameters

Based on the work of Sheikh-Bagheri and Rogers [She02a], the method for the determination of (E_i,R_i) parameters in this work begins with the determination of the electron energy by observing the agreement of MC calculated relative depth-dose curves with measurements for the largest simulated field size, 30 x 30 cm^2. For this field, the procedure above described for the MC simulations was thus repeated for several combinations of (E_i, R_i) for the incident electron beam (Table 6.1), as it is next described in more detail. This parameters were chosen based on the experience from previous commissioning efforts by other authors [She02a] [Pena07].

The process was first started with the determination of the energy for the primary electron beam. For this purpose, relative central axis depth dose curves measured experimentally were compared with those PDD curves calculated using three different electron energies (table 6.1). In each MC simulation, the electron beam radius was set to 1.0 mm.

Figure 6.5a presents the sensitivity of the PDD curves to the energy of the electron beams. In particular, two on-axis PDD curves calculated using electron energies of 6.0 and 6.4 MeV are shown for a field size of 30 x 30 cm^2.

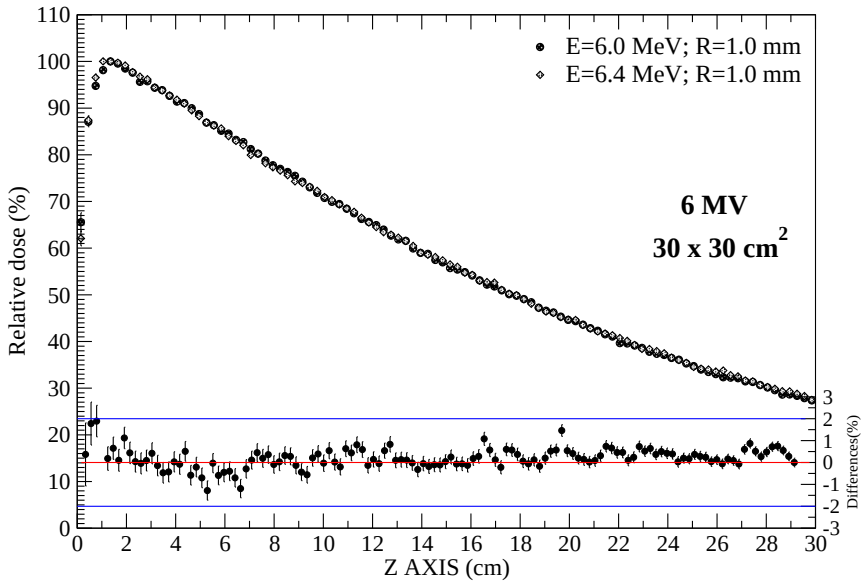

(a)

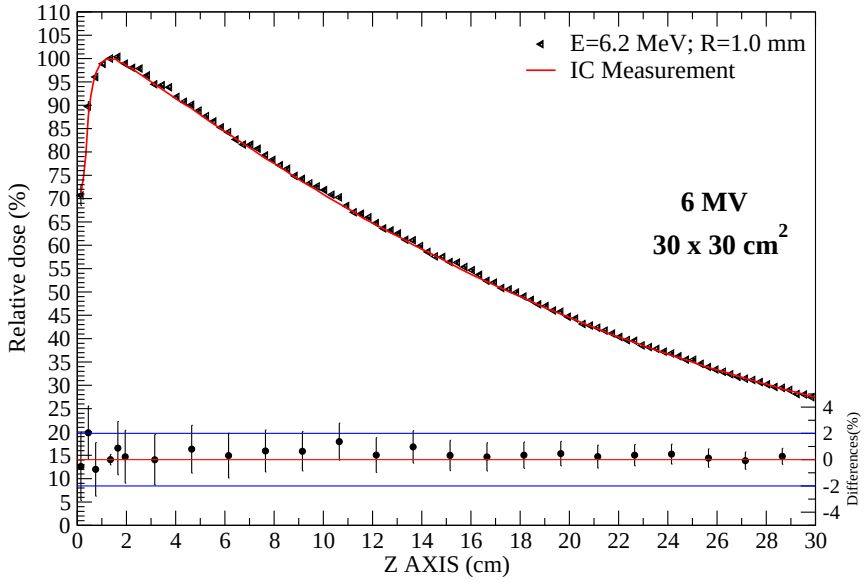

(b)

Figure 6.5: (a) Central PDD curves calculated (dots) using two different energies and fixed radius (R = 1.0 mm) of the primary electron beam incident on the target for a 30 x 30 cm^2 field (SSD = 100 cm); (b) Calculated PDD curve for an energy of 6.2 MeV (R = 1.0 mm) in comparison to the measured PDD (red line). Each curve is normalized to the respective maximum dose, D_{max}. The figures show also the differences between the Monte Carlo PDD curves (a) and the MC and the experimental PDD curves (b). For each dose difference, it is also shown the uncertainty calculated by propagation.

It is important to mention here that the PDD curves were taken in an area of 0.9 x 0.9 cm^2 with a resolution of 0.3 cm in depth, although the voxel size used for the calculations was 0.3 x 0.3 x 0.3 cm^3. Using the option ”rebinning” of the program STATDOSE [McGo07], the size of the bins was

modified along the X and Y axis by a factor of 3. Thus, the values in 3 voxels were added together and averaged in order to calculate the new dose values. In this particular case of an homogeneous field, this option allows to decrease the statistical uncertainty from 1 % to 0.5 % at the maximum dose value (D_{max}) without affecting the dose distribution.

As seen in the figure, the influence of the electron energy on the PDD is more relevant at deeper positions (z > 15 cm), where differences of up to 1.5 % are observed between both curves. Note that all curves were normalized to the value of maximum dose, which is around 1.35 cm for the 6 MV photon beam with a 30 x 30 cm^2 field size.

From the comparison of the experimental and MC calculated PDD curves, it was verified that the PDD calculated for the energy of 6.0 and 6.2 MeV predicted the best agreement (1 %) with the measured PDD beyond the build-up region (i.e. from surface dose to d_{max}), within the statistical uncertainty of MC calculations of 0.5 % at D_{max}. Figure 6.5b shows the comparison of experimental PDD and the calculated PDD obtained considering an energy of 6.2 MeV and radius R = 1.0 mm for the incident electron beam and a field size of 30 x 30 cm^2. The figure only included this PDD curve for a better evaluation of the differences with the measured curve. The final choice of the beam energy was based on the lateral profiles.

According to previous work [She02a], the energy of the electron beam has also a great influence on the lateral profiles. Figure 6.6 presents the sensitivity of Y profiles at 1.5 cm depth calculated using three different values of incident electron beam energy for the field of 30 x 30 cm^2. The change of the energy leads to a variation in the shape of the lateral profiles at distances off the central axis ($y > \pm 8.0 cm$). As seen, the profile at the off-axis positions drops as the energy of the beam is increased; in particular, a decrease of about 4 % is observed when the energy of the electron beam increases from 6.0 MeV to 6.4 MeV. The experimental profile measured at the same conditions as simulated one is also shown in this figure by the continuous red line. By comparing measured with calculated profiles, it is clear that the best matching (1 %) is achieved for an energy of 6.2 MeV.

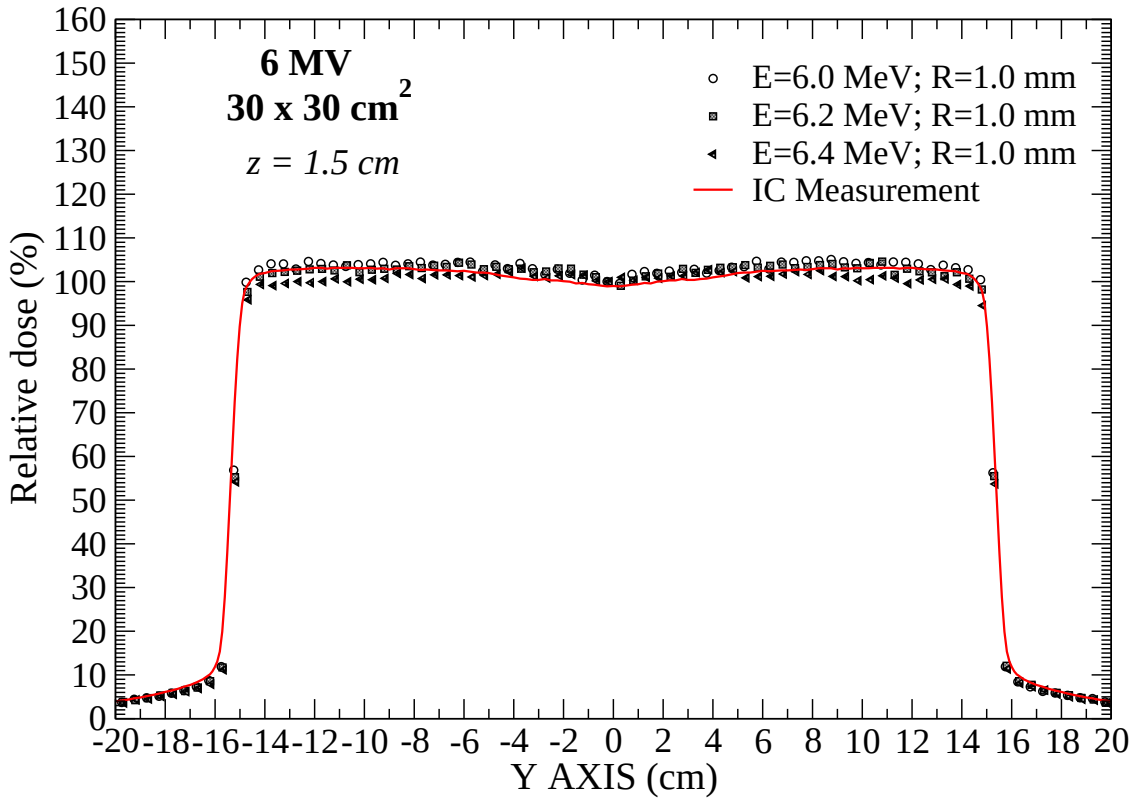

(a)

Figure 6.6: Influence of the electron beam energy on lateral profiles calculated (symbols) for a 30 x 30 cm^2 field (SSD = 100 cm) at 1.5 cm in water phantom using three different energies (6.0, 6.2 and 6.4 MeV) a fixed radius (R = 1 mm) for the primary electron beam incident on the target. The profiles are calculated in a voxel size of 0.5 x 0.5 x 0.5 cm^3 and the statistical uncertainty is within 1 % along the entire field. The continuous line illustrates the measured profiles. All curves are normalized to the on-axis dose value.

Once the electron energy was estimated, the comparison of lateral dose profiles measured experimentally and calculated using two different beam radius (1.0 and 1.5 mm) was used to derive the radius of the electron beam. The best matching (2 % at the central region and 2 mm at the penumbra region) between measured profiles and MC calculated profiles, to within a statistics of 1 %, corresponds to a radius of 1.5 mm as shown in figure 6.7a for a dose profile obtained at d_{max} (1.5 cm) and 5 cm depth for the field size of 30 x 30 cm^2.

All profiles were normalized to the value of central dose at a depth of 1.5 cm. The statistical uncertainty for the MC calculations was less than 2 % for the profiles scored at different depths. The dependence of lateral profiles on the radius of the electron beam was also evaluated through the comparison of calculated profiles for two different radius (6.7a). It can be appreciated that the profiles for different radius do not show a variation across the central part of the field; however, small

differences (about 2 %) are observed at off-axis distances beyond ±6 cm. After comparison of MC calculated and experimental profiles at several depths in the phantom, it is determined that the best agreement (less than 1 %) is found for an electron beam radius of 1.5 mm (6.7b).

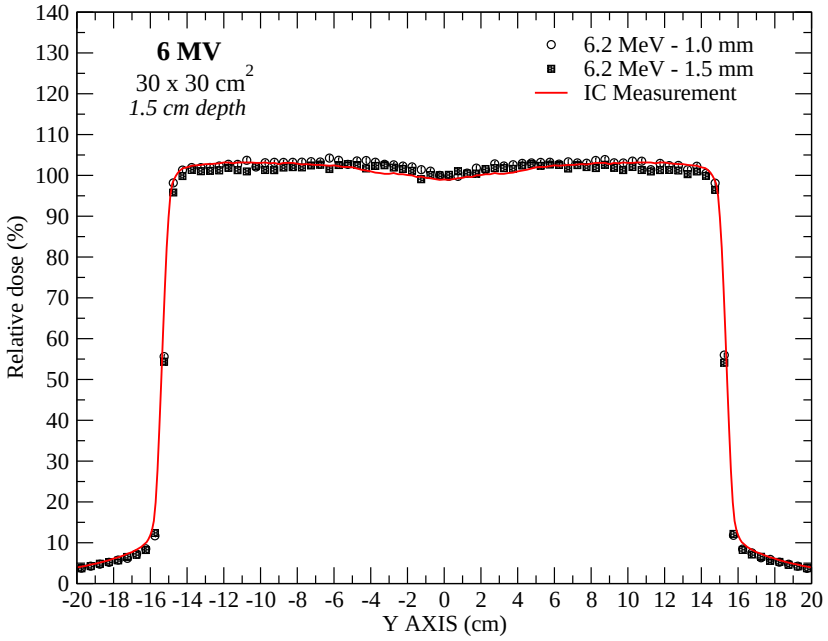

(a)

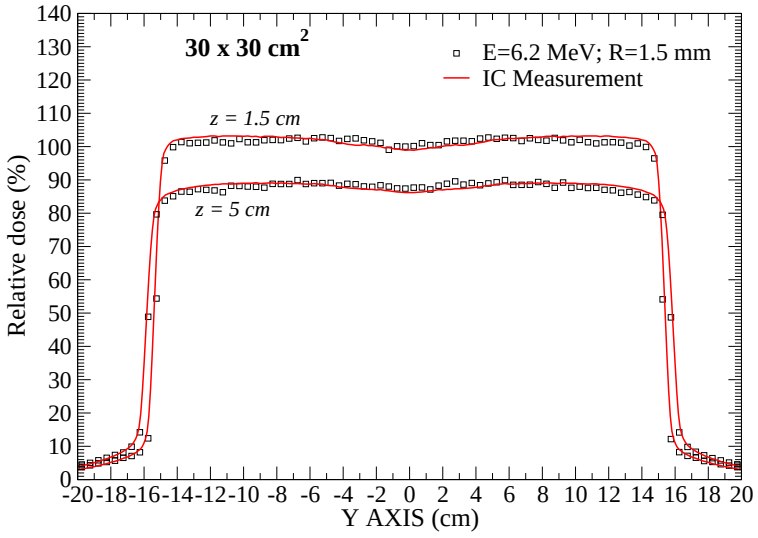

(b)

Figure 6.7: (a) Influence of the electron beam energy on lateral profiles calculated (symbols) at 1.5 cm in water phantom using a fixed energy (E = 6.2 MeV) and two different radius (1.0, 1.5 mm) of the primary electron beam incident at the target for a 30 x 30 cm^2 field (SSD = 100 cm); (b) Calculated (circle) and measured dose profiles (red line) at 1.5 cm and 5.0 cm depths for the final combination of 6.2 MeV and 1.5 mm. All curves are normalized to an on-axis dose value.

After the determination of both parameters defining the initial electron beam, MC calculated depth-dose curves and lateral profiles at several depths were checked against experimental measurements for different field sizes in order to ensure the reproducibility of the accelerator fluences. In particular, simulations for 4 x 4, 10 x 10 and 20 x 20 cm^2 were performed using the previous determined Energy/Radius combination of the initial beam, i.e. 6.2 MeV and 1.5 mm and subsequently compared with the profiles measured using the ionization chamber. The results of this comparison are presented in figure 6.8.

As seen, the agreement between calculated and measured depth-dose curves for all field sizes was within 1 % at depths beyond the depth of maximum dose (d_{max}). In the build-up region, differences up to 4 % are found between calculated and measured dose values. As mentioned in previous sections, the build-up is a region of high electronic disequilibrium where the ionization chamber may not measure correctly. According to some authors [Abdel06], the correction factors applied for the conversion of the measured ionization profiles to absorbed dose profiles can vary significantly in the build-up region and this variation should be therefore taken into consideration. It is important to point out that the depth of maximum dose changed with the field size. For the smallest fields (from 4 x 4 to 10 x 10 cm^2), it was found a maximum depth of 1.5 cm, whereas for the largest field of 20 x 20 and 30 x 30 cm^2 the depth decreased to 1.35 cm. This shift in the maximum depth is attributed to the increase in particle scattering at larger field sizes. As reported by [Met97], the increase in the contribution of the scattered radiation at larger field sizes is observed more strongly at depths beyond the d_{max}, however it is also usually found a slightly shift of the d_{max} to shallower positions when the field size is increased.

MC calculated lateral profiles at 5 and 10 cm depths were also reproduced (within 2 %) well by the experimental measurements when the combination of 6.2 MeV and 1.5 mm for the incident electron beam parameters were considered.

In conclusion, the final incident electron parameters derived from this commission process was **6.2 MeV** electron and **1.5 mm** radius.

Once the electron beam parameters were determined, the phase-space files were analyzed in order to characterize the modeled 6 MV photon beam at the phantom surface. Further detail of the beam characterization analysis is presented next.

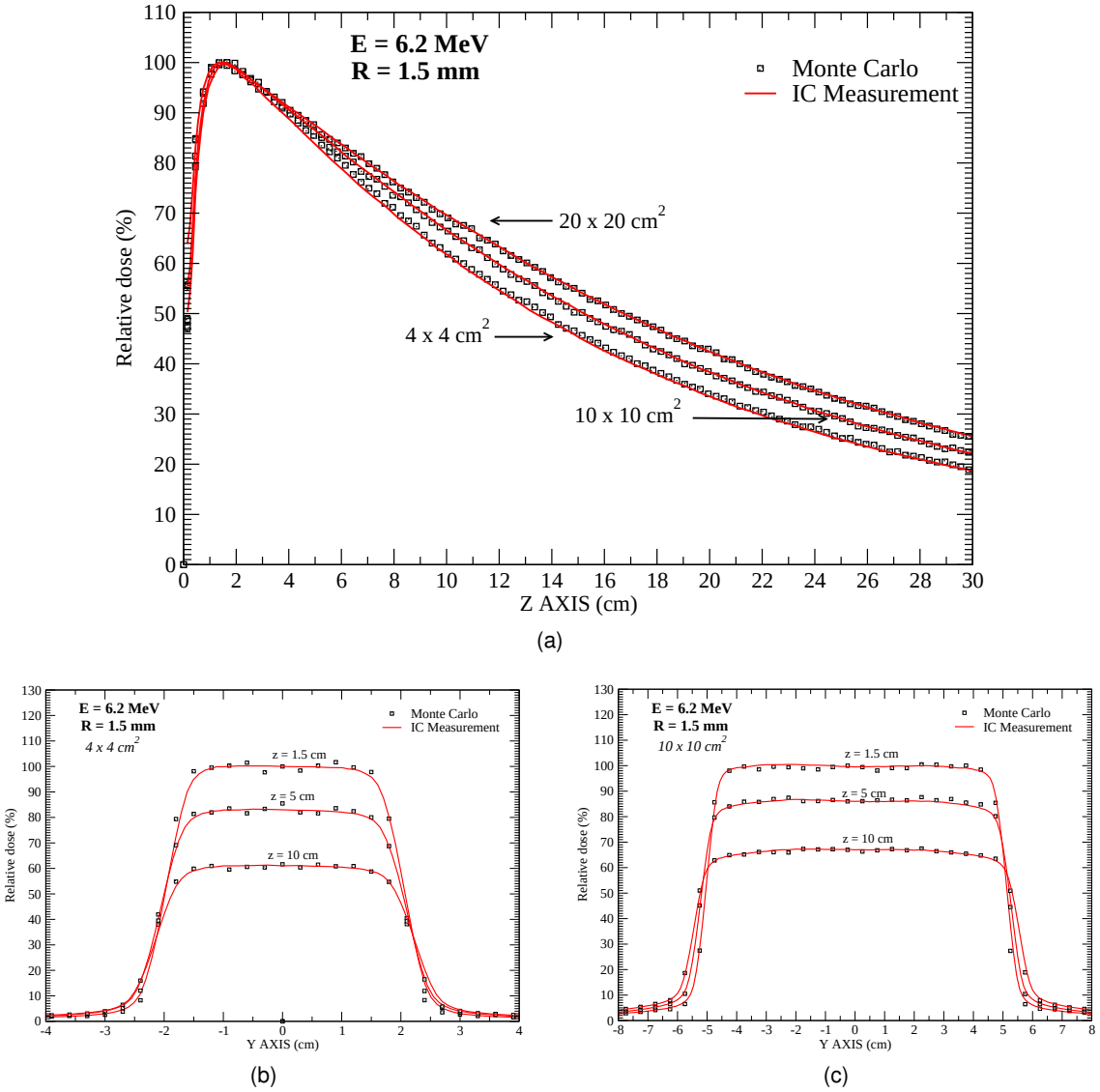

Figure 6.8: Comparison of (a) central PDD curves and (b)-(c) lateral profiles at several depths calculated (symbols) in a water phantom for 4 x 4 cm^2 and 10 x 10 cm^2 fields (SSD = 100 cm). Profiles were obtained using a final combination (E = 6.2 MeV, R = 1.5 mm) for the primary electron beam incident at the target. Measured profiles using the ionization chamber (0.125 cm^3 volume) are also presented (red line).

6.3 Beam spectral characterization at phantom surface

The precise knowledge of the photon energy spectra produced by medical linear accelerators plays an important role in the accuracy of the dose delivered to the patient in all the procedures involved in treatment planning (dose distribution in media, beam quality, beam calibration).

In this section, it will be presented some relevant characteristics of the 6 MV photon beam pro-

duced by the Varian 2100C/D, which was previously benchmarked. Particularly, a variety of photon spectra (energy distribution, fluence profiles, angular distribution, etc.) will be analyzed in detail for the standard field of 10 x 10 cm^2. The influence of the contaminant electrons produced by the interaction of photons with the different linac components will be assessed. Moreover, it will be evaluated the different component of scattered photons contributing to the total photon fluence. In addition to the spectral analysis performed for 10 x 10 cm^2 field, the variation of the energy spectra with field size will be also studied in order to assess the influence of the beam dimension. For this purpose, the energy spectra of different fields (from 4 x 4 cm^2 to 30 x 30 cm^2) will be compared. All the spectra were generated using the phase-space files of previous simulations in the data processor BEAMDP [Ma09].

Fluence profiles and ZLAST distribution

The first spectra relate to the planar fluence of photons as a function of the distance to the central beam axis, as shown in figure 6.9.

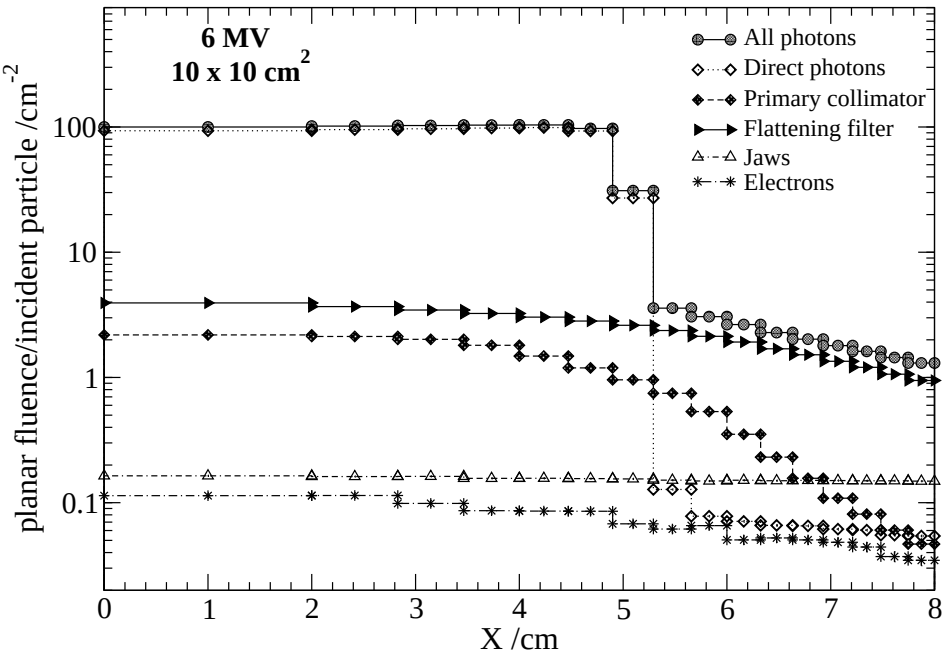

Figure 6.9: Planar fluence profiles of photons and electrons reaching a plane located at 100 cm from the source for a 10 x 10 cm^2 field. The relative contributions from all photons, direct photons and photons scattered by several components of the accelerator are shown. All fluence profiles are scored in an area of 8 cm half-width divided in 16 equal square bins.

The spectra include the fluence of all photons reaching the phantom surface at 100 cm SSD for a

field of 10 x 10 cm^2. Furthermore, the contribution to the total fluence of the photons scattered from different components of the linac (flattening filter, the primary collimator and the jaws collimator) as well as the electron contaminating the photon beams is also presented. All values are normalized to the total photon fluence calculated in the central value at the x-position of 1 cm.

As seen from this figure, the total planar fluence (labeled as *"all photons"*) remains relatively constant inside the field and decreases sharply immediately after the geometric edge of the field (x $>$ 5 cm). The *"direct"* photons dominate the photon fluence inside the field with a relative contribution of 94.6 % and their contribution decreases down to 0.1 % beyond the edge of the field. It is important to mention that as *direct photons* are considered those photons emitted from the target that do not interact with any component of the linac until they reach the scoring plane at 100 cm distance from the source.

The number of photons scattered from the accelerator head represents thus 5.4 % of the total number. On the other hand, it is clear that the larger contribution of scattered photons to the total fluence comes from the flattening filter (3.3 %). The flattening filter contribution is shown to be slightly more intense ($\sim$ 3.9 %) at the central region of 2 cm half-width and it decreases across the field. This decrease is specially more relevant in the region outside the field (from 5 to 8 cm) where the fluence is reduced down to about 1 %.

The second component influencing the total fluence is the primary collimator with a 1.75 %. Its influence is large at the central axis (about 2 %) and decreases with the distance to the central beam axis, reaching a value of 0.05 % at 8 cm. The number of photons scattered from the secondary collimator or jaws presents a low (0.16 %) and relatively constant contribution to the total fluence. Finally, it is observed that the electrons generated as the photons travel along the linac represent a very low contribution (about 0.1 %) to the total fluence. This contribution is shown to be more significant inside the field with a average value of 0.1 %, decreasing down to 0.05 % at distances away from the central axis (x = 8.0).

Table 6.4 presents the absolute and relative contribution of the different components of the total fluence reaching the plane at 100 cm for the 10 x 10 cm^2 field. The fluence values shown in the table were obtained in a square central region of 5 cm half-width. The fluences are normalized to the value of total fluence.

Table 6.4: Photon fluence contribution from different components of the accelerator on a plane located at 100 cm (SSD) for a 10 x 10 cm^2 field and 6 MV photon beam. The fluence is scored inside field in a square bin of 5 cm half-width.

	Planar fluence per incident particle (cm^{-2})	**Relative uncertainty (%)**	**Relative contribution (%)**
All photons	$2.0338x10^{-5}$	0.005	100
Direct photons	$1.9225x10^{-5}$	0.007	94.6
Primary collimator	$3.5726x10^{-7}$	0.13	1.75
Flattening filter	$6.7522x10^{-7}$	0.09	3.3
Jaws	$3.2108x10^{-8}$	0.44	0.16
Electrons	$1.9375x10^{-8}$	2.54	0.095

A similar evaluation has been also performed for other field sizes. Table 6.5 and 6.6 show the values of the fluence calculated for 4 x 4 and 30 x 30 cm^2 in a square bin of 2 cm and 15 cm half-width, respectively. Comparing these results, it is seen how the contribution of all photons scattered in the different parts of the linac increases from 2.53 % to 6.93 % when the field size increases from 4 x 4 to 30 x 30 cm^2. For both cases, the largest source of scattered photons is also the flattening filter and it is followed by the contribution of the primary collimator, as it has been previously observed. The contribution of the flattening filter reaches a value of 3.93 % for the largest field. A significant increase of contaminant electrons is also found as the field size increases. In fact, the contribution of the electrons to the total fluence varies from 0.037 % to 0.23 % as the field size increases from 4 x 4 to 30 x 30 cm^2.

Table 6.5: Photon fluence contribution from different components of the accelerator on a plane located at 100 cm (SSD) for a 4 x 4 cm^2 field and 6 MV photon beam. The fluence is scored inside field in a square bin of 2 cm half-width.

	Planar fluence per incident particle (cm^{-2})	**Relative uncertainty (%)**	**Relative contribution (%)**
All photons	$1.805x10^{-5}$	0.06	100
Direct photons	$1.7593x10^{-5}$	0.06	97.47
Primary collimator	$2.1175x10^{-7}$	0.54	1.17
Flattening filter	$2.2169x10^{-7}$	0.53	1.23
Jaws	$1.0069x10^{-8}$	2.5	0.056
Electrons	$6.75x10^{-9}$	13.6	0.037

Table 6.6: Photon fluence contribution from different components of the accelerator on a plane located at 100 cm (SSD) for a 30 x 30 cm^2 field and 6 MV photon beam. The fluence is scored inside field in a square bin of 15 cm half-width.

	Planar fluence per incident particle (cm^{-2})	**Relative uncertainty (%)**	**Relative contribution (%)**
All photons	2.3559×10^{-5}	0.01	100
Direct photons	2.1927×10^{-5}	0.01	93.07
Primary collimator	4.6313×10^{-7}	0.05	1.97
Flattening filter	9.2642×10^{-7}	0.04	3.93
Jaws	9.8981×10^{-8}	0.44	0.42
Electrons	5.5153×10^{-8}	0.64	0.23

The previous fluence results may be confirmed by the ZLAST distribution, giving the information about the position along the beam axis (Z axis) where a photon scored in the phase-space file was last interacted or generated. The ZLAST distribution for 6 MV and a 10 x 10 cm^2 field is presented in figure 6.10. As it can be observed, three major peaks appear in the distribution, which correspond to the contribution of photons last interacted from the target, primary collimator and flattening filter. These results are in agreement with the previous findings observed in the fluence profiles.

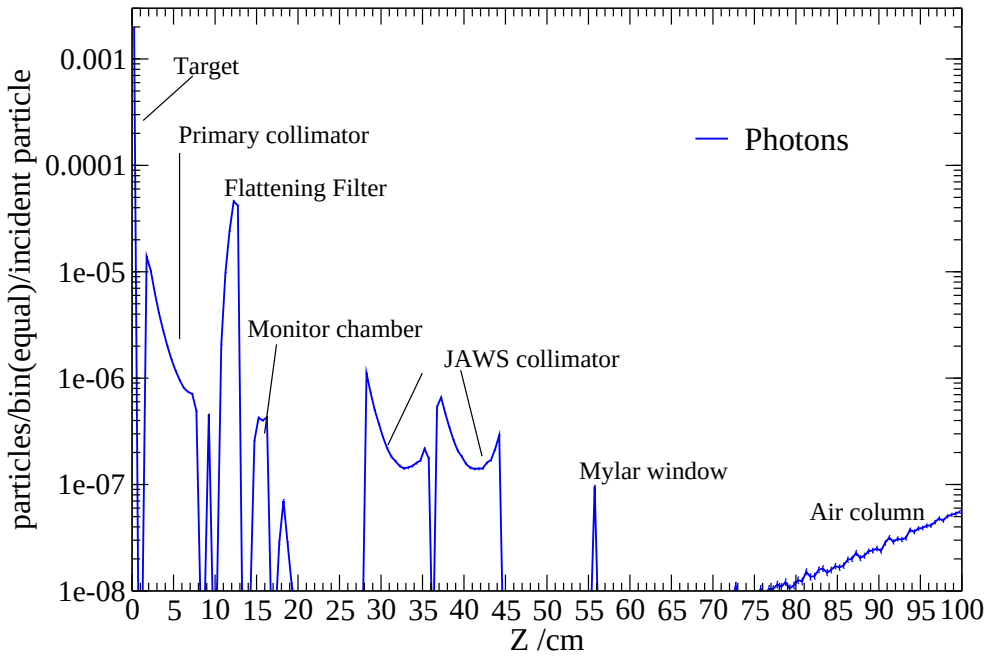

Figure 6.10: Distribution of the total number of photons scored within a given ZLAST position, i.e. the position along the Z-axis where the photon has been last interacted. The distribution is scored for a 6 MV photon beam with 10 x 10 cm^2 field at SSD of 100 cm. The distribution is calculated in a scoring region of 10 x 10 cm^2.

Energy spectra

In figure 6.11, the photon and electron energy spectra are presented for the 6 MV beams with a field size of 10 x 10 cm^2 at the phantom surface. For photons, the energy spectra show a very defined peak at around 0.5 MeV, while the spectrum of contaminant electrons peaks at a slight lower energy, around 0.3 MeV. It is also clear from these spectra that the fluence of photons at the peak are four orders of magnitude higher than those of contaminant electrons.

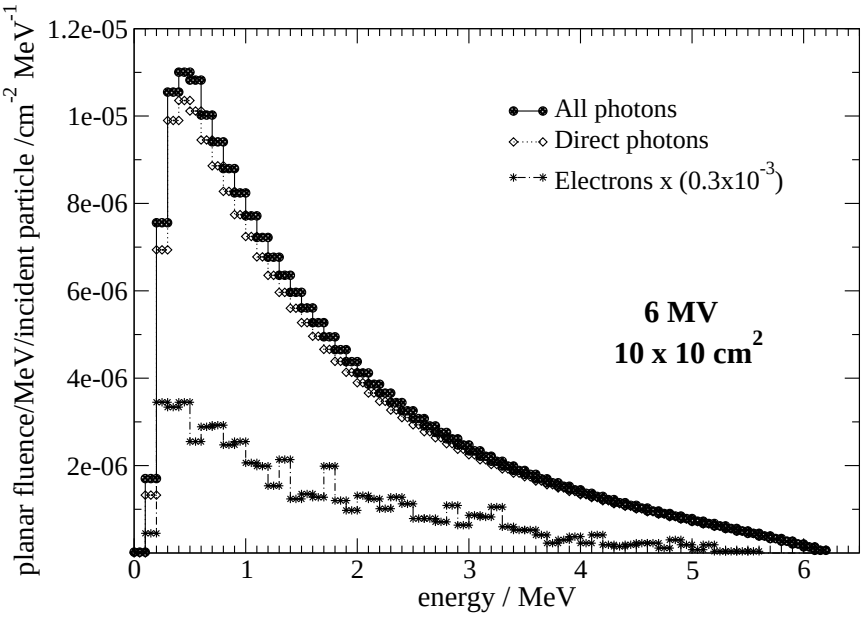

Figure 6.11: On-axis energy spectra of photons and electrons reaching a plane at 100 cm and calculated inside a scoring region equal of the field size, i.e. 10 x 10 cm^2. The contributions of photons which have not interacted with any part of the linac after the target (direct photons) are also shown. Energy bins are 100 keV wide.

Direct photons contribute around 95 % to the total photon energy distribution. As expected, the contribution of the direct photons is small in the interval of low energy (up to $\sim$ 2 MeV), since by definition, this photons are unscattered photons and therefore they don't loose energy when traveling along the linac. On the other hand, it can be observed that photons scattered from the linac components predominate at low energies and they represent around 5 % of total photons.

The variation of the energy spectra distributions with field size is also evaluated, as shown in figures 6.12a and 6.12b.

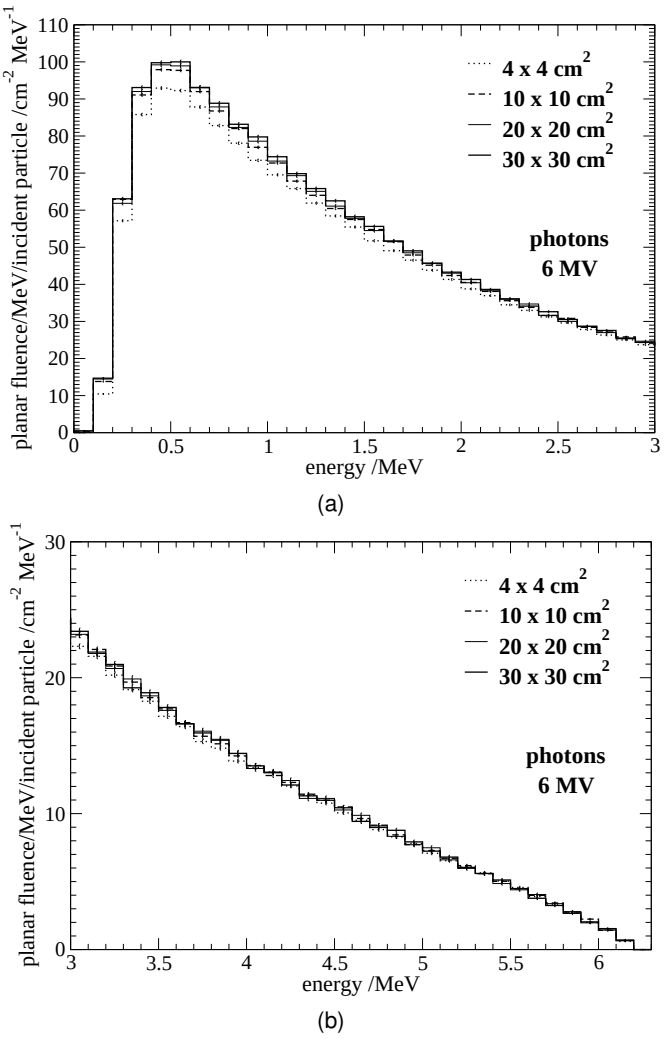

Figure 6.12: Comparison of on-axis energy spectra of photons reaching a plane at 100 cm SSD for 3 different field sizes (4 x 4, 10 x 10 and 20 x 20 cm^2) at 6 MV photon beam. The spectra are calculated in a scoring region of 2 x 2 cm^2 with an energy bin of 100 keV wide. For a better visualization, the spectra are divided into two intervals: (a) from 0 to 3 MeV and (b) from 3 to 6 MeV.

These figures illustrate a comparison of energy spectra calculated for field sizes of 4 x 4 cm^2, 10 x 10 cm^2, 20 x 20 cm^2 and 30 x 30 cm^2. All spectra are scored in a central region of 2 x 2 cm^2 and they are normalized to the maximum value of photon fluence calculated for the largest field size (30 x 30 cm^2). As illustrated in these figures, the field size affect the photon fluence in the energy range below 1.5 MeV. The largest variation of the photon fluence with field size occurs at energies lower than 1 MeV, where the photon fluence increases up to 7 % when the field increases from 4 x 4 cm^2 to 30 x 30 cm^2. Between 1 and 1.5 MeV energy, the variation of the energy spectra with the increase of the field size is less than 2 %. At higher energies ($>$ 1.5 MeV), the fluence of photons is

not significantly different for the four field sizes.

Mean energy distribution

Figure 6.13 shows the mean energies of photons and electrons as a function of the distance to the central beam axis at 100 cm SSD in a 10 x 10 cm^2 field. For photons, it can be seen that the mean energies are almost constant along the radial position inside the region limited for the jaws (from 0 to 5 cm). In particular, the mean energy varies from 1.76 MeV (central position) to 1.68 MeV (field edge), which represents hence a change of about 4.5 % relative to the central mean energy. Near the field edge the mean energy decreases dramatically down to 1.3 MeV.

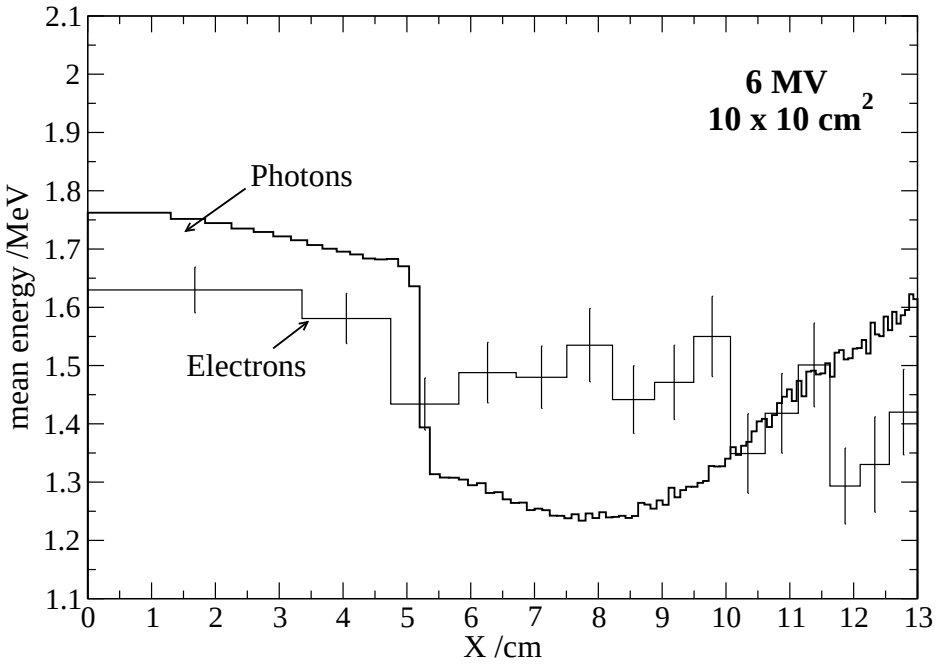

Figure 6.13: Mean energies of the photons and electrons as function of the distance to the central beam axis for a 6 MV photon beam and a 10 x 10 cm^2 field at SSD of 100 cm. The spectra are calculated in the area defined by half-width of 13 cm. This area is divided in 50 and 15 equal square bins for the photon and electron spectra, respectively.

It is interesting to point out from this figure that as the distance increases from the field edge, there is an increase of the photon mean energy with the distance to the beam axis. This effect is due to the beam hardening produced by the jaws collimator, which attenuates the low energy photons going through the collimators, remaining hence photons of higher energy.

For electrons, the distribution of the mean energy shows a decrease away from central axis with

a lower value compared to the mean energy of photons inside the field. Note that the mean energy distribution for electrons shows a high uncertainty (2.5 %) due to the low fluence of electrons present in the beam.

Angular distribution

Figure 6.14 presents the angular distribution of photons and electrons at the phantom surface for a 10 x 10 cm^2 fielda and a 6 MV beam. It is seen that the angular distribution of photons is very similar to a point source. The photons are leaving the accelerator head in the forward direction with angles ranging from 0 to 5 °. On the contrary, the contaminant electrons show a wide angular spread, reflecting the fact that a lot of them are created or scattered in the air gap between the accelerator head and the phantom surface. Note that it is again observed the low contribution of the contaminant electrons, with a factor of 10^4 lower than the photon one.

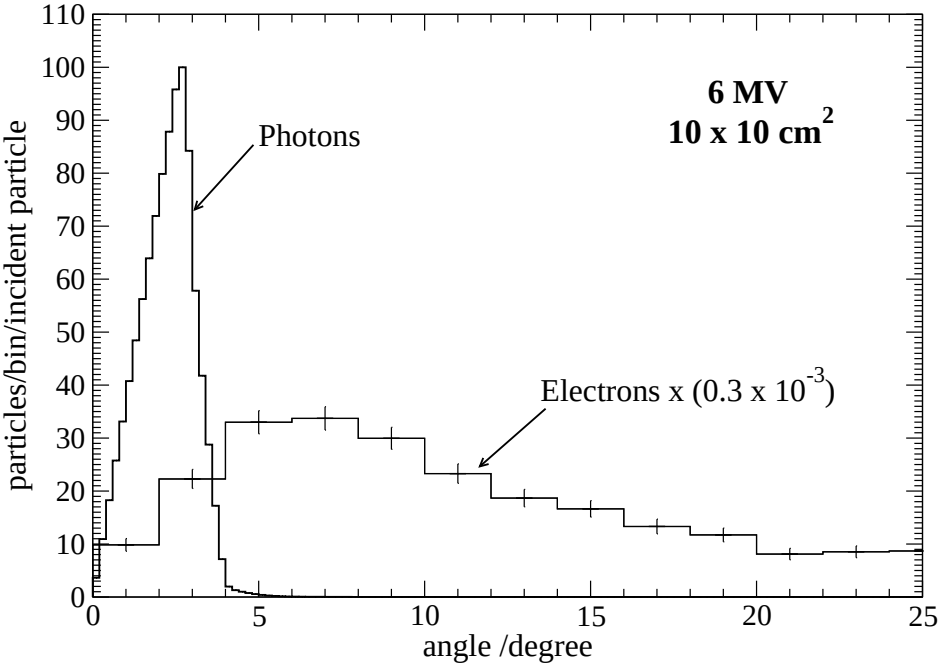

Figure 6.14: Angular distribution of photons and electrons scored at SSD = 100 cm and inside a square region of 10 cm width for a 6 MV photon beam. The angle bin is 0.2 ° and 2 ° for the photon and electron spectra, respectively. Due to the low number of electrons, the angle bin for the case of the electrons is considered larger than for photons to reduce the statistical uncertainty.

6.4 Conclusions

In the present chapter, it has been presented the simulation and characterization of the 6 MV photon beam from the Varian Clinac 2100C/D accelerator installed at the *"Centro Oncólogico Dra. Natália Chaves"*. The accelerator was fully modeled using the MC BEAMnrc code for field sizes ranging from 4 x 4 cm^2 to 30 x 30 cm^2 at a SSD of 100 cm. The phase-space files scored from previous BEAMnrc simulations were used as input of DOSXYZnrc code for MC calculations in a homogeneous water phantom. The accuracy of the modeled accelerator was subsequently validated against experimental measurements performed with an ionization chamber. Furthermore, by comparing measurements and simulations for several energy/radius combinations of the initial electron beam it was determined the values that yield the best matching, which are 6.2 MeV energy and 1.5 mm radius.

Finally, the phase space files for the above-mentioned field sizes were analyzed to obtain fluence profiles, energy spectra, mean energy distributions and angular distributions at the phantom surface located at 100 cm from the source. It was observed that, for a field size of 10 x 10 cm^2, the number of photons scattered from the accelerator head represents about 5 % of the total number of photons reaching the plane at 100 cm SSD. The largest source of scattered photons is the flattening filter with a contribution of 3.3 %, followed by the primary collimator with a contribution of about 1.7 %. The electrons produced by the interaction of photons with the different components of the accelerator do not contribute significantly (about 0.1 %) to the total fluence. For this field, the photon energy spectrum shows a very defined peak at around 0.5 MeV, while the spectrum of the contaminant electrons presented the peak at slightly lower energy, at 0.3 MeV. Increasing the field size from 4 x 4 cm^2 to 20 x 20 cm^2 caused a variation of about 7 % on the on-axis photon fluence for energies below 700 keV, while at higher energies the on-axis fluence does not change (1 %) significantly with the field size. The mean energy of the photons is about 1.7 MeV inside the field and it decreases down to 1.3 MeV near the field edge (at 5 cm). The photons leave the accelerator with a very forward-peaked angular distribution with angles ranging from 0° to 5°. On the contrary, the contaminant electrons show a wide angular spread with angles between 0° to 30°.

The information extracted from the spectra will enhance the knowledge of the 6 MV photon beam for subsequent applications, such as the simulations of real IMRT treatments of prostate cancer (chapter 9).

Chapter 7

Varian Millennium 120-leaf MLC in Monte Carlo simulations

In this chapter the model of the dynamic Millennium 120-leaf MLC used for MC simulations is presented. Details of the geometry and the MC model of the MLC are described in the first section. Next, the accuracy of the MLC model is verified by comparison of calculated dose distributions with those measured with ionization chamber and radiographic films. Results of this comparison are discussed in the second part of this chapter.

7.1 Monte Carlo MLC model description

One of the most important collimator system integrating the great majority of clinical accelerator heads is the multileaf collimator. As mentioned in chapter 3.1, this device has become currently the main tool in advanced radiotherapy techniques (3D- CRT, IMRT, Arc, etc.) because of the ability of delivering optimized non-uniform and complex intensity profiles using the finite size and dynamic flexibility of its leaves.

The importance of modeling the details of the MLC, in order to calculate accurately patient dose distributions and account for the impact of the leakage and scatter effects caused by the leaves of this device on dose distributions, has been recognized by several investigators [Hea03, Jan06, Tyagi07]. Various MLC models have been proposed in different MC codes to simulate the detailed geometry of different designs of MLCs [Van03, Hea03, Jan06, Tyagi07]. The pioneer among the

models was introduced in the BEAMnrc code where various CM specific for MLC have been developed, such as MLC, MLCQ, VARMLC and DYNVMLC. The first of these BEAMnrc-based CM (MLC) allows to model a simplified collimator with flat faces using just a single layer. MLCQ and VARMLC CM model the leaves as a set of diverging slabs with rounded ends. A single type of leaf geometry is defined in both previous models with only the leaf width being variable from one leaf to the next. The VARMLC models include also some complex details of the leaves such as the tongue-and-groove design. Recently, the Varian Millennium 120 leaf collimator has been introduced with smaller leaf widths in order to provide a higher resolution for delivery of smaller fields. The complicated design of the leaves for this collimator and the variable leaf-to-leaf geometry made very difficult to model this MLC using the simplified geometry proposed in the three previous CMs. To override these problems, Emily Heath *et al* [Hea03] implemented a new CM in the BEAMnrc, named DYNVMLC, to design specifically the Varian Millennium 120-leaf collimator. This latter CM was used in the present work to model the Millennium MLC incorporated in the Varian 2100C/D linac at the *Centro Oncológico Dra. Natália Chaves (Carnaxide)*.

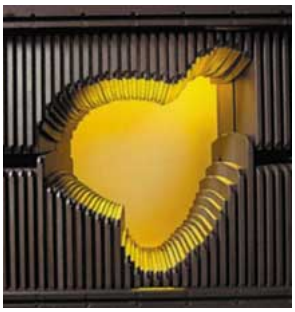

(a)

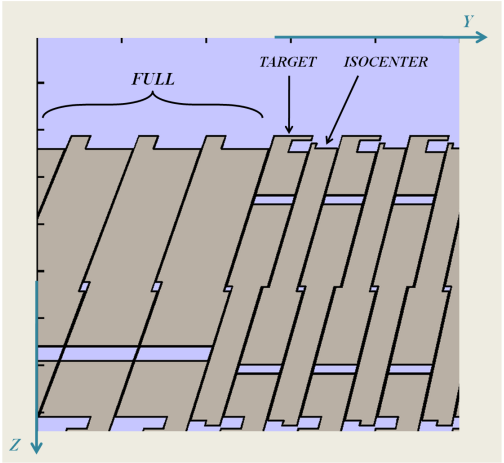

(b)

Figure 7.1: (a) A Varian Millennium MLC with 120 leaves defining an arbitrary leaf arrangement. [Varian Medical Systems, Palo Alto, CA]; (b) Schematic drawing of the geometry of DYNVMLC component module illustrating the three leaf types of Millennium MLC system: FULL, TARGET and ISOCENTER.

Specifically, the Millennium MLC system consists of two banks of 60 independent leaves facing each other, traveling along the X axis linearly perpendicular to the beam axis. Of the 60 pairs of leaves, there are 20 outer leaves, named FULL, projecting a leaf width of 1 cm at isocenter. The rest 40 pairs with a narrower project (0.5 cm) are internally arranged in an alternating pattern of two

types of leaves, named TARGET leaf (thicker end of the leaf towards the target) and ISOCENTER leaf (thicker end of the leaf towards the isocenter). The outer and inner leaves are 6.7 cm and 6.5 cm in height, respectively and they are composed of a tungsten alloy (90 % W, 6 % Ni, 2.5 % Cu and 1.5 % Fe).

Leaf edges are focused towards the photons source at z= 0.0 in order to minimize the geometric penumbra across the leaves and to account for the beam divergence. A cross-sectional view of the leaf types is illustrated in figure 7.1b.

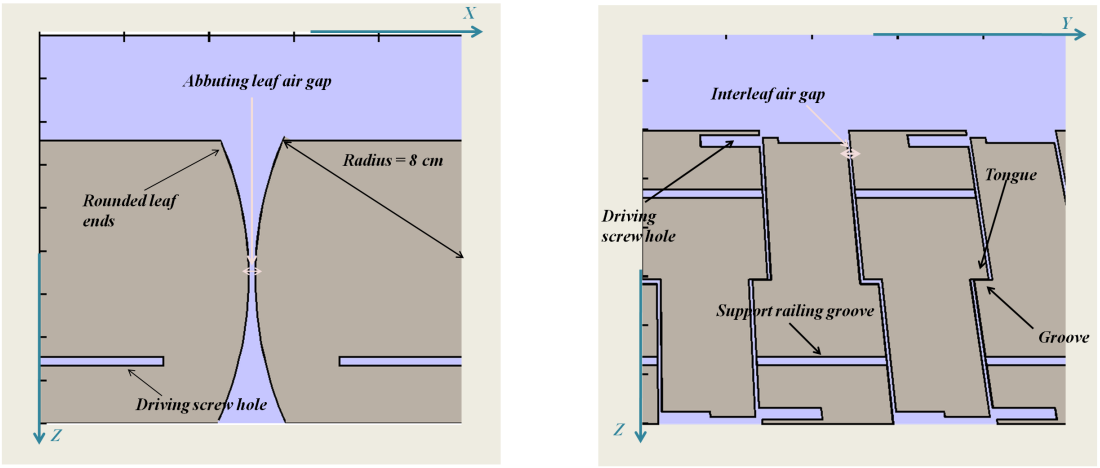

(a) (b)

Figure 7.2: (a) Side view of two opposed leaves showing rounded end and (b) cross-sectional view of MLC leaves illustrating tongue and groove design, support railing groove and driving screw hole.

It is important to point out that leaves of the Millennium MLC present two special design characteristics, as shown in figure 7.2: a rounded end with a radius of 8 cm (Fig. 7.2a) and a ”tongue-and-groove” arrangement between adjacent leaves (Fig. 7.2b). While the rounded leaf end is designed to maintain a fairly constant penumbra size independent of leaf position, the tongue-and-groove is designed to reduce the radiation transmission between the leaves (interleaf leakage). In addition to tongue-and-groove design, neighboring leaves are separated by a small air gap (Y axis direction), known as *interleaf air gap*, which will minimize the friction between the leaves during their movement.

To avoid the collision between opposing leaves, another small air gap (X axis direction) exists when leaves are completely closed (Figure 7.2a). This gap is commonly designated as *abutting air gap* and its function is just to avoid the collision of the opposed leaves which could cause a mechanical disequilibrium of the MLC system. The abutting gap in combination with the rounded ends lead to a significant radiation leakage between each closed opposing leaf pair, usually designed as

abutting leaf leakage (see later in section 7.2).

Other important aspect, which characterize the DYNVMLC CM in contrast to other models, is that the DYNVMLC CM is also able to reproduce details of the carriage on which the leaves travel across the field. These details are specifically the driving screw hole and the support railing groove and they can be seen in figures 7.2b and 7.2a.

Most of the leaf dimensions necessary for the model were obtained from the manufacturer's technical drawings. There are however some specific MLC features, which were not provided by manufacturers; namely, the physical density of leaves and the widths of the interleaf air gap and the abutting air gap. This three leaf characteristics have a high impact on dose distributions and therefore they need to be accurately estimated in the Monte Carlo simulations. The determination of these parameters is presented in the next section where the validation of the MLC model is performed by comparing simulated MLC pattern with experimental measurements.

The considered MLC model presents also the ability of simulating the motion of the MLC leaves during an IMRT treatment. For this purpose, the model performs a sampling of the leaf positions for each incident history produced on the target. From the treatment planning systems, it is exported a leaf sequence file specifying the projection of the leaf positions in the isocentre plane as a function of the fraction of delivered monitor units (MU). This leaf sequence file is converted to a format for input to the BEAMnrc code, which includes calculating the physical positions of the leaves in the plane of the MLC based on a geometrical relationship between the leaf position and the projection of the position at the isocentre (100 cm). During the simulation, the leaf positions are determined by obtaining a random number which is then used for sampling a field segment based on the MU index. The model can be used for the simulation of both delivery techniques of IMRT, dynamic ("sliding window") and static ("step and shoot") techniques. For a dynamic technique, the MUs continually increase for each segment, while for a static technique, the MU index of every second field is constant while the leaf position change. The method implemented in the model for sampling the sequence files was based on the the work carried out by Liu *et al* [Liu01] for the the additional BEAMnrc CM, called DMLCQ.

7.2 Experimental commissioning of MLC model

Dose distributions of MLC-based radiotherapy have shown to be very sensitive to the detailed geometry of the MLC leaves [Hea03, Jan06]. This section presents an extensive verification of the accuracy of the above described MLC geometry model. Monte Carlo simulations performed using various MLC intensity patterns were compared with experimental measured ones in order to assess the main MLC features influencing the final dose output. In particular, tests were focused on the verification of the rounded leaf and tongue-and-groove design, the leaf-positioning accuracy and, finally, the sampling of leaf positions incorporated in the DYNVMLC model to create dynamic MLC-based dose distributions [Liu01].

As a part of the experimental validation, the determination of the unknown MLC parameters (leaf mass density, interleaf air gap and abutting air gap width) was also carried out. The leaf density and interleaf gap width were chosen to match simulated dose profiles of MLC leakage with those profiles obtained with film measurements. For that, it was used a 10 x 10 cm^2 field defined by the jaws where the MLC was blocking the entire open field with the ends of the leaves closed behind the edge defined by the jaws. The abutting air gap was also determined by fitting the calculated transmission with experimental measurements. In this case, a 10 x 10 cm^2 field defined by the jaws was fully blocked by the MLC leaves closing on the central axis. More details about this process are given next.

7.2.1 Monte Carlo simulations

In order to perform MC calculations, the DYNVMLC-based MLC model described in section 7.1 was added to the previous model of the 6 MV Varian 2100C/D accelerator in the BEAMnrc code (chapter 6). For the modeling of the accelerator head including now the MLC, two phase-space planes were defined along the beam direction. A first phase-space of particles was established directly above the JAWS collimator (at 27.9 cm distance to the target) and a second plane was below the protection mylar window at 95 cm from the target. The first phase-space plane corresponds to simulations of the patient independent components of the treatment head, i.e. from the target up to the shielding collimator. This section of the geometry is the same for any field configuration and therefore this step was simulated just once. This resulted in a phase-space file of 15 Gbyte containing around 480 million particles per 500 million of electrons impinging on the target, from which 99.98 % are

photons and the remaining particles are electrons and positrons. The simulation was performed on a AMD Opteron 2 GHz processor and it took about 50 hrs.

The previous file was then used as input for the subsequent BEAMnrc run modeling the remaining patient dependent components, i.e. the jaws and the MLC. The protection window was also included in this part. In this second simulation stage, the positions of the jaws and MLC leaves for each field considered in the verification process were simulated and the resulting particles reaching the second plane were scored in a phase-space file. The positions of the MLC leafs for each field configuration were read directly to the BEAMnrc from the MLC leaf-sequence file (a .mlc file) that was previously exported from the TPS. According to Heath *et al* [Hea03], the motion of the MLC leaves during a dynamic delivery is simulated by sampling the leaf positions from this .mlc file.

In order to decrease the fluctuations of the particle fluence at the exit of the linac and hence to minimize the latent variance[4] of the phase-space files, several runs of the second simulation step were generated for each test. Each run used the same number of simulated histories but different random numbers to guarantee the random nature of the simulation. As result of each run, a phase-space file was scored at the second plane. These files were then combined using the program BEAMDP [Ma09], resulting in a final phase-space with a larger final number of particles. It is important to mention that the final number of particles scored in the final phase-space file was dependent on the size of the field shaped by the jaws and the MLC leaves. For most simulations, approximately 4 - 90 million particles were collected in the phase space file. As an example, about 45 x 10^6 particles were scored in the final phase-space file for an open field defined by the jaws with a size of 10 x 10 cm^2, whereas the phase-space file for the same jaws field blocked by the MLC (leaf tip closed behind the jaws edge) contained about 3.5 x 10^6 particles. For dynamic fields shaped by the MLC in 11.4 x 10.4 cm^2 field defined by the jaws, around 37 x 10^6 particles were scored in the final phase space files at 95 cm SSD. The output file was then applied for DOSXYZnrc dose calculations in a water phantom of 30 x 30 x 30 cm^3.

Most BEAMnrc accelerator simulations are done in two stages to eliminate the need for resimulating the upper part of the treatment head (from target to jaws) whenever the details of the field defined by the MLC and the jaws are changed [Mor01, Kaw06, Tyagi07].

To improve the efficiency of the two stages of the linac modeling, bremsstrahlung splitting with

[4]The term of "latent variance of a phase-space file" was introduced by Sempau *et al* [Sem01] to distinguish between the uncertainty in a dose calculation due to the random nature of the particle transport in the phantom from the statistical fluctuations in the phase-space file. According these authors, this is an intrinsic property of a phase-space file which can be used to measure the "quality" of a phase-space file for a particular calculation and as a guide to optimize its size.

a photon split factor of 20 and the Russian roulette techniques were used [Deng99]. Electron and photon cutoff energies, ECUT and PCUT, were set to 0.700 MeV and 0.01 MeV, respectively, for the simulations performed with both BEAMnrc and DOSXYZnrc. More details about the variance reduction techniques have been given earlier (Sec. 4.4.4).

For each individual field configuration, several DOSXYZnrc runs were performed. For each run, the particles scored in the final BEAMnrc phase-space file were reused between 10 and 20 times based on the study reported by Walters *et al* [Wal02] regarding the impact on the uncertainty introduced by particle recycling (Chapter 4). For the two previous stages of the linac simulation, the phase-space files were not recycled.

The number of DOSXYZnrc runs considered for each field configuration was chosen depended-ing on the field size and the number of particles included in the respective phase-space file. As result of each DOSXYZnrc run, a file with extension *.3ddose* containing the 3D dose distributions calculated in the defined phantom was generated. Then, all .3ddose files obtained in each run for a given field configuration were combined using the option ”combine” of the old version of the interactive program STATDOSE used for analyzing 3D dose distributions [McGo07]. For each final file resulting in the combination, the mean dose and the standard uncertainty in every voxel were calculated over the number N of independent runs used for the combination, as presented in the following equations:

$$D(x,y,z) = \frac{\sum_i^N D_i(x,y,z)}{N} \tag{7.1a}$$

$$\sigma_D(x,y,z) = \sqrt{\frac{\sum_i^N (\sigma_{D_i}(x,y,z))^2}{N(N-1)}} \tag{7.1b}$$

where $D_i(x,y,z)$ is the dose value in a voxel (x,y,z) of a run i and σ_{D_i} the correspondent standard uncertainty. This option allowed to get the final dose distributions with a reduced statistical uncertainty without affecting the dose distribution in the phantom.

Sufficient histories (between 2 x 10^8 - 10^9) incident on the phantom were simulated for each field configuration in order to reach an overall statistical uncertainty lower than 2 %.

7.2.2 Experimental measurements

Experimental measurements for the verification of MC dose results were done using two different methods :

- *Radiographic film measurements*:

  For the acquisition of leakage dose profiles as well as the verification of the MLC model to reproduce the tongue-and-groove design of the leaves and dynamic distributions, extended dose range (EDR) Kodak films were exposed in a solid water phantom. The films were properly developed with a regular film processor and then digitized using the VXR-16 film scanner by Vidar Company (Herndorn, VA). Subsequently, the images with a resolution of 0.0178 cm were analyzed using the RIT 113 Film Dosimetry software (Radiological Imaging Technology, Inc. Colorado, CO).

  A film calibration curve providing the conversion from optical density to dose was defined in the same session as the other measurements. For that purpose, eight films were exposed perpendicularly to the beam axis for a 10 x 10 cm^2 open field (with the MLC retracted) at dose levels ranging from 0 to 259.1 cGy. The films were sandwiched between slabs of solid water at a depth of 5 cm. All irradiations for the film calibration were carried out for 6 MV photon beams at 100 cm SSD. The value of the absorbed dose corresponding to each calibration film was obtained with an ionization chamber of 0.125 cm^3 (PTW 31001 model) located at 10.5 cm depth in the solid water phantom. The values given by the chamber were corrected following the TRS-398 protocol (see section 3.2.1) and, subsequently, transformed to the dose at 5 cm through the use of relationship between the doses at different depths given by the PDD curve.

  In order to minimize potential experimental errors with radiographic film dosimetry, several precautions were taken based on previous works [Chet02, Pai07]. Following the recommendations and investigations reported by these works, the total uncertainty of EDR film response was estimated to be within 5 %. More details of dosimetry with radiographic films have been described before in section 3.2.

- *Ionization chamber measurements*:

  Due to the radiation transmission through the rounded shape of the leaves ends, the radiation penumbra of a given field defined by the MLC is slightly widened when compared to the penumbra defined by the light projection of the leaf end. According to [Boy97], the MLC leaf

positions far from the central axis can typically differ from the positions that would be obtained using simple back projection along a tangential path from the leaf end (commonly known as light-field projection). Thus, it is important to check the MLC leaf end model far from the central axis to ensure that the leaf ends are correctly positioned. In order to verify the accuracy of leaf positioning and the model of the leaf ends, transversal dose profiles and depth-dose curves were measured with a PinPoint ionization chamber (model PTW 31014) for a series of fields defined by the MLC leaves with sizes ranging from 2 x 2 to 20 x 20 cm^2. The chamber has a 2 mm radius and a sensitive volume of 0.015 cm^3 and it was mounted in a Wellhöfer water scanning system. The profiles were adaptively step scanned at a depth of 5 cm using a minimum step of 0.1 cm. The effective point of measurement of this chamber was positioned at its geometric center according to the specifications of the chamber. The corrections with stopping power ratios and other perturbation factors were applied following the recommendations of the IAEA TRS-398 protocol (see section 3.2.1). The estimated relative uncertainty for chamber measurement was equal to 2 %.

7.2.3 Benchmark tests and results

To benchmark the MLC model, results obtained with the Monte Carlo model were compared with measurements for a variety of test cases. Further details about each validation measurements and simulations are given next for each individual case.

I. MLC leakage validation

a) Determination of leaf material density and interleaf air gap width

The choice of the leaf material density and the interleaf air gap width of the MLC model was performed by comparing calculated and measured MLC leakage dose profiles. These profiles were generated perpendicular to the direction of the MLC leaf motion (Y axis) using a field where all 60 leaf pairs were blocking the fields with the jaws collimator set to 10 x 10 cm^2. In fact, the ends of the leaves were closed behind the jaws at 7 cm off the central axis as shown in figure 7.3a. Such field is referred as *"MLC-blocked"* from here.

Individual MC simulations for various combinations of leaf material density (Table 7.1) and two interleaf air gaps (0.006 and 0.008 cm) were performed using the MLC blocked field to determine

the influence of these parameters on the MC leakage dose profiles and to identify the optimal set of these MLC features corresponding to the film measured results. The densities and interleaf gap widths were chosen based on published values by Heath *et al* [Hea03], which proposed a density ranging from 16.94 to 18.5 gcm^{-3} and a 0.006 cm interleaf gap. Simulated leakage dose profiles were calculated in a water phantom with a resolution of 0.1 x 0.1 x 0.1 cm^3.

Additional dose calculation for a 10 x 10 cm^2 open field defined with the jaws and the leaves retracted was also carried out in a water phantom with a voxel size of 0.2 x 0.2 x 0.1 cm^3. The relative statistical uncertainty was approximately 1 % at the depth of maximum dose. Using these calculations, the percent leakage transmission through the MLC was determined by the ratio of the blocked field dose profiles to the on-axis dose value of the 10 x 10 cm^2 open field. It should be noted that the resolution of the dose calculations for the blocked field was chosen smaller compared to the resolution for the open field in order to reproduce the details of the leakage between the leaves.

With a leaf density of 17.7 gcm^{-3}, it was first evaluated the influence of the interleaf gap on the percent MLC leakage. The comparison of dose profiles calculated using two different interleaf gap widths and the correspondent measured profiles (EDR film) perpendicular to the leaf direction along the center axis (x = 0.0 cm) at 5 cm depth in the water phantom is plotted in figure 7.3b. The profiles were characterized by a statistical uncertainty of 2 % for all points in the inner region ([-4.0,4.0]).

As seen from these profiles, the width of the interleaf air gap has influence on the percent leakage transmission of the MLC and the overall pattern of the profile. As the air gap from 0.006 cm to 0.008 cm, the peaks and valleys of the leakage profiles, which correspond to the interleaf and intraleaf leakage respectively, vary by about 9 % and 7 %, respectively.

By evaluating the average value of the percent leakage transmission (determined as the average among the dose values in the inter- and intra-leaf regions inside the field), it is observed that the change of the air gap from 0.006 to 0.008 cm results in a change of the magnitude of the average transmission from 1.44 % to 1.57 %. Using the same procedure as for calculations, an average value of 1.42 % has been obtained for the percent leakage transmission profile measured using radiographic EDR films. Comparing this experimental value with the calculated values for the different interleaf gap widths, it is observed that an interleaf gap of 0.006 cm gives the closest agreement between MC calculation and measurements, considering the uncertainty of 2 % for MC calculations and 5 % for film measurements.

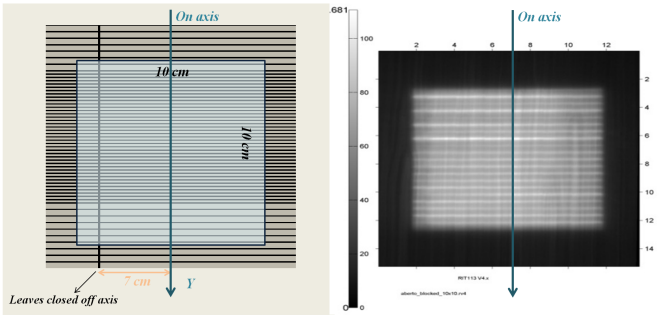

(a)

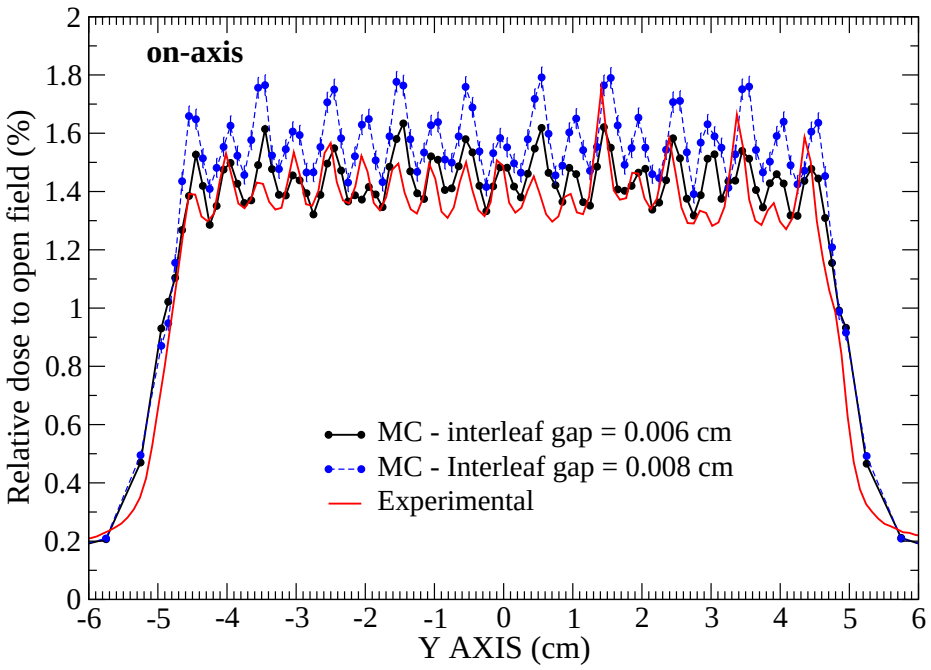

(b)

Figure 7.3: MC calculated (full circles) MLC leakage profiles along the central axis for two different interleaf air gaps, 0.006 cm and 0.008 cm. The profiles were obtained at a depth of 5 cm in a homogenous water phantom with a SSD of 95 cm using a "MLC blocked" field for a 6 MV photon beam. The density of the leaves was set to 17.7 gcm^{-3}. Film measured are illustrated by the continuous red line.

It can be also observed in figure 7.3 how the size of the interleaf air gap also lead to differences in the pattern of the leakage profiles. In fact, it is seen that the differences between the interleaf (dose peaks) and intraleaf (dose valleys) leakage became less pronounced with a smaller air gap, mainly due to the high reduction of the interleaf transmission compared with the intraleaf one. In fact, the overall difference are about 0.18 % and 0.23 % for the interleaf air gap of 0.006 and 0.008 cm, respectively. Experimentally, the differences between inter- and intra-leaf transmission was about 0.19 %. This results confirms the previous finding that a width of 0.006 cm for the interleaf air gap

shows the best agreement between MC calculation and measurements within our statistics.

After the interleaf gap determination, on-axis leakage dose profiles at a depth of 5 cm in the homogeneous phantom were calculated for three different values of leaf density: 17.7, 17.35 and 17.0 gcm^{-3}. The calculated profiles were subsequently compared with the profiles measured at the same location and under the same conditions as the calculations. The calculated profiles were characterized by a statistical uncertainty of 2 % for all points in the inner region ([-4.0,4.0]). The results of the comparison are shown in figures 7.4a and 7.4b.

From figure 7.4a, it is clearly seen that the percent leakage dose profiles are sensitive to changes in the MLC density. Changing the density of the MLC from 17.0 to 17.7 gcm^{-3}, the interleaf and intraleaf dose values increases by about 15 %.

Table 7.1: Film measured and MC calculated MLC transmission with different leaf densities at a depth of 5 cm with a SSD of 95 cm for a 6 MV photon beam. The transmission through the MLC for each point of the MLC dose profile was calculated by dividing the dose in the MLC blocked field by the on-axis dose value in the 10 x 10 cm^2 open field. The average value and the respective standard deviation of all transmission points along the field are registered in the table.

MLC material density	Monte Carlo average MLC transmission	Experimental average MLC transmission
17.0 gcm^{-3}	1.54 ± 0.09 %	
17.35 gcm^{-3}	1.44 ± 0.08 %	1.40 ± 0.09 %
17.7 gcm^{-3}	1.33 ± 0.07 %	

Table 7.1 summarizes the measured and calculated average value of the MLC leakage transmission. As seen, a change in the density from 17.0 to 17.7 gcm^{-3} leads to a decrease from 1.54 ± 0.09 % to 1.33 ± 0.07 % in the average leakage transmission. By comparing the average value of the percent leakage calculated for the three different leaf densities whit that value measured with EDR film, it can be concluded that a density of 17.35 gcm^{-3} provides the best agreement between the measured and the calculated average leakage within our statistics of 2 % for the MC calculations and 5 % for the film measurements (figure 7.4b).

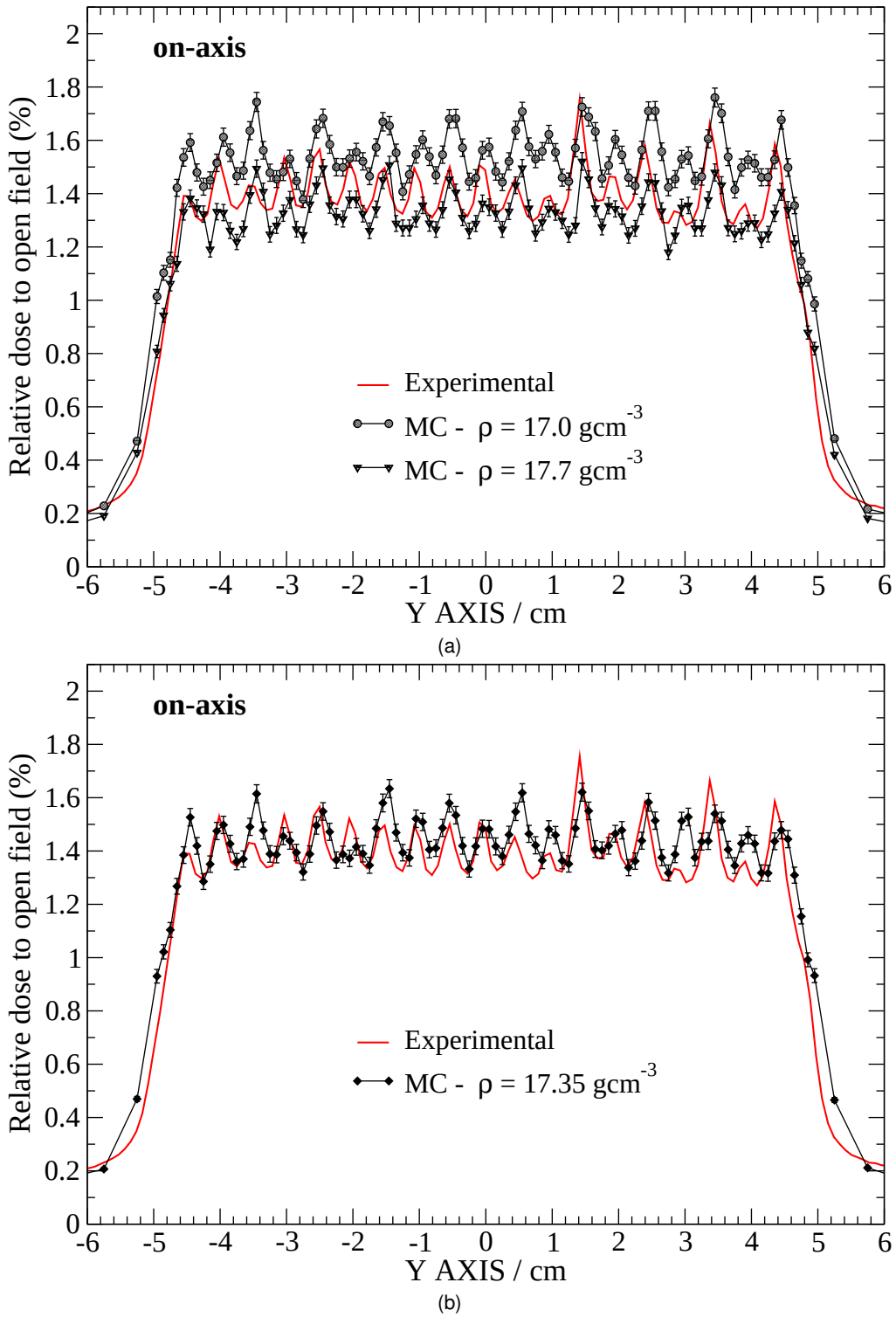

Figure 7.4: Film measured (red line) and calculated (symbols) MLC leakage profiles for three different values of MLC leaf density. All profiles were plotted along the central axis as indicated by the continuous black line in (a). The effects of leaf density on the leakage profiles is shown for 6 MV photon beam from MC calculations. The profiles were obtained at a depth of 5 cm in a homogenous water phantom with a SSD of 95 cm using a "MLC blocked" field. The interleaf air gap was set to 0.006 cm.

b) Determination of abutting leaf air gap width

As previously mentioned, a small air gap (*abutting leaf gap*) exists between a completely closed leaf pair to avoid collision between opposing leaves. The accurate determination of this gap is an important task, since the transmission through this gap can contribute up to 25 % of the dose for the open field and the simulated dose can be affected significantly if it is not perfectly modeled [Hea03].

In order to identify the optimal size of this gap for the MLC model, calculated and measured dose profiles were compared for a 10 x 10 cm^2 field defined by jaws with the MLC leaves closed to the central axis. This field is referred to "*MLC closed*" field and it is shown in figure 7.5a.

Figure 7.5b shows the dose profiles obtained along the direction of leaf movement at 5 cm depth of a water phantom obtained from film measurements and MC calculations with two different abutting air gaps. The MC results were computed with an interleaf air gap of 0.006 cm and a leaf density of 17.35 gcm^{-3}. MC calculations were performed in the water phantom with a resolution of 0.1 x 0.1 x 0.1 cm^3.

As seen, a significant fraction of radiation transmitted through the rounded leaf ends was found both experimentally and with MC calculations. It should be also noted that the profile of the transmission was strongly sensitive to changes in the abutting gap width. As the gap width changed from 0.004 to 0.04 cm, the magnitude of the transmission increased from 25.9 % to 38.3 %. The statistical uncertainty of the maximum transmission was 1 %. An abutting leaf gap of 0.004 cm width provided the best agreement between calculated and measured transmission within measurements and simulations uncertainties, respectively. This data is summarized in table 7.2.

Table 7.2: Maximum transmission through the rounded leaf edge measured using radiographic films and calculated with MC simulations for two different sizes of abutting leaf air gap at a depth of 5 cm with a SSD of 95 cm for a 6 MV photon beam. The transmission values were calculated by dividing the doses in the MLC closed field by the on-axis dose value in the 10 x 10 cm^2 open field. The statistical uncertainty of the calculated maximum transmission are presented for each value. The uncertainty of the film measurements is within 5 %.

MLC abutting leaf gap	Monte Carlo abutting leaf leakage	Experimental abutting leaf leakage
0.04 cm	38.41 ± 0.29 %	27.23 %
0.004 cm	25.97 ± 0.24 %	

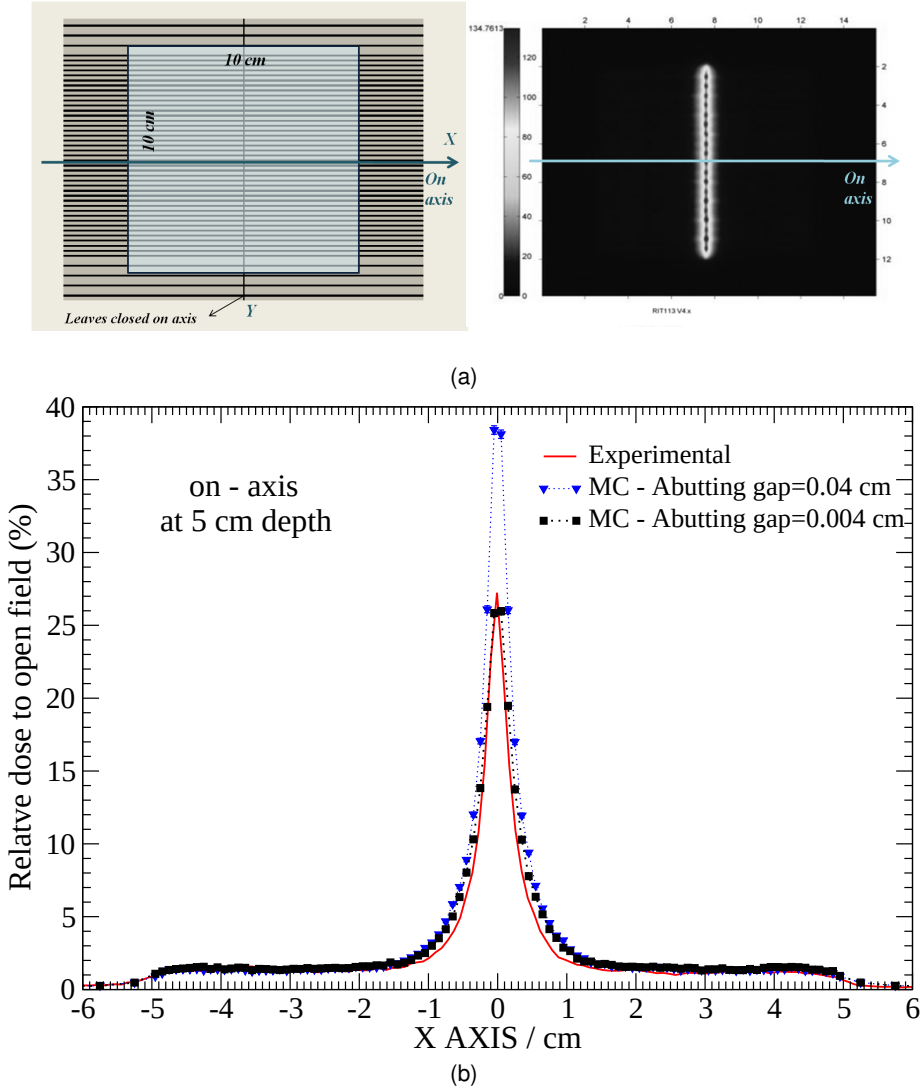

Figure 7.5: Film measured (red line) and calculated (symbols) leakage dose profile in percentage through opposing leaves completely closed at the central axis of a 10 x 10 cm^2 field defined by jaws. The effect of abutting air gap width is shown for a 6 MV photon beam. The profiles were obtained at a depth of 5 cm in a homogenous water phantom with a SSD of 95 cm. The profiles are normalized to the on-axis value calculated for a 10 x 10 cm^2 field.

Overall, the MC model reproduces accurately the considered MLC rounded leaf-tip curvature. However, in the bottom region of the peak, i.e. the tail region from ± 0.5 cm to ± 1 cm, the calculation appears to overestimate slightly the film data by ∼ 2 %. A combination of factors such as the higher spatial resolution of the film (0.0178 cm) compared to the resolution of the MC calculations (0.1 cm) or the energy dependence of the film in low dose regions, as it occurs in this region, can presumably explain the differences in the tail region of the transmission peak.

II. Leaf positioning accuracy verification

It is important to check whether the MLC model predicts correctly the position and geometry of the leaf ends. For this purpose, depth dose and transversal profiles at 5 cm depth were calculated in a water phantom for a series of fields defined with the MLC ranging from 2 x 2 cm^2 to 20 x 20 cm^2. The jaw openings were wider than the MLC field with their position 5 mm backed up of the leaf positions in the leaf motion direction. A voxel size of 0.1 x 0.1 cm^2 along the X and Y axis was used for all the defined fields. For the Z axis, the first 5 cm were divided into voxels of 0.2 cm and the rest in 0.5 cm voxels.

Experimental profiles were taken with a PinPoint ionization chamber in a water phantom, in this case. The measurements and calculations of this verification stage are compared in figures 7.6. Depth dose curves were normalized to the corresponding maximum value of dose for each field, whereas dose profiles were normalized to an on-axis dose value.

As it can be seen, the agreement between measured and simulated PDD curves beyond the build-up region ($d > d_{max}$) is about 1 % for all field sizes, within the MC statistical uncertainty at the maximum dose of about 1% for the small field (2 x 2 cm^2) and 1.6 % for the largest field (20 x 20 cm^2). Large discrepancies (up to 3-4 %) between measurements and calculations were observed in the build-up region. As stated earlier in previous chapters, the build-up region is characterized for a lack of charged particle equilibrium. Under these non-equilibrium conditions, the placement of a detector causes electron fluence perturbations, which, as consequence, results typically in overestimation of the dose. Furthermore, according to other authors [Abdel06], the correction factors applied for the conversion of the measured ionization profiles to absorbed dose profiles can vary significantly in this region. The variation of this factors should be therefore taken into consideration; however, these factors are not yet well established in the literature.

Regarding transversal dose profiles, it is observed an excellent agreement (less than 1 %) between measured and calculated dose profiles along both X axis and Y axis.

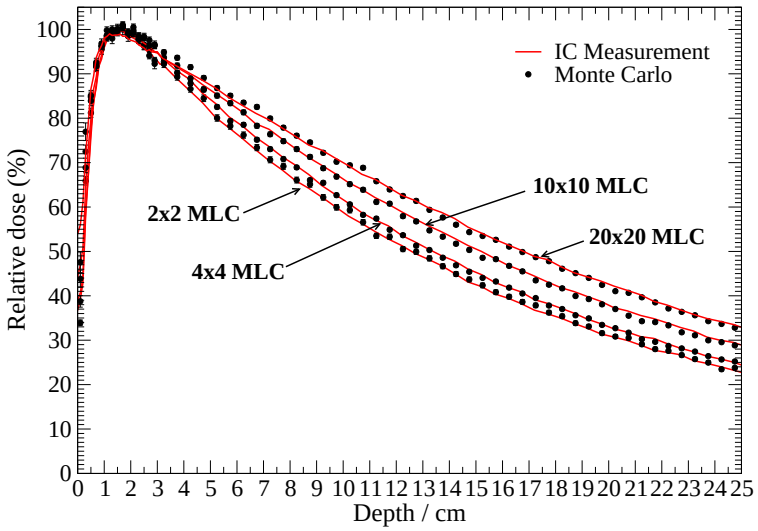

(a)

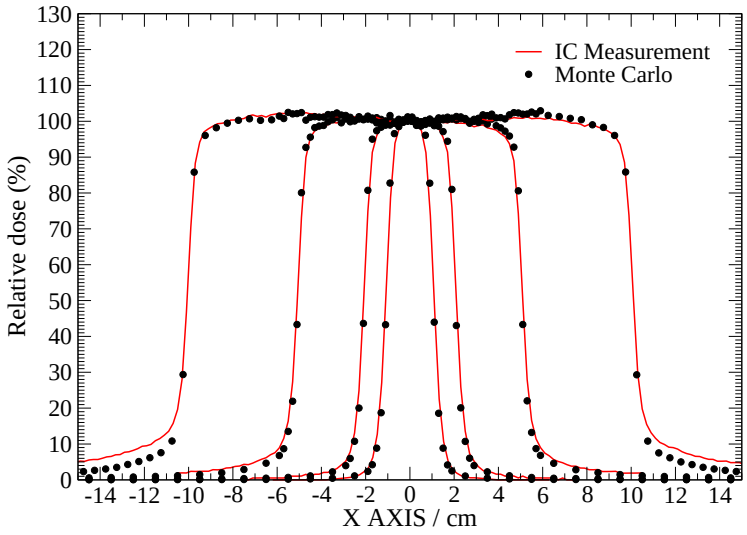

(b)

Figure 7.6: Comparison of depth-dose (a) and transversal dose profile along the X axis (b) of a homogeneous water phantom for 2 x 2 cm^2, 4 x 4 cm^2, 10 x 10 cm^2 and 20 x 20 cm^2 MLC defined fields. Red solid lines indicates measurements using a PinPoint ionization chamber, while full circles correspond to MC calculations. Profiles were obtained at 5 cm depth in water for a 6 MV photon beam and 95 cm SSD.

III. Tongue-and-groove leaf end verification

The impact of the tongue-and-groove design was investigated by creating a test field with alternating closed at the central axis and open leaves (Fig. 7.7a). This field was configured with the jaws set to produce a 10 x 10 cm^2 field. Films were exposed again at 5 cm depth with a 95 cm SSD and compared with MC calculations performed under the same conditions. The MC statistical uncer-

tainty was 2 % for the maximum dose values; the uncertainty associated with film measurements was within 5 %. Results of the comparison are shown in figure 7.7b. Considering the sources of uncertainty in calculations and measurements, it can be seen that the calculated dose profile correctly predicts the pattern of the experimental dose profiles. The average discrepancies between the simulation and measurement are about 3 % along the entire field. The maximum discrepancy found between the dose peaks and valleys of the dose profiles comparing film dosimetry with the simulations is of 5 %. These largest differences are likely due to issues of response and reproducibility of the film.

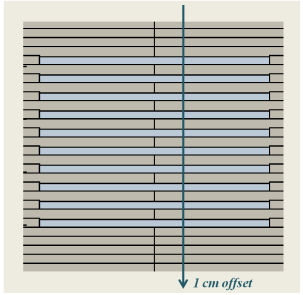

(a)

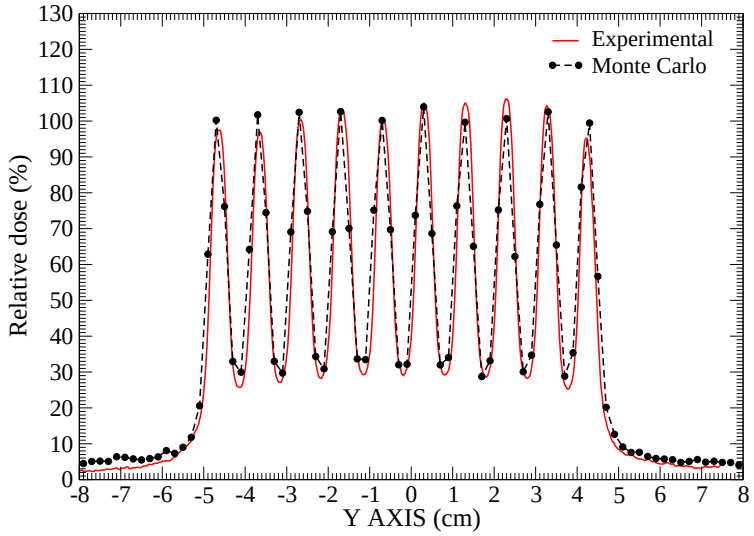

(b)

Figure 7.7: Film measured (red line) and MC calculated (full circles) dose profile for 10 x 10 cm^2 jaws-defined field blocked by even numbered MLC leaves with odd numbered MLC leaves retracted behind the jaws. Profiles were obtained at 5 cm depth in water along the axis perpendicular to leaves direction (blue line in (a)) for a 6 MV photon beam with a 95 cm SSD. The MC statistical uncertainty was 2 % for the peak of maximum dose.

IV. Dynamic leaf position sampling verification

To verify the accuracy of the sampling technique included in the DYNVMLC model for simulating the delivery of complex and dynamic MLC intensity distributions, the dose distributions for a pyramid pattern with five intensity levels of 100, 80, 60, 40 and 20 % (Fig.7.8a) delivered using a dynamic mode was simulated in a water phantom and compared with film measurements taken under the same conditions. This field shape is one of the tests suggested by Varian (Varian Medical Systems, Palo Alto, CA) to assess and record the quality assurance aspects of the multileaf collimator when used for clinical treatments on a regular basis [Var00]. In particular, this test is used to verify the

accuracy and calibration of the leaves as well as to evaluate the ability of the MLC to produce complex intensity modulated patterns. For the irradiation of this field, the Varian proposes the use of a build-up thickness of 2 cm above the dosimeter, i.e. the EDR film in our case.

Results of the comparison between measured and calculated transversal dose profiles are illustrated in figures 7.8b and 7.8c. The profiles in these figures were obtained in a water phantom (2.3 cm depth) along the X and Y axis at the position indicated by blue lines in the image 7.8a. The voxel size used for the calculation were 0.1 x 0.1 x 0.1 cm^3 along X, Y and Z axis, respectively. The jaws opening were set to define a field of 11.4 x 10.4 cm^2. The statistical uncertainty of the MC calculations is 2 % at the values of maximum dose of the profiles (at x = -4.5 cm and x = 4.5 cm). EDR2 films for the measurements were exposed in a solid water phantom under the same conditions as the calculations.

In general, the calculated and measured dose profiles along the Y axis shows a good agreement (better than 2 %) over the overall region of the profile. However, there are isolated dose values around - 2.5 cm and 1.5 cm where discrepancies (up to 5 %) were noted. Considering the uncertainty estimated for the film measurements, these discrepancies may be likely attributed to issues related to the response and reproducibility of the EDR films.

For the X profiles, the measurements and the calculations dose values shows an agreement better than 5 % along the negative region of the profile. In contrast, a worst agreement (up to 8 %) between the MC calculated dose values and the film measurements is however observed along the positive region. By observing the shape of the measured profile along the X axis, it may be seen that the profile presents a slight asymmetry, while the MC shows a more symmetric behavior along the entire field. This asymmetry of the beam along the X axis was observed for other type of fields (see transversal dose profile for a 20 x 20 cm^2 MLC-defined field). This fact along with the high uncertainty of the film response could explain the large differences observed in this profile region.

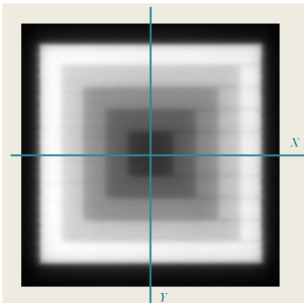

(a)

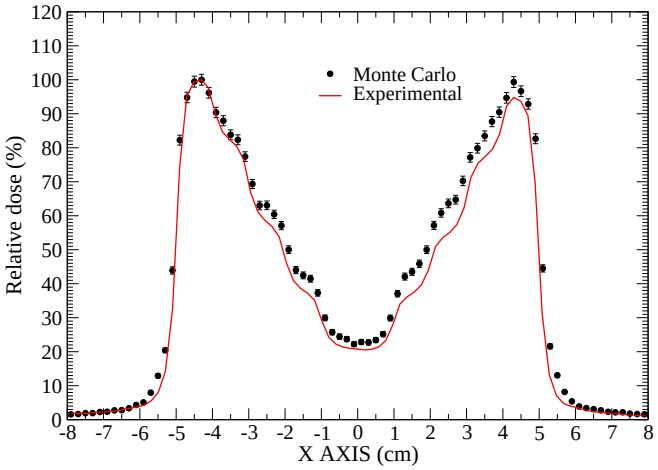

(b)

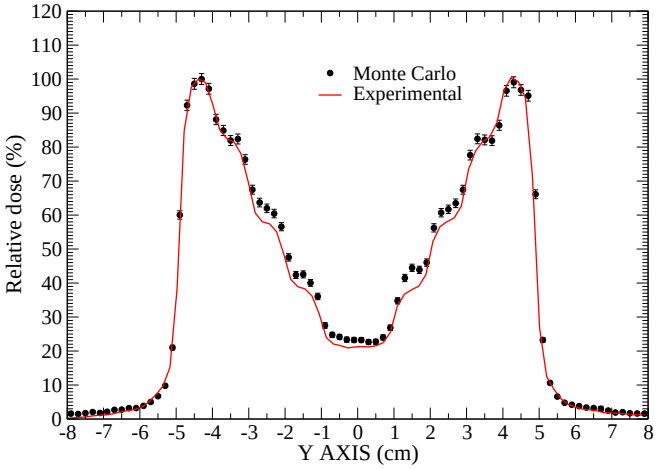

(c)

Figure 7.8: Comparison of (a) X and (b) Y profiles at a depth of 2.3 cm in water for a pyramid pattern with five intensity levels (100, 80, 60, 40 and 20 %) delivered using a dynamic mode. The red solid lines indicate the film measurement in a solid water phantom with EDR film and full circles represent MC calculations. The statistical uncertainty of the MC calculations is within σ = 2 % at the maximum dose values of the profile. Profiles were obtained for a 6 MV photon beam at 95 cm SSD with a 11.4 x 10.4 cm^2 field defined by the jaws.

7.3 Conclusions

A detailed model of the Varian Millennium 120-leaf multileaf collimator was incorporated in the Monte Carlo simulations of the Varian 2100C/D linac previously commissioned in chapter 6. The component module DYNVMLC coded by Emily Heath *et al* [Hea03] was used to simulate the full geometry of the three different leaf types forming this collimator. The MLC model described here was able to reproduce complex geometry details of the MLC, such as the tongue-and-groove designs, rounded leaf ends, support railing groove and driving screw hole.

The specifications of the MLCs necessary for the MC model were mostly provided by the manufacturers. There were however certain parameters affecting the simulation of the MLC's in terms of dose distributions, which were not well specified or even not provided by the manufacturers. In particular, the unspecified parameters included MLC leaf density, interleaf gap width (gap between adjacent leaves) and abutting gap width (gap between fully closed opposing leaf pair). Due to the high influence of these parameters on the dose distributions, it was necessary to determine them by fitting MC calculations to measurements. For this purpose, MLC leakage profiles were calculated for various sets of these unknown parameters to determine their dosimetric effects and their optimal combinations to give the closest agreement with EDR film measured results.

Final values of these MLC characteristics were:

- Leaf density : 17.35 gcm^3
- Interleaf air gap: 0.006 cm
- Abutting air gap: 0.004 cm

Once the geometry of the MLC was perfectly modeled and the unspecified MLC parameters were determined, a series of tests consisting of leaf positioning and static MLC shapes were performed to verify the details of the MLC model, such as the tongue-and-groove design and the rounded ends included in the model. The calculations showed agreement within 1 and 2 % with radiographic film (type EDR2) and ionization chamber (PTW PinPoint model) measurements for these static shapes. Dynamic MLC configurations were also calculated and compared to EDR film measurements to validate the accuracy of the sampling technique used for simulating the delivery of dynamic fields. The overall agreement with EDR film measurements were within 4 - 5 % for these dynamic fields. This may be probably attributed to issues of response and reproducibility of the EDR films.

Overall, it has been shown that the model of the MLC reproduced with high precision a series of experimental test fields, including static and dynamic fields of a variety of MLC shaped patterns. The output of the model was found to be very sensitive to the density of the tungsten alloy composing the leaf as well as to the interleaf and abutting air gaps. In fact, a change of leaf density from 17.0 to 17.7 gcm^{-3} results in a decrease of about 15 % of the average MLC leakage. A smaller influence (about 8 %) on the interleaf leakage was found for the increase of the interleaf air gap from 0.006 to 0.008 cm. Finally, an increase of the abutting air gap from 0.004 to 0.04 cm leads to an enhancement of up to 40 % in the average transmission through closed leaf pairs.

It is therefore concluded from the present results that the described MLC model is able to reproduce quite accurately the characteristics of the Millenium MLC (leaf geometry, tongue and groove design, rounded leaf end design) as well the motion of the leaves defining dynamic distributions. The MLC model is thus used for the MC calculations of the clinical radiotherapy applications presented in the following chapters.

Chapter 8

Assessing Multileaf Collimator effect on the build-up region for 6 MV photon beams

8.1 Motivation

As referred in chapter 7, the multileaf collimator (MLC) has become one of the most important devices for external radiotherapy, specially since the implementation of the Intensity Modulated Radiation Therapy (IMRT) technique.

As discussed in detail in previous sections, the MLC presents a complicated geometry, with rounded leaf ends and a tongue-and-groove design. Several works have reported that MLC geometry characteristics can cause specific delivery issues and affect the final dose distributions [Kim01, Hea03, Leal04, Jan06, Tyagi07]. In general, the contribution of the MLC is presented in terms of: (a) scattered photons and electrons from the leaves; (b) transmission and leakage between the leaves and the rounded leaf edge and (c) a beam hardening caused by the attenuation of the low energy photons. An additional influence of the MLC occurs as a consequence of the tongue-and-groove design, named ”tongue-and-groove” effect. This special arrangement designed to minimize the interleaf transmission can lead to an underdosing of the region where the tongue

and groove overlap.

An important issue regarding the dosimetric contribution of a MLC is related to its impact on the surface dose and the build-up region. In radiotherapy, the accurate determination of the absorbed dose in both surface and build-up regions are of major importance to physicists and medical physicist for two reasons: on one hand, in order to prevent dermatological complications during a treatment and, on the other hand, because there are some clinical situations (head and neck cancer) where the target volumes or normal tissue volumes have superficial extension close to the skin.

It is well known that the largest contribution to the surface dose comes from the electron contamination emanating from the accelerator head; in particular, electrons originated primarily from the flattening filter, secondarily from the air between the treatment head and the patient and, finally, from the collimation system of the accelerator head. The electron contamination contributes to the dose at zero depth but decreases rapidly from the head. Near the surface, the low-energy head-scattered photons provide a negligible contribution, but quickly increase to the dose with depth [Pur86, Houn99, Yok04]. As previously discusses in the chapter 6, head-scattered photons come primarily from the linac components placed above the secondary collimators, namely the flattening filter and the primary collimator.

The use of the MLCs for field shaping represent an additional source of contaminant electrons and scattered-photons which can affect the dose in the surface and build-up region. According to [Yok04], the build-up region dose depends on the position of the MLC leaves during the beam delivery and thus can be also influenced by the delivery technique.

Kim *et al* (2000) [Kim01] found using detailed MC simulations of simple static fields that the MLC is a great source of electrons and scattered photons contributing to the surface dose. In particular, they found that the electrons ejected from the MLC can contribute up to 18 % to the surface dose for a 6 MV photon beam of a 10 x 10 cm^2 MLC blocked field.

The quantification of the surface dose and build-up dose has been subject of many studies using experimental measurements and Monte Carlo simulations [Abdel06, Par08, Bilge08]. From the experimental point of view, various techniques (extrapolation chamber, parallel chamber, TLD, etc.) have been used to measure dose in these regions. Among all these techniques, the established instrument of choice to perform measurements in regions of high-dose gradient such as the build-up region is the extrapolation chamber. However, few radiotherapy departments have extrapolation chambers at their disposal and, alternatively, thimble or parallel-plate chambers are mostly employed

for this purpose. These last detectors show however some limitations in obtaining accurate dose at the surface or build-up region, especially due to the perturbation of the electron contamination originated from their design, which tend to provide a dose overresponse in these regions [Abdel06].

Few of the mentioned previous works evaluating the dose at the surface and in the build-up region report quantitative information about the overall MLC effect, as well as, the dependence of this effect on the field size. Kim et al 2000 [Kim01] performed the investigation only for a 10 x 10 cm^2 field fully blocked by the MLC and, on the other hand, they made an extrapolation of the dose calculated in the voxel from 0 to 0.2 cm depth to the surface, in order to evaluate the surface dose.

In the present chapter, the effect of the MLC on the build-up region dose for symmetric and asymmetric MLC defined field sizes of 2 x 2, 4 x 4, 10 x 10 and 3 x 7 cm^2 was investigated. For this purpose, Monte Carlo simulations were performed using the detailed linear accelerator and MLC model described in previous chapters 6 and 7. To quantify the surface dose, the dose value was scored directly in a voxel of 0.025 cm thickness. Moreover, the contributions from the MLC contaminant particles to the total build-up dose were determined. Fluence and energy spectra of photons and electrons reaching the phantom surface placed at 95 cm SSD were investigated. The contribution of the particles scattered from the MLC to total fluence was separated from the contribution of the particles scattered from the rest of the accelerator components.

Additionally, experimental measurements in a water phantom were also carried out with two different ionizations chambers (IC) for the same set-up as the MC calculations. In order to determine the MLC contribution, percentage depth ionizations (PDIs) curves were measured including and excluding the MLC for the collimation of the beam. The results of this experimental work are presented in the second part of this chapter.

Finally, this chapter ends with the experimental validation of the MC calculated doses in the build-up region. The PDD curves obtained with Monte Carlo were compared with the PDI curves measured using the ionization chambers. The discrepancies observed between both approaches are also discussed.

8.2 Monte Carlo evaluation of the MLC effect

8.2.1 Monte Carlo calculation techniques

For this investigation, the previously modeled Varian 2100C/D linear accelerator including the 120-leaf Millenium MLC (Chapters 6 and 7) was used for a 6 MV photon beam.

The Monte Carlo simulations were split into three different stages (figure 8.1).

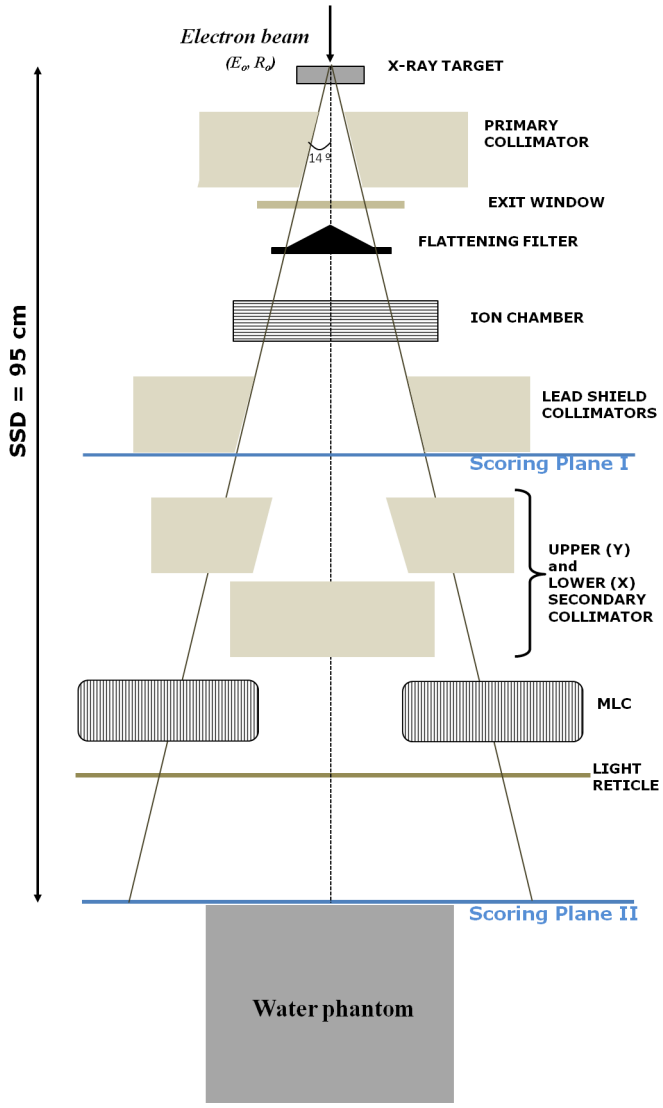

Figure 8.1: Schematic representation of the simulated geometry of the Varian 2100C/D linac head and water phantom, showing also the location of the two phase space scoring planes considered for the simulations.

First, a phase-space file at a plane before the jaws (at z = 27.09 cm) was obtained. This phase-space file was simulated just once since the components of the linac considered in this part were fixed and independent of the field size and configuration. In the second stage, a set of output phase space files for the various MLC and jaws field size configurations were obtained using previous phase-space file just above the phantom surface located at a SSD of 95 cm. Finally, these phase-space files were then used as source of the water phantom simulations, which were performed using the CHAMBER CM of the BEAMnrc code. Figure 8.1 shows details of the treatment head configuration, including the different stages considered in the simulations.

For the study, MLC symmetric openings of 2 x 2, 4 x 4 and 10 x 10 cm^2 and asymmetric 3 x 7 cm^2 field were simulated. For all these openings, the collimating jaws were set to back up the leaf positions by 5 mm in X and Y direction, defining 3 x 3, 5 x 5 and 11 x 11 cm^2 and 4 x 8 cm^2 fields, respectively. For the purpose of this study, we name each of these configurations "*MLC defined field*". In order to analyze the contribution of the MLC, it was useful to define a field in which the MLC leaves were withdrawn beneath the jaws so as to not intercept the beam (50 x 50 cm^2 MLC opening). The field size was then defined by the above mentioned collimating jaws opening. For this study, we name each of these configurations "*MLC open field*".

The dose calculations were performed for a water phantom of 20 cm radius and 3 cm thick, with a central axis scoring region of radius r, as shown in figure 8.2. Voxels of 0.025 cm were set up at shallow phantom depths (from 0 to 0.4 cm depth). Larger voxels of 0.05 and 0.1 cm thickness were used along the remaining phantom [Mor99]. The radius r was set to 1 cm for the 10 x 10 cm^2 field and 0.5 cm for the 4 x 4 cm^2, 2 x 2 cm^2 and 3 x 7 cm^2 field sizes.

To avoid underestimating the surface dose, the electron cutoff energy (ECUT) and the photon cutoff energy (PCUT) for all simulation stages were set to 0.521 MeV and 0.01 MeV, respectively. However, auxiliary calculations with ECUT equal to 0.700 MeV and PCUT equal to 0.01 MeV were performed in order to analyze the influence of this parameter on the results. Differences of about 0.5 % were observed between the PDD along the build-up region calculated using different ECUT values for the MLC defined field of 10 x 10 cm^2 size. Although the differences were not relevant, the final ECUT considered for all three phases of the calculation was 521 keV since the work pretended to determine the dose at the surface and build-up region with the highest possible level of precision.

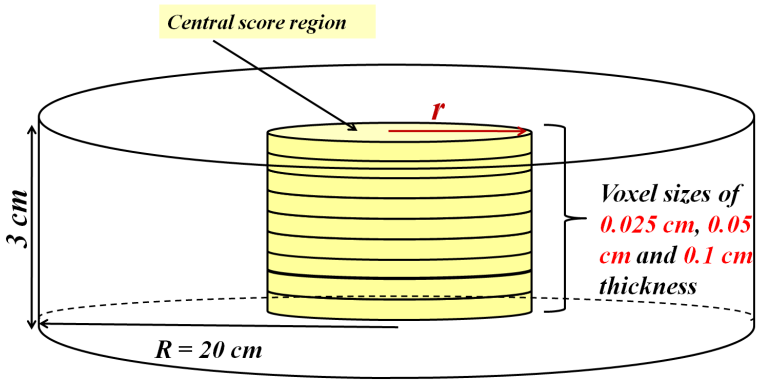

Figure 8.2: Simulated water phantom geometry. Voxels of 0.025, 0.05 and 0.1 cm were set up from 0 to 3 cm depth. The radius r was varied between 1 and 0.5 cm according the field size. The phantom was modeled using the CHAMBER CM of the BEAMnrc code. (This figure is not to scale)

To improve the calculation efficiency, various variance reduction techniques, such as uniform bremsstrahlung splitting with a photon split of 20 [Rog05] and range rejection with ESAVE of 1 MeV were employed for the first two steps of the accelerator simulation. This last technique introduces one approximation by ignoring the possibility that the electron produces a photon which could then escape from the current region. Auxiliary calculations without this approximation were done and no effect in the calculated photon and electron spectra was found.

For the first phase of the simulations, 5 x 10^8 electrons were incident on the target which resulted in about 4.8 x 10^8 particles from which 99.9 % were photons. These particles were then transported along the second part of the treatment head containing the jaws and the MLC collimator. For this second phase of the simulation, the previous particles were not recycled any time. This second stage resulted in phase-space files containing about 3.6 x 10^6 (2 x 2 cm^2) and 8.8 x 10^7 (10 x 10 cm^2) of particles reaching the second scoring plane at 95 cm SSD. Finally, a number of histories of 3.6 x 10^7 (2 x 2 cm^2) and 8.8 x 10^8 (10 x 10 cm^2) was run for the phantom calculations to ensure that the error for each voxel in the central axis scoring region was less than 1% (1σ) at depth of maximum dose (1.5 cm), d_{max}. For each dose calculation, the particles of the phase-space files generated in the second stage of the simulation process were thus recycled 9 times.

8.2.2 Dose contribution from the total- and MLC-scattered particles: dependence on field size

In this section, we investigate the influence of the MLC on the dose build-up curve in a homogeneous water phantom. Figures 8.3a - 8.3f and 8.4a - 8.4b present the comparison of relative central-axis PDD curves for several MLC defined field sizes (10 x 10, 4 x 4, 2 x 2 and 3 x 7 cm^2) to the MLC open field respective ones. For each situation, the curves were normalized to the dose at the depth of maximum dose for the MLC open field configuration.

I. MLC dose contribution to total dose as function of field size

The effects of the MLC on the dose build-up curves are clearly seen from the differences between the dose values calculated for the MLC defined field (black solid line) and those values calculated for the MLC open field (black dashed line) for all the fields studied. In Figures 8.3a - 8.3d, it can be seen that the contribution to the dose of the MLC (10 x 10 and 4 x 4 cm^2 MLC defined fields) is very small (< 1 %).

For these fields, the differences between MLC defined field and MLC open field curves are less than 1%.

For the smallest field size (2 x 2 cm^2), the MLC contributes about 2 % of the total dose at a depth larger than 7 mm.

Figure 8.4a - 8.4b present the dose build-up curves for the asymmetric field (3 x 7 cm^2); the observed MLC effect is roughly the same we observed for the 4 x 4 and the 10 x 10 cm^2 field sizes.

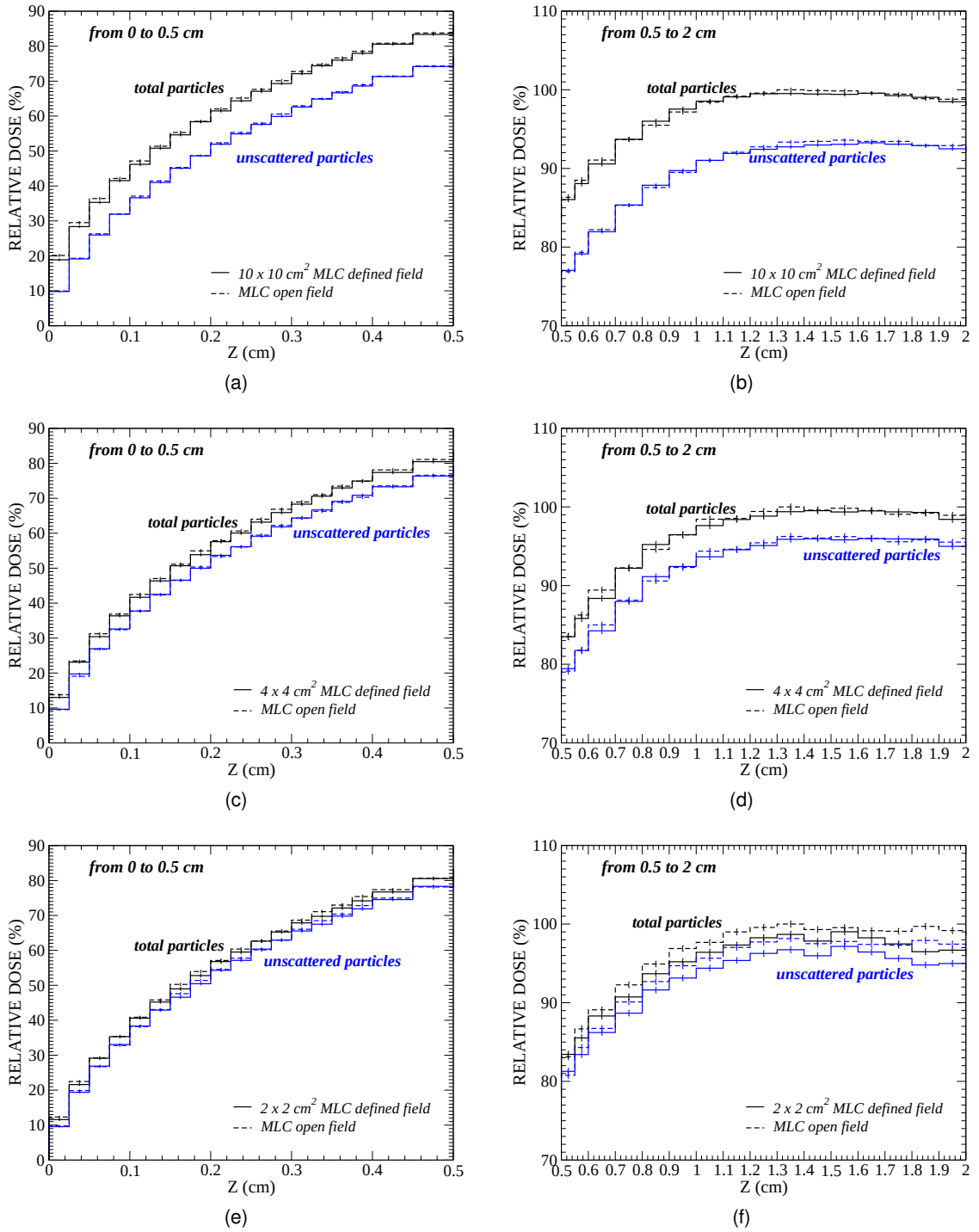

Figure 8.3: MC calculated depth dose curves in the build up region for the MLC defined field size of (a-b) 10 x 10 cm^2, (c-d) 4 x 4 cm^2, (e-f) 2 x 2 cm^2 in comparison to the MLC open field respective ones (dashed line). The curves were separated in two intervals: from 0 to 0.5 cm depths (left) and from 0.5 to 2 cm depths (right) for a better visualization. The components of the dose due to unscattered particles are shown (blue line). All curves were normalized to D_{max} of the total dose curve for the MLC open field.

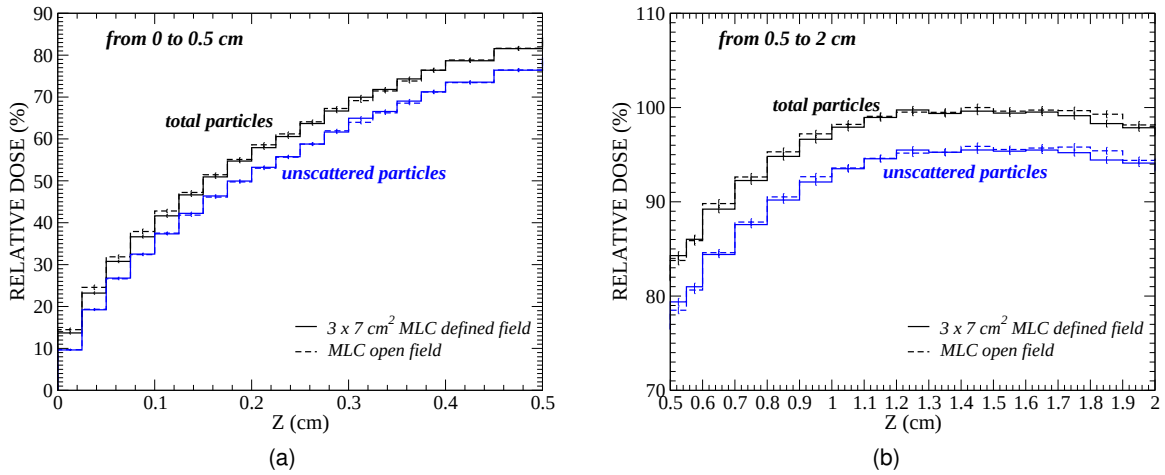

Figure 8.4: MC calculated depth dose curves in the build up region for the MLC defined field size of 3 x 7 cm^2 in comparison to the MLC open field respective one (dashed line). The curve was separated in two intervals: from 0 to 0.5 cm depths (left) and from 0.5 to 2 cm depths (right) for a better visualization. The components of the dose due to unscattered particles are shown (blue line). The curves were normalized to D_{max} of the total dose curve for the MLC open field.

II. Total head-scattered particles contribution to total dose as function of field size

Figures 8.3a - 8.3f and 8.4a - 8.4b present also the relative central-axis depth dose curves calculated for unscattered particles only, for MLC defined fields and MLC open fields. By comparing the total dose and the dose due only to unscattered particles, the overall effect of the accelerator head (including also the effect of the MLC) on the build-up dose curve may be assessed.

For the largest field (10 x 10 cm^2), the contribution of the accelerator head results in an enhancement of the relative dose for the unscattered particles by a factor of 1.5 in the first 7 mm from the surface, and it decreases gradually to a factor of 1.2 at the depth of maximum dose. As we expected, the contribution of the scattered particles decreases with the field size and, as it is observed, the dose for the total particles relative to the unscattered dose contribution is higher by a factor of 1.04. Finally, for the asymmetric field, the overall head accelerator contribution increases the dose for the unscattered particles with a factor of 1.07.

By comparing the curves for the MLC defined fields and MLC open fields, it can be seen that the behavior of the MLC effect in the build-up region for the unscattered particles contribution is similar to the one obtained for total dose curves, i.e. the differences between MLC defined field and MLC open field curves are less than 1% for all fields, except for the 2 x 2 cm^2 field size where a difference of 2 % is found at a depth larger than 7 mm.

Table 8.1 summarizes the differences between the total dose and the dose due only to unscat-

tered particles near the phantom surface. These surface dose values were calculated directly in the voxel from 0 to 0.025 cm depth. From the table, it is seen that the scattered particles component is responsible for the increase of the relative surface dose from about 10 % to 19 % for the 10 x 10 cm^2 field. This enhancement effect decreases with field size, being a factor of 4 smaller for the 2 x 2 cm^2 field.

Table 8.1: Surface dose calculated in the voxel from 0 to 0.025 cm depth for different MLC defined field sizes, as shown in figures 8.3 and 8.4. Total and unscattered particles contributions are shown. The relative uncertainty is less than 2 %.

MLC defined field size	**Surface dose (Total dose)** [%]	**Surface dose (Unscattered particles)** [%]
10 x 10 cm^2	18.88	9.80
4 x 4 cm^2	13.02	9.65
2 x 2 cm^2	11.58	9.56
3 x 7 cm^2	13.68	9.63

8.2.3 MLC effect on spectra at the phantom surface

Figures 8.5a - 8.5c present the normalized total fluence of particles and individual contribution of electrons reaching the plane at SSD = 95 cm for the studied MLC symmetric openings. Figures 8.6 show the contribution of particles and electrons scattered from MLC and jaws to the total fluence. All presented fluence spectra were scored within the field and also 3 cm beyond the geometric respective edge for each MLC defined field. Several subdivisions are considered according to the last scattering process suffered by electron and particles: from MLC only, from jaws only and from both jaws and MLC. For each field, all values are normalized to the maximum value of total particle fluence. The relative statistical uncertainty of the fluence inside the field is less than 0.5 % for the total particles and around 5 % for the total electrons.

It can be seen that the electrons contribution represent only about 0.15 % of the total number of particles reaching the phantom surface for the 10 x 10 cm^2 MLC defined field and it decreases with field size, from 0.045 % for 4 x 4 cm^2 to 0.025 % for the smallest (2 x 2 cm^2) MLC defined field. The figure also shows that the electron contribution outside the field vary slightly ($\sim$ 20 %) with the distance to the beam axis.

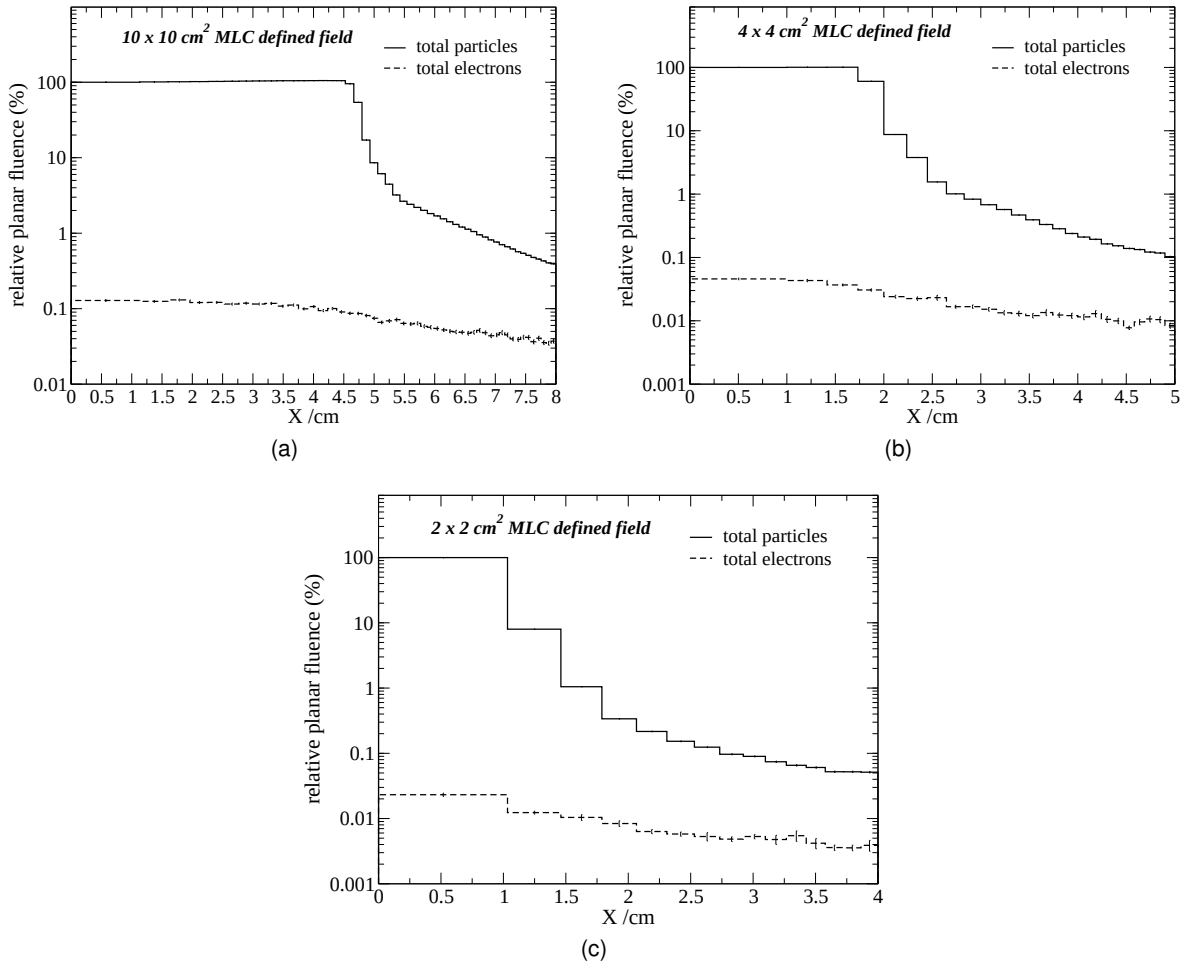

Figure 8.5: Relative planar fluence of total particles and electrons as a function of the distance to the beam axis (X axis). The MLC defined field was simulated to get a (a) 10 x 10 cm^2, (b) 4 x 4 cm^2 and (c) 2 x 2 cm^2 at 95 cm SSD. The planar fluence was calculated in the area defined by half-width of (a) 8 cm, (b) 6 cm and (c) 4 cm which was divided in 50, 25 and 15 equal square bins, respectively.

In figures 8.6b and 8.6d, it is observed that about 8 %, for 10 x 10 cm^2, and 3 % for smaller fields, of the total electron fluence is due to electrons scattered from jaws only, from MLC only or from both, jaws and MLC. There are no significant differences between the jaws and MLC independent contributions to the total electron fluence.

The fluence of particles at the phantom surface including contributions from jaws and MLC is also shown for the 10 x 10 cm^2 MLC defined field in figures 8.6a and 8.6b. The relative uncertainty of the fluence inside the field (including the fluence spectra for the contribution from jaws and MLC) is within 1 % and 2 % for the particles and electrons in the 10 x 10 cm^2 field size, respectively. For the smallest field, the relative uncertainty inside the field is within 3 - 6 %. It can be seen that the number of particles scattered from jaws only represents about 0.2 % of the total number reaching

the phantom surface for the broad beam (10 x 10 cm^2) and no significant differences are observed for the contribution from MLC only. Lower contributions are observed as the field size decreases, being 0.05 % for 4 x 4 cm^2 and 0.02 % for 2 x 2 cm^2 MLC defined fields.

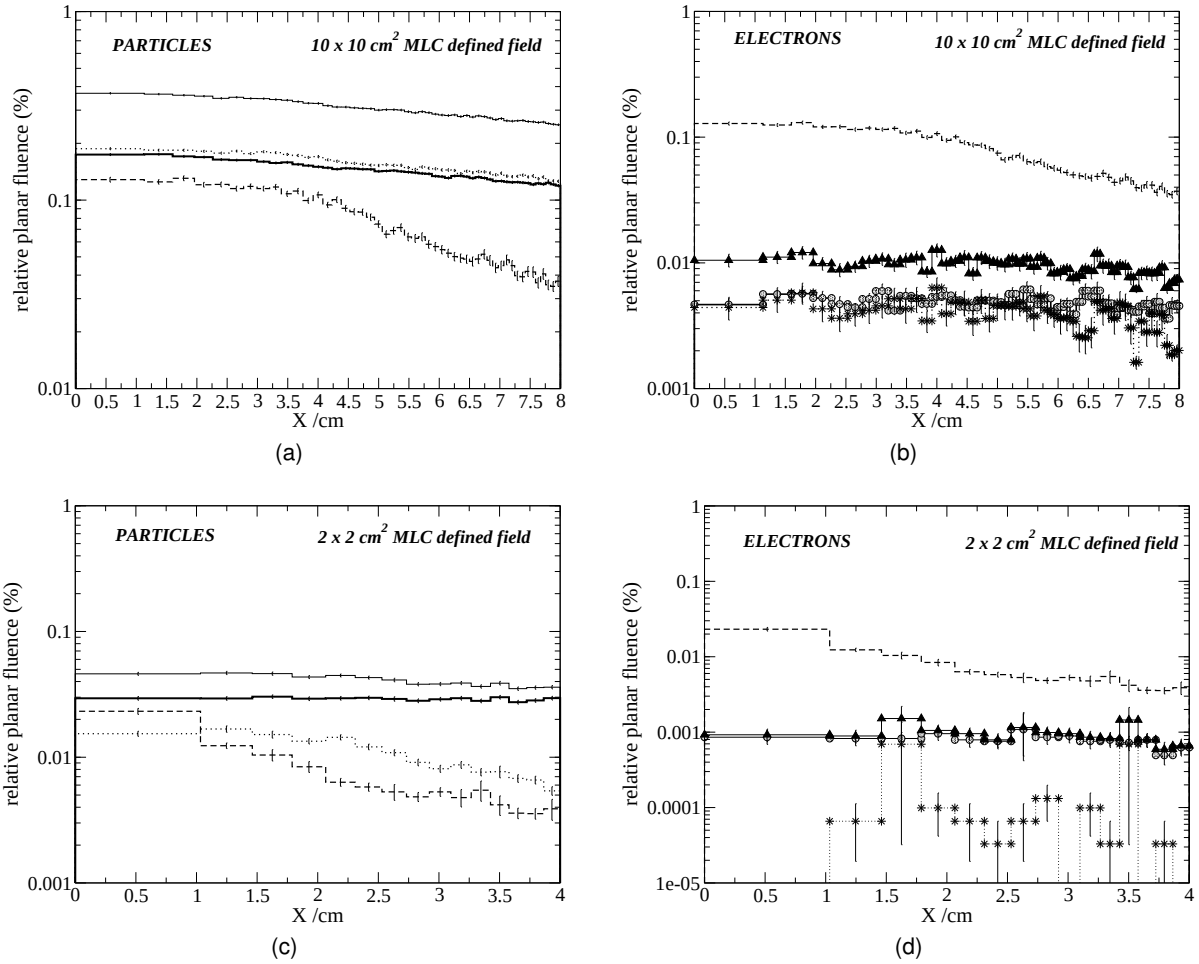

Figure 8.6: Relative planar fluence of particles and electrons as a function of the distance to the beam axis for 10 x 10 (top) and 2 x 2 cm^2 (bottom) MLC defined fields. Total electron contribution (dashed line) and various contributions of particles (left) and electrons (right) to the total fluence are represented: particles scattered from MLC only (thick solid line), from jaws only (dotted line) and from both MLC and jaws (thin solid line); electrons scattered from MLC only (circles), from jaws only (stars) and from both MLC and jaws (triangle up).

The on-axis photon and electron energy spectra are presented in figures 8.7 for the 2 x 2 cm^2 and 10 x 10 cm^2 MLC defined fields and the respective MLC open fields. The energy bins used for the calculation were 100 keV and 200 keV wide for photons and electrons, respectively. The relative uncertainty is less than 1 % for the total photons spectra and both fields. For the total electrons, the uncertainty increases to 6 % for the 10 x 10 cm^2 field size and up to 15 % for the 2 x 2 cm^2 fields.

The electron spectra shown in figures 8.7a - 8.7b were calculated for 3 x 3 cm^2 and 8 x 8 cm^2 for

the smallest and largest field sizes, respectively, because of the poorer statistics. For the field of 2 x 2 cm^2 the electron spectra were also calculated for 1 x 1 cm^2 scoring region and the results were similar because the electrons spread well outside the photon beam. For each field configuration, the spectra were normalized to the maximum value of total particle fluence calculated for the MLC defined field curve.

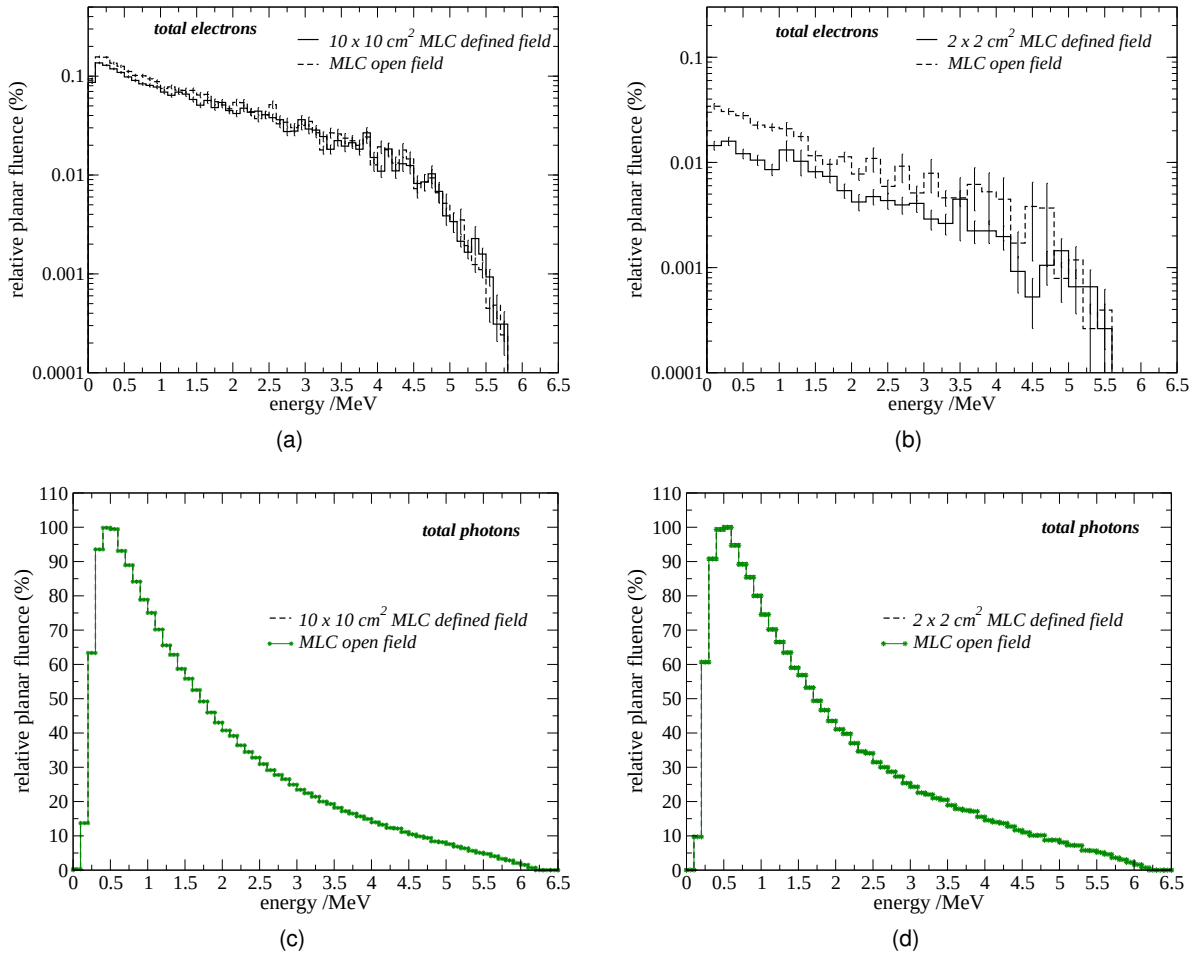

Figure 8.7: On-axis energy spectra of electrons reaching the scoring plane at 95 cm SSD for 2 x 2 cm^2 (right) and 10 x 10 cm^2 (left) MLC defined fields and the respective MLC open fields. The electron spectra were calculated for scoring regions of 3 x 3 cm^2 (right) and 8 x 8 cm^2 (left), with 200 keV energy bins.

In relation to total photon fluence, there are not differences between the MLC defined fields and the MLC open fields in the overall spectra. Maximum values in the photon spectra are found around 0.55 MeV and 0.45 MeV for the 2 x 2 cm^2 and 10 x 10 cm^2 MLC defined field, respectively. The same values are obtained for the respective MLC open fields.

In figure 8.6a it can be seen that the electron fluence for the 2 x 2 cm^2 MLC defined field repre-

sents about 0.016 % of the total number of particles for the lower energies (< 0.5 MeV). However, this value is about 0.034 % for the respective MLC open field. For the 10 x 10 cm^2 MLC defined field the electron fluence is about 10 times higher than those values for the 2 x 2 cm^2 field. For both fields, the electron fluence decreases with the energy. The relative uncertainty of the calculated electron fluence for the 10 x 10 cm^2 field is about 2 % for lower energies (until 1.5 MeV) and it is poorer for the rest of the spectra. For the 2 x 2 cm^2 case, the electron fluence have a relative uncertainty of about 9 % for the energy region below 1 MeV. After that, the uncertainty decreases.

8.3 Experimental evaluation of the MLC effect

8.3.1 Ionization chamber measurements

Percentage depth ionization (PDI) curves along the central axis were measured in a PTW Freiburg computerized water tank (model 31001) for the MLC defined field sizes described in the previous section 8.2.

Two different detectors were used for this investigation: a PTW Roos plane-parallel ionization chamber (model 34001) and a PTW cylindrical ionization chamber (model 31002). Some characteristics of both ionization chambers are summarized in table 8.2.

These chambers were mounted in the scanning system of the phantom, which, at the same time, was connected to the PTW software Memphysto mcc to automatically control the chambers for data acquisition of depth ionization profiles.

The effective point of measurement for the cylindrical ionization chamber was taken at 2 mm upstream of the center of the chamber cavity, consistent with the IAEA TRS-398 protocol [And00]. Following also this protocol, the effective point for the Roos chamber was situated at 1.1 mm upstream from the top surface of the chamber.

In order to analyze the contribution of the MLC, measured PDI curves for the different MLC defined fields were compared to the PDI curves measured for the respective "*MLC open field*", where the MLC was set with a 50 x 50 cm^2 opening and the jaws were set at the same position as in the MLC defined field. PDI curves measured with both chambers were done at the depths ranging from the phantom surface to 2.5 cm with a scanning step of 0.02 cm.

Table 8.2: Geometric characteristics of the ionization chambers used in this investigation: PTW Roos plane-parallel (model 34001) and PTW cylindrical (model 31002).

Chamber	PTW 31002 (cylinder IC)	PTW 34001 (Roos chamber)
Inner ϕ	5.5 mm	-
Length	7.5 mm	-
Chamber ϕ	-	15.0 mm
Cavity volume	0.125 cm^2	0.35 cm^2

8.3.2 MLC effect on depth ionization curves: dependence on field size

Figures 8.8 present the comparison of measured PDIs for the studied MLC defined field sizes to the respective MLC open field. On the left side of the figure, it is shown the comparison for the PDI measured using the cylindrical chamber and, on the right side, the measured PDI curves were obtained using the Roos chamber.

As it can be observed from the figures, there was no significant (~0.3 %) difference between the build-up dose values measured including MLC and those values measured for the MLC open field for all the studied field sizes.

According to the specification of the Roos chamber, this chamber is suited for the measurement of high-energy photon depth dose curves up to 2.5 mm below the water surface. This may probably explain the observed flatted and non-characteristic shape of depth dose measured with this chamber at ~0.25 cm shallow depths. Moreover, it must be taken into account that the Roos chamber may have a perturbing effect at smaller field sizes (2 x 2 cm^2) due its larger radius.

For the PTW cylindrical chamber, the observed MLC effect is roughly the same we observed for the Roos chamber. At shallow depths (up to 0.25 cm), differences of about 0.6 % were found for both ionization chambers. However, due to at these depths, half of the active volumes of the used chambers are outside the water phantom, it cannot be concluded that these differences could be caused by the MLC effect.

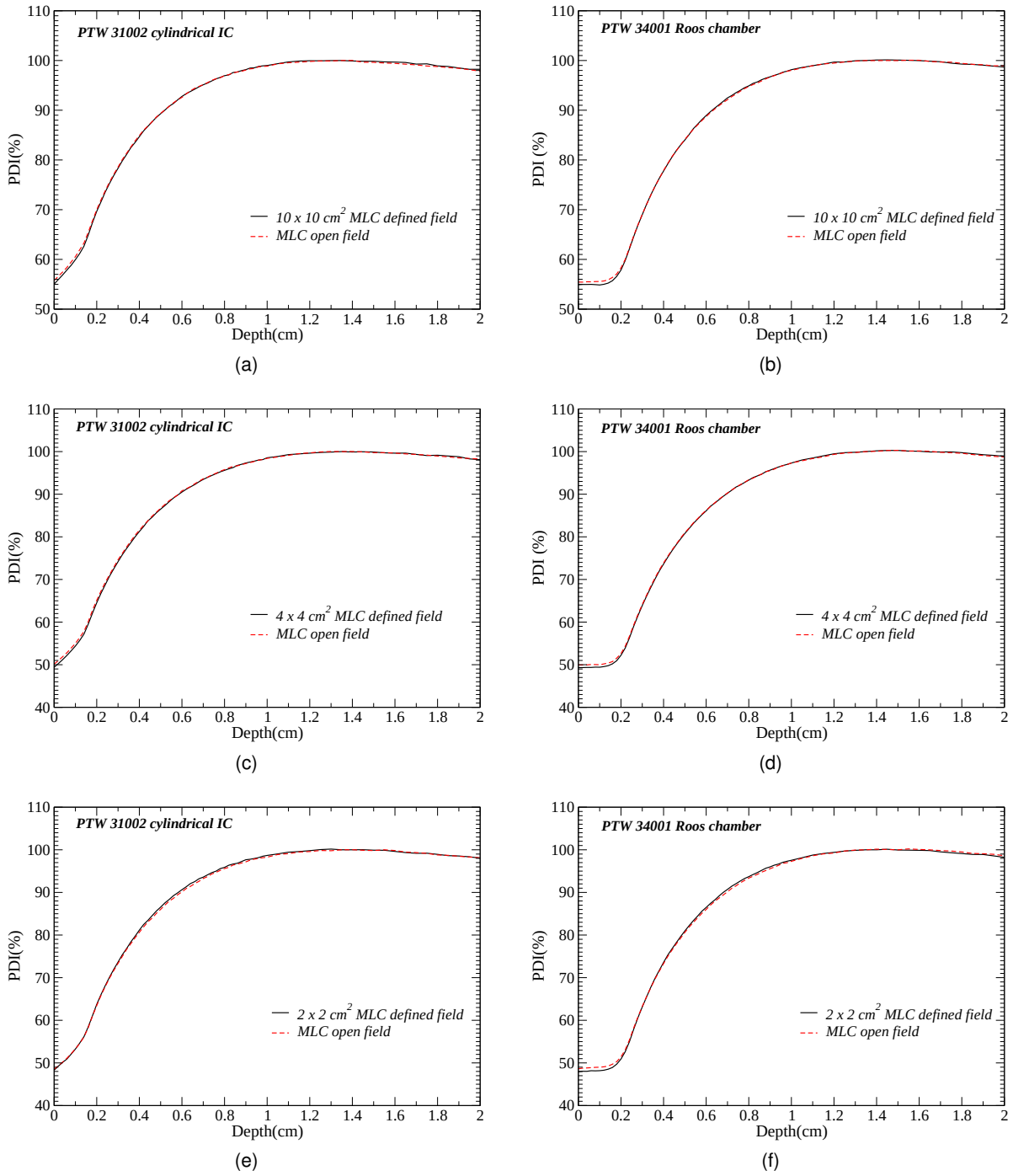

Figure 8.8: Measured PDIs in the dose build-up region of a water phantom with a cylindrical IC as well as a Roos parallel-plate ionization chamber for 10 x 10 cm^2, 4 x 4 cm^2 and 2 x 2 cm^2 MLC defined fields and the respective MLC open fields.

8.4 Experimental validation of MC calculated dose in the build-up region

This section aims to evaluate the differences between previous MC calculated and measured depth dose curves in the build-up region for the MLC defined fields of 2 x 2, 4 x 4 and 10 x 10 cm^2.

Figures 8.9 present the measured PDIs and MC calculated PDDs in the dose build-up region of the 6 MV photon beam for the three investigated fields.

For all cases, it is observed that the measured PDIs differ from the calculated PDDs and this difference depends on the measuring chamber type. While the PDIs obtained from the cylindrical chamber are higher than the PDDs obtained with MC simulations, an opposite behavior is observed when the PDIs are measured using the parallel-plate chamber.

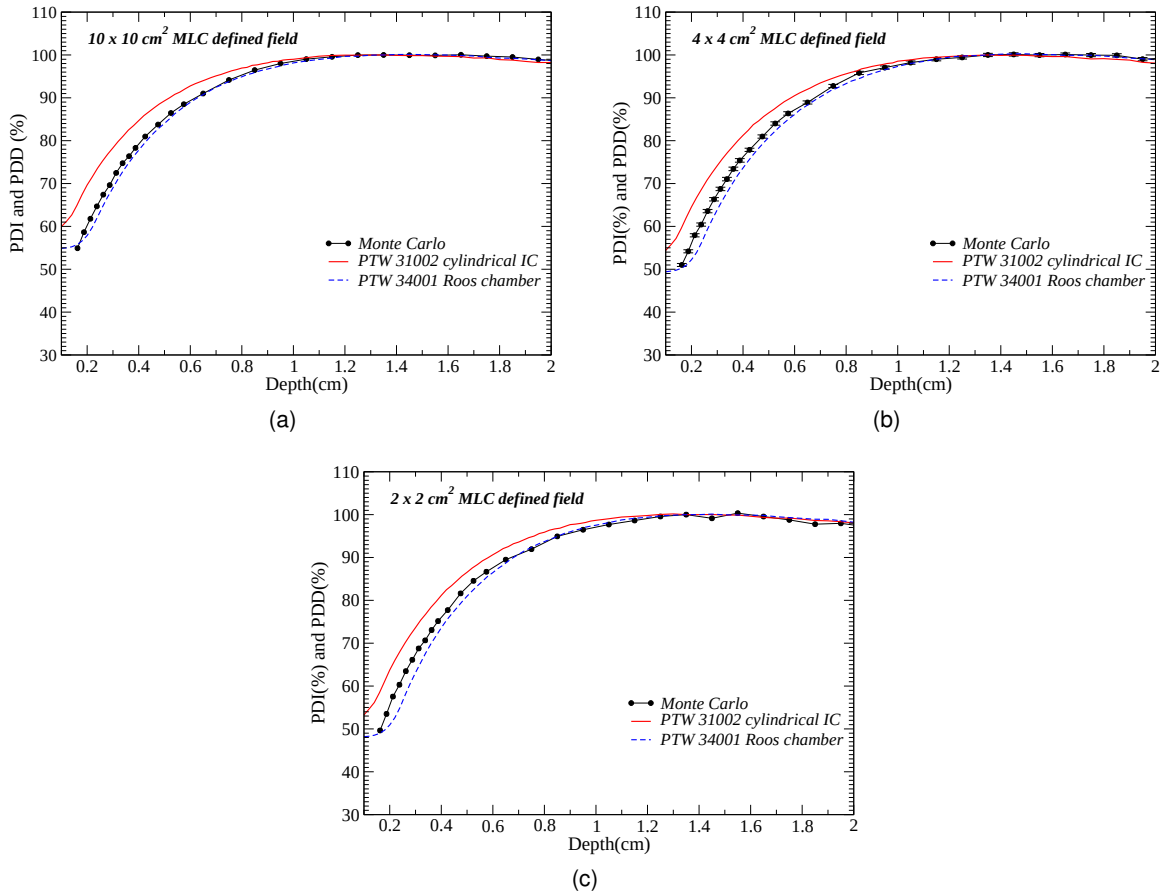

Figure 8.9: Measured PDIs in the build up region in water with a PTW 31002 cylindrical IC (solid red line) as well as a Roos parallel-plate ionization chamber (dashed blue line) for (a) 10 x 10 cm^2, (b) 4 x 4 cm^2 and (c) 2 x 2 cm^2 MLC defined fields, at 95 cm SSD for a 6 MV photon beam, compared with MC calculated PDDs.

In figures 8.9, it can be seen that the MC PDDs match the Roos measurements within ~1% for depths larger than 2.5 mm for the 10 x 10 cm^2 field size. For the 2 x 2 cm^2 field, a difference of about 2 % between Roos measured PDI and MC PDD was found.

On the other side, it can be seen that the PDIs acquired with the cylindrical chamber are larger than the MC PDDs by a factor of 1.1 for depths larger than 0.25 cm and for all field sizes.

Table 8.3 summarize the differences between calculated and measured doses at depths of 0.25 cm and 0.52 cm in the water phantom for each investigated field size. As seen, the maximum deviation between MC and measurements is within 7 - 8 % at the depth of 0.25 cm when the dose was obtained using the cylindrical chamber. Using the Roos chamber for the measurements, the differences with MC calculations at this depth are within 6 % for the smallest field size, decreasing to about 3 % for the field size of 10 x 10 cm^2.

At the depth of 0.52 cm, the discrepancies between MC calculated doses and the doses measured with both chambers are lower than those found at the previous depth. In this case, the doses obtained with both chambers differ by about 2 - 3 % with MC dose values for the field size of 2 x 2 and 4 x 4 cm^2. A smaller deviation (1 %) is however observed for the largest field (10 x 10 cm^2).

Table 8.3: MC calculated and measured doses at depths of 0.25 and 0.52 cm in a water phantom for a 6 MV beam and three different MLC defined fields.

	Field size (cm^2)	PTW 31002 (cylinder IC)	PTW 34001 (Roos chamber)	Monte Carlo calculations
z = 0.25 cm	2 x 2	70.12	57.94	63.47
	4 x 4	70.76	59.06	63.53
	10 x 10	75.28	64.61	67.41
z = 0.52 cm	2 x 2	86.55	82.21	84.54
	4 x 4	87.32	81.96	84.01
	10 x 10	90.02	85.12	86.46

It is important to point out that the values obtained with the ionization chambers are estimated as energy deposited inside the air-sensitive volume of the chamber cavity and averaged over this volume at a given depth z. This magnitude is directly related to the ionization charge measured by an electrometer, which has been properly corrected for recombination, saturation and atmospherical conditions. Hence, in order to relate the calculated PDD to the measured PDI, the PDI curves must be converted to the PDDs using the following relationship [Abdel06]:

$$PDD(z) = PDI(z)\frac{[(\frac{\overline{L_\Delta}}{\rho})^{med}_{air} P_{fl} P_{wall} P_{cel}]_z}{[(\frac{\overline{L_\Delta}}{\rho})^{med}_{air} P_{fl} P_{wall} P_{cel}]_{zmax}} \tag{8.1}$$

where $PDI(z)$ is the cavity ionization at depth z normalized to that at the depth of maximum dose (z_{max}), $(\overline{L_\Delta}/\rho)$ is the mean restricted collision stopping power ratio medium to air and P_{fl}, P_{wall} and P_{cel} are the fluence, wall and central electrode perturbation factors, respectively.

As discussed by Abdal - Rahman et al [Abdel06], the factors correcting the chamber ionization ($(L_\Delta\rho)^{med}_{air}, P_{fl}, P_{wall}, P_{cel}$) remain constant with depth z in regions where CPE (charge particle equilibrium) conditions can be assured, i.e. at depths beyond the maximum depth z_{max}. As a result, the PDD and the PDI for $z \geq z_{max}$ can be considered equal.

Contrarily, in those regions where there are conditions of non-CPE such as the build up region, the situation is totally different. In this case, the restricted stopping power ratio as well as the perturbation factors $P_{fl}, P_{wall}, P_{cel}$ must be evaluated and a conversion factor depending on the depth is necessary to convert PDI curves into PDD curves.

In order to evaluate the differences between the measured PDI and calculated PDD, the variation of the stopping power ratio with the depth was evaluated, using MC techniques for the specific model of the Varian 2100C/D.

Figure 8.10 shows the restricted stopping power ratios $(L_\Delta\rho)^{med}_{air}$ against depth in the build up region for the 6 MV photon beam and the MLC defined fields of 2 x 2, 4 x 4 and 10 x 10 cm^2 at SSD of 95 cm. The ratios were calculated using the SPRRZnrc/EGSnrc user code [Rog01] with a energy threshold Δ = 10 keV. Previous phase-space files of the modeled Varian 2100 C/D were used as input of the SPPRZnrc. Note that the $(L_\Delta\rho)^{med}_{air}$ illustrated in figure 8.10 are normalized to 1.0 at the maximum dose depth z_{max} (1.5 cm). As shown in the figure, the correction to the stopping power ratios is relatively small (≤ 1.009) and it depends on the field size. On the phantom surface (z = 10 μm), the relative stopping power ratio is $\sim$ 1.009 for the 2 x 2 and 4 x 4 cm^2 MLC defined fields and decreases to $\sim$ 1.006 for the MLC defined field of 10 x 10 cm^2. For all fields, the relative stopping power ratios decrease with the depth up to about 1 cm. After this depth, they remain relatively constant and close to 1.0. It is also observed that the relative stopping power ratios along the entire depth range illustrated in the figure are highest for the small field and decrease with the field size.

Using the cylindrical chamber, the correction factor introduced by the stopping power ratios does not account for the discrepancy observed between the measured PDIs and the calculated PDDs.

Moreover, this correction works in the wrong direction and actually increases by 0.5 % the discrepancy between the corrected PDI and the calculated PDD. For the Roos chamber, the agreement between the PDI and the calculated PDD is slightly better (0.5 %) if the PDI is corrected for the depth dependence of the stopping power ratio.

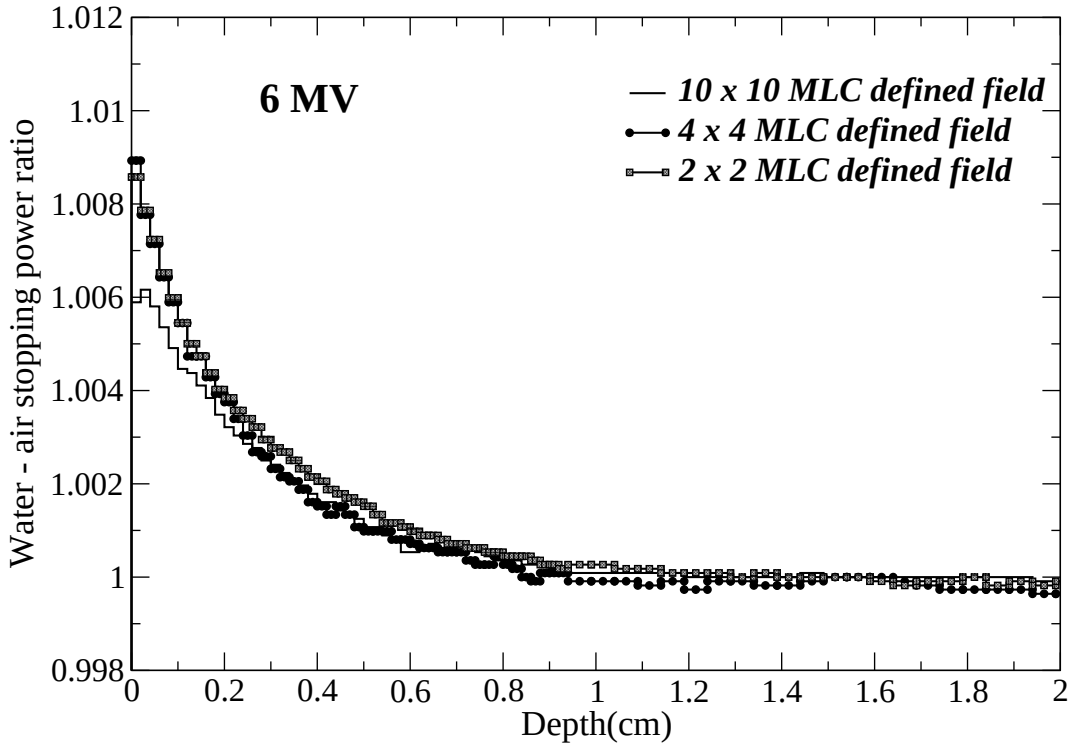

(a)

Figure 8.10: Water to air stopping power ratio against depth for 10 x 10 cm^2 (a), 4 x 4 cm^2 (b) and 2 x 2 cm^2 (c) MLC defined fields, at 95 cm SSD for 6 MV photon beam.

In conclusion, the stopping power ratios have not a significant influence in the conversion of the measured PDI to PDD curves. As above referred, the dependence of the perturbation factors ($P_{fl}, P_{wall}, P_{cel}$) on the depth could have also some impact in the PDI to PDD conversion in the build up region.

8.5 Conclusions

The effect of the MLC on the build-up region dose has been studied using Monte Carlo simulations and measurements carried out with two different ionization chambers. Percentage dose curves in the build up region for MLC defined fields were compared to those fields in which the MLC does not

intercept the beam and therefore the scattering of the MLC does not affect the field.

From the MC calculations, it has been determined that the effect caused by the presence of the MLC is practically negligible (less than 1 %) for 10 x 10 and 4 x 4 cm^2 MLC defined fields. A bigger effect (about 2 %) was observed for the 2 x 2 cm^2 MLC defined field. In the build up region, the overall head accelerator contribution to the total dose (including MLC) is of about 10 % for the 10 x 10 cm^2 field and it decreases with field size (2 - 3 % for 2 x 2 cm^2 field size). It was found that the scattering of particles from the accelerator head and the MLC is responsible for the increase of about 7% on the surface dose.

Experimentally, the same evaluation of the MLC effect as that performed with MC methods was also investigated using measurements obtained with two different ionization chambers in a water phantom. Specifically, the chambers were a PTW cylindrical chamber and a Roos parallel-plate chamber. A negligible effect (less than 1 %) of the MLC on build up doses was observed for all MLC defined field sizes considered in this investigation. The most relevant differences between PDI curves measured for MLC defined and MLC open fields were observed at shallow depths (from surface to 0.25 cm depth). However, due to the geometrical characteristics of the chambers which do not allow to measure correctly at these depths, it can not be concluded that these observed differences could be caused by the MLC. So, the measurements cannot validate the MC calculated surface dose values.

The MC calculated PDD and measured PDI curves were also compared for the studied MLC defined fields. In general, it was observed that the measured PDIs differ from the calculated PDDs and this difference depends on the measuring chamber type. Particularly, our dose values measured with Roos chamber agree with the MC values within 2 % for all MLC field sizes and depths greater than 2 mm. Differences of about 4 % between the values measured with cylindrical ionization chamber and calculated MC values were observed.

Measured PDIs in the build up region were corrected to the depth dependence of the water-to-air stopping power ratios in order to investigate the observed differences relative to MC calculations. The variation of the water-to-air stopping power ratios with the depth was found to be relatively small (less than 1.009) and it was found to be dependent on the field size. For the PDI measured with the cylindrical chamber, the correction for this effect can not account for the discrepancy between the PDI and the calculated PDDs. However, this correction applied to the Roos chamber values increases slightly (0.5 %) the agreement between the measured PDI and the MC calculated PDDs.

Chapter 9

The use of non-standard CT conversion ramps for Monte Carlo verification of 6 MV prostate IMRT plans

9.1 Motivation

IMRT has rapidly become an effective technique for the treatment of prostate cancer because of the ability of delivering highly conformal dose distributions to tumor targets, reducing doses especially to the rectum [Guck06]. The improved dose conformity achieved with the IMRT technique leads however to an increase of the complexity of the treatment, involving the use of small fields and large intensity dose gradients. Consequently, inaccuracies of the dose calculation algorithms may be introduced in any of the above situations, magnifying the possible dosimetric inaccuracies of the calculation algorithms likely caused by the presence of tissue inhomogeneities such as air cavities or bone tissues. Hence, a rigorous verification of the IMRT plans is required in order to ensure the accurate determination of the absorbed dose before the treatment delivery [IMRT01].

Commonly, the direct measurements using ionization chambers and films in homogeneous phantoms are the widely-used method for checking the IMRT dose distributions. Nevertheless, there are some factors which may cause experimental data to be insufficient to completely characterize

the IMRT dose distributions. On one side, it is known that the dosimeters present some limitations for IMRT fields due to the presence of high dose gradients, small fields or dynamic beam delivery [Low11]. On the other side, the use of an homogeneous phantom as a medium for the verification measurements cannot provide direct checks on the accuracy of the patient dose calculation, since it does not really represent a true and heterogeneous patient geometry [Ma03].

In contrast to the measurements, MC dose algorithms have shown to be a more reliable tool to provide improved dose accuracy in such situations due to the ability of modeling realistic radiation transport through the accelerator treatment head, the multileaf collimators (MLCs) and the patient-specific geometry with heterogeneities. Currently, with the rapid development in computer technology, MC algorithms have been implemented for the dosimetric verification of IMRT plans generated by conventional treatment planning systems (TPS) [Ma00b, Ma02, Leal03].

It is well known that conventional dose calculation algorithms implemented in most TPSs, such as pencil beam or superposition/convolution algorithms, compute and report the absorbed dose to water (D_w), assuming that the majority of the patient body (between 45 - 75 %) consist of water [Sieb00]. Historically, measured and prescribed doses have been also reported in terms of D_w and modern dosimetry protocols have been also based on this consideration (AAPM TG-51 [Alm99] and IAEA 2000 [And00]). In contrast, MC dose calculation algorithms calculate and report the absorbed dose to medium (D_m). In fact, MC patient dose calculations can be performed in the explicit media of phantoms built from real patient CT (computed tomography) anatomical information.

With the use of MC algorithms as a tool for the verification of the dose accuracy computed by TPS conventional algorithms, it is therefore necessary to convert dose to medium to dose to water in order to properly compare both calculated dose distributions [Chet07]. For this purpose, Siebers *et al* (2000) [Sieb00] proposed a method based on the Bragg-Gray cavity theory, where MC-based D_m are converted into D_w using the average stopping power ratio of water to medium. In this study, they showed that the difference between D_m and converted D_w for a head-and-neck plan was in the order of 1-2 % for soft tissues, whereas this difference could increase up to 10 % in the presence of higher density materials, such as cortical bone. For prostate IMRT plans generated with 18 MV photon beams, Dogan *et al* (2006) [Dog06] stated that systematic dose errors of up to 8 % may be introduced when hard-bone structures are present and MC calculated D_m are converted to D_w using the method described by Siebers *et al* (2000)[Sieb00].

Ma *et al* (2000)[Ma00b] used the MC method for the verification of IMRT dose distributions

previously computed by the Corvus TPS, employing a finite-size pencil beam algorithm. In their work, they also investigated the dosimetric effect of the conversion of calculated dose to different materials for a vertebra IMRT dose plan delivered with photon beams of 15 MV. For this purpose, they compared the dose distributions calculated for different materials with different densities and those dose distributions calculated for water-equivalent-tissue with corresponding densities. They reported differences of 2-3 % between the dose to bone and the dose calculated in tissue with bone density. However, these differences reached up to 10 % for regions with hard bone when the dose to bone was converted to tissue using the stopping power ratio for tissue to bone following the method of Siebers *et al* (2000)[Sieb00]. They concluded thus that this method leads to results not equivalent to MC doses calculated in tissue of variable densities.

Additional works published by Ma *et al* (2009, 2011)[Ma09b, Ma11] investigating the same subject showed for 6 MV differences < 4 % between the doses calculated in different layered phantoms including bone heterogeneity and those distributions calculated in the same phantoms with the bone replaced by water of bone density. They also observed that the conversion of dose to bone to dose to water using the stopping-power ratios resulted in differences higher than 10 %. Similar discrepancies were also observed on dose distributions calculated in CT-based patient phantoms for an IMRT plan delivered with 15 MV photon beams.

In resume, there is some work on the conversion of D_m to D_w related to layered phantoms as well as to patient phantoms irradiated by high-energy photon beams (> 10 MV). However, most of these works devoted to the subject of IMRT treatments of prostate or vertebra regions were performed using photon beams with energy of 15 and 18 MV [Dog06, Ma09b, Ma11] and there is a lack of studies performed for photon beams with lower energy, namely 6 MV.

The use of low-energy photons (6 MV) for IMRT treatments has been extensively encouraged by several authors [DeB07, Wel07, Tha11] and it remains a possible option for the delivery of prostate IMRT. The low-energy photon beams have shown to have certain advantage for IMRT plans over the high-energy photons (> 10 MV) due to the negligible neutron contamination. In contrast to 3D Conformal radiotherapy, the increased number of monitor units (MU) required for IMRT delivery of the same dose as conformal treatments causes an increase in the secondary radiation to tissues outside the treated area from leakage and scatter, as well as a possible increase in the neutron dose from photon interactions in the machine head. This contamination becomes more relevant at higher photon energies, resulting in a concern about the production of secondary malignancies at these

energies.

The purpose of the present work was to evaluate the effect of converting MC-based D_m and D_w for the verification of prostate IMRT dose distributions generated using 6 MV photon beams. IMRT plans were predicted by the Eclipse TPS using a pencil beam convolution algorithm in which tissue heterogeneities are accounted for by a Modified Batho Power Law correction method. MC - IMRT plans were designed using BEAMnrc code for each patient and dose calculations were subsequently performed with the DOSXYZnrc code in real CT-based patient phantoms built with three different CT ramps: a conventional four material CT ramp and two simplified conversion ramps of air and water of different density configurations. The intercomparison between MC dose distributions allowed us to isolate the material composition effect from the density effect on calculated doses. Our MC plans were also evaluated using the stopping power ratio method proposed by Siebers *et al* (2000)[Sieb00] for the conversion of MC-based D_m to D_w.

9.2 Material and methods

9.2.1 Treatment planning

Dynamic or "sliding windows" IMRT treatment plans for 3 prostate cancer patients were generated with inverse planning using the Eclipse TPS (version 7.0). Patients were scanned in a supine position with a resolution of 0.0977 x 0.0977 x 0.3 cm^3 using a Siemens CT scanner. Photon beams of 6 MV produced by a Varian 2100C/D linear accelerator equipped with a 120 - leaf Millenium MLC were used for treatment delivery (see chapters 6 and 7).

For all three plans, the treatment was divided into 3 different phases to produce a final prescribed dose of 76 - 78 Gy to the prostate and seminal vesicles, delivered in daily 2-Gy fractions. The first phase (Phase I) was planned to deliver 44 Gy to the volume PTV1 containing the prostate, lymph regional nodes, seminal vesicles and pelvic lymph nodes. In a second phase (Phase II), the field defined by the MLC was reduced to conform the PTV2 (prostate, seminal vesicles and lymph regional nodes) for 10 Gy (patient 1 and 2) and 8 Gy (patient 3). In a last phase (Phase III), a total dose of 24 Gy was provided to the PTV3 including the prostate and the seminal vesicles. Figure 9.1a illustrates transversal CT slices including the regions delineated for the target volume (PTV) in each phase as well as the regions defined for two critical structures: the femoral heads and the bladder. From the figure, it can be clearly seen how the PTV region was significantly reduced from

Phase I to Phase III, where a volume highly conformed to the prostate and the seminal vesicles was finally delineated.

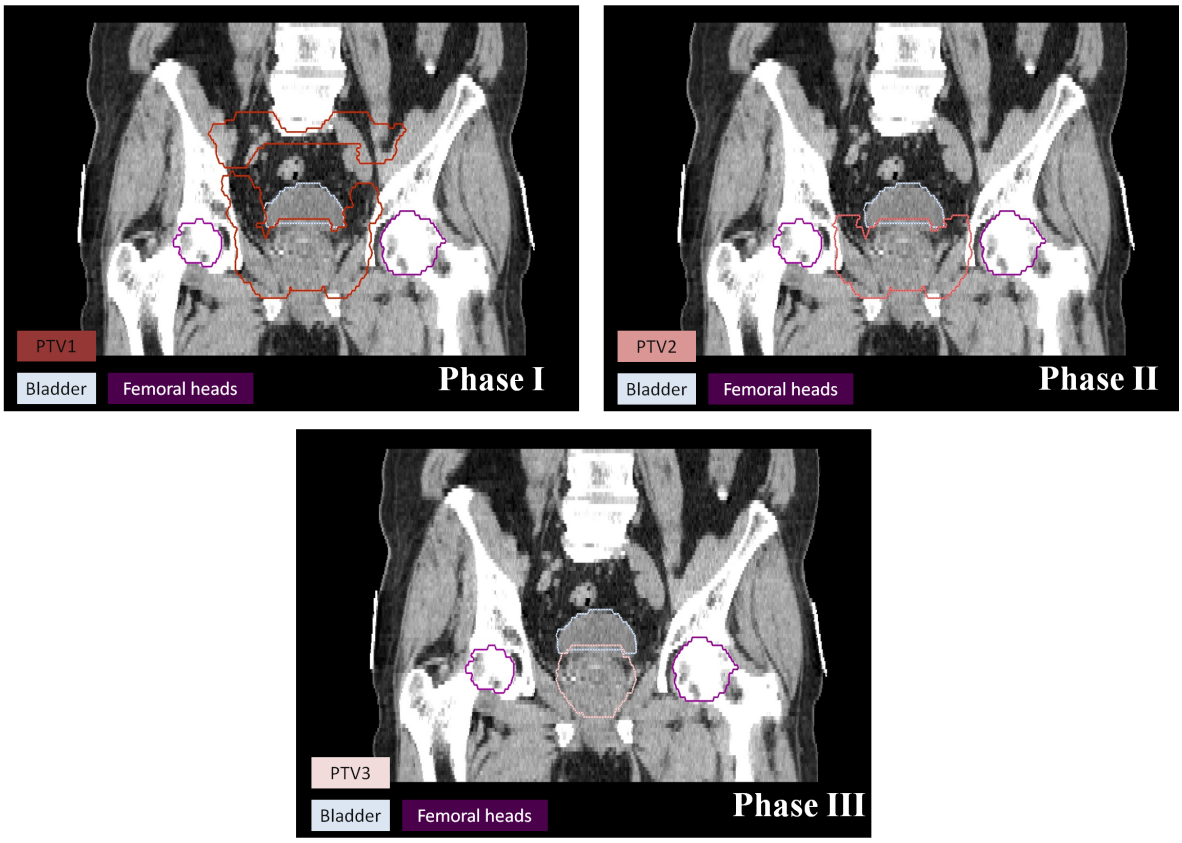

(a)

Figure 9.1: Transversal CT slices for patient 3 illustrating the delineations of the PTV volumes for each treatment phase as well as two critical structures, the femoral heads (purple) and the bladder (light). For Phase I, the PTV1 (red) contains the prostate, lymph regional nodes, seminal vesicles and pelvic lymph nodes. For Phase II, the PTV2 (pink) includes the prostate, seminal vesicles and lymph regional nodes. For Phase III, PTV3 (light pink) contains the prostate and the seminal vesicles.

For the IMRT plan used in Phase I, a seven-field (patient 1 and 3) and a five-field (patient 2) coplanar beam arrangement were applied with jaws field sizes of approximately 19 x 17 cm^2. For Phase II and III, the IMRT plan was composed of five coplanar fields (patient 1 and 2) and seven coplanar fields (patient 3), with average field sizes of 15 x 10 cm^2 and 12 x 10 cm^2, respectively. Table 9.1 summarizes the characteristics of the treatment plans, including the typical jaws aperture and gantry angles for each treatment phase.

Patient dose calculations were performed using a pencil beam convolution (PBC) algorithm

[Ahn92, Sto96, Sto99] in which tissue heterogeneities are accounted for by a Modified Batho Power Law correction method [Son77, Pod05]. The PBC algorithm represents one of the model-based algorithms using a kernel-based method, i.e. a method based on the concept of a *kernel* as a representation of the distribution of energy imparted to a medium due to an elementary incident photon beam. Within kernel-based methods, the energy deposition kernels fall into two different types, depending on the geometry of the elementary beam that delivers the incident energy: point and pencil kernels. The PBC algorithm is based on the latter type of kernel, where point kernels are summed along a line in a phantom to obtain a pencil beam type dose distribution. The dose distribution is generated by integrating the pencil beam over the radiation field (accounting for changes in primary fluence) and modifying its shape with depth and local tissue density. The pencil kernels are usually derived from the results of Monte Carlo calculations [Moh86], either directly as monoenergetic pencil kernels or as a superposition of point kernels.

The doses reported by these algorithms are calculated in water and subsequently corrected by the electron density, which, in a general way, it is equivalent to calculate the dose using water with different electron densities.

Table 9.1: Typical number of beams, beam angles and jaws openings of IMRT treatment plans.

Treatment Phase	**♯ beams (Gantry angle)**			**Typical JAWS openings**
	Patient 1	Patient 2	Patient 3	
Phase I	7 beams (280, 90, 340, 25, 240, 125, 185)	5 beams (265, 95, 325, 25, 180)	7 beams (280, 90,350,15, 240,125,185)	19 x 17 cm^2
Phase II	5 beams (270, 100, 330, 40, 180)	5 beams (0, 85, 130, 230, 275)	7 beams (280, 90,350, 15, 240)	15 x 10 cm^2
Phase III	5 beams (270, 100, 320, 45, 180)	5 beams (125, 75, 0, 275, 235)	7 beams (90, 15,350, 280,240,185)	12 x 11 cm^2

9.2.2 Monte Carlo calculations

The Varian 2100C/D linear accelerator equipped with a 120-leaf Millenium MLC was accurately modeled for a 6 MV photon beam using the BEAMnrc user code [Kaw03, Rog05](see chapter 6).

As previously described in chapters 6-7, the detailed geometry and dimensions of each component were set based on the manufacturer's specifications. A parallel circular electron beam hitting

on the target with 6.2 MeV energy (monoenergetic) and a radius of 0.15 cm was chosen to match within 2 %/2 mm the calculated depth dose and off-axis profiles in water with the experimental data measured with an ionization chamber (PTW 31002 model). The MLC device was fully modeled and accurately commissioned against experimental data.

The MC simulations performed in the present work were split into three different stages as illustrated in figure 9.2.

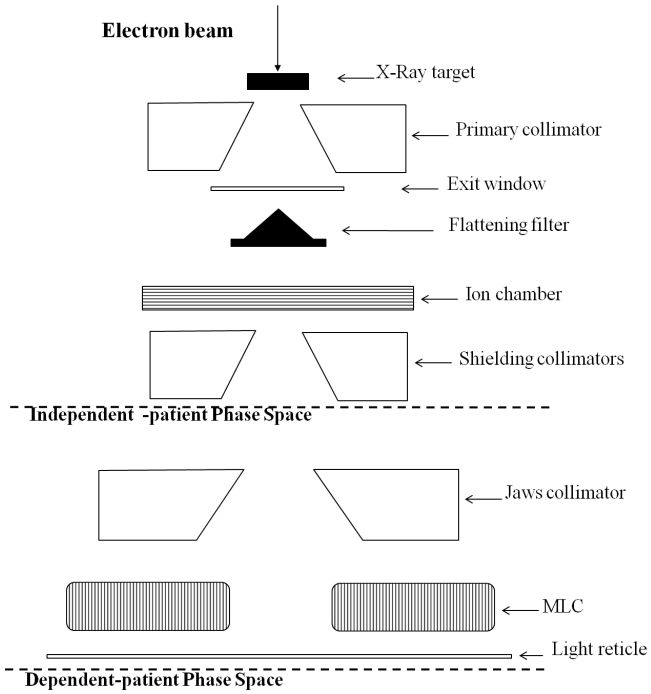

(a)

Figure 9.2: Schematic diagram of set-up for the MC simulation of IMRT treatment plans performed using BEAMnrc code. The independent-patient part involves the fixed component modules of the Varian 2100C/D linear accelerator, resulting in a phase space file scored above the jaws. This independent-patient phase space file is then used as a source of the dependent-patient part including the jaws and the MLC. Outputs of the last part are input of DOSXYZnrc code for the dose calculation in the patient geometry built from the CT data.

The first stage simulated the passage of the particles through the patient-independent part of the linac, i.e. up to a plane just upstream of the secondary collimators or jaws (at 27.9 cm from the electron source). This step was performed only once with the resulting particle coordinate (energy, location, direction and particle type) scored in a phase space file for subsequent use in the next

step of the simulation. In the second stage, a set of output phase space files for the various MLC and jaws field size configurations were obtained below the MLC (at 54 cm from the bremsstrahlung target). This stage is referred here as ”patient-dependent” part as it changed for each patient field configuration. Finally, the phase-space files scored in the second step were used as a source of the DOSXYZnrc code [Wal05] to calculate dose distributions in the CT - based patient phantoms. For each patient, the plan information data, i.e. jaw positions, gantry angles and patient isocenter position, was exported from the clinical Eclipse TPS and subsequently introduced in the correspondent input files of the BEAMnrc and DOSXYZnrc code for the MC simulations. Additionally, the position of the MLC leaves were directly read from the BEAMnrc code using the leaf sequence file exported previously from the TPS (a .mlc file).

Five hundred million electrons were incident upon the bremsstrahlung target, resulting in about 477 million photons at the phase space plane located above the collimator jaws. For the patient-dependent part, four independent runs (with different random number seeds) using the total number of particles scored in the previous stage (i.e without recycling) were simulated for each beam of the treatment phases I and II. The resulting phase-space files for the 4 independent runs of a beam were then combined in a final phase-space file using the data analysis utility BEAMDP [Ma09]. The combination of the phase-space files resulted in a final phase-space file with a large number of particles while still retaining the characteristics (energy, angle, position, etc.) of the particles. For the beams of the phase I, the final phase-space files had between $2x10^7$ and $7x10^7$ particles, while, for the beams of the phase II, the files contained around $2x10^7$ and $4x10^7$ particles. The number of particles scored in the phase-space files was dependent on the size of the field defined by the jaws and the MLC for each beam arrangement. Using these final phase-space files, the individual beams for each phase of the treatment were simulated independently in the CT-based phantom. For that, the information of patient-dependent phase space particles were used repeatedly (around 10 - 12 times) in the DOSXYZnrc-based calculations for both treatment phases.

The final dose distribution for each phase was the summation of the dose distributions from all individual beam arrangements. The average statistical uncertainty for the final distribution was less than 2 % in the regions of the targeted volumes (PTV and critical structures) and about 2.5 % in the regions close to the confluence of the treatment beams. These statistics were considered sufficient for the dose analysis (DVH and dose distributions) based on the results reported by Keall *et al* (2000) [Keall00b]. According to these authors, a statistical uncertainty of 2 % has minimal effect on isodose

levels, DVHs or biological indices.

The following transport parameters were set for the first two steps of the accelerator simulation: ECUT = AP = 700 keV, PCUT = AP = 10 KeV, where AP and AE are the low-energy thresholds for the production of secondary bremsstrahlung and knock-on electrons, respectively; while ECUT and PCUT define the global cutoff energy for electron and photon transport, respectively. In order to improve the calculation efficiency, various variance reduction techniques were employed, such as uniform bremsstrahlung splitting with a photon splitting factor of 20, Russian Roulette and range rejection technique with ESAVE of 0.7 MeV in the bremsstrahlung target and 1 MeV for the other accelerator components [Rog05]. On the other hand, MC dose calculations in phantoms were carried out for ECUT and PCUT set to 0.521 MeV and 0.01 MeV, respectively. The value of the parameter ESTEPE (maximum fractional energy a charged particle can lose per step) was set to its default value of 25 %. Phantoms were created via the DICOM RT toolbox [Spez02] using the planning CT patient dataset as input.

The conversion of CT numbers to materials and mass densities was handled by using several CT conversion ramps as described below in section 9.2.3. Finally, dose distributions were visualized in voxel phantoms using the visualization tool dosxyz_show included as part of the BEAM distribution [Kaw07].

9.2.3 CT conversion ramps

MC phantoms were created using the planning CT patient dataset as input of the DICOM RT toolbox [Spez02]. As previously mentioned, the original CT slices with a resolution of 512 x 512 and a pixel size of 0.0977 cm were taken with a distance of 0.3 cm. MC simulations were performed in a reduced CT patient geometry identical to that geometry used for TPS dose calculations, which did not include objects and air region positioned outside the patient contour. Additionally, the resolution of this reduced geometry was also set to the same resolution as the TPS, i.e. 0.25 x 0.25 x 0.3 cm^3 in the X, Y and Z direction, respectively.

To build MC phantoms, three different ramps using a four material bin scheme were considered to convert CT data into material and mass density:

1. The conventional CTCREATE/DOSXYZnrc [Wal05] conversion ramp using four materials (air, lung, tissue and bone with the proper mass density) was considered (figure 9.3). We denote the MC phantom created using this CTCREATE ramp as "*conventional phantom*".

2. A simplified CT ramp using air and water of variable density (referred as "*water variable* ρ") was also used to build MC patient phantoms. For this conversion ramp, the cross sections of three materials, called as LUNG_WATER, TISSUE_WATER and BONE_WATER, were generated by the PEGS4 [Kaw03] data-preprocessing code. These new materials were defined as having the composition of water and the mass density of lung (ρ = 0.26 gcm^{-3}), tissue (ρ = 1.0 gcm^{-3}) and bone (ρ = 1.85 gcm^{-3}) materials considered in the conventional CT ramp.

3. MC patient phantoms using a second simplified ramp, referred as "*water unit*ρ", which considered only air and water with unit density, were also constructed.

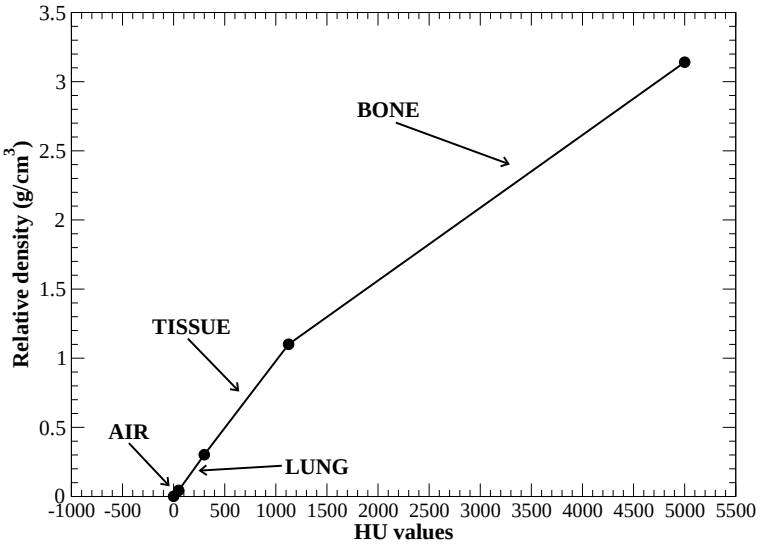

(a)

Figure 9.3: The CT ramp for the conversion of CT values to material type and densities according to the conventional CTCREATE ramp which uses four materials: air, lung, tissue and bone [Wal05]. The density and composition of the materials used in this ramp were the values included in the PEGS4 cross-section data file. Segments of the (CT values, ρ) conversion relationship are straight lines. Note that the CT numbers considered for the DOSXYZnrc presents an offset of 1000 with respect to the standard definition of Hounsfield number ([-1000, 1000]).

The density for a given voxel is assigned by linear interpolation of a mass density versus CT number curve. The CT number range and density range for the materials used in each ramp have been reported previously in chapter 4. Both CT number and density ranges were maintained for the three different ramps considered in this investigation and only the material considered for each range was modified. Table 9.2 summarizes the material intervals of the four bins used in each CT conversion procedure. MC- IMRT dose calculations for the three patients included in this study were

performed in the three above referred phantoms using DOSXYZnrc, as described above in previous section.

Table 9.2: CT conversion ramps used to build Monte Carlo phantoms from the CT data set of patients. The interval of mass density and corresponding CT number are illustrated in figure 9.3. The EGSnrc/521ICRU materials database was considered [Kaw03]. The materials LUNG_WATER, TISSUE_WATER and BONE_WATER were generated using the PEGS4 processor [Kaw03]. The low energy thresholds for the production of knock-on electrons was set to AE = 0.521 MeV (total energy) and the threshold for bremsstrahlung events was set to AP = 0.010 MeV for all materials.

CT CONVERSION RAMPS			
Material interval	**Conventional CTCREATE**	**Simplified 1**	**Simplified 1**
1	AIR	AIR	AIR
1	LUNG	LUNG_WATER	WATER
1	TISSUE	TISSUE_WATER	WATER
1	BONE	BONE_WATER	WATER

9.2.4 Dose to medium to dose to water conversion

To explore the effect of the conversion of dose to medium to dose to water, the MC dose distributions D_m obtained in the phantom created using a conventional CT ramp were converted to dose to water (D_w) using the method proposed by Siebers *et al* (2000)[Sieb00]. This method is based on the Bragg-Gray cavity theory and provides a relation between D_w and D_m given by:

$$D_w = D_m S_{w,m} \tag{9.1}$$

where $S_{w,m}$ is the unrestricted water-to-medium mass collision stopping power ratio averaged over the energy spectra of primary electrons produced by photon interactions at the point of interest. Siebers *et al* (2000)[Sieb00] assessed the dependence of $S_{w,m}$ on energy for the materials of the patient-like geometry and they found that $S_{w,m}$ varies less than 1 % throughout the field for a given photon beam energy. Therefore, a single correction factor for each material was proposed to convert D_m to D_w for a given photon beam energy.

The conversion of the dose based on the previous relation (Eq. 9.1) can be accomplished using two different methods. Based on the fact that $S_{w,m}$ is approximately invariant for patient-like materials throughout a photon radiation therapy field, the dose conversion may be performed in a post-processing step[Sieb00]. Alternatively, the conversion may be carried out during the execution of the particle transport on a track-by-track basis by multiplying the energy deposited in a voxel

by the stopping power ratio [Kaw01]. This last method is done in the MC transport code, thereby directly obtaining D_w. As it has been previously shown by Siebers *et al* (2000)[Sieb00], converting the dose in a post-processing step is valid for photon beams. In 2007, Gardner *et al* (2007)[Gard07] reported that the differences between the two methods were clinically insignificant in homogeneous phantoms ranging in density from 0.3 g cm^{-3} to 2.5 g cm^{-3}, in a bonelungbone phantom with steep density gradients as well as in several prostate and head-and-neck patient cases. In the present work, the conversion from dose to medium to dose to water was carried out in a post-processing step using the DICOMRT- toolbox [Spez02].

9.3 Results and discussion

9.3.1 Material composition and density effect on MC dose distributions

In this section, we present the MC dose distributions calculated in conventional and both simplified phantoms for 3 prostate IMRT plans (Phase I and II) in order to evaluate the individual contributions of material composition and density to dose distributions.

Figure 9.4a shows the comparison of an X dose profile calculated for three MC phantoms which were created using the CT conversion ramps summarized in Table 9.2.

The profile was plotted through the transversal CT slice containing the isocentre (z = - 0.1734 cm) for the treatment Phase II of patient 1 (figure 9.4b). The exact position of the profile is indicated by the horizontal white lines in figure 9.4b. The gray highlighted region in figure 9.4b represents the extent of bony regions situated along the profile axis.

As shown from this figure, the differences between the profiles calculated in water with variable densities and the profiles calculated in water with unit density were found to be less than 1 % in all regions, including those containing bone. This fact indicates that differences in mass density of the water do not affect significantly the MC dose distributions.

On the other hand, it is seen that the dose calculated in both simplified water phantoms showed differences of about 4 % with the dose values calculated using the conventional phantom in regions close to bones. These discrepancies may be explained by the effect of the bone media (high atomic number and high density), which was accurately accounted for MC dose calculations performed in conventional phantoms, but not in simplified water phantoms.

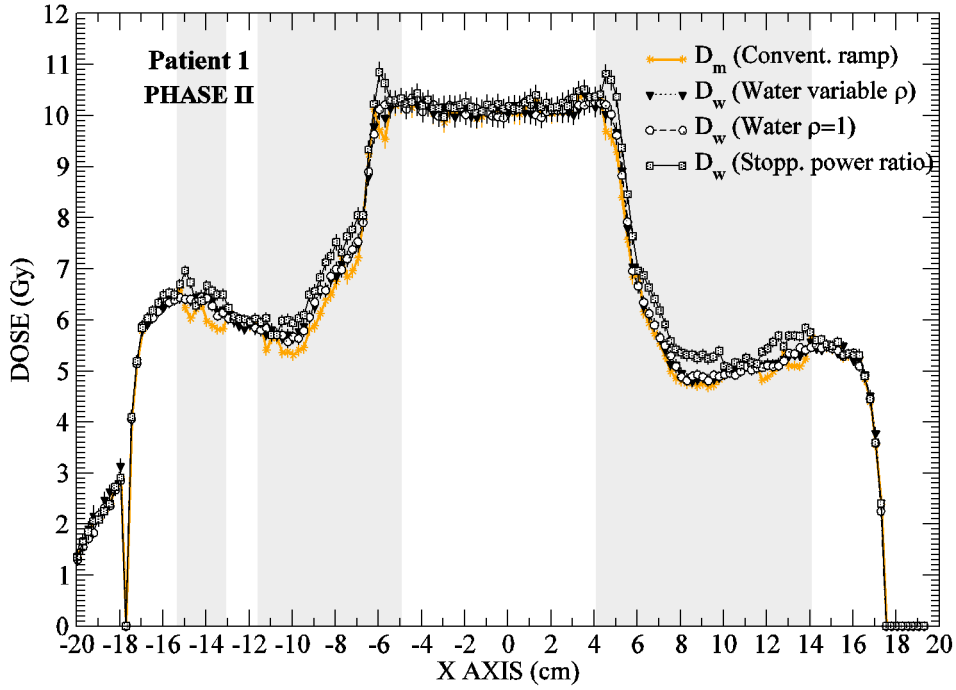

(a)

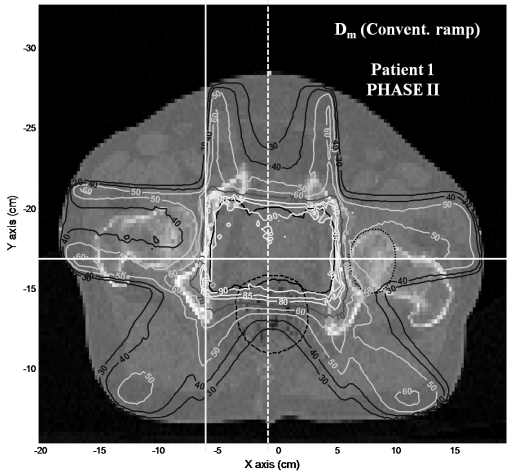

(b)

Figure 9.4: (a) Comparison of dose profiles calculated along the X axis for MC phantoms built using conventional (CTCREATE) and simplified CT ramps ("water variable ρ" and "water unit ρ"). Profiles were taken at the position y = -16.13 cm of the transversal CT image slice (b), which contain the isocenter (z = -0.1734 cm) for the Phase II of the IMRT treatment of patient 1. The horizontal white lines in the CT image indicate the position where the profile is plotted. MC dose profile D_m (Convent. ramp) converted using the stopping power ratios for water to medium is also presented. The isodose lines are given as 30, 40, 50, 60, 70, 80 and 90 % of the maximum dose of this case (10.95 Gy). Black lines on CT image indicate the PTV volume (continuous line) and both rectum and left femoral head (dashed line).

Similar observations were made for dose profiles within the other patients included in this study, as shown in figure 9.5a for patient 2. This figure illustrates the comparison of dose profiles calculated with MC in conventional and simplified phantoms in a transversal slice through the respective isocentre, in positions where bony regions are present.

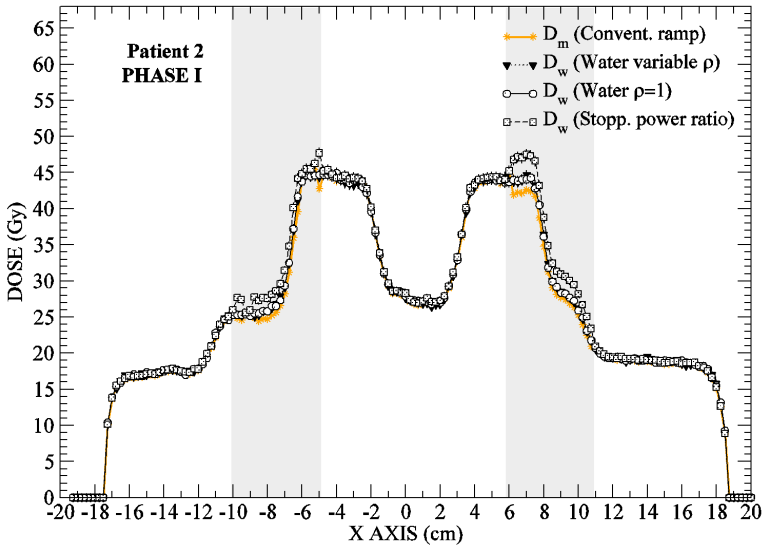

(a)

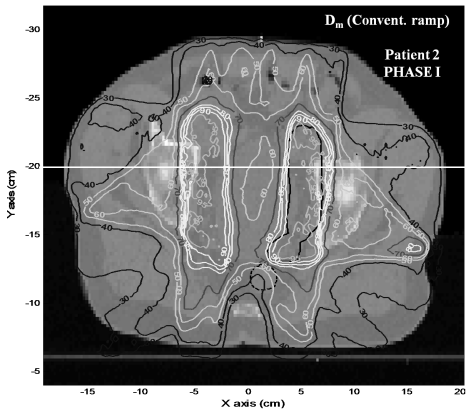

(b)

Figure 9.5: (a) Comparison of dose profiles calculated along the X axis for MC phantoms built using conventional (CTCREATE) and simplified CT ramps (”water variable ρ” and ”water unit ρ”). Profiles were taken at the position y = -20 cm of the transversal CT image slice (b), which contain the isocenter (z = 4.8328 cm) for the Phase I of the IMRT treatment of patient 2. The horizontal white lines in the CT image indicate the position where the profile is plotted. MC dose profile D_m (Convent. ramp) converted using the stopping power ratios for water to medium is also presented. The isodose lines are given as 30, 40, 50, 60, 70, 80 and 90 % of the maximum dose of treatment (46.44 Gy). Represented volumes on CT image are PTV volume (black continuous line) and rectum (black dashed line).

Figures 9.6 present the comparison of dose profiles for the same MC phantoms as in figure 9.4, but in this case along the Y axis at two different positions of the CT slice (figure 9.4b).

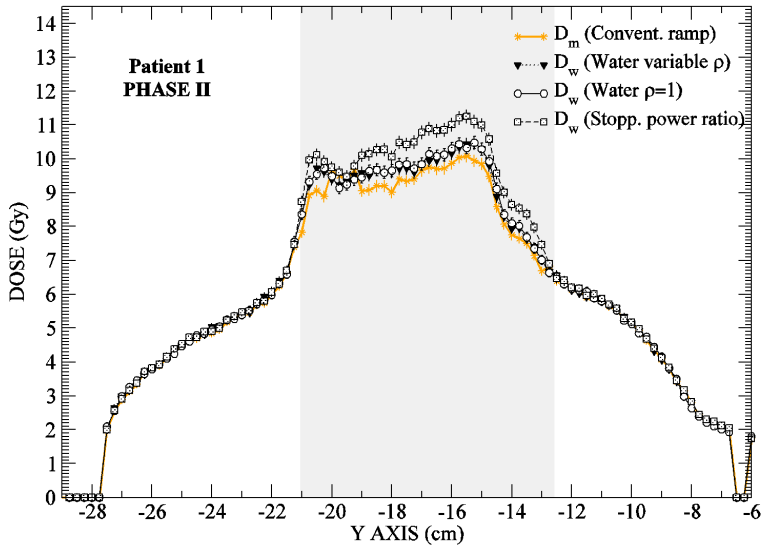

(a)

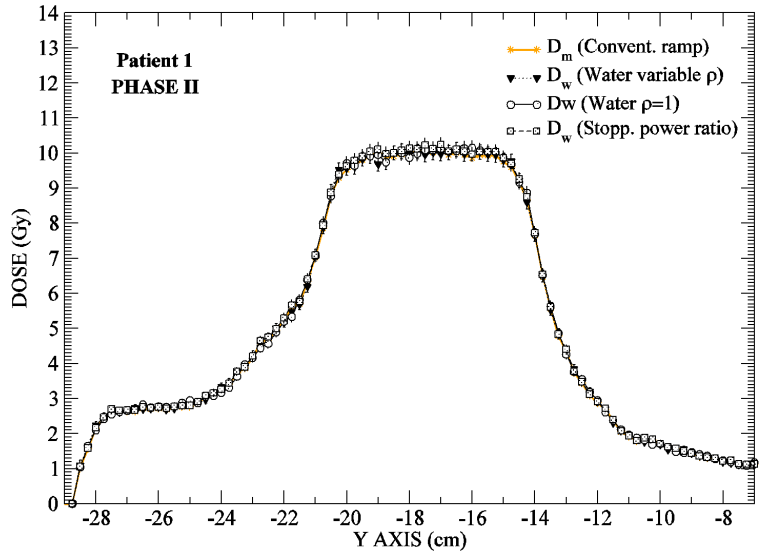

(b)

Figure 9.6: Comparison of dose profiles calculated along the Y axis for MC phantoms built using conventional (CTCREATE) and simplified CT ramps (”water variable ρ” and ”water unit ρ”). Profiles were taken at the position (a) x= -6.03 cm (vertical continuous line) and (b) x= -0.78 cm (vertical dashed line) of the transversal CT image slice (figure 9.4b), which contain the isocenter (z = -0.1734 cm) for the Phase II of the IMRT treatment of patient 1. MC dose profile D_m (Convent. ramp) converted using the stopping power ratios for water to medium is also shown.

In figure 9.6a, a profile was plotted in a region adjacent to the femoral heads, whereas the profile illustrated in figure 9.6b was calculated through a region containing less bone structures. The positions of both profiles are represented by the vertical continuous and dashed white lines in figure 9.4b, respectively. It is clear from figure 9.6a that the differences between dose profiles for the two simplified water phantoms, i.e. water with variable density and water with unit density, are also negligible as shown in the X profile.

Larger discrepancies up to 4 % are observed between the profiles calculated in medium (conventional phantom) and in water of unit and variable density. From figure 9.6b, it should be noted that, due to the lack of regions with bone, the observed differences between dose to medium and both dose to water with unit density and variable density are not significant (1 %) compared to Y profiles of figure 9.6a.

MC dose profile calculated in medium (D_m) obtained considering the conventional ramp to built the patient phantom were converted to dose to water (D_w) using the stopping power ratios for water to medium, as described in section 9.2.4. The converted dose profiles are also included in figures 9.4 - 9.6.

Comparing the dose to medium and the converted D_w dose profiles, it is clear from figure 9.5a that the conversion of dose with stopping power ratios increases by about 9 % the dose D_m in the femoral heads regions (bony structures), while it does not affect the dose in the tissue surrounding these regions. The cause of this increase in the bone areas is mainly due to the higher mass stopping power ratio $S_{w,m}$ for bone (1.114 for 6 MV photon beam), compared to the value for tissue (1.01 for 6 MV photon beam). These results are consistent with the previous results published by Ma *et al* (2000)[Ma00b].

The dosimetric effect caused by differences in the materials used in MC phantoms was also evaluated through the dose-volume histogram (DVH) curves. Figures 9.7 illustrate the comparison of DVHs calculated by Monte Carlo for the phantoms constructed using the CT ramps of table 9.2. The DVHs of target volumes (PTV) and two critical structures (left femoral head and rectum) are displayed for the Phase I (figure 9.7a) and II (figure 9.7b) of patient 1. As seen, there is no significant differences between the DVH of the PTV calculated using a conventional ramp and both simplified ramp with water for both treatment phases.

On the contrary, discrepancies of 3 % are observed between DVHs of the femoral heads for the MC phantoms created using the conventional CT ramp and those created with both simplified CT

ramps.

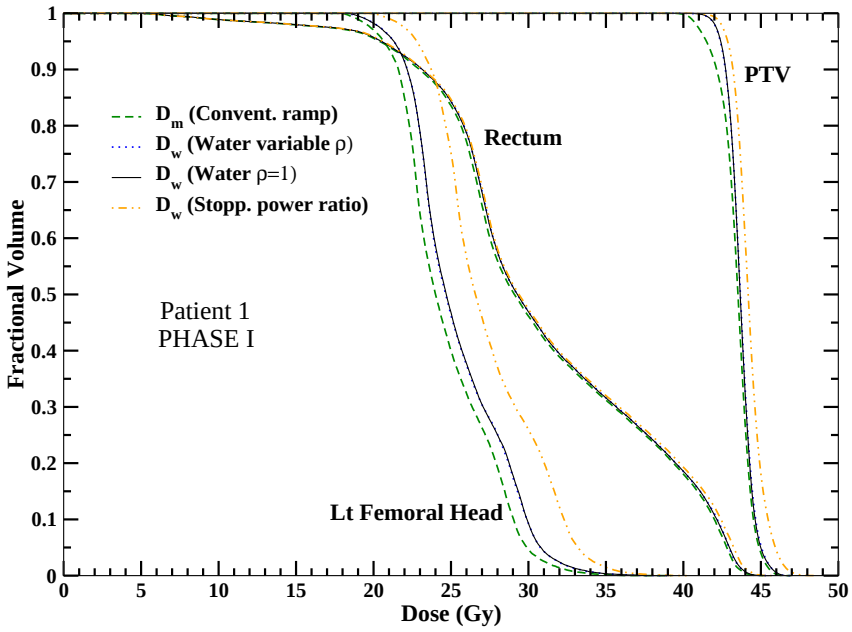

(a)

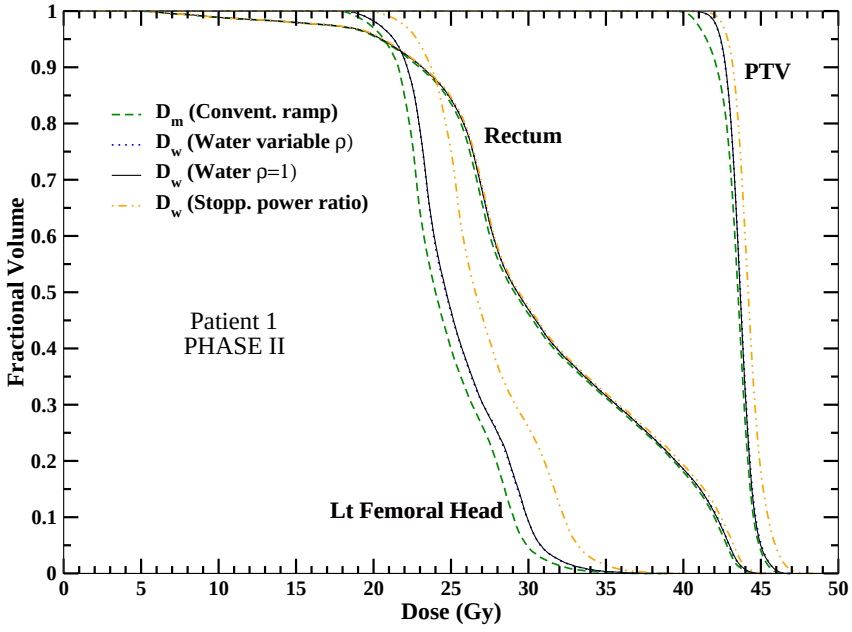

(b)

Figure 9.7: DVHs of the PTV, rectum and left femoral head calculated by MC in patient phantoms built using different CT conversion ramps (table 9.2) for the Phase I (a) and II (b) of patient 1. DVH for the D_m (Convent. ramp) distribution converted to dose to water using stopping power ratio (Siebers *et al* 2000) is also shown.

Additionally, it is also noted from figures 9.7 that there is a significant shift by about 6 % in the DVH of the femoral heads for the plan calculated using water of variable densities compared to the

plan converted from medium (conventional ramp) to water using the stopping power ratio method. However, the DVHs of the PTV are not affected by the conversion of D_m to D_w for both treatment phases. These results confirm the tendency observed previously in the dose profiles (figures 9.4 - 9.6).

The comparison of rectum DVHs calculated in conventional and simplified phantoms does not show significant differences (1 %). Note that the air was defined with the same composition and density for all three CT ramps used in this study (table 9.2).

9.3.2 Eclipse TPS and MC dose comparison

The discrepancies between IMRT plans calculated with MC simulations and predicted by the Eclipse system (pencil beam algorithm) were evaluated in terms of isodose distributions and DVHs of the target (PTV), rectum and left femoral head structure. Figures 9.8a - 9.8c compare isodose distributions obtained from the Eclipse system with Monte Carlo simulations performed in conventional phantoms (D_m) and in simplified phantom of water with variable density (D_w) for the Phase I of the IMRT plan in patient 1.

Moreover, the isodose curves from Monte Carlo simulations calculated in medium and converted to dose to water using stopping power ratios are illustrated in figure 9.8d. It is seen from figures 9.8 that the MC dose distributions (conventional and simplified phantoms) in the target showed a good agreement (about 2 %) with Eclipse TPS.

In regions including heterogeneities (air and bone), differences up to 3 - 4 % could be observed between the Eclipse calculations and the Monte Carlo simulation in the conventional phantom. In bone regions, large differences (6 %) in isodose curves were observed between MC simulations and the Eclipse system when the MC distributions were converted to dose to water using the stopping power ratios. As seen in figure 9.8a and 9.8d, the 27.87 Gy line (light green line) varied noticeably between these two dose distributions within the region of the left femoral head (region limited by the red line).

DVH curves from the Eclipse system were compared with DVHs calculated using Monte Carlo in the different phantoms above described for Phase I and II of patient 1 and 2, as shown in figures 9.9. DVHs for the MC dose distribution converted from medium to water using stopping power ratios are also shown in the figures.

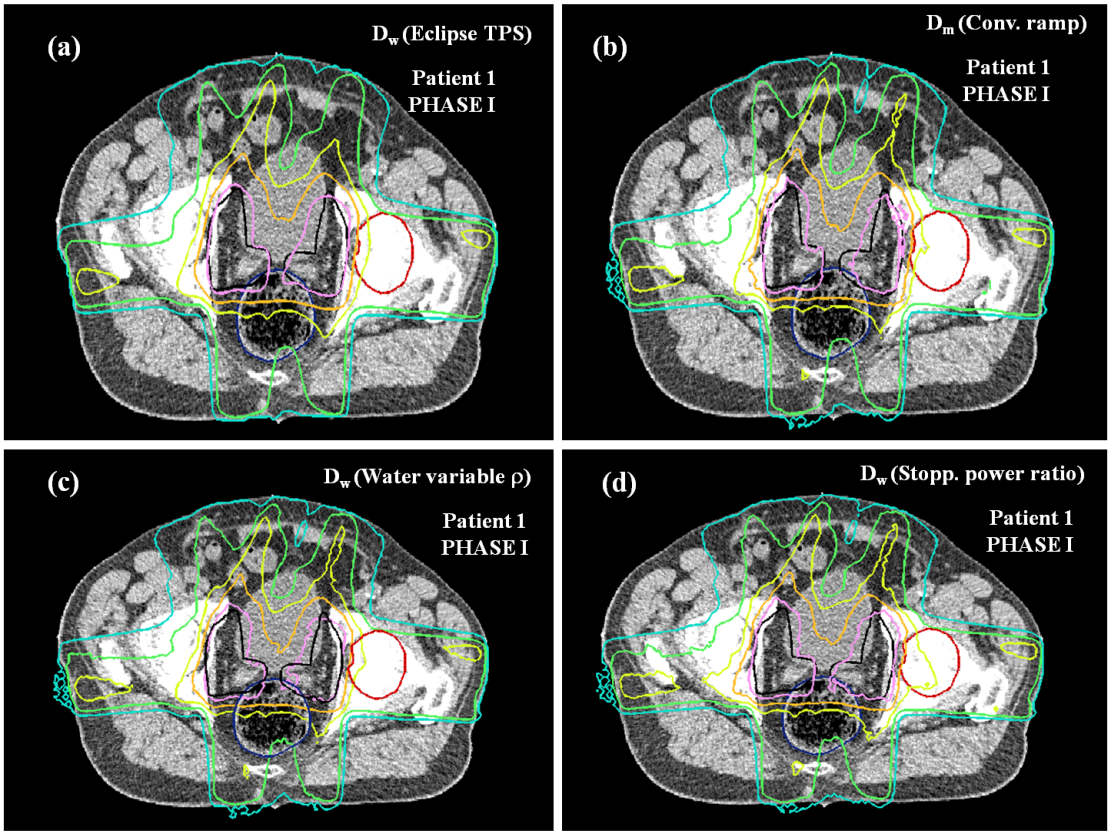

Figure 9.8: Comparison of isodose distribution for the Phase I of the IMRT treatment in patient 1 calculated by Eclipse TPS (a) and by Monte Carlo using: (b) a conventional phantom (D_m), (c) simplified water phantom of water with variable density (D_w) and (d) converted D_m to D_w with stopping power ratio (Siebers *et al* 2000). The isodose lines are 13.9, 20.9, 27.87, 34.84 and 41.81 Gy. Represented volumes on CT images are PTV volume (black), rectum (blue) and left femoral head (red).

For all cases, the target DVHs calculated using MC simulations (all phantoms) agreed within 1 % with the DVHs calculated by the TPS.

For femoral heads, discrepancies by about 3 % were found in the DVH computed by the Eclipse system as compared with MC calculations in medium (conventional phantom). The conversion of MC dose distributions from D_m to D_w results in a difference of about 6 % with the TPS for the femoral structure. For the target, however, the DVHs of converted dose distributions do not show such large differences when compared with the Eclipse system.

For the rectum, DVHs curves from the Eclipse system for patient 1 show a good agreement (2 %) with the DVH curves calculated using MC simulations in medium and those converted from medium

to water. For the patient 2, it can be seen that the Eclipse system estimates a higher dose, up to 5 - 6 %, than both MC dose values calculated in medium and those converted from medium to water using the stopping power ratios, in particular for the range of low doses.

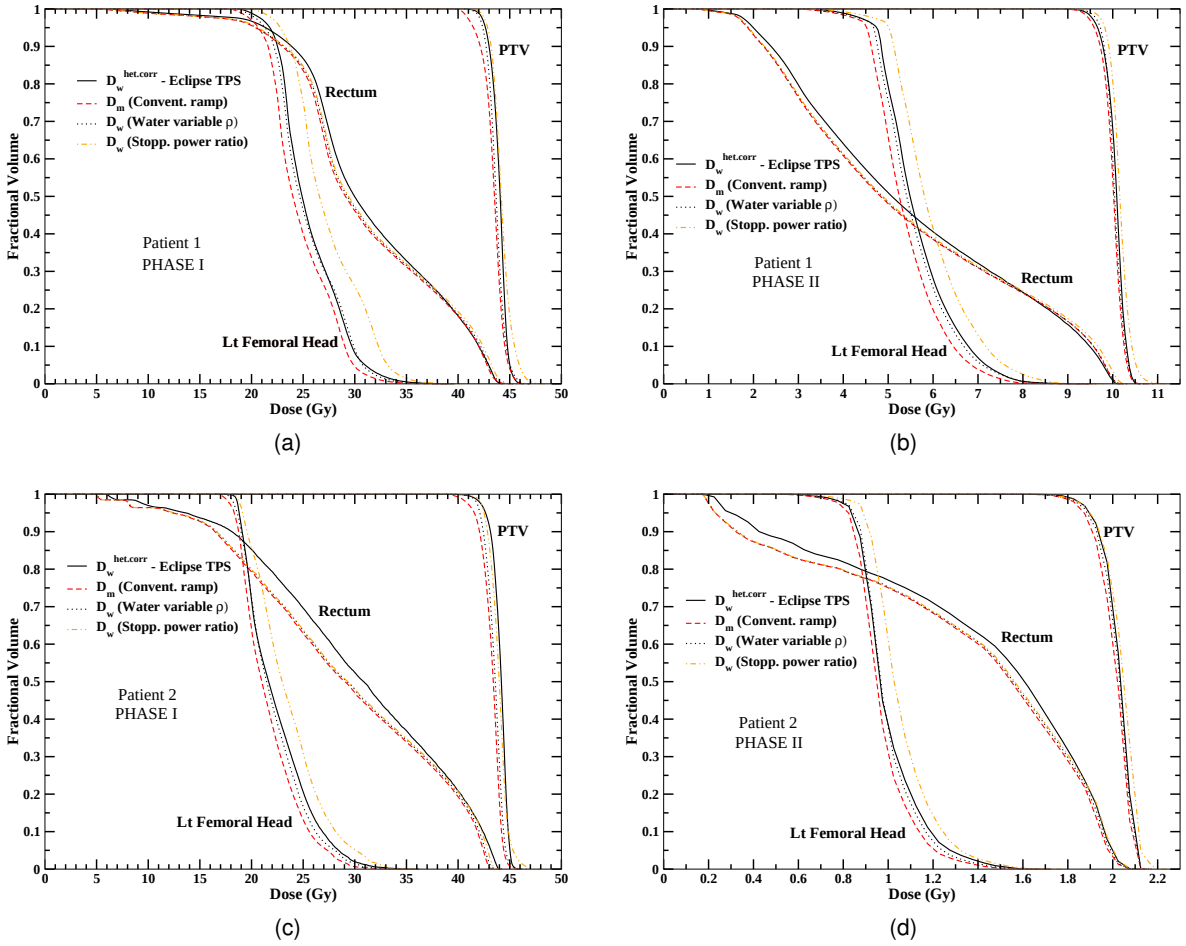

Figure 9.9: Comparison of DVH curves calculated by Eclipse TPS (continuous line) and by Monte Carlo (dashed lines) for the PTV, rectum and the left femoral head. Monte Carlo calculations were performed in phantoms built with a conventional CT ramp and the simplified CT ramp of water of variable densities. DVH for the D_m distribution converted from dose to medium to dose to water using stopping power ratio (Siebers *et al* 2000) is also shown. DVHs are illustrated for Phase I (a-c) and II (b-d) of patient 1 and 2.

This fact may be a consequence of the field arrangements considered for the treatment of both patients. For patient 2, the posterior region containing the rectum was irradiated using a large number of fields in comparison with the number of fields considered for the patient 1, resulting probably in a higher dose effect of the air contained in this structure. It is important to point out that MC calculations are reported as dose to air, whereas the Eclipse TPS are given as dose to water corrected by the air density. Despite of this fact, the discrepancies observed between both

distributions for the rectum should alert the radiophysicist for the treatment of prostate cancer where an wide region near the rectum should be irradiated.

Similar findings for DVHs were observed within patient 3 (not shown).

9.4 Conclusions

The dose distributions of three IMRT plans of prostate patients planned by Eclipse TPS with 6 MV photon beams were evaluated using the MC calculation method. The initial plans were computed by the Eclipse system using a pencil beam algorithm with a Modified Batho Power Law heterogeneity correction. Plans were subsequently recalculated using DOSXYZnrc code in conventional and simplified CT-based phantoms.

Conventional phantoms were created from CT patient data using a conventional four material ramp (CTCREATE) to convert CT numbers into material and mass density. Simplified phantoms were created using simplified ramps: air and water with variable density as well as air and water with unit density.

The individual contribution to dose of material properties (composition and density) presented in MC phantoms was investigated for these plans. The effect of the elemental composition of materials was found to be less than 1 % on dose profiles and DVHs of soft tissue. This effect increased up to 3 % in regions where bone structures such as the femoral heads were present.

On the other hand, the mass density of materials presented in the MC phantoms did not show a significant influence (about 1 %) on dose profiles and DVHs for all tissues. The conversion of MC dose distributions from medium to water using the stopping power ratios (Siebers *et al* 2000)[Sieb00] introduced an increase of about 9 % in DVHs of bony structures such as femoral heads. In contrast, such dose conversion did not affect significantly (1 %) the dose in other tissues and critical structures containing air, such as the rectum.

The isodose comparison between Eclipse TPS and MC simulations in conventional phantoms showed a good agreement (2 %), except for heterogeneous regions containing bone and air (femoral heads or rectum structures), where differences of up to 4 % were observed. This finding was confirmed by the DVH comparison, where Monte Carlo calculations performed in conventional phantoms presented discrepancies of 1 % and 3 - 6%, with TPS for the PTV volumes and for critical structures (femoral head and rectum), respectively.

A good agreement was reached between dose distributions predicted by the Eclipse system and those calculated with MC in simplified phantoms of air and water with variable densities. Using these simplified phantoms, differences of about 1 % were found in the DVHs of target, femoral heads and rectum compared to TPS.

On the other hand, after converting MC doses from medium to water with the stopping power ratios, DVH of MC calculated distributions for femoral heads became up to 6 % higher than predicted TPS distributions. For the rectum, the Eclipse system estimates a higher dose (up to 6 %) than MC dose calculated in medium as well as those D_m converted using the stopping power ratios.

In conclusion, MC calculations using a simplified CT ramp of water with variable density lead to results very close (3 %) to more precise MC calculations including all different media. Consequently, it can be concluded that TPS photon dose calculation algorithms computing doses using water with different densities provide values close to doses to different media as computed by Monte Carlo algorithms.

In order to follow the AAPM TG 105 recommendations to convert MC dose results from media to water, our results show that, for prostate IMRT plans delivered with 6 MV photon beams, no conversion of MC dose from medium to water using stopping power ratio is needed. In contrast, MC dose calculations using water with variable density may be a simple way to solve the problem found by using the dose conversion method [Sieb00].

The results discussed in the present chapter have been presented orally at the 9th Biennal ESTRO meeting on Physics and Radiation Technology for Clinical Radiotherapy (2010).

Part V

CONCLUSIONS

Chapter 10

Conclusions

The present thesis consisted of several dosimetric studies which demonstrated the potential clinical impact of MC dose calculations in comparison with conventional algorithms and measurements on two different fields of external radiotherapy: electron beam and photon beam radiotherapy. The use of MC in this thesis allowed, first, to evaluate dose distributions in challenging situations in which conventional dose calculation algorithms and measurements have shown some limitations and difficulties, namely superficial and heterogeneous regions. Second, it provided more comprehensive information on the dosimetric and spectral characteristics of clinical electron and photon beams in different and complex field configurations. And, finally, it allowed to make a contribution for solving one of the current problems regarding the use of MC for radiotherapy treatment planning, namely the clinical impact of converting dose-to-medium to dose-to-water in treatment planning and dosimetric evaluation.

The performed studies aimed at making a contribution for the implementation and use of the MC methods for radiotherapy treatment planning.

The main conclusions arisen from the studies are detailed next for each particular study.

Electron Beam Radiotherapy Application

A systematic study assessing the perturbation of air cavities on electron dose distributions has been carried out by using both MC simulations and measurements (Gafchromic EBT film). The cavities (top surface) were embedded at shallow depths in a acrylic (PMMA) homogeneous phantom, at 2 mm from the surface.

The dependence of the effect on cavity size (area and thickness) and the energy of the electron beam (12 and 18 MeV) was systematically evaluated using both methods (MC simulations and film measurements) for the standard field size of 10 x 10 cm^2. For this field, the impact caused by the presence of air was also analyzed through the electron energy and angular spectra calculated below the cavity. The influence of the cavity size was additionally assessed with MC simulations for real treatment fields collimated by cerrobend cutouts and a beam energy of 12 MeV.

The most important results on this investigation can be summarized as follows:

- **For a standard 10 x 10 cm^2 field size:**
  - The presence of the cavity caused an increase of the maximum dose value as well as a shift forward of the position of the depth-dose curve, compared to the depth-dose curve for the homogeneous phantom.
    - The presence of an air cavity introduced variations of up to 70 % on the maximum dose value with respect to the homogeneous case.
    - For cavities with a same area (1 x 1 cm^2) and variable thickness, the highest increase (70 %) and shift (0.6 cm) of the maximum dose was found for a cavity thickness of 2.8 cm.
    - For cavities with a same thickness (1.8 cm) and variable area, the highest increase (60 %) of the maximum dose was found for the cavity of smallest area (1 x 1 cm^2), whereas the largest shift (1.4 cm) was observed for the cavity with the largest area (3.8 x 3.8 cm^2).
  - The shape of the dose transversal profiles changed dramatically due to the cavity. Pronounced discontinuities of the dose in the regions close to the lateral cavity edges were observed. A sharp increase of the dose (more than 20 %) in the lateral sides inside of the cavity edge was found compared to the uniform dose for the homogeneous phantom. On other hand, decreases of about 10 % in the dose values in the lateral sides outside the cavity edge are observed relative to the homogeneous profile.
  - The results indicate that the cavity effect on the dose distributions is more pronounced (about 6 %) for the 12 MeV electron beam when compared with 18 MeV, except for the largest cavity (3.8 x 3.8 cm^2) where an increase of 6 % of the maximum dose is found in comparison with the increase of 1 % previously obtained for the beam energy of 12 MeV.

  - The experimental results confirm the MC predicted behavior of the dose near the interface of the cavity with water. The agreement between the Monte Carlo calculations and EBT film measurements was about 2 % and 6 % for the 12 MeV and 18 MeV electron beam, respectively.

- **For fields collimated by a cerrobend block:**

  - The influence of the air cavity on dose distributions calculated showed a similar behavior on dose profiles as that observed for the field of 10 x 10 cm^2. The presence of the cavity may result in a significant increase (up to 70 %) of the maximum dose in the depth-dose curve compared to the homogeneous curve; pronounced discontinuities (cold and hot spots) were observed on the isodose distributions in the regions close to the lateral cavity edges.

In conclusion, the perturbations in the dose presented in this work due to the presence of shallow cavities, should alert radiophysicists, using treatment planning based on pencil beam algorithm, for cases of head and neck and others treated with electron beams, that underestimation and overestimation of the dose is expectable. Monte Carlo verification as a quality assurance protocol is strongly recommended for these situations.

Photon Beam Radiotherapy Application

A full MC simulation of the Varian Clinac 2100C/D linear accelerator head in 6 MV photon mode was performed. Dose distributions calculated in water phantoms were benchmarked against experimental data measured with a cylindrical ionization chamber (volume 0.125 cm^3).

The comparison of calculated and measured dose distributions also allowed determining the optimal values of parameters characterizing the incident electron beam, namely energy E and radius R.

The geometry of the Millenium MLC was accurately modeled and incorporated into the model of the accelerator. A series of test consisting of leaf leakage, static MLC shapes and dynamic fields were performed to verify the details of the MLC model and to determine also the unknown parameters of the model, i.e. MLC leaf density, interleaf gap width (gap between adjacent leaves) and abutting gap width (gap between fully closed opposing leaf pair). Simulated dose distributions

for static arbitrary MLC shapes and dynamic patterns were found to agree with film measurements to within 4 %.

In summary, the benchmark evaluations of the Varian 2100C/D accelerator and Millenium MLC models demonstrated the ability of these models to be used as input of phantom dose calculations for 6 MV photon beams. The models were used to simulate two real complex clinical studies and the most important conclusions of these studies are summarized next.

- **Case study 1: Assessing MLC effect on the build-up region for 6 MV photon beams**

  The effect of the MLC on the build-up region dose has been studied using MC simulations and measurements carried out with two different ionization chambers. Percentage dose curves in the build up region for MLC defined fields were compared to those fields in which the MLC does not intercept the beam and therefore the scattering of the MLC does not affect the field.

  - From the MC calculations, it has been determined that the effect caused by the presence of the MLC is practically negligible (less than 1 %) for 10 x 10 and 4 x 4 cm^2 MLC defined fields, within a statistical uncertainty of 1 % at the depth of maximum dose. The bigger effect (about 2 %) was observed for the 2 x 2 cm^2 MLC defined field. In the build up region, the overall head accelerator contribution to the total dose (including MLC) is of about 10 % for the 10 x 10 cm^2 field and it decreases with field size (2 - 3 % for 2 x 2 cm^2 field size). It was found that the scattering of particles from accelerator head and MLC is responsible for the increase of about 7% of the surface dose by comparing 2 x 2 and 10 x 10 cm^2 field sizes.
  - Experimentally, the same evaluation was done experimentally with two different ionization chambers in a water phantom. Specifically, the chambers were a PTW PinPoint cylindrical chamber (volume 0.015 cm^3) and a Roos parallel-plate chamber (volume 0.35 cm^3). A negligible effect (less than 1 %) of the MLC on build up doses was observed for all MLC defined field sizes considered in this investigation.
  - The MC calculated PDD and measured PDI curves were also compared for the different MLC defined fields. In general, it was observed that the measured PDIs differ from the calculated PDD and this difference depends on the measuring chamber type. Particularly, the dose values measured with Roos chamber agree with MC values within 2 % for all MLC field sizes and depths greater than 2 mm, while differences of about 4 %

were found between the values measured with the cylindrical ionization chamber and MC values.

Based on the previous results by [Kim01] which observed a contribution of 18 % to the surface dose due the electrons generated by the MLC for 6 MV irradiation of a 10 x 10 cm^2 field fully blocked by the MLC, the dosimetric effect of the MLC to the build-up region should be taken into account. According to that, this effect could overestimate the dose in the superficial regions. However, our results show that the influence of the MLC is not so very significant (withn 2 %) for typical field sizes used in the radiotherapy treatments.

- **Case study 2: The use of non-standard CT conversion ramps for Monte Carlo verification of 6 MV prostate IMRT plans**

  The dose distributions of three IMRT plans of prostate patients planned by an Eclipse TPS for 6 MV photon beams were evaluated using the MC calculation method. The initial plans were computed by the Eclipse system using a pencil beam algorithm with a Modified Batho Power Law heterogeneity correction. Plans were subsequently recalculated using DOSXYZnrc code in conventional and simplified CT-based phantoms with an average statistical uncertainty of 2 % in the regions of the targeted volumes (PTV and critical structures).

  Conventional phantoms were created from CT patient data using a conventional four material ramp (CTCREATE) to convert CT numbers into material and mass density. Simplified phantoms were created using simplified ramps: air and water with variable density as well as air and water with unit density.

  - The individual contribution to dose of material properties (composition and density) presented in MC phantoms was investigated for these plans:
    - The effect of the elemental composition of materials was found to be less than 1 % on dose profiles and DVHs of soft tissue and it increased up to 3 % in regions where bone structures such as the femoral heads were present.
    - The mass density of materials did not show a significant influence (about 1 %) on dose profiles and DVHs for all tissues.
  - The conversion of MC dose distributions from medium to water using the stopping power ratios (Siebers *et al* 2000)[Sieb00] introduced an increase of about 9 % in DVHs of bony

structures such as femoral heads. In contrast, such dose conversion did not affect significantly (1 %) the dose in other tissues and critical structures containing air, such as the rectum.

- The isodose comparison between Eclipse TPS and MC simulations in conventional phantoms showed a good agreement (2 %), except for the heterogeneous region containing bone and air (femoral heads or rectum structures), where differences of up to 4 % were observed. This finding was confirmed from the DVH comparison, where Monte Carlo calculations performed in conventional phantoms presented discrepancies of 1 % and 3 %, with TPS for the PTV volumes and for critical structures (femoral head and rectum), respectively.
- A good agreement was reached between dose distributions predicted by the Eclipse system and those calculated with MC in simplified phantoms of air and water with variable densities. Using these simplified phantoms, differences of about 1 % were found in the DVHs of target, femoral heads and rectum compared to TPS.
- After converting MC doses from medium to water with the stopping power ratios, DVH of MC calculated distributions for femoral heads became up to 6 % higher than predicted TPS distributions.
- For the rectum, the Eclipse system may estimate a higher dose (up to 6 %) than the MC dose calculated in medium D_m as well as D_m converted to water using the stopping power ratios. This overestimation is more significant for the treatment plans considering a higher number of fields (3 posterior fields) to irradiate the rectum region.

MC calculations in water with variable density as well as in water of unit density lead to results very close (3 %) to more precise MC calculations including all different media. Consequently, it can be concluded that TPS photon dose calculation algorithms computing doses using water with different densities provide values close to doses to different media as computed by Monte Carlo algorithms. On the other side, these results indicate that it should not be necessary to apply heterogeneity correction to the TPS results, except to the air regions which must be considered explicitly due to the observed results.

Our results show that, for prostate IMRT plans delivered with 6 MV photon beams, no conversion of MC dose from medium to water using stopping power ratio is needed. Indeed, MC

dose calculations using water with variable density may be a simple way to solve the problem found by using the dose conversion.

Bibliography

[Att86] Attix, F. H., 1986. Introduction to radiological physics and radiation dosimetry. ISNB-13:978-0-471-01146-0

[AAPM85] Papanikolaou N., Battista J., Boyer A., Kappas C., Klein E., Mackie T.R., Sharpe M. and Van Dyk J., 2004 Tissue Inhomogeneity Corrections for Megavoltage Photon Beams. AAPM Report No 85, Task Group No 65 of the Radiation Therapy Committee of the American Association of Physicist in Medicine. Madison: Medical Physics Publishing.

[Abdel06] Abdel-Rahman W., Seuntjens J. P., Verhaegen F., Deblois F., Podgorsak E. B., 2004 Validation of Monte Carlo calculated surface doses for megavoltage photon beams. Med. Phys. 32 (1) 286 - 298

[Ago03] Agostinelli S., et al., 2003 G4 - a simulation toolkit. Nuclear Instruments and Methods in Physics Research Section A: Accelerators, Spectrometers, Detectors and Associated Equipment, 506(3): 250 - 303

[Alm99] Almond P. R., Biggs P. J., Coursey B. M., Hanson W. F., Saiful Huq M., Nath R. and Rogers D. W. O., 1999 AAPM's TG-51 protocol for clinical reference dosimetry of high-energy photon and electron beams. Med. Phys. 26, 1847 - 1870

[And91] Andreo P., 1991 Monte Carlo techniques in medical radiation physics. Phys. Med. Biol. 36, 861 - 920

[And00] Andreo P., Burns D.T., Hohlfeld K., Hug M.S., Kanai T., Laitano F., Smyth V.G. and Vynckier S., 2000 Absorbed dose determination in external beam radiotherapy: an international code of practice for dosimetry based on standards for absorbed dose to water. Vol. 398 of Technical Report Series, IAEA, (International Atomic Energy Agency, Vienna)

[Ahn92] Ahnesjö A., Saxner M. and Trepp A., 1992 A pencil beam model for photon dose calculation. Med. Phys. 19, 263 - 273

[Beh06] Behrens C. F., 2006 Dose build-up behind air cavities for Co-60, 4, 6 and 8 MV. Measurements and Monte Carlo simulations. Phys. Med. Biol. 51, 5937-5950

[Ber63] Berger M. J., 1963 Monte Carlo Calculation of the penetration and diffusion of fast charged particles in Methods in Computational, Physics, edited by B. Alder, S. Fernbach, and M. Rotenberg Academic, New York, Vol. 1, pp. 135 215

[Bet53] Bethe H. and Ashkin J. in Experimental Nuclear Physics. Vol 1 ed. E. Segr, J. Wiley, New York, 1953, p. 253

[Biel87] Bielajew A. F. and Rogers D. W. O., 1987 PRESTA: The Parameter Reduced Electron-Step Transport Algorithm for electron Monte Carlo transport. Nucl. Instrum. Methods Phys. Res. B 18, 165181

[Biel01] Bielajew A. F., 2001 Fundamentals of the Monte Carlo method for neutral and charged particle transport. University of Michigan. $http : //www - personal.engin.umich.edu/\ bielajew/MCBook/book.pdf$

[Bilge08] Bilge H., Cakir A., Okutan M., Acar H., 2009 Surface dose measurements with Gafchromic EBT film for 6 and 18 MV photon beams. Phys. Med. 25 (2) 101 - 104

[Brie00] Briesmeister J., 2000. MCNP - a general monte carlo n-particle transport code. Technical report, Los Alamos National Laboratory.

[Bou09] Bouchard H., Lacroix F., Beaudoin G., Carrier J. F., and Kawrakow I., 2009 On the characterization and uncertainty analysis of radiochromic film dosimetry. Med. Phys. 36, 1931 - 1946

[Boy97] Boyer A. L. and Li S., 1997 Geometric analysis of light-field position of a multileaf collimator with curved ends. Med. Phys. 24, 727 - 762

[Buts03] Butson M. J., Yu P. K. N., Cheung T., and Metcalfe P., 2003 Radiochromic film for medical radiation dosimetry. Mat. Sci. Eng. R 41, 61-120

[Chet02] Chetty I. J. and Charland P. M., 2002 Investigation of Kodak extended dose range (EDR) film for magavoltage photon beam dosimetry. Phys. Med. Biol. 47, 3629-3641

[Chet07] Chetty I. J. et al., 2007 Report of the AAPM Task Group No. 105: Issues associated with clinical implementation of Monte Carlo-based photon and electron external beam treatment planning. Med. Phys. 34, 4818-53

[Chi07] Fan-Chi S., Liu Y., Stathakis S., Shi C., Esquivel C., and Papanikolaou N., 2007 Dosimetry characteristics of GAFCHROMIC EBT film responding to therapeutic electron beam. App. Rad. Iso. 65, 1187-1192

[Chow10] Chow J. C. L., Grigorov G. N., 2010 Dosimetry of a small air cavity for clinical electron beams: a Monte Carlo study. Med. Dosim. 35, 92-100

[Cyg04] Cygler J. E., Daskalov G. M., Chan G., and Ding G. X., 2004 Evaluation of the first commercial Monte Carlo dose calculation engine for electron beam treatment planning. Med. Phys. 31, 142-153

[Dea96] Deasy J. O., Almond P. R., and McEllistrem M. T., 1996 Measured electron energy and angular distributions from clinical accelerators Med. Phys. 23, 675-704

[DeB07] De Boer S. F., Kumek Y., Jaggernauth W. and Podgorsak M. B., 2007 The effect of beam energy on the quality of IMRT plans for prostate conformal radiotherapy. Technol. Cancer. Res. Treat. 6, 139 - 146

[Deng99] Deng J., Jiang S. B., Kapur A., Jinsheng L., Pawlicki T, and Ma C-M., 1999 Photon beam characterization and modelling for Monte Carlo treatment planning. Phys. Med. Biol. 45, 411-427

[Ding06] Ding G. X., Duggan D. M., Coffey C. W., Shokrani P., and Cygler J. E., 2006 First macro Monte Carlo based commercial dose calculation module for electron beam treatment planning - new issues for clinical consideration. Phys. Med. Biol. 51, 2781- 2799

[Dog06] Dogan N., Siebers J. V., and Keall P. J., 2006 Clinical comparison of head and neck and prostate IMRT plans using absorbed dose to medium and absorbed dose to water. Phys. Med. Biol. 51, 4967-4980

[Eck87] Eckhardt R., 1987 Stan Ulam, John von Neumann, and the Monte Carlo method. Los Alamos Science, Special Issue 15, 131 137

[Eva55] Evans R. D., 1955 The Atomic Nucleus. McGraw-Hill, New York

[Fern95] Fernndez-Varea J. M., Baro J., Sempau J. and Salvat. F., 1995 Penelope - an algorithm for Monte Carlo simulation of the penetration and energy-loss of electrons and positrons in matter. Nucl. Instrum. Methods Phys. Res., A 100:31 - 46

[Fer09] Ferreira B.C., Lopes M.C., and Capela M., 2009 Evaluation of an Epson flatbed scanner to read Gafchromic EBT films for radiation dosimetry. Phys. Med. Biol. 54, 1073-1085

[Gard07] Gardner J. K., Siebers J. V. and Kawrakow I., 2007 Comparison of two methods to compute the absorbed dose to water for photon beams. Phys. Med. Biol. 52, N439 - N447

[Guck06] Guckenberger M., Flentje M., 2006 Intensity-Modulated Radiotherapy (IMRT) of Localized Prostate. Cancer. Strahlenther. Onkol. 2, 57 - 62

[Hea03] Heath E., Seuntjens J., 2003 Development and validation of a BEAMnrc component module for accurate Monte Carlo modelling of the Varian dynamic Millenium multileaf collimator. Phys. Med. Biol. 48, 4045 - 4063

[Hua83] Huang P. H., Kase K. R., Bjarngard B. E., 1983 Reconstruction of 4-MV bremsstrahlung spectra from measured transmission data. Med. Phys. 10 778

[Houn79] Hounsfield G. N., Computed Medical Imaging $http : //www.nobelprize.org/nobel_prizes/medicine/laureates/1979/hounsfield - lecture.pdf$

[Houn99] Hounsell A. R. and Wilkinson J. M., 1999 Electron contamination and build-up doses in conformal radiotherapy fields. Phys. Med. Biol. 44, 43 - 55.

[ICRU24] ICRU. Determination of absorbed dose in a patient irradiated by beams of x- and gamma rays in radiotherapy procedures. ICRU Report 24, ICRU, Washington D.C., 1976

[IMRT01] Intensity Modulated Radiation Therapy Collaborative Working Group., 2001 Intensity-Modulated Radiotherapy: Current status and issues of interest. Int. J. Radiat. Oncol. Biol. Phys. 51, 880 - 914

[Jak03] Jakel O., Schulz-Ertner D., Karger C. P., Nikoghosyan A. and Debus J., 2003 Heavy ion therapy: status and perspectives. Technol. Cancer Res. Treat. 2, 377 87

[Jal06] Jalbout W. T. and Spyrou N. M., 2006 Spectral reconstruction by scatter analysis for a linear accelerator photon beam. Phys. Med. Biol. 51, 2211 - 2224

[Jan06] Jang S. Y., Vassiliev O. N., Liu H. H., Mohan R. and Siebers J. V., 2006 Development and commissioning of a multileaf collimator model in Monte Carlo dose calculations for intensity-modulated radiation therapy. Med. Phys. 33 (3) 770 - 781

[Jus08] Juste B., Miró R., Campayo J. M., Díez S. and Verdú G., 2008 Photon Spectra calculation for an Elekta linac beam using experimental scatter measurements and Monte Carlo thecniques. Proceedings of 30th Annual International IEEE EMBS Conference, Vancouver, Canada, p. 3289.

[Jut05] Jutemark B., 2005 Monte Carlo based investigation of the influence of accelerator head geometry on megavolt photon beam quality in radiotherapy. Master of Science Thesis.

[Kan98] Kan W. K., Wu P. M., Leung H. T., Lo T. C., Chung C. W., Dora L. W. K., and Sham S. T., 1998 The effect of nasopharyngeal air cavity on x-ray interface doses. Phys. Med. Biol. 43, 529-537

[Kaw00a] Kawrakow I., 2000 Accurate condensed history Monte Carlo simulation of electron transport (Part I). Med. Phys. 27, 485 - 498

[Kaw00b] Kawrakow I., 2000 Accurate condensed history Monte Carlo simulation of electron transport (Part II). Med. Phys. 27, 499 - 513

[Kaw01] Kawrakow I. and Fippel M., 2001 VMC++, electron and photon Monte Carlo calculations optimized for radiation treatment planning Advanced Monte Carlo for Radiation Physics, Particle Transport Simulation and Applications: Proc. Monte Carlo 2000 Meeting (Lisbon) pp 22936

[Kaw03] Kawrakow I, Rogers D.W.O., 2003 The EGSnrc Code System: Monte Carlo simulation of electron and photon transport. National Research Council of Canada Report No. 701, Ottawa, Canada

[Kaw06] Kawrakow I. and Walter B. R., 2006 Efficient photon beam dose calculations using DOSXYZnrc with BEAMnrc. Med. Phys. 33, 3046 - 3056

[Kaw07] Kawrakow I., 2007 The dose visualization tool dosxyz_show. NRCC Report PIRS-0624

[Keall00] Keall P. J., Siebers J. V., Arnfield M., Kim J. O. and Mohan R., 2000 Monte Carlo dose calculation for dynamic IMRT treatments. Phys. Med. Biol. 46, 929 - 941

[Keall00b] Keall P. J., Siebers J. V., Jeraj R. and Mohan R., 2000 The effect of dose calculation uncertainty on the evaluation of radiotherapy plans. Med. Phys. 27, 478 - 484

[Khan90] Khan F. M., Doppke K. P., Hogstrom K. R., Kutcher G. J., Nath R., Prasad S. C., Purdy J. A., Rozenfeld M., and Werner B. L., 1990 Clinical electron beam dosimetry: Report of AAPM Radiation Therapy Committee Task Group No. 25.

[Kim01] Kim J.O., Siebers J.V., Keall P.J., Arnfield M.R., Mohan R., 2001 A Monte Carlo study of radiation transport through multileaf collimators. Med. Phys. 28, 2497 - 2506

[Klein93] Klein E., Lee M. C., Rice R. K., and Mijnheer B. J., 1993 The influence of air cavities on interface doses for photon beams. Int. J. Radiat. Oncol. Biol. Phys. 27, 419-26

[Klev92] Klevenhagen S. C., 1992 Specification and energy determination of clinical electron beam. AMPI Medical Physics Bulletin 17 34-47

[Leal03] Leal A., Snchez-Doblado F., Arrns R., Rosell J., Carrasco Pavn E. and Lagares J. F., 2003 Routine IMRT verification by means of an automated Monte Carlo simulation system. Int. J. Rad. Oncol. Biol. Phys. 56, 58 - 68

[Leal04] Leal A., Sanchez-Doblado F., Arrans R., Capote R., Lagares J. F., Carrasco E., Rosello J., 2004 MLC leaf width impact on the clinical dose distribution: a Monte Carlo approach. Int. J. Radiat. Oncol. Biol. Phys. 59 (5) 1548 - 1559

[Lev76] Levy L. B., Waggener R. G., Wright A. E., 1976 Measurement of primary bremsstrahlung spectrum from an 8-MeV linear accelerator. Med. Phys. 3 173

[Li00] Li X. A., Yu C. and, Homes T., 2000 A systematic evaluation of air cavity dose perturbation in megavoltage x-ray beams. Med. Phys. 27, 1011-1017

[Liu00] Liu H. H., Mackie T. R. and McCullough E. C., 2000 Modeling photon output caused by backscattered radiation in the monitor chamber from collimator jaws using a Monte Carlo technique. Med. Phys. 27 737-44

[Liu02] Liu H. H. and Keall P., 2002 D_m rather than D_w should be used in Monte Carlo treatment planning. Med. Phys. 29, 922 - 24

[Liu01] Liu H. H., Verhaegen F. and Dong L., 2001 A method of simulating dynamic multileaf collimators using Monte Carlo techniques for intensity-modulated radiation therapy. Phys. Med. Biol. 46, 2283 - 98

[Low11] Low D. A., Moran J. M., Dempsey J. F., Dong L. and Oldham M., 2011 Dosimetry tools and techniques for IMRT. Med. Phys. 38, 1313 - 1338

[Ma00a] Ma C. M., Pawlicki T., Lee M. C., Jiang S. B., Li J. S., Deng J., Yi B., Mok E. and Boyer A. L., 2000 Energy- and intensity-modulated electron beams for radiotherapy. Phys. Med. Biol. 45, 2293311

[Ma00b] Ma C. M., Pawlicki T., Jiang S. B., Li J. S., Deng J., Mok E., Kapur A., Xing L., Ma L. and Boyer A. L., 2000 Monte Carlo verification of IMRT dose distributions from a commercial treatment planning optimization system. Phys. Med. Biol. 45, 2483-2495

[Ma02] Ma C. M., Li J., Pawlicki T., Jiang S., Deng J., Lee M., Koumrian T., Luxton M. and Brain S., 2002 A Monte Carlo dose calculation tool for radiotherapy treatment planning. Phys. Med. Biol. 47, 1671-1689

[Ma03] Ma C. M., Jiang S. B., Pawlicki T., Chen Y., Li J. S., Deng J. and Boyer A. L., 2003 A quality assurance phantom for IMRT dose verification. Phys. Med. Biol. 48, 561 - 572

[Ma04] Ma C. M., Price Jr. R. A., Li J. S., Chen L., Wang L., Fourkal E., Qin L. and Yang J., 2004 Monitor unit calculation for Monte Carlo treatment planning. Phys. Med. Biol. 49, 1671 - 1687

[Ma04b] Ma C. M., Li J. S., Jiang S. B., Pawlicki T., Xiong W., Qin L. H. and Yang J., 2004 Effect of statistical uncertainties on Monte Carlo treatment planning. Phys. Med. Biol. 50, 891 - 907

[Ma09] Ma C. M., and Rogers D. W. O., 2009 BEAMDP Users Manual. NRCC Report PIRS-0509(C) revA

[Ma09b] Ma C. M. and Li J. S., 2009 Monte Carlo dose calculation for radiotherapy treatment planning: dose to water or dose to medium?. IFMBE Proceedings 25/I, pp. 326 - 329

[Ma11] Ma C. M. and Li J., 2011 Dose specification for radiation therapy: dose to water or dose to medium?. Phys. Med. Biol. 56, 3073 - 3089

[Mar08] Martisikova M., Ackermann B., and Jkel O., 2008 Analysis of uncertainties in Gafchromic EBT film dosimetry of photon beams. Phys. Med. Biol. 53, 7013-7027

[McGo07] McGowan H. C. E., Faddegon B. A., and Ma C., 2007 STATDOSE for 3D dose distributions, NRCC Report PIRS-0509(F)

[Met97] Metcalfe P., Kron T. and Hoban P., 1997 The Physics of Radiotherapy X-rays from linear accelerators, Medical Physics Publishing, Madison, Wisconsin

[Mih06] Mihailescu D. and Borcia C., 2006 Water equivalency of some plastic materials used in electron dosimetry: a Monte Carlo investigation. Romanian Reports in Physics, 58, 415 - 425

[Moh85] Mohan R., Chui C., and Lidofsky L., 1985 Energy and angular distributions of photons from medical linear accelerators. Med. Phys. 12, 592 - 597

[Moh86] Mohan R., Chui C., and Lidofsky L., 1986 Differential pencil beam dose computation model for photons. Med. Phys., 13, 64 73

[Mor99] Mora G. M., Maio A., and Rogers D. W. O., 1999 Monte Carlo Simulation of a Typical 60Co Therapy Source. Med. Phys. 26, 2494 - 2502

[Mor00] Mora G. M., Pawlicki T., Maio A., and Ma. C. M., 2000 Effect of Voxel Size on Monte Carlo Dose Calculations for Radiotherapy Treatment Planning. Advanced Monte Carlo for Radiation Physics, Particle Transport Simulation and Applications, p. 549 - 554, Proceedings of the Monte Carlo 2000 Conference, Lisbon, October 2000. E-archive: www.springer.com/dal/home/generic/search/results?SGWID=1-40109-22-2146938-0,

[Mor01] Mora G. M., 2001 Application of Monte Carlo simulation techniques in clinical radiation therapy dosimetry, Ph.D. thesis, Faculty of Sciences, Lisbon University.

[Nel85] Nelson R., Hirayama H. and Rogers D. W. O., 1985 The EGS4 Code System. Standorf Linear Accelerator Center Report SLAC - 265 (Stanford, CA:SLAC)

[Nir94] Niroomand - Rad A., Harter K. W., Thobejane S., and Bertrand K., 1994 Air cavity effects on the radiation dose to the larynx using Co- 60, 6 MV and 10 MV photon beams. Int. J. Radiat. Oncol. Biol. Phys. 29, 1139-46

[Nir98] Niroomand - Rad A., Blackwell C.R., Coursey B. M., Gall K. P., Galvin J. M., McLaughlin W. L., Meigooni A. L., Nath R., Rodgers J. E., and Soares C. G., 1998 Radiochromic film dosimetry: Reccomendations of AAPM Radiation Thrapy Committee Task Group 55. Med. Phys 25, 2093-2114

[Nuss75] Nsslin F., 1975 The influence of air cavities on the dose distribution of high-energy electron beams. Phys. Med. Biol. 20, 728-734

[Pael03] Paelinck L., Reynaert N., Thierens H., De Wagter C., and De Neve W., 2003 The value of radiochromic film dosimetry around air cavities: experimental results and Monte Carlo simulations, Phys. Med. Biol. 48, 1895-1905

[Pai07] Pai S., Das I.J., Dempsey J. F., Lam K. L., LoSasso T. J., Olch A. J., Palta J. R., Reinstein L. E., Ritt D. and Wilcox E. E., 2007 TG - 69: Radiograhpic film for megavoltage beam dosimetry Med. Phys. 34 (6) 2228 - 2258

[Par08] Parsai E. I., Shvydka D., Pearson D., Gopalakrishnan M., Feldmeier J. J., 2008 Surface and build-up region dose analysis for clinical radiotherapy photon beams. Appl. Radiat. Isotopes 66 (10) 1438 - 1442

[Pena07] Pena J., Gonzlez-Castano D. M., Gmez F., 2007 Automatic determination of primary electron beam parameters in Monte Carlo simulation. Med. Phys. 34, 1076 - 1084

[Pod05] Podgorsak E. B., 2005 Radiation Oncology Physics: A handbook for teachers and students, $www - pub.iaea.org/mtcd/publications/pdf/pub1196_web.pdf$

[Pur86] Purdy J. A., 1986 Buildup/Surface dose and exit dose measurements for a 6 MV linear accelerator. Med. Phys. 13, 259 - 262

[Reyn07] Reynaert N., Van der Marck S. C., Shaart D. R., Van der Zee W., Van Vliet-Vroegindeweij C., Tomsej M., Jansen J., Heijmen B., Coghe M. and De Wagter C., 2007 Rad. Phys. Chem. 76, 643 - 686

[Rog95] Rogers D.W.O., Faddegon B.A. Ding G.X., Ma C-M., We J. and Mackie T. R., 1995 BEAM: a Monte Carlo code to simulate radiotherapy treatment units. Med. Phys. 22, 503 - 504

[Rog01] Rogers D.W.O., Kawrakow I., Seuntjens J.P. and Walters B.R.B., 2001 NRC user codes for EGSnrc National Research Council of Canada Report PIRS-701 National Research Council of Canada

[Rog05] Rogers D.W.O., Walters B., Kawrakow I., 2005 BEAMnrc Users Manual. National Research Council of Canada Report PIRS-0509(A)revK

[Rog11] Rogers D.W.O., Kawrakow I., Seuntjens J.P., Walters B.R.B, Mainegra-Hing E., 2011 NRC User Codes for EGSnrc. National Research Council of Canada Report PIRS-702(revC)

[Salg09] Salguero F. J., Palma B., Arrans R., Rosello J., and Leal A., 2009 Modulated electron radiotherapy treatment planning using a photon multileaf collimator for post-mastectomized chest walls. Radiother. Oncol. 93, 625-32

[Salg10] Salguero F. J., Arrans R., Palma B., and Leal A., 2010 Intensity- and energy-modulated electron radiotherapy by means of an xMLC for head and neck shallow tumors. Phys. Med. Biol. 55, 1413-27

[Sem01] Sempau J., Sánchez-Reyes A., Salvat F., Oulad ben Tahar H., Jiang S. B. and Fernández-Varea J. M., 2001 Monte Carlo simulation of electron beams from an accelerator head using PENELOPE. Phys. Med. Biol. 46 1163 - 86

[She00] Sheikh-Bagheri D., Rogers D. W. O., Ross C. K., and Seutjens J. P. 2000 Comparison of measured and Monte Carlo calculated dose distributions from the NRC linac. Med. Phys. 27, 2256-2266

[She00] Sheikh-Bagheri D. and Rogers D. W. O. 2001 Monte Carlo calculation of nine megavoltage photon beam spectra using the BEAM code. Med. Phys. 29, 391-402

[She02a] Sheikh-Bagheri D. and Rogers D. W. O., 2002 Sensitivity of megavoltage photon beam Monte Carlo simulations to electron beam and other parameters. Med. Phys. 29, 379-390

[She02b] Sheikh-Bagheri D. and Rogers D. W. O., 2002 Monte Carlo calculation of nine megavoltage photon beam spectra using the BEAM code. Med. Phys. 29, 391-402

[Shi06] Shi C., Papanicolaou N., Yan Y., Weng X. and Jiang H., 2006 Analysis of the sources of uncertainty for EDR2 film-based IMRT quality assurance. J. Appl. Clin. Med. Phy. 7(2) 1-9

[Shor86] Shortt K. R., Ross C. K., Bielajew A. F., and Rogers D. W. O., 1986 Electron beam dose distributions near standard inhomogeneities. Phys. Med. Biol. 1, 235-249

[Sieb00] Siebers J. V., Keall P. J., Nahum A. E. and Mohan R., 2000 Converting absorbed dose to medium to absorbed dose to water for Monte Carlo based photon beam dose calculations. Phys. Med. Biol. 45, 983-95

[Sieb02] Siebers J. V., Keall P. J., Kim J. O. and Mohan R., 2003 The EGSnrc Code System: Monte Carlo simulation of electron and photon transport. National Research Council of Canada Report No. 701

[Sieb02b] Siebers J. V., Keall P. J., Kim J. O. and Mohan R., 2002 A method for photon beam Monte Carlo multileaf collimator particle transport. Phys. Med. Biol. 47, 3225 - 3249

[Son77] Sontag M. R., Cunningham J.R., 1977 Corrections to absorbed dose calculations for tissue inhomogeneities. Med. Phys. 4, 431 - 436

[Spez02] Spezi E., Lewis D. G. and Smith C. W., 2002 A DICOM-RT-based toolbox for the evaluation and verification of radiotherapy plans. Phys. Med. Biol. 47, 4223 - 4232

[Sec05] Seco J., Adams E., Bidmead M., Partridge M. and Verhaegen F., 2005 Head and neck IMRT treatment assessed with a Monte Carlo dose calculation engine. Phys. Med. Biol. 50, 817 - 830

[Sto96] Storchi P. and Woudstra E., 1996 Calculation of the absorbed dose distribution due to irregularly shaped photon beams using pencil-beam kernels derived form basic beam data. Phys. Med. Biol. 41 63756

[Sto99] Storchi P., van Battum and Woudstra E., 1999 Calculation of a pencil-beam kernel from measured photon beam data. Phys. Med. Biol. 44 291728

[Such01] Suchoweska N., Hoban P., Butson M., Davison A., and Metcalfe P., 2001 Directional dependence in film dosimetry: radiographic and radiochromic film. Phys. Med. Biol. 46, 1391-1397

[Suth10] Sutherland J. G. H., and Rogers D. W. O., 2010 Monte Carlo calculated absorbed - dose energy dependence of EBT and EBT2 film. Med. Phys. 37, 1110 - 1116

[Tyagi07] Tyagi N., Moran J. M., Litzenberg D. W., Bielajew A. F., Fraass B. A., Chetty I. J., 2007 Experimental verification of a Monte Carlo-based MLC simulation model for IMRT dose calculation. Med. Phys. 34 (2) 651 - 663

[Tha11] Thangavelu S., Jayakumar S., Gavindarajan K. N., Supe S. S, Nagrajan V. and Nagarajan M., 2011 Influence of photon energy on the quality of prostate Intensity Modulated Radiation Therapy plans based on analysis of physical indices. J. Med. Phys. 36, 29 - 34

[Var00] QA test patterns and procedures. Varian Medical Systems, Inc., Palo Alto, CA.

[Van03] Van de Walle J, Martens C, Reynaert N, Palmans H, Coghe M, De Neve W, De Wagter C and Thierens H., 2003 Monte Carlo model of the Elekta SL*i*plus accelerator: validation of a new MLC component module in BEAM for a 6 MV beam. Phys. Med. Biol. 48, 371 - 385

[Van07] Van Battum L. J., Hoffmans D., Piersma H., and Heukelom S., 2007 Accurate dosimetry with GafchromicTM EBT film of a 6 MV photon beam in water: What level is achievable?. Med. Phys. 35, 704-716

[Ver00] Verhaegen F., Symonds-Tayler R., Liu H. H. and Nahum A. E., 2000 Backscatter towards the monitor ion chamber in high-energy photon and electron beams: charge integration versus Monte Carlo simulations. Phys. Med. Biol. 45 3159-70

[Ver03] Verhaegen F. and Seuntjens J., 2003 Monte Carlo modelling of external radiotherapy photon beams. Phys. Med. Biol. 48, R107-R164

[Webb03] Webb S., 2003 The physical basis of IMRT and inverse planning. British Journal of Radiology 76, 678 - 689

[Wal02] Walters B., Kawrakow I., Rogers D.W.O., 2002 History by history statistical estimators in the BEAM code system. Med. Phys. 29, 2745 - 2752

[Wal05] Walters B., Kawrakow I., Rogers D.W.O., 2005 DOSXYZnrc Users Manual. National Research Council of Canada Report PIRS-794revB, Ottawa

[Wel07] Welsh J. S., Mackie T.R. and Limmer J. P., 2007 High-energy photons in IMRT: Uncertainties and risks for questionable gain. Technol. Cancer. Res. Treat. 6, 147 - 149

[Wil46] Wilson R. R., 1946 Radiological use of fast protons. Radiology. 47, 487 91

[Wil52] Wilson R. R., 1952 Monte Carlo of shower production. Phys. Rev. 86, 261 9

[Yang05] Yang J., Li J., Chen L., Price R., McNeeley S., Qin L., Wang L., Xiong W. and Ma C-M., 2005 Dosimetric verification of IMRT treatment planning using Monte Carlo simulations for prostate cancer. Phys. Med. Biol. 50, 869-878

[Yok04] Yokoyama S., Roberson P. L., Litzenberg D. W., Moran J. M., Fraass B. A., 2004 Surface buildup dose dependence on photon field delivery technique for IMRT. J. Appl. Clin. Med. Phys. 5, 71 - 81

[Zar07] Zarza-Moreno M., Leal A., Teixeira N., Jesus A.P., Mora G., 2007 Evaluation of air cavity effect for electron beams dose calculations using Monte Carlo method. Rad. Oncol. 84, S227

[Zar08] Zarza Moreno M., Teixeira N., Jesus A.P., Mora G., 2008 Assesing multileaf collimator effect on the build-up region using Monte Carlo method. Pol. J. Med. Phys. Eng. 14 (3) 163-182

[Zar08b] Zarza-Moreno M., Mateus D., Varelas I., Pontes M., Souto A. C., Borges C., Cardoso I., Teixeira N., Jesus A. P. and Mora G., 2008 Assessment of the multileaf collimator characteristics for Monte Carlo modeling of Intensity Modulated Radiotherapy. Proceedings of the 16th National Conference of Physics (Lisbon, Portugal) p 153